SF 298 MASTER COPY KEEP THIS COPY FOR REPRODUCTION PURPOSES

REPORT DOCUMENTATION PAGE

Form Approved
OMB NO. 0704-0188

1. AGENCY USE ONLY *(Leave blank)*	2. REPORT DATE	3. REPORT TYPE AND DATES COVERED
	9/14/97	Technical Report

4. TITLE AND SUBTITLE

An Apparatus for the Study of Friction and Heat Transfer in Microchannels

5. FUNDING NUMBERS

DAAH04-94-G-0348

6. AUTHOR(S)

Darin K. Bailey
Timothy A. Ameel

7. PERFORMING ORGANIZATION NAME(S) AND ADDRESS(ES)

Louisiana Tech University
P.O. Box 7923 T.S.
Ruston, LA 71272

8. PERFORMING ORGANIZATION REPORT NUMBER

9. SPONSORING / MONITORING AGENCY NAME(S) AND ADDRESS(ES)

U.S. ARMY RESEARCH OFFICE
P.O. BOX 12211
RESEARCH TRIANGLE PARK, NC 27709-2211

10. SPONSORING / MONITORING AGENCY REPORT NUMBER

ARO 33844.5-PH-DPS

11. SUPPLEMENTARY NOTES

The views, opinions and/or findings contained in this report are those of the author(s) and should not be construed as an official Department of the Army position, policy, or decision, unless so designated by other documentation.

12a. DISTRIBUTION / AVAILABILITY STATEMENT

Approved for public release; distribution unlimited.

12b. DISTRIBUTION CODE

13. ABSTRACT *(Maximum 200 words)*

An experimental apparatus was designed to test friction and heat transfer characteristics of microchannels (diameters of 500 μm or less). Two sets of microchannels were tested: a set of nine 508 μm square channels and a single 254 μm square channel. The laminar friction factor for the 508 mm channels was lower than expected and was Reynolds number dependent. This result was attributed to experimental uncertainty. The turbulent data followed theoretical predictions. The heat transfer data were also lower than expected. Again, this result was attributed to experimental uncertainties. The 254 μm channel resulted in lower friction factor, but showed the same trends shown in the Moody diagram: laminar, transition, then turbulence. The Nusselt number data were shown to be within 10% of the theoretical predictions.

In addition, an analytical model which accurately predicts the heat transfer and friction characteristics for the 508 μm rectangular channels tested in this work was developed. The model may be used to predict optimal configurations for future tests. However, the model requires further experimental validation for smaller channel sizes.

14. SUBJECT TERMS

This document describes the design, construction, and qualification of a universal flow loop developed to study flow and heat transfer in microgeometries.

15. NUMBER OF PAGES

248

16. PRICE CODE

17. SECURITY CLASSIFICATION OR REPORT	18. SECURITY CLASSIFICATION OF THIS PAGE	19. SECURITY CLASSIFICATION OF ABSTRACT	20. LIMITATION OF ABSTRACT
UNCLASSIFIED	UNCLASSIFIED	UNCLASSIFIED	UL

AN APPARATUS FOR THE STUDY OF FRICTION AND HEAT TRANSFER IN MICROCHANNELS

TECHNICAL REPORT

DARIN K. BAILEY
TIMOTHY A. AMEEL

JUNE, 1996

U.S ARMY RESEARCH OFFICE

CONTRACT/GRANT NUMBER
DAAH04-94-G-0348

LOUISIANA TECH UNIVERSITY
P.O. BOX 7923 T.S.
RUSTON, LA 71272

ABSTRACT

An experimental apparatus was designed to test friction and heat transfer characteristics of microchannels (diameters of 508 μm or less). Two sets of microchannels were tested: a set of nine 508 μm square channels and a single 254 μm square channel. The laminar friction factor for the 508 μm channels was lower than expected and was Reynolds number dependent. This result was attributed to experimental uncertainty. The turbulent data followed theoretical predictions. The heat transfer data were also lower than expected. Again, this result was attributed to experimental uncertainties. The 254 μm channel resulted in a lower friction factor, but showed the same trends shown in the Moody Diagram: laminar, transition, then turbulence. The Nusselt number data were shown to be within 10% of the theoretical predictions.

In addition, an analytical model which accurately predicts the heat transfer and friction characteristics for the 508 μm rectangular channels tested in this work was developed. The model may be used to predict optimal channel configurations for future tests. However, the model requires further experimental validation for smaller channel sizes.

APPROVAL FOR SCHOLARLY DISSEMINATION

The author grants to the Prescott Memorial Library of Louisiana Tech University the right to reproduce, by appropriate methods, upon request, any or all portions of this Thesis. It is understood that "proper request" consists of the agreement, on the part of the requesting party, that said reproduction is for his personal use and that subsequent reproduction will not occur without written approval of the author of this Thesis. Further, any portions of the Thesis used in books, papers, and other works must be appropriately referenced to this Thesis.

Finally, the author of this Thesis reserves the right to publish freely, in the literature, at any time, any or all portions of this Thesis.

Author Dawn K. Bailey

Date May 11, 1996

GS Form 14
(2/88)

TABLE OF CONTENTS

LIST OF TABLES

LIST OF FIGURES

NOMENCLATURE

A	=	heat transfer area
A_c	=	free-flow area
$Area$	=	cross-sectional area
B	=	bias error
C	=	friction constant ($f\,Re$)
C^*	=	normalized friction constant
C_a	=	acoustic velocity
C_c	=	contraction ratio
C_f	=	Fanning friction factor
C_{max}	=	$\dot{m}C_p$ (maximum value)
C_{min}	=	$\dot{m}C_p$ (minimum value)
C_p	=	specific heat
d	=	depth
d_m	=	molecular diameter
D	=	diameter
D_{eff}	=	effective diameter
D_h	=	hydraulic diameter
D_L	=	laminar equivalent diameter

f	=	Darcy (Manning) friction factor
g	=	gravitational acceleration ($g = 9.81\ m/s^2$)
g_c	=	gravitational constant ($g_c = 1\ kg\ m / (N \cdot s^2)$)
G	=	ρV = mass velocity
h	=	convective heat transfer coefficient
H	=	height
H_c	=	height of channel
h_f	=	head loss (pressure drop)
i	=	current
k	=	thermal conductivity
K	=	loss coefficient
K_d	=	velocity distribution coefficient
Kn	=	Knudsen number
$K(x)$	=	incremental pressure drop number
l	=	length of heated element for plate
L	=	characteristic length
m	=	fin parameter
Ma	=	Mach number
M_{in}	=	Mach number in
$\dot{m}$	=	mass flow rate
n	=	number of samples (data points) taken
N	=	Newton

NTU	=	number of transfer units (heat exchangers)
Nu	=	Nusselt number
P	=	pressure
p	=	perimeter
P	=	precision error
Pe	=	Peclet number
Po	=	Poiseuille number
$Power$	=	power supplied to electric heater on test section
Pr	=	Prandtl number
Q	=	volumetric flow rate
q	=	heat transfer
q''	=	heat flux (q / A)
r	=	molecular radius
r	=	radius of pipe
R	=	resistance of heating element
Re	=	Reynolds number
R_h	=	hydraulic radius
S	=	sample standard deviation
t	=	thickness
t	=	two-sided student's t statistic
T	=	temperature

u	=	x velocity
U	=	overall heat transfer coefficient
U	=	uncertainty interval
v	=	y velocity
V	=	velocity
V	=	voltage
w	=	width of channel
W_c	=	width of channel
x	=	streamwise coordinate
x_o	=	insulated starting length for plate
y	=	normal coordinate

Greek Nomenclature

α	=	aspect ratio (H_c / W_c)
α^*	=	$\alpha^* = 1 / \alpha$ or $\alpha^* = \alpha$ such that $0 \le \alpha^* \le 1$
μ	=	dynamic viscosity
υ	=	kinematic viscosity
υ	=	degrees of freedom (statistical analysis)
λ	=	mean free path
γ	=	ratio of specific heats for gases
ρ	=	density or molecular density (Equation 2.10)
τ_w	=	shear stress evaluated at the wall

ΔP	=	differential pressure
ΔT_{mean}	=	mean temperature difference
δ	=	boundary layer
ϵ	=	roughness
ϵ	=	heat exchanger effectiveness
σ	=	free flow to frontal area ratio
θ	=	overall thermal resistance
θ_m	=	sensitivity coefficient (partial derivative)
θ"	=	modified overall thermal resistance
Θ	=	temperature difference
η_{fin}	=	fin efficiency

ACKNOWLEDGEMENTS

I wish to express my sincere gratitude to several people who helped me on this thesis. Judi Cuta, of Battelle Pacific Northwest Laboratories in Richland, Washington, was extremely helpful with some of the initial equipment and material specifications. She helped to eliminate some of the guess work and mistakes that are often involved in experimental work. Dr. Craig Friedrich fabricated the microchannels and was extremely helpful with the metrology of the microchannels. Murray Rasbury and Jimmy Cook helped me tremendously in the machine shop. Dr. Duli Yu helped to set up the data acquisition system and answered many questions that I had over the past few months. He kept me on the right path many times. Roger Stanley, who is considering two-phase flow in microchannels, brought invaluable experimental experience to the project. He also helped to set up the data acquisition system. I would also like to express my gratitude to Dr. Tim Ameel for his knowledge and guidance over the past few months. Without Dr. Ameel, this project would not have been possible. There are other faculty and staff who have helped me on this project that I would also like to thank: Dr. Barron, Dr. Callens, Dr. Warrington, and Bonnie Sellers. Finally, I would like to thank my wife, Molly, for being patient and supportive over these past few months.

CHAPTER 1

INTRODUCTION

In the past decade, a growing interest in microscale systems and devices, or microelectromechanical systems (MEMS) technology, has developed. The applications and uses for these items are foreseen to be many although, at this time, a significant market for them does not exist. One possible application for this technology is microchip cooling. Past work on MEMS technology has primarily been directed toward fabrication techniques, and considerable progress has been made in this area. Processes such as LIGA, micro-diamond machining and electron beam micro-machining have reached a stage that allows them to be used effectively to produce components for micro-systems. As a consequence, emphasis in MEMS technology is beginning to include areas of analysis and design of micro-systems. Single-phase convection is one area that is beginning to receive a wider emphasis.

An extensive review of the available publications related to microscale single-phase friction and forced convection indicates that the current body of knowledge does not support solid conclusions and sometimes gives conflicting results. In general, most researchers show that friction factor is lower and heat transfer is higher than macroscale

correlations predict. However, some investigations have shown the exact opposite. The one solid conclusion that can be reached is the need for more research in this area.

The objective of this investigation is to design and test an experimental apparatus that may be used to conduct microscale heat transfer and friction experiments. It is hoped that this work will provide information about the current state of knowledge concerning microscale phenomena, show effects present in microchannel flow, and help determine the level at which macroscale correlations may break down.

The experimental apparatus may be used to conduct heat transfer and friction experiments for a variety of fluids and flow conditions. Design considerations were made for both single- and two-phase studies; furthermore, the apparatus is designed to test fluids such as water, light oils, and refrigerants in microchannels with diameters ranging from 10 μm to 500 μm. However, only one fluid, deionized water, was tested for this thesis. The friction and heat transfer tests were performed for a single 254 μm channel and nine 508 μm channels.

CHAPTER 2

LITERATURE REVIEW OF SINGLE-PHASE MICROSCALE PHENOMENA

2.1 Introduction

Work began in the early 1980s on cooling very large scale integrated (VLSI) circuitry with microchannel heat exchangers. Tuckerman (1984) developed a thermal resistance model to predict the thermal performance of heat sinks made up of many large aspect ratio rectangular channels with hydraulic diameters of approximately 95 μm. The channel arrays were approximately 1.4 cm in length by 2 cm in width. Tuckerman (1984) includes data for the heat transfer and friction characteristics of the microchannels. Tuckerman (1984) showed that a heat flux of 790 W/cm^2 could be dissipated with a pressure drop of only 31 psi and a circuit temperature rise of 71°C above the fluid temperature. Phillips (1987) improved on the Tuckerman (1984) model by including more resistance terms, including developing flow friction and Nusselt number correlations, and by considering turbulent and laminar flow. Phillips (1987) developed three resistance models based on 1) a tall aspect ratio, 2) moderate aspect ratio, and 3) a short aspect ratio to account for the different heating situations. Phillips (1987) also wrote an extensive FORTRAN program, MICROHEX, which accurately predicts the thermal performance

of microchannels. His experimental results seem to agree with his predictions for channels of the same approximate sizes as Tuckerman's (1984). Both models are primarily used as design tools to determine the shapes and sizes of channels that will give good thermal performance. The analysis of the friction and forced convection, however, is based on macroscale correlations and contains no microscale effects. Goodling (1993) provides an excellent review of other microchannel heat exchanger work.

Several small scale systems that make use of single-phase convection have been studied. Van Oudhausen (1992) discussed the importance of single-phase convection in the design and application of small scale silicon thermal flow sensors. Microscale pressure sensors have been developed by Pong et al. (1994). Micromembrane pumps, which use both single- and two-phase convection, have been built and studied (Gravesen et al., 1993). Wu and Little (1983, 1984) have developed microscale Joule-Thompson devices for applications in microscale refrigeration cycles. Both single- and two-phase convection models are needed to implement these types of systems.

Several effects, which are normally neglected when considering macroscale flow, may exist in microscale convection. The first of these microscale phenomena are two- and three-dimensional transport effects. As characteristic lengths are reduced to the same order of magnitude as the thermal and hydrodynamic boundary layer thicknesses, both momentum and heat transfer in directions other than the streamwise direction can increase significantly (Ma and Gerner, 1993). Another observed microscale effect is that of temperature variations of the transport fluid (Pfahler et al., 1991) which can cause a significant variation in fluid properties throughout a microsystem, invalidating the often

used assumption of constant properties. In liquids, the influence of molecular polar forces increases (Pfahler et al., 1990, 1991). Changes in the apparent fluid viscosity have also been considered in flow through microchannels (Pfahler et al., 1990).

Besides these effects, some conditions can exist in microscale flow that are not normally seen in macroscale systems, such as slip flow (Beskok and Karniadakis, 1992, Pong et al., 1994, Arkilic et al., 1994). Rarefied gas dynamics show that the continuum assumptions are invalid when the mean free path of the gas is on the order of the characteristic dimension. The Knudsen number relates the mean free path to the characteristic dimension and is defined as (Holman, 1990)

$$Kn = \frac{\lambda}{L} = \sqrt{\frac{\pi\gamma}{2}}\frac{Ma}{Re} \tag{2.1}$$

Microscale effects may also be seen when the mean free path of gases is increased by lowering the pressure or the temperature. Microscale effects may also be observed when flow velocities approach the acoustic velocity of the transport fluid (Gravesen et al., 1993).

The rarefied dynamics model (John, 1984) is based on flow of molecules near a surface which may be classified as specular or diffuse. For perfectly specular surfaces, molecules are reflected at the same angle as the incidence angle. For diffuse surfaces, the molecule can be reflected in any direction regardless of the incidence angle. In reality, most engineering surfaces are diffuse, so some momentum is always lost at the wall. For continuum flow, where the mean free path is very short, there are many molecules in the

region very close to the wall. Momentum exchange between the molecules is more likely to occur. This exchange will result in a zero velocity at the wall. Free molecular flow represents the other extreme where interaction between molecules rarely occurs. There is little build-up of molecules near the wall, as in continuum flow, causing the flow to move along the surface caused by a net velocity in the flow direction. Slip flow occurs between these extremes when there are slight rarefication effects.

While the above-mentioned effects and conditions are not new, none of them has been studied extensively in relation to microscale flow. At this time, it is not completely clear when slip flow becomes important as fluid convection systems are reduced in size. Presently, there are too few experimental data to make this determination. Additionally, there are likely more micro-specific effects and conditions that have yet to be observed. Although the definition of microscale phenomena is incomplete, a fundamental question still arises regarding the classification of microsystems in terms of the effects and/or conditions that are present.

Several authors have proposed "length scales" to classify the occurrence of micro-effects and conditions. For flat plate flow, Ma and Gerner (1993) have proposed a scale using the ratio of thermal boundary layer thickness to the length of the heated element. The scale is applicable to both liquids and gases. Flik et al. (1992) have proposed using the ratio of mean free path to hydrodynamic boundary layer thickness as a scale to determine when slip flow occurs in gases. In defining when slip flow occurs, a value of $Kn \geq 0.01$ is given. Beskok and Karniadakis (1992) have proposed the use of the Knudsen number to classify four flow regimes for gases as

		Kn	$\leq$	10^{-3}	Continuum Flow
10^{-3}	$<$	Kn	$<$	0.1	Slip Flow
0.1	$<$	Kn	$<$	10	Transition Flow
10	$\leq$	Kn			Free Molecular Flow

Beskok and Karniadakis (1992) also attempt to define an empirical scale similar to the Knudsen number for application to liquids. This empirical scale is viewed more as an experimental result and not as the predictor for future experiments. This "liquid Knudsen number" requires further experimental validation.

Defining a single length scale for all types of flow is difficult. Boundary layer thicknesses are convenient for external flows but cannot be applied to duct and tube flows. The question also arises concerning the application of the classical relations for calculating boundary layer thickness in the microscale. Empirical scales for liquids, such as that proposed by Beskok and Karniadakis (1992), would require extensive experimentation to determine. Since full knowledge of these effects has not yet been realized, any length scales used now will likely be only an interim solution.

As mentioned earlier, research into microsystems is just now beginning to shift into areas other than fabrication. Work on microscale single-phase convection is presently not in abundance, but the number of investigators is increasing. In discussing microscale convection research, four general areas are considered: 1) friction factors in microchannels, 2) heat transfer in microchannels, 3) free molecular and continuum flow, and 4) related research (qualitative information.) Some of the following referenced

investigations were not conducted in a microscale system; however, the results from these studies can provide insight into microscale flow and heat transfer phenomena.

2.2 Friction Factors

Friction factors have been measured for microchannels with 0.5 μm ≤ D_h ≤ 100 μm. This section is a summary of the results from seven different investigations. The data include polar and non-polar liquids and data for some gases. The experimental data from the authors mentioned in this section are shown in Figures 2.1 - 2.3 and the channel and flow data are compiled in a concise form in Table 2.1.

For fully developed, incompressible, laminar flow, the friction factor is considered dependent only on the Reynolds number. The common expression for friction factor in laminar tube flow is $f = 64/Re$ (Manning or Darcy friction factor) or $C_f = 16/Re$ (Fanning friction factor.) For rectangular channels, the theoretical fully developed friction factor varies with the aspect ratio (α), where $\alpha = H / w$. A relation for the Manning friction factor is given by Hartnett and Kostic (1989) as

$$f\ Re = 94(1-1.3553\alpha+1.9467\alpha^2-1.7012\alpha^3+0.9564\alpha^4-0.2537\alpha^5) \qquad (2.2)$$

When referring to the Fanning friction factor, it is a common practice to use the Poiseuille number ($C_f\ Re$). Some authors use this form to express their data while others use f as a function of Re. Here, all of the tube and channel data will be reported as a

normalized friction constant (C^*) vs. Re for reasons of consistency. The normalized friction constant is defined as

$$C^* = \frac{f\,Re_{experiment}}{f\,Re_{theory}} \tag{2.3}$$

Wu and Little (1983) conducted experiments measuring the friction factor of gases in microchannels to evaluate the performance of Joule Thomson cryogenic devices. The channels tested in this experiment are unique to this type of application; however, the results may be quantitatively compared to other friction data.

The channels tested by Wu and Little (1983) are larger than most other channels discussed herein. The hydraulic diameter ranges from 50 to 80 μm whereas the channels from other experimenters reported are generally less than 20 μm. The channel descriptions are included in Table 2.1. A unique aspect of the channels is that the surfaces have one smooth side (glass cover plate) and have large relative roughness on the others. Wu and Little (1983) tested both silicon and glass channels. The silicon channels were formed by an etching technique whereas the glass channels were fabricated by an abrasive etching technique similar to sand blasting.

The results of the Wu and Little (1983) experiment were compared to the Moody diagram to decide whether it could be used to aid in the design of microminiature Joule-Thomson devices. The friction factors were shown to be much higher than theory predicted. When the results are compared to the Moody diagram data, it is apparent that the friction data have the same shape as the Moody diagram but are greater in magnitude.

Apparently, the large relative roughness causes greater friction and earlier transition to turbulence. In the roughest channels, the onset of transition to turbulence starts as low as $Re = 350$, while the smoothest microchannel approximately follows the prediction for a smooth pipe.

The Wu and Little (1983) data are shown in Figure 2.1. Some error is introduced into the figures because these data points were originally plotted on log-log graphs. The important point is to realize that the normalized friction constant is greater than unity for all cases, which indicates higher friction than predicted by macroscale (i.e., traditional) theory. The glass channels show the greatest deviation from macroscale theory which is probably due to roughness effects caused by the fabrication technique. In relation to the other data presented here, the relative roughness of Wu and Little's (1983) channels is much larger.

Wu and Little (1983) present three correlations for the laminar, transition, and turbulent regimes for flow in glass channels:

$$f = \frac{(110 \pm 8)}{Re} \qquad Re \leq 900 \quad (2.4)$$

$$f = 0.165(3.48 - \log (Re))^{2.4} + (0.081 \pm 0.007) \qquad 900 < Re < 3{,}000 \quad (2.5)$$

$$f = \frac{(0.195 \pm 0.017)}{Re^{0.11}} \qquad 3{,}000 < Re < 15{,}000 \quad (2.6)$$

The University of Pennsylvania group have presented several papers on microscale convection heat transfer and transport processes. The following is an overview of three of their papers (Harley et al., 1989; Pfahler et al., 1990 and 1991). The objective of their work was to determine the relationship that governs friction for fluid flow in very small channels by attempting to answer the following questions: 1) "At what length scales do the continuum assumptions break down?" 2) "Do the Navier Stokes equations adequately model the fluid flow at these very small scales or should they be modified and if so, how?" 3) "Do certain phenomena become important on microchannels that are neglected in larger channels?" and 4) "Is transition to turbulence affected by the small size of the channels?"

The friction factor used for the experimental results was determined by the macroscale relation for laminar, fully developed, incompressible, steady flow, a no-slip condition at the wall, and constant properties:

$$f = \frac{2D_h \Delta P}{\rho V^2 L} = \frac{8\tau_w}{\rho V^2} \tag{2.7}$$

By rewriting Equation (2.7) for the friction constant $C = f\,Re$, one can see that a very accurate depth measurement is required because of the third order dependency on d (channel depth).

$$C = \frac{8}{\mu}\frac{\Delta P}{LQ}\frac{wd^3}{(1+\frac{d}{w})^2} \tag{2.8}$$

There are twenty sets of data from the three references compiled in Table 2.1. The channels tested are approximately 100 μm wide with depths ranging from 0.5 μm to 50 μm. Many channels tested were relatively wide when compared to the depth (small aspect ratio). The cross-sections of the channels were either trapezoidal or rectangular. The channels were considered very smooth with relative roughness values of approximately 1%, so the roughness effects were negligible. The experimental uncertainties in the friction factors were shown to be no worse than 10%.

Four fluids were tested in the experiments. The liquids included alcohol (polar fluid) and silicon oil (non-polar fluid), while the gases tested were nitrogen and helium.

Some differences were noted between the polar and non-polar liquids (Figures 2.2 and 2.3). For example, the silicon oil exhibited a dependence on the Reynolds number while the alcohol showed a dependence on the channel size and had a smaller apparent viscosity. In the smaller channels (e.g., Figure 2.2, Pfahlr13 $D_h \approx 5.84$), the friction factor for the silicon oil increased with *Re*. Pfahler et al. (1991) claim that this may be a result of shear thickening instead of the expected shear thinning.

The density is assumed constant for the liquids although very high pressures were used in the experiments. The authors point out that the instrumentation is not available to measure temperature profiles and density directly in microchannels, so assumptions on fluid properties and flow characteristics are necessary. Density variation is usually neglected for liquid flow, but it cannot be neglected in gas flow for this experiment.

A compressible flow analysis was used for the gases since very high pressures were used in the experiment. The experimental results show that the friction factors were lower

than those predicted by theory (see Figure 2.1). A slight dependence on Reynolds number was also observed in the smaller channels for both gases. One suggestion for this phenomenon is that the channel dimensions are approaching the size of the mean free path of the gas. With compressible flow at very low Reynolds numbers, a reduction in molecular density (ρ) of the gas may occur and cause the mean free path (λ) of the gas to increase, as shown by Vincinti and Kruger (1965) in the following relationship, where d_m is the diameter of the molecule.

$$\lambda = \frac{1}{\sqrt{2}\pi\rho d_m^2} = \frac{0.707}{4\pi\rho r^2} \tag{2.9}$$

Should this occur, the momentum and energy exchange caused by molecular collisions with the wall becomes a larger percentage of the total exchange. However, Pfahler et al. (1991) did not perform an analysis to determine any rarefication effects. Pfahler et al. (1991) also suggest that this behavior may be due to a viscosity increase in the gas for the smaller channels since the gas is more likely to be at the substrate temperature.

The smaller channels ($D_h < 40$ μm) showed more deviation from the predictions of the Navier-Stokes Equations than the larger channels. Results suggest that the apparent viscosity in the smaller channels decreases when the channel height is reduced. This result may imply that certain phenomena become important at the smaller length scales or that the Navier-Stokes equations are not adequately modeling microchannel flow. For gas flow in very small channels, it was shown that continuum assumptions may break down when the mean free path is of the order of the dimensions of the channel. Pfahler et al. (1991)

suggest that there is no good theoretical explanation for the reduction in friction factor for the larger channels.

Choi (1991a) conducted experiments on the friction and heat transfer characteristics of gaseous nitrogen in circular microtubes with diameters ranging from 3 μm to 81 μm. This work is one of the first to use microtubes instead of microchannels. Most of the work by other researchers deals with the flow characteristics in etched silicon channels with glass covers.

The pressures involved in the experiments were high enough to warrant the use of compressible flow analysis. The Fanno line expression was used to determine the friction factor.

$$f\frac{L}{D} = \frac{1-M_{in}^2}{\gamma M_{in}^2} + \frac{\gamma+1}{2\gamma}\ln\frac{(\gamma+1)M_{in}^2}{2+(\gamma-1)M_{in}^2} \tag{2.10}$$

An uncertainty analysis revealed that the friction factor uncertainty was approximately 13% based on the independent variables.

The results show that the friction factors, for microtubes less than 81 μm, are lower than those predicted by theory (see Figure 2.1). Choi et al. (1991b) did not observe any roughness dependence in the tubes tested; however, the tubes were shown to be very smooth with a relative roughness of 0.0003. The data was correlated using the following expressions for nitrogen flow in microtubes (Choi et al. 1991b):

$$f = \frac{64}{Re}[1 + (30 \pm 7)\frac{\upsilon}{DC_a}]^{-1} \qquad Re < 2{,}300 \quad (2.11)$$

$$f = 0.140Re^{-0.182} \qquad 4{,}000 < Re < 18{,}000 \quad (2.12)$$

Urbanek et al. (1993) considered the temperature dependence of the Poiseuille number in microchannel flow. The laminar Poiseuille number is considered independent of fluid properties and only a function of the cross-section of the channel in macroscale theories. This experiment tested the behavior of different isomers of alcohol (1-, 2-propanol and 1-, 3-pentanol) in microchannels. The fluid temperatures ranged from 0°C to 90°C. The silicon test channels were both triangular and trapezoidal in shape with hydraulic diameters of 5 μm, 12 μm, and 25 μm.

The experimental Poiseuille number was calculated from Equation 2.13:

$$Po_{\exp} = \frac{AreaD_h^2\Delta P}{2\mu QL} \qquad (2.13)$$

which indicates that there is a fourth order dependence on the channel dimensions. The experimenters carefully measured channel dimensions and fluid properties. The results are presented with a 2% uncertainty.

Urbanek et al. (1993) showed that *Po* is not a constant and that values of *Po* were consistently greater than the values predicted by theory. The data also show that the channel size and fluid chemistry had minimal effect on the temperature dependence of *Po*.

These results may represent a deviation from the Navier-Stokes equations because of the temperature dependence. Unfortunately no experimental flow rates were presented, making direct comparison with data presented by other sources impossible. The normalized Poiseuille number, Po_{exp} / Po_{theory}, ranges in value from 1.01 to 1.25. The higher friction values are consistent with the results shown by Wu and Little (1983).

It should be noted that the experimental Poiseuille number is derived from a steady flow energy equation with no heat transfer effects. It is evident that, if heat transfer were to occur, the experimental results would no longer be valid. Consequently, the experimenters used a separate section to heat the fluid and a thermally isolated section to measure the friction characteristics.

Yu et al. (1994) extended the work of Choi (1991a) by conducting experimental and theoretical studies of flow and heat transfer characteristics in microtubes. Yu et al. (1994) determined the friction factors of distilled water as well as gaseous nitrogen in circular tubes ranging in diameter from 19 μm to 102 μm.

Like Choi et al. (1991b), Yu et al. (1994) used the Darcy-Weisbach formula to define the friction factor for incompressible flow and used the Fanno line expression for compressible flow. Yu et al. (1994) determined that the laminar friction constant ($C = fRe$) was approximately 19% less than the theoretical value of 64. This behavior is consistent with Choi et al.'s (1991b) results. The average friction constant ranged from 49.35 to 51.56, which is lower than that obtained by Choi et al. (1991b) ($C \approx 53$). The turbulent friction factors were also lower than the theoretical predictions.

Transition to turbulence occurred at $Re \approx 2{,}000$. The maximum Re was limited to 20,000 because of limitations of the inlet pressure. Turbulent friction factors were about 5% less than the theoretical correlation.

The data given by Yu et al. (1994) is plotted with Choi et al.'s data (1991b) in Figure 2.1 so that the friction factors from similar independent experiments can be compared. Yu et al. (1994) also give friction factor correlations for their data in the following form:

$$f = \frac{50.13}{Re} \qquad Re < 2{,}000 \quad (2.14)$$

$$f = \frac{0.302}{Re^{0.25}} \qquad 6{,}000 < Re < 20{,}000 \quad (2.15)$$

2.3 Heat Transfer

In order to determine the theoretical heat transfer in tubes, the velocity field must be coupled with the temperature field through the energy equation. Given the changes in microscale friction data and the dependence of friction factor on the velocity gradient at the wall, it is evident that the heat transfer characteristics should also change. This section presents the available investigations on heat transfer in microchannels. A summary of the results is included in Table 2.2.

The experiments conducted by Choi (1991a) included evaluating the heat transfer characteristics of microtubes and determining if the friction characteristics could be determined using the Reynolds analogy. Choi found that the Reynolds analogy under-

predicted heat transfer by as much as a factor of seven. Therefore, Choi concluded that the Reynolds analogy does not hold for microchannel flow and that this may be due to suppression of the turbulent eddies in the small channels.

Choi (1991a) found that the Nusselt number (*Nu*) dependence on *Re* was quite different from traditional correlations in both laminar and turbulent flow. The measured values for heat transfer coefficient were larger than theoretical predictions for turbulent flow. Correlations are given for both laminar and turbulent flow regimes:

$$Nu = 0.000972 Re^{1.17} Pr^{1/3} \qquad Re < 2{,}000 \quad (2.16)$$

$$Nu = (3.82 x 10^{-6}) Re^{1.96} Pr^{1/3} \qquad 2{,}500 < Re < 20{,}000 \quad (2.17)$$

The uncertainty in both the heat transfer coefficient and *Nu* was reported as approximately 24%.

Wu and Little (1984) considered heat transfer using nitrogen gas in microchannels that were similar to the channels used in their earlier work on friction factors (Wu and Little, 1983.) The glass channels had large relative roughness, asymmetric roughness, and an approximate hydraulic diameter of 150 μm, which is relatively large when compared to Choi's (1991a) channels.

The experimental set up is applicable mainly to Joule-Thomson refrigerators. The channels have heat transfer on three sides and are considered insulated on the glass top, which causes the heat flux to vary over the surface of the channel. The relative roughness

of the channels complicates the analysis because there are no correlations that can be directly applied to this situation.

Wu and Little (1984) show a higher heat transfer coefficient than predicted by theory which is attributed to the rougher surfaces. It was also shown that the Reynolds analogy did not apply to microchannel flow. This was attributed to the "nonsimilarity of the heat transfer and friction processes for roughened surfaces in these configurations." Three regimes were found for heat transfer: a laminar regime ($Re < 1{,}000$), a transition regime ($1{,}000 < Re < 3{,}000$), and a turbulent regime ($Re > 3{,}000$). The data are correlated by Equation 2.18 for the turbulent regime and are also shown in Figure 2.4.

$$Nu = 0.00222 Pr^{0.4} Re^{1.09} \tag{2.18}$$

Yu et al. (1994) found that the heat transfer data at low Reynolds numbers in both macro- and microtubes were approximately the same. The values diverge as Re increased, with the microtube values being higher than those predicted by theory. This same behavior was observed by Wu and Little (1984) and Choi (1991a). The correlations from these three investigations are compared in Figure 2.4. Yu et al. (1994) also verified that the Reynolds analogy did not hold for microchannel flow and recommend the following heat transfer correlation for microtubes in turbulent flow:

$$Nu = 0.0007 Re^{1.2} Pr^{0.2} \qquad 6{,}000 < Re < 20{,}000 \tag{2.19}$$

Yu et al. (1994) conducted a scaling analysis on the turbulent momentum and energy equations for an incompressible fluid to try to explain the microscale effects they

observed. They suggest that the dissipation energy caused by instabilities is smaller in a microscale flow and that this may explain why a lower friction factor occurs in microtubes.

To explain the increased heat transfer, Yu et al. (1994) use an analogy that compares turbulent lumps of fluid to nucleate boiling processes. Yu et al. (1994) quote Kays and Crawford (1985) to describe a "bursting" process as follows:

> The concept of a sublayer in which relatively large elements of fluid lift off the surface, to be replaced immediately by other fluid from the fully turbulent region, the "bursting" phenomenon discussed earlier, demands a sublayer model for the eddy diffusivity retains a finite magnitude throughout the sublayer and goes to zero only at the wall itself. It should be perfectly possible for an eddy to lose all its x momentum while it still has velocity in the y direction, and thereby to carry heat a greater distance than momentum.

Yu et al. (1994) continue to explain that these turbulent lumps "burst" into the wall in all flow regimes. However, these events occur more often in microsized channels. Thus, an analogy is formed that may explain the reduced friction factor with a corresponding increase in heat transfer for turbulent flow.

2.4 Free Molecular Flow and Continuum Flow

In continuum flow, the no-slip boundary condition is assumed to be applied at the wall; however, it has been speculated by many that slip flow phenomena may occur on the microscale. The Knudsen number (Kn) is commonly used to differentiate between the continuum flow regime, the free molecular flow regime, or a transition region for gases.

Choi (1991a) found that slip flow must be considered for the 3-μm tube with $Kn = 0.022$. The other tubes used in his study ($3\ \mu m \le D \le 81\ \mu m$) resulted in continuum flow. Yu et al. (1994) determined that all of their microtubes fell in the continuum regime.

Beskok and Karniadakis (1992) developed a numerical method that describes momentum transport in "time-dependent slip flows in complex micro-geometries." Their method is based on the spectral element technique that has previously been used to model the Navier-Stokes equations for incompressible flow. To validate their method, they applied it to Couette and Poiseuille flow for which analytical solutions exist. Differences in results for drag coefficients were negligible. They also applied their method to helium flow investigated by Pfahler et al. (1991) which corresponds to $Kn = 0.044$. A numerical value of $C^* = 0.79$ was obtained using the slip flow model. The experimental values given by Pfahler et al. (1991) were $0.8 \leq C^* \leq 0.85$. The slip flow model, however, did not work as well for the shallower channels, which corresponded to $Kn > 0.1$. An attempt was also made to define an empirical parameter for liquid flow based on experimental data obtained by Pfahler et al. (1991). It was decided that further validation of this technique was needed.

Arkilic et al. (1994) investigated helium flow through microchannels (52.25 μm wide, 1.33 μm deep, and 7,500 μm long) for pressure drops of 0.2 to 1.5 atmospheres. It was found that the Navier-Stokes equations with a slip flow boundary condition accurately modeled the flow situation given the following assumptions: steady, incompressible, isothermal flow, negligible entrance and exit effects, and pressure as a function only of the flow direction. The results showed that the pressure drop over the channel length was less than the continuum flow results which is consistent with the data shown in Figures 2.1 - 2.3 (Pfahler et al., 1991; Choi, 1991a; Yu et al., 1994). It must

also be noted that the experimental results by Arkilic et al. (1994) were for very low Reynolds number flow, $0.5 \leq Re \leq 4\text{x}10^{-3}$.

Pong et al. (1994) investigated helium and nitrogen gas flow through microchannels (5 μm wide and 40 μm wide, 1.2 μm deep and 3,000 μm long) using a micro-machined flow system. Pressure sensors were fabricated as an integral part of the flow channels. It was found that the pressure distribution is not a linear function as indicated by a continuum flow analysis, which indicates a lower pressure drop through the channel length than continuum flow. The non-linear pressure distribution becomes more pronounced as *Kn* is increased. It is thought that the non-linearity is caused by compressibility and *Kn* effects. It was also indicated that an asymptotic pressure distribution was not reached although the length-to-height ratio was more than 3,000. Pong et al. (1994) also normalized the pressure data and determined that there is a large viscous effect.

Liu and Tai (1995) used the same flow system described by Pong et al. (1994) to obtain experimental data for gaseous flow. Experimental results were obtained for both uniform and non-uniform cross-section channels. The uniform channel dimensions were 40 μm wide, 1.2 μm high, and 4.5 mm long. The pressure drop distribution was shown to be non-linear. This is consistent with the results shown by Pong et al. (1994). Unfortunately, Liu and Tai (1995) were unable to find a definite relationship between flow rate and pressure. Because of the very low Reynolds numbers in the experiment, the inertial effects were neglected in the mathematical model. It was found that a steady, isothermal, and continuum flow (Navier-Stokes) with a slip boundary condition accurately

modeled the flow situation. However, experimental results showed that the pressure gradients near the inlet and outlet were small, which cannot be explained by the model.

2.5 Related Investigations

Several related investigations have been conducted which are important contributions to the body of knowledge for microscale effects. Ma and Gerner (1993) developed an average Nusselt number relation for steady, two-dimensional flow over a very small heated flat plate with insulated starting lengths. Near the leading edge where the boundary layer thickness is on the order of the length of heated area, boundary layer theory is invalid; thus, microscale effects must be accounted for. The following correlation, which accounts for leading and trailing edge effects, is accurate to within 2%.

$$\overline{Nu}_l = 0.6626 Pr^{1/3} Re_{(x_o+l)}^{1/2} \left[1 - \left(\frac{x_o}{x_o+l}\right)^{3/4}\right]^{2/3} \left[1 + \frac{0.3981 (x_o/l)^{0.5987}}{Pr^{0.3068} Re_{x_o}^{0.4675}}\right] \tag{2.20}$$

This equation has the following restrictions: $0.5 \le Pr \le 100$, $x_o / l \le 50$, and $Re \ge 100$. The derivation of this equation is based on the energy equation in which both the axial and normal heat diffusion terms are retained (the axial term is usually neglected for flat plate flow.)

Dennis and Smith (1966) obtained combined analytical-numerical solutions for steady, incompressible, two-dimensional, isothermal flat-plate flow at very low Reynolds numbers. In their analysis, they used a form of the energy equation that also includes the axial conduction term. Their results indicate that *Nu* is higher than the macroscale results.

Eringen (1964, 1972) extended continuum fluid theory to describe microfluid behavior which is dependant upon the local behavior of individual fluid particles. Called microcontinuum theory, this analysis attempts to describe translation, rotation, and deformation of individual fluid elements. To accomplish this, Eringen adds three relations: "conservation of microinertia," a "balance of momentum moments," and an "entropy inequality" to the classical mass, momentum and energy conservation equations. A disadvantage of this analysis is the large number of "viscosity coefficients" used for simple microfluids. Fluids for which this theory may be applied are anisotropic fluids, liquid crystal fluids, blood flow, and suspensions. Ariman et al. (1973) review numerous microcontinuum theories that have been developed in addition to Eringen's original work.

Jacobi (1989) conducted a study in which microcontinuum theory was applied to flow in microchannels. Fully developed, laminar flow was considered in a circular duct with constant heat flux. The investigation showed that the velocity and temperature profiles were "taller" than the classical profiles. This result would indicate that the wall shear stress is greater for micropolar fluids than for normal engineering fluids. Jacobi (1989) showed that *Nu* is reduced by as much as 7% for micropolar fluids from the theoretical value of 4.36. It should be noted that this result is not consistent with most of the experimental data that have previously been presented. However, the fluids used in the experiments discussed herein are not micropolar fluids as the size of the fluid molecules is much smaller than the characteristic dimension (channel diameter).

2.6 Conclusions

This review suggests that there may be several hydrodynamic and thermal effects that should be considered on the microscale. At this time, the differences in the fundamental mechanisms is highly speculative. Wu and Little (1983) showed higher friction factors than traditional theory would predict, a premature transition to turbulence, and slightly higher heat transfer rates. Urbanek et al. (1993) also showed that the friction factors were higher than theory. In both these studies, the high friction factor data conflict with other investigations. Wu and Little (1983) indicate that the higher friction factors may result from the high relative roughness of their channels. No explanation is given for the friction factor results of Urbanek et al. (1993). The University of Pennsylvania group (Harley et al., 1989; Pfahler et al., 1990 and 1991) showed that as channel depth decreased, there was deviation from macroscale theory by having a higher laminar friction factor that changed with *Re*. In addition, apparent viscosities decreased for smaller channels. There were also some differences observed between polar and non-polar fluids; the friction factor for the polar fluids showed more dependency on the channel size. For gas flow in very small channels, it was shown that continuum assumptions may break down when the mean free path is of the order of the dimensions of the channel. Choi (1991a), Choi et al. (1991b), and Yu et al. (1994) showed that microtubes with diameters less than 80 μm result in lower friction factors than predicted by macroscale theory. However, these results are still inconclusive because of the discrepancies between the various investigations. Additional work is required with increased measurement accuracy to arrive at conclusive evidence of microscale effects.

As alluded to in the introduction, these differences may be caused by deviation from the classical assumptions, namely, the no-slip condition and the one-dimensional transport assumption. These factors can affect the shape of velocity and temperature profiles to the extent that heat and momentum transport are no longer of the same order of magnitude. Thus, the Reynolds analogy is no longer valid. It must be noted that most of the channels tested resulted in fluids which may be considered in the continuum regime, so the slip flow theory for gases cannot explain why lower friction factors were obtained for some experimenters. Yu et al. (1994) have presented a theory for turbulent flow that may explain the reduction in friction factor and the increase in heat transfer in microchannel flow.

Based on the relevant investigations in single-phase microscale heat transfer, several general conclusions can be made. It should be noted that these are preliminary conclusions and future work may alter our perception of microscale heat transfer fundamentals.

1. Friction factors in laminar microchannel flow are apparently lower than macroscale predictions.

2. Turbulent heat transfer is apparently higher than theory predicts.

3. Microscale effects seem to become more prominent for channels smaller than $D_h \leq 40$ μm; however, Yu et al. (1994) showed that microscale effects may be seen in channels with $D_h \geq 80$ μm.

4. Slip flow theories appear to be applicable to only the smallest channels in gas flow. Arkilic et al. (1994) have shown that the pressure gradient was reduced and the mass flow rate profile is not as fully developed as macro theories predict.

5. There is no universally accepted theory to predict the behavior of liquid flow in microchannels.

6. The Reynolds analogy appears to be invalid in the microscale regime.

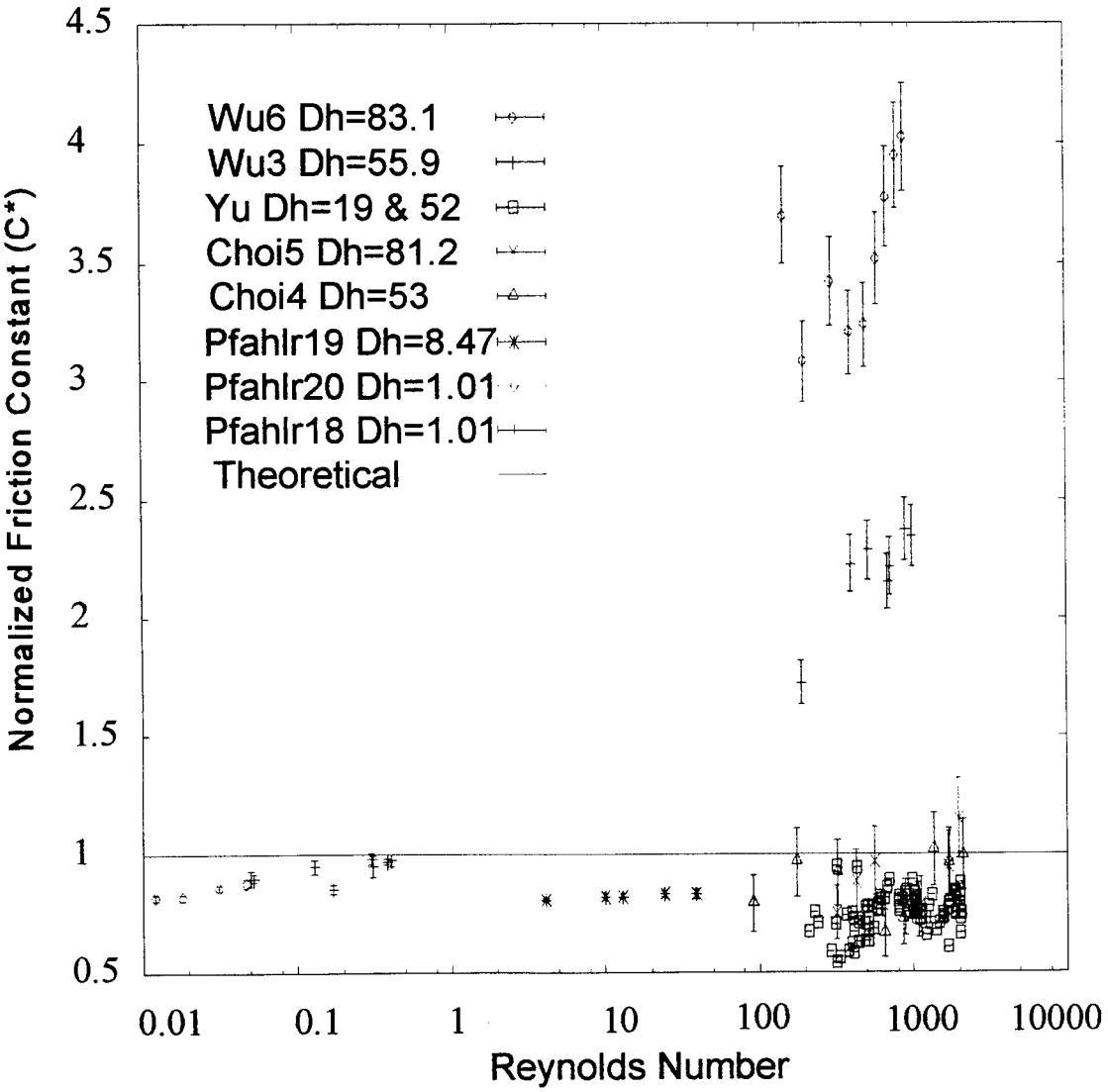

Figure 2.1: Laminar Friction Data for Microchannel Flow (gases)

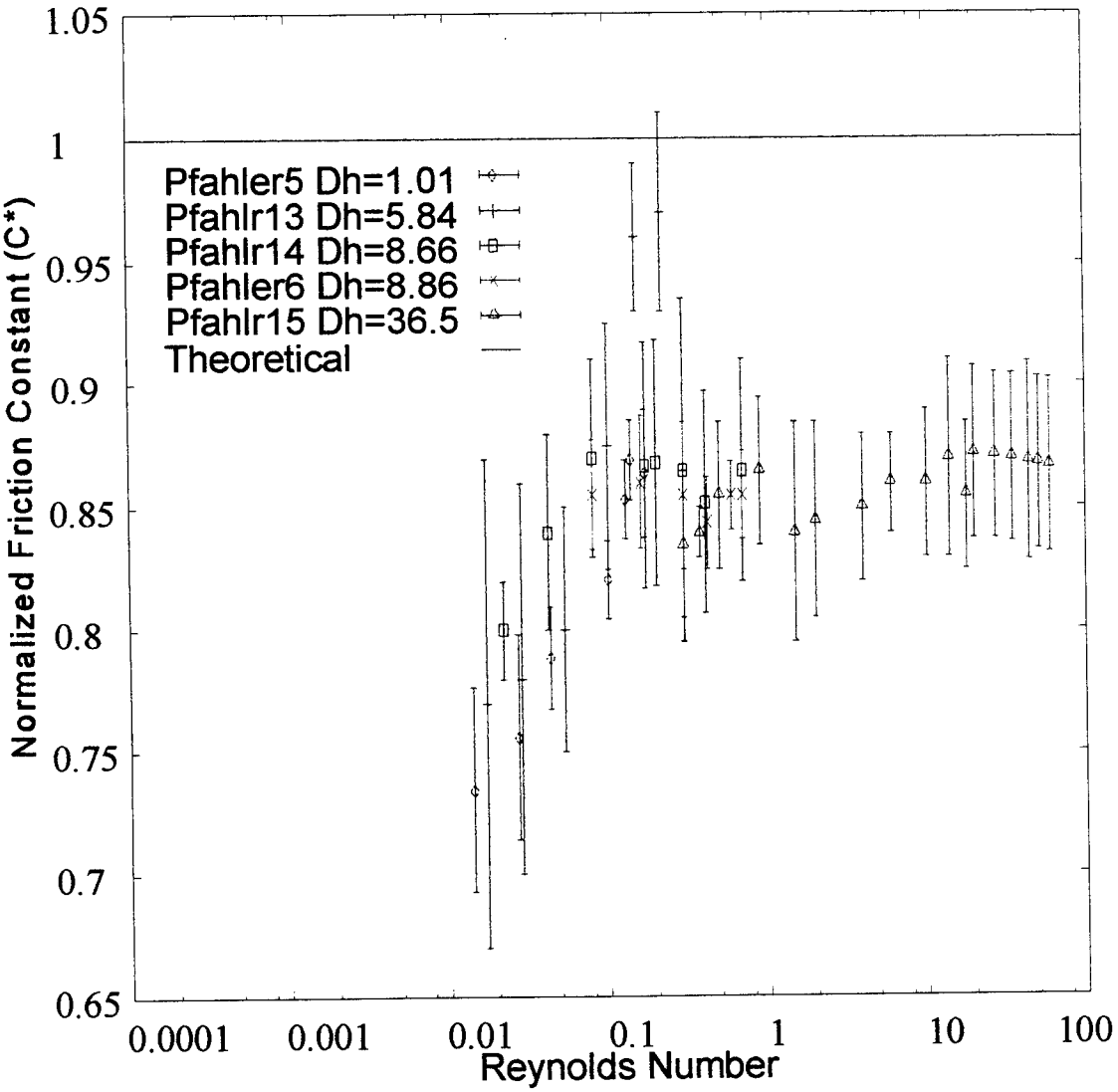

Figure 2.2: Laminar Friction Data for Microchannel Flow (Silicon Oil)

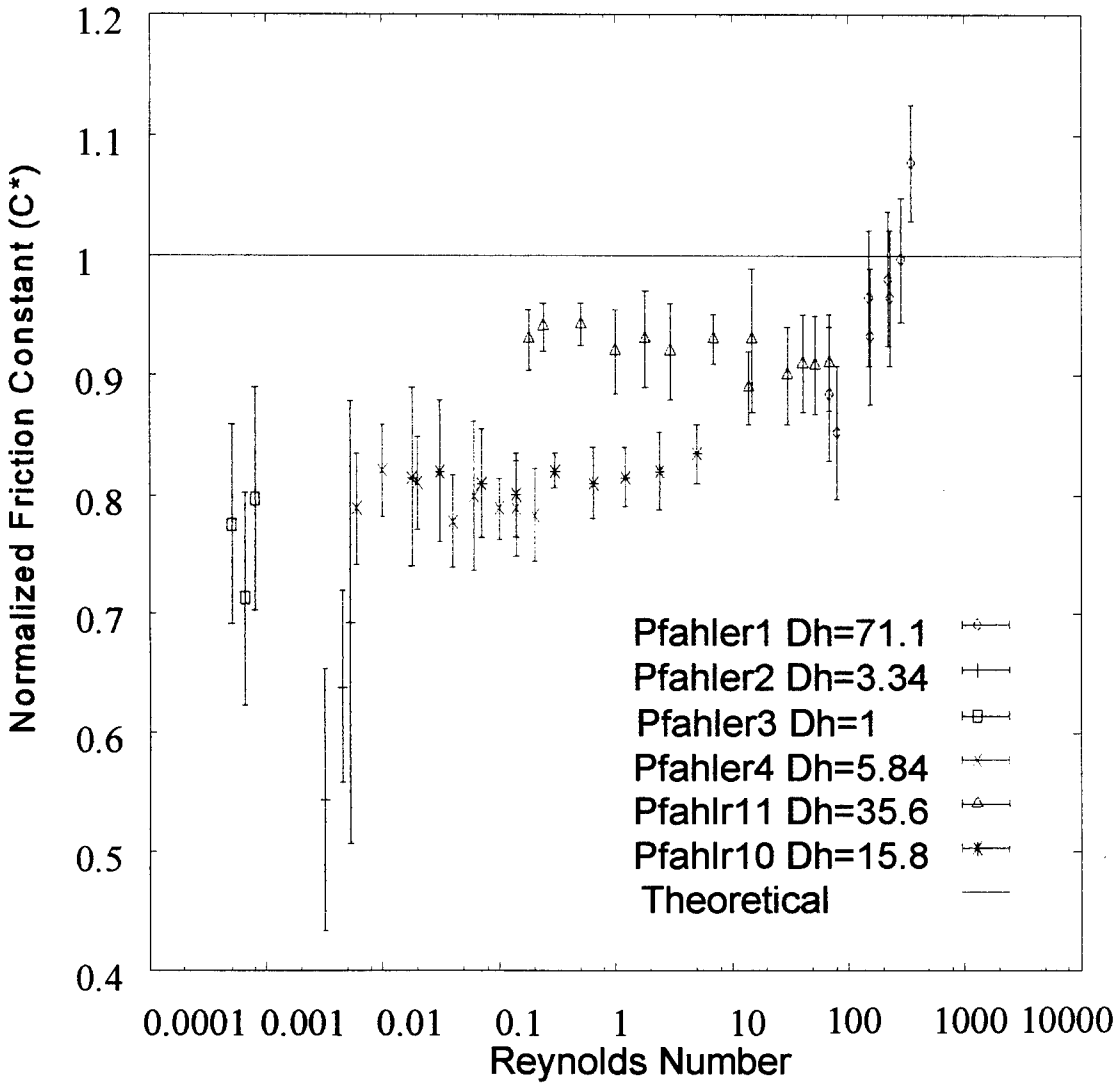

Figure 2.3: Laminar Friction Data for Microchannel Flow (n-propanol)

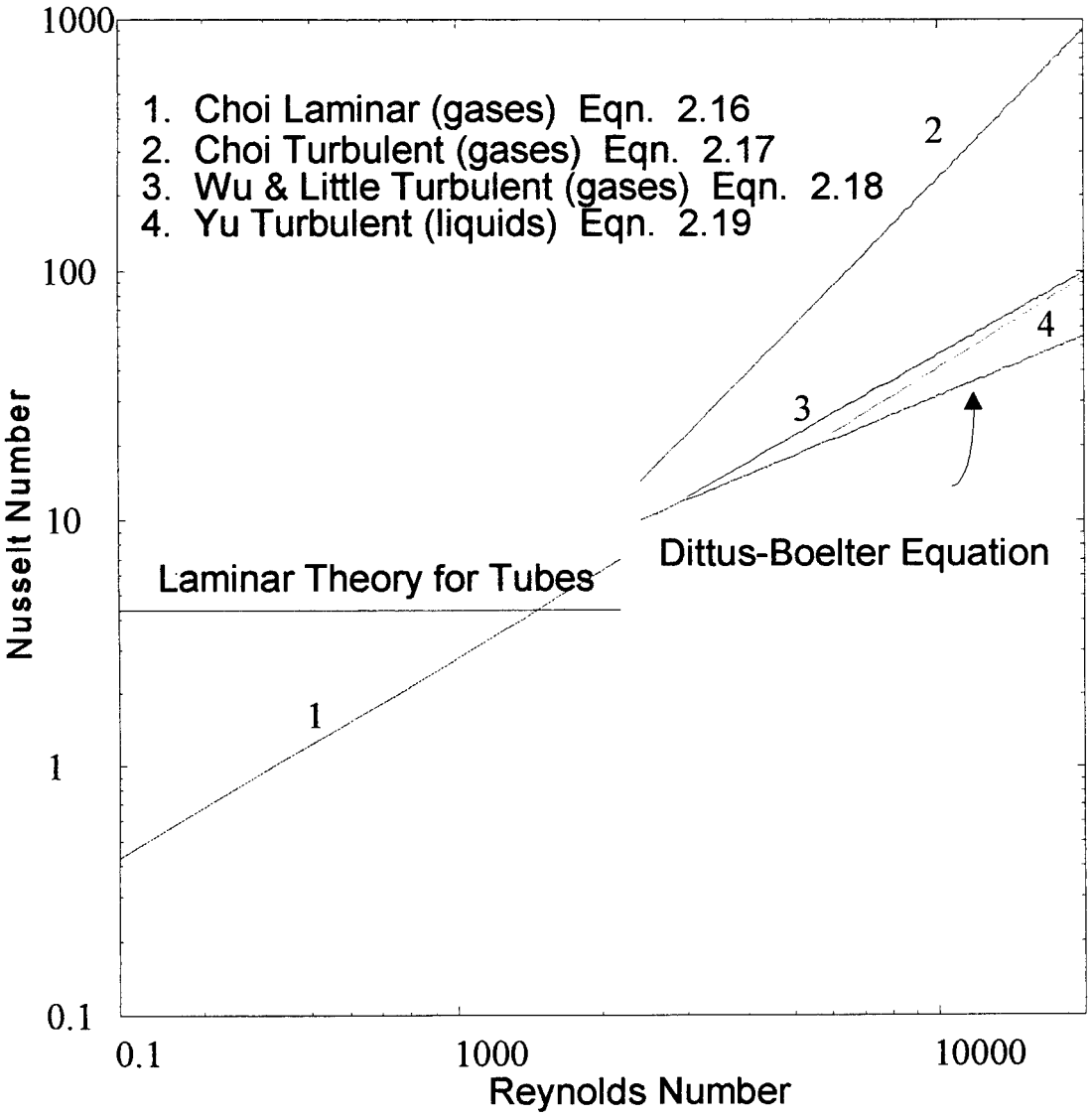

Figure 2.4: Comparison of Heat Transfer Correlations from Various Researchers

Table 2.1: Summary of Friction Data in Microgeometries

Paper	Data Set	Channel	Upper Width (μm)	Lower Width (μm)	Depth (μm)	Aspect Ratio	$f Re = C_{th}$ (theory)	D_h (μm)	Length (mm)	Fluid	Comments
Choi 1991a	Choi 1	tube	n/a	n/a	n/a	n/a	64	3	?	N2	2
	Choi 2	tube	n/a	n/a	n/a	n/a	64	6.9	?	N2	2
	Choi 3	tube	n/a	n/a	n/a	n/a	64	9.7	?	N2	2
	Choi 4	tube	n/a	n/a	n/a	n/a	64	53	?	N2	2
	Choi 5	tube	n/a	n/a	n/a	n/a	64	81.2	?	N2	2
Wu 1993	Wu 1	S(1)	136	77.9	41	0.38	66.3	55.8	7.6	N2	3
	Wu 2	S(1)	136	77.9	41	0.38	66.3	55.8	7.6	Ar	3
	Wu 3	S(2)	145	88.5	39.6	.034	68.16	55.9	40.3	N2	3
	Wu 4	S(3)	146	54	65	0.65	60.1	72.4	7.6	N2	3
	Wu 5*	G(1)	133	133	28	0.21	75.55	45.5	30.3	N2 / He	3, rough channels
	Wu 6*	G(2)	149	149	63	0.42	64.86	83.1	30.3	N2 / He	3, rough channels
	Wu 7*	G(4,5,6)	~195	~195	~47	0.24	~73.5	~73	7.6 to 40.3	N2 / He	3, curvefit in eqns. 4,5,6
Harley 1989	Pfahler 1	rectangle	104	104	54	0.52	62.18	71.1	?	n-propanol	1, entry length effect
	Pfahler 2	rectangle	100	100	1.7	0.02	93.84	3.34	?	n-propanol	1, 2
Pfahler 1990	Pfahler 3	D(5)	115	115	0.5	0.004	95.44	1	10.5	n-propanol	1
	Pfahler 4	E(3)	110	110	3	0.003	95.58	5.84	10.5	n-propanol	1
	Pfahler 5	E(3)	110	110	3	0.003	95.58	5.84	10.5	Si oil	1, 4, non-Newtonain?
	Pfahler 6	NG2	95	95	4.65	0.049	90.06	8.86	10.9	Si oil	2
	Pfahler 7	channel #10	98.7	98.7	4.65	0.047	90.27	8.88	?	N2	2, compressible flow

Comments:
1) Reynolds number dependence
2) C theory > C experimental
3) C theory < C experimental
4) C experimental dependent upon channel dimensions
5) Lower apparent viscosity

Notes:
a) All Wu data approximately follows the shape of the Moody diagram, but C experimental is always larger than C theory
b) C theoretical obtained for the trapezoidal channels by taking an average width
c) * glass channels

Table 2.1: (Continued)

Paper	Data Set	Channel	Upper Width (μm)	Lower Width (μm)	Depth (μm)	Aspect Ratio	$f Re = C_{th}$ (theory)	D_h (μm)	Length (mm)	Fluid	Comments
Pfahler 1991	Pfahler 8	D(5)	115	115	0.5	0.004	95.44	1	10.5	isopropanol	4, 5
	Pfahler 9	E(3)	110	110	3	0.003	95.58	5.84	10.5	isopropanol	4, 5
	Pfahlr 10	K2NS	55	40	10	0.105	71.29	15.8	10.2	isopropanol	4, 5
	Pfahlr 11	VJ8	105	67.2	24.4	0.252	66.83	35.6	10.9	isopropanol	4, 5
	Pfahlr 12	JP5	77.5	22.5	38.7	0.387	54.2	39.7	10.2	isopropanol	~ follows theory
	Pfahlr 13	E(3)	110	110	3	0.003	95.58	5.84	10.5	Si oil	1, 2
	Pfahlr 14	NG2	95	95	4.65	0.049	90.3	8.66	10.2	Si oil	1, 2
	Pfahlr 15	VJ5	105	70	24.5	0.140	67.57	36.5	10.9	Si oil	2
	Pfahlr 16	JP9	96.2	88.6	4.44	0.048	90.13	8.47	10.9	N2	2
	Pfahlr 17	JH10	104	93.7	4.65	0.047	90.37	8.88	10.9	N2	2
	Pfahlr 18	JH6	96.6	96.6	0.51	0.005	95.13	1.01	10.9	N2	2
	Pfahlr 19	JP9	96.2	88.6	4.44	0.048	90.13	8.47	10.9	He	2, slight *Re* dependence
	Pfahlr 20	JH6	96.6	96.6	0.51	0.005	95.13	1.01	10.9	He	1, 2
Yu 1994	Yu 1	tube	n/a	n/a	n/a	n/a	64	19.6	~41	N2	$f Re \sim 49$
	Yu 2	tube	n/a	n/a	n/a	n/a	64	52.1	~41	N2	$f Re \sim 52$
	Yu 3	tube	n/a	n/a	n/a	n/a	64	52.1	~41	water	$f Re \sim 50$
	Yu 4	tube	n/a	n/a	n/a	n/a	n/a	102	~41	water	only turbulent results, 5% lower friction

Comments:
1) Reynolds number dependence
2) *C* theory > *C* experimental
3) *C* theory < *C* experimental
4) *C* experimental dependent upon channel dimensions
5) Lower apparent viscosity

Notes:
a) All Wu data approximately follows the shape of the Moody diagram, but *C* experimental is always larger than C theory
b) *C* theoretical obtained for the trapezoidal channels by taking an average width
c) * glass channels

Table 2.2: Summary of Single-Phase Heat Transfer Data in Microgeometries

Paper	Data Set	Channel Config.	Width (μm)	Depth (μm)	Aspect Ratio	D_h (μm)	Working Fluid	Comments on *Nu*
Choi 1991a	Choi 2	1 tube	n/a	n/a	n/a	9.7	Nitrogen	slightly lower than theory
	Choi 3	1 tube	n/a	n/a	n/a	53	Nitrogen	higher than theory for all *Re*
	Choi 4	1 tube	n/a	n/a	n/a	81.2	Nitrogen	higher than theory for all *Re*
Wu 1984	Wu 1	2 adjacent. rectangular	548, 548	92	0.1678	156	Nitrogen	at $Re < 700$ below theory, above theory for higher *Re*
	Wu 2	2 adjacent. rectangular	493, 493	92	0.1866	153	Nitrogen	at $Re < 400$ below theory, above theory for higher *Re*
	Wu 3	2 adjacent. rectangular	572, 572	97	0.1696	164	Nitrogen	at $Re < 370$ below theory, above theory for higher *Re*
	Wu 4	3 adjacent. rectangular	312, 526, and 312	89	0.2853 and 0.1692	134, 151	Nitrogen	at $Re < 350$ below theory, above theory for higher *Re*
Yu 1994	Yu 1	1 tube	n/a	n/a	n/a	19	Nitrogen / water	higher heat transfer in turbulent regime, no data for laminar
	Yu 2	1 tube	n/a	n/a	n/a	52	Nitrogen / water	higher heat transfer in turbulent regime, no data for laminar
	Yu 3	1 tube	n/a	n/a	n/a	102	Nitrogen / water	higher heat transfer in turbulent regime, no data for laminar

CHAPTER 3

HYDRODYNAMIC FLOW THEORY

The purpose of this chapter is to review the conventional hydrodynamic flow theory and correlations used for tube flow. The discussion will be extended to channel flow for various aspect ratio rectangular channels. This will be the basis for a mathematical model which will be used to predict the pressure drop in single rectangular channels in the laminar, transition, and turbulent flow regimes.

3.1 Laminar Friction Factor

The Darcy friction factor relates roughness effects to pressure drop in pipes and is defined by the following equation:

$$f = \frac{\tau_w \, 8}{\rho \, u_{avg}^{\,2}} \tag{3.1}$$

The Darcy-Weisbach equation, Equation 3.2, is derived by solving the energy and momentum equations for fully developed pipe flow and combining the result with the Darcy friction factor relation. This equation is used to determine the head loss, or pressure drop, in pipes. The Darcy-Weisbach equation holds true for both laminar and turbulent flow.

$$h_f = f \frac{L}{D} \frac{V^2}{2g} \tag{3.2}$$

The laminar solution for head loss in pipes may be found by solving the continuity and momentum equations for the Hagen-Poisseuille flow problem. The wall shear stress is evaluated using the following relation and then substituted in the Darcy friction factor equation.

$$\tau_w = - \mu \frac{\partial u}{\partial r} \tag{3.3}$$

The result is the commonly used laminar Darcy friction factor.

$$f = \frac{64}{Re} \tag{3.4}$$

The Reynolds number (*Re*) is defined as

$$Re = \frac{\rho V D}{\mu} \tag{3.5}$$

It has been shown by Choi (1991a) that the friction constant (*f Re*) for tube flow, as shown in Equation 3.4, may not apply to microscale flow. Choi (1991a) showed that this constant is actually closer to 53 for tubes with diameters of the order of 100 μm. The purpose of this study is to design a test apparatus to determine the pressure drop characteristics of flow through microchannels. To be conservative, the estimates for laminar friction factor will be calculated using conventional correlations.

Laminar fully developed friction factors in rectangular-shaped ducts are usually determined by referring to a table or graph of friction constants for different aspect ratios (α^*). The aspect ratio in this case is defined such that $0 \leq \alpha^* \leq 1$. Thus, α^* may be defined as height/width or width/height. White (1986) gives the analytical solution to the laminar friction constants for various aspect ratio rectangular channels. The solutions are given in Table 3.1.

Table 3.1: Laminar Friction Constant for Various Aspect Ratio Rectangular Channels

α^*	$f Re_{Dh}$
0	96
0.05	89.91
0.1	84.68
0.125	82.34
0.167	78.81
0.25	72.93
0.4	65.47
0.5	62.19
0.75	57.89
1	56.91

The friction constant is only a function of aspect ratio. For computer applications, the Darcy friction factor may be calculated using Equation 3.6 (Hartnett and Kostic, 1989) that is accurate to 0.05% of the analytical values.

$$f\,Re = 96(1 - 1.3533\alpha^* + 1.9467\alpha^{*2} - 1.7012\alpha^{*3} + 0.9564\alpha^{*4} - 0.2537\alpha^{*5}) \qquad (3.6)$$

The Fanning friction factor may also be determined by dividing Equation 3.6 by four.

3.2 Developing Laminar Friction Factor

Developing flow must be considered in pipes when the distance from the pipe entrance is less than the entry length. White (1986) defines the entry length (L_e) for laminar flow in circular tubes as

$$\frac{L_e}{D} \cong 0.06\ Re_D \qquad (3.7)$$

The boundary layer (δ) is usually defined as the distance from the wall to where the velocity is equal to 99% of the free stream value for flat-plate flow. For pipe flow, the boundary layer begins to grow from the wall beginning at the tube entrance and will continue to grow until the shear layers meet. Flow is considered fully developed after the boundary layers have met at some distance downstream from the entrance and the centerline velocity has reached 99% of the fully developed value. The velocity profile will then have the typical parabolic shape.

The region of developing flow has a higher pressure drop than the fully developed flow region. This is easy to see by considering the definition of wall shear stress (Equation 3.3). Near the entrance region, the boundary layer is very small. This means that the velocity equals zero at the wall, often called the "no-slip condition," and the velocity a very short distance away is 99% of the free stream value. The change in velocity with respect

to the radial direction is very large (i.e., the shear stress is large). This condition relates to a larger friction factor and, thus, a higher pressure drop in this region.

To model the pressure drop in rectangular channels, an apparent Fanning friction factor (f_{app}) will be used (see Table 3.2).

Table 3.2: Apparent Friction Factor in Rectangular Ducts

$x^+ = (x/D_h)/Re$	$f_{app}\,Re$			
	$\alpha = 1.0$	**$\alpha = 2.0$**	**$\alpha = 5.0$**	**$0.1 \le \alpha \le 10.0$**
≈ 0	142	142	142	287
0.001	111	111	111	112
0.003	66	66	66.1	67.5
0.005	51.8	51.8	52.2	53
0.007	44.6	44.6	45.3	46.2
0.009	39.9	40	40.6	42
0.01	38	38.2	38.9	40.4
0.015	32.1	32.5	33.3	35.6
0.02	28.6	29.1	30.2	32.4
0.03	24.6	25.3	26.7	29.7
0.04	22.4	23.2	24.9	28.2
0.05	21	21.8	23.7	27.4
0.06	20	20.8	22.9	26.8*
0.07	19.3	20.1	22.4	26.4*
0.08	18.7	19.6	22	26.1*
0.09	18.2	19.1	21.7	25.8*
0.1	17.8	18.8	21.4	25.6*
0.2	15.8	17	20.1	24.7*
≥ 1.0 (fully developed)	14.2	15.5	19.1	24

* Based on a linear interpolation

The apparent friction factor is a function of the dimensionless parameter x^+.

$$x^+ = \frac{x}{D_h \, Re_{D_h}} \tag{3.8}$$

The Reynolds number based on the hydraulic diameter (D_h) is defined as

$$D_h = \frac{(4 \quad cross\text{-}sectional \ area)}{(wetted \ perimeter)} \tag{3.9}$$

This apparent friction factor accounts for both the wall shear and momentum change caused by the developing velocity profile. Phillips (1987) used the data shown in Table 3.2 to account for developing flow in rectangular-shaped channels. It should be noted that the original data were obtained from numerical calculations performed by Curr et al. (1972). Hartnett and Kostic (1989) showed that the analytical predictions for this type of flow were generally higher than the experimentally determined values. Thus, these apparent friction factor values predict slightly higher than experimental values.

Shah and Bhatti (1987) included the parameters for which hydrodynamically developing flow is defined. Shah and Bhatti (1987) define a dimensionless pressure drop from the inlet ($x = 0$) to the point of interest as

$$\Delta P^* = \frac{P_o - P}{\rho \, u_m^2 / 2 \, g_c} = f_{app} \, \frac{x}{R_h} \tag{3.10}$$

where,

$$R_h = \frac{D_h}{4} = \frac{(cross\text{-}sectional \ area)}{(wetted \ perimeter)} \tag{3.11}$$

Shah and Bhatti (1987) also define an incremental pressure drop number, $K(x)$, for the hydrodynamically developing region which takes into account the change in momentum and the additional wall shear.

$$K(x) = (f_{app} - f_{Fanning}) \frac{x}{R_h} \tag{3.12}$$

where,

f_{app} = *apparent Fanning friction factor*
$f_{Fanning}$ = $f_{Darcy} / 4$

The value of $K(x)$ has a value of zero at the entrance of the pipe and approaches a constant value in the fully developed regime. This result is consistent with theory, because the flow will reach a point where it is no longer accelerating and the change in momentum will be zero. In addition to this, the friction factor should approach some constant value in the fully developed regime.

By using $K(x)$, the pressure drop may be defined in both a dimensionless form (ΔP^*) and in a dimensional form (ΔP).

$$\Delta P^* = (f_{app} \, Re) 4x^+ = K(x) + f \, Re(4x^+) \tag{3.13}$$

$$\Delta P = \frac{4 \, (f_{app} \, Re) \, \mu u_m \, x}{2 g_c \, D_h^2} = \frac{4 \, (f \, Re) \, \mu u_m \, x}{2 g_c \, D_h^2} + \frac{K(x) \, \rho u_m^2}{2 g_c} \tag{3.14}$$

The value of f_{app} must be multiplied by four to give the Darcy friction factor because this derivation is based on the Fanning friction factor. It is evident that f_{app} may be used directly as the developing region friction factor because, once a value of $x^+ > 1$ is reached, the fully developed value will be used. To account for the developing flow in the mathematical model, the x^+ ratio is calculated for the length of the tube. Next, $f_{app}Re$ is found by using Table 3.2 to linearly interpolate between $\alpha = 1$ (square ducts) and $\alpha \leq 0.1$ (gap).

3.3 Transition Friction Factor

Shah and Bhatti (1987) note that there are no reliable correlations to handle friction and heat transfer for arbitrary aspect ratio channels in the transition regime. However, they indicate that it is usually acceptable to use circular pipe correlations with the hydraulic diameter substituted for the diameter. Shah and Bhatti (1987) list the critical *Re* for various aspect ratio channels with sharp, abrupt entrances (similar to the microchannel heat exchanger entrances.)

Table 3.3: Critical Reynolds Numbers in Rectangular Ducts

α^*	0	0.1	0.2	0.2555	0.3425	1
***Re* (critical)**	3,100	2,920	2,500	2,400	2,360	2,200

Although it is realized that transition will occur at various *Re*, to simplify the mathematical model, the transition *Re* will be arbitrarily chosen as 2,300.

3.4 Turbulent Friction Factor

White (1986) recommends using the Prandtl pipe friction law to calculate the friction factor in rectangular ducts.

$$\frac{1}{\sqrt{f}} = 2.0 \log(Re_d f^{1/2}) - 0.8 \qquad (3.15)$$

White (1986) further states that, as a general rule, Re_{Deff} is used in place of Re_D when rectangular ducts are used. The concept of the effective diameter, D_{eff}, is used to calculate Re_{Deff}.

$$Re_{Deff} = \frac{\rho u_{avg} D_{eff}}{\mu} \qquad (3.16)$$

$$D_{eff} = D_h \frac{64}{(f\,Re)_{LAMINAR}} \qquad (3.17)$$

Equation 3.15 is a transcendental equation in f which adds to the complexity of the math model and increases the likelihood of convergence problems. White (1986) explains that the Haaland equation is accurate to within 2% of the Moody diagram and is explicitly defined. It is for this reason that the Haaland equation, defined by Equation 3.18, will be used.

$$\frac{1}{\sqrt{f}} = -1.8 * \log\left[\frac{6.9}{Re_D} + \left(\frac{\epsilon/D}{3.7}\right)^{1.11}\right] \qquad 4{,}000 \le Re \le 10^8 \qquad (3.18)$$

The value of the diameter (D) in the Haaland equation is usually taken as the hydraulic diameter (D_h) or the effective diameter (D_{eff}) for rectangular geometries. The effective diameter will be used in the model. The approximate values for roughness for the tubes tested by Choi (1991a) are listed in Table 3.4. A value of $\epsilon = 0.0174$ may be used for the friction factor calculations to estimate the losses in microchannels if no other data are available. The tubes used by Choi (1991a) are considered to be very smooth. For a conservative estimate of f, a higher roughness value than those listed will be used until roughness measurements are made on the microchannels tested. From these values, estimates of the friction factor can be made prior to experimentation.

Table 3.4: Roughness Data Used by Choi (1991a)

D (μm)	ϵ/D	ϵ (μm)
3	0.0058	0.0174
6.93	0.0115	0.0796
9.7	0.0011	0.0107
53	0.0003	0.0159
81	0.0002	0.0162

Phillips (1987) used an approach similar to the effective diameter method to determine fully developed friction factors. He used a "laminar equivalent diameter" to define a "laminar equivalent Reynolds number." Shah and Bhatti (1987) also recommended the use of the equivalent Reynolds number (Re^*) which is defined as

$$D_L = [(2/3) + (11/24)\alpha^*(2-\alpha^*)]\, D_h \tag{3.19}$$

where α^* = (short side / long side) such that $0 \leq \alpha^* \leq 1$

$$Re^* = \frac{\rho_f V D_L}{\mu_f} \tag{3.20}$$

It was found that the use of Re^* and Re_{Deff} gave similar values for the friction factor. The laminar equivalent Reynolds number will be used for the pressure drop model.

To obtain the friction factor, Phillips (1987) substituted Re^* into a revised form of the Karman-Nikuradse equation for smooth circular pipes:

$$\frac{1}{\sqrt{f}} = 1.737 \ln[Re^*(f)^{1/2}] - 0.4 \tag{3.21}$$

Phillips (1987) states that a 5% uncertainty should be placed on the values obtained in this manner.

3.5 Developing Turbulent Friction Factor

The entry length in turbulent flow is not as much of a problem as it is with laminar flow. This is because turbulent boundary layers grow faster than laminar boundary layers. White (1986) defines the turbulent entry length for tube flow as

$$\frac{L_e}{D} \cong 4.4\, Re_D^{1/6} \tag{3.22}$$

Phillips (1987) considered developing flow in his thesis. He presents the following curvefit for both fully developed and developing flow. The original data were obtained from Kays and Perkins in Rohsenow et al. (1985).

$$f_{app} = A(Re)^B \qquad Re < 28{,}000 \qquad (3.23)$$

where, $A = -0.09290 + 1.01612 / (x/D_h)$
$B = -0.26800 - 0.31930 / (x/D_h)$

Equation 3.23 is a best fit of the data and represents an average turbulent friction factor. The curvefit has a correlation of ± 4.1% with the original data. To obtain the friction factor for rectangular channels, *Re* is replaced by *Re**. This equation agrees to within 2% of the Karman-Nikuradse correlation for fully developed flow and is assumed, by Phillips (1987), to be reasonably accurate in the developing region.

It must be noted that the curvefit (Equation 3.22) does not take roughness effects into account. Phillips tested four configurations of microchannels each with a $D_h \approx 100$ μm. He also reported that the roughness of the channels ranged from 5 μm to 10 μm. The relative roughness, (ϵ / D_h), is on the order of 0.05 which is considered to be very rough when observing typical values shown on the Moody diagram. It is probably inappropriate to use Equation 3.23 for microchannel flow because the small diameters will result in high values of relative roughness.

The author is not aware of any turbulent developing flow friction factor correlations for rough ducts. To resolve this problem, we can choose a channel length that is sufficiently long, so that the entry length in turbulent flow will occupy only a small

percentage of the total length. Since turbulent boundary layers grow much faster than laminar boundary layers, we can then neglect developing turbulent flow.

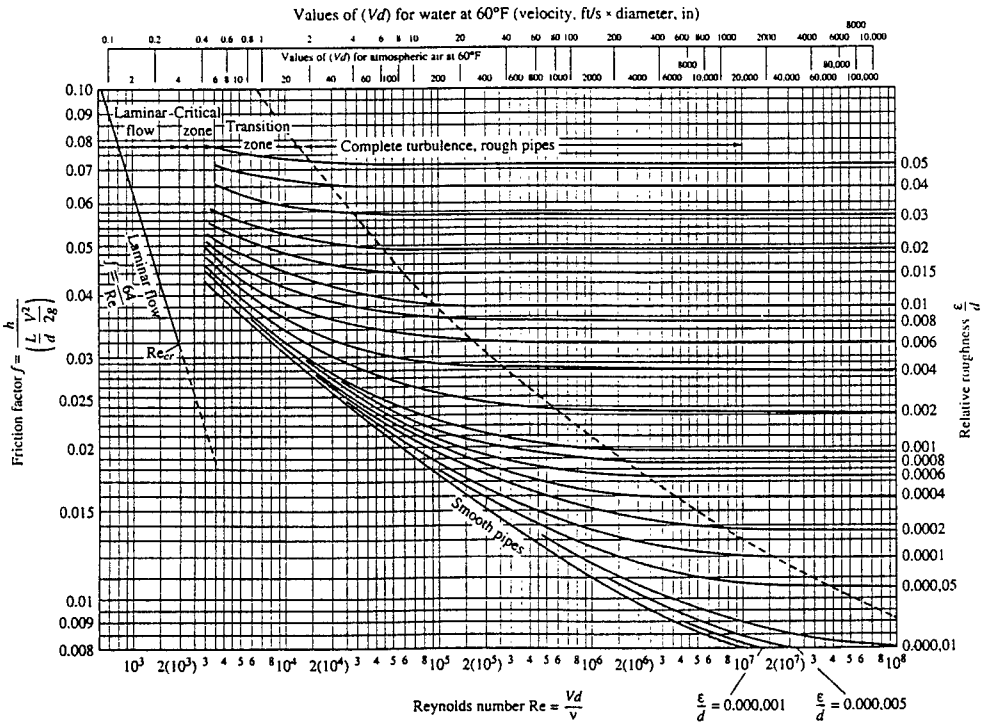

Figure 3.1: Moody Diagram

CHAPTER 4

PRESSURE DROP MODEL

The mathematical model used to determine pressure drop in single channels can be extended to predict pressure drop in multiple channels. Chapter 3 discusses how to analyze hydrodynamic flow in straight tubes and channels. However, with the microchannels used for this thesis, there are effects such as bends, contractions, and expansions that must be accounted for. Chapter 4 shows the development of a model, which may be used for either single or multiple channels, which includes these effects.

4.1 Pressure Drop in Heat Exchangers

The most commonly used heat exchanger pressure loss model was originally presented by Kays and London (1964) and is also given in Hodge (1990). This model includes entrance and exit effects, accelerating flow effects, and the effects of wall friction. The model is applicable to single as well as multiple tubes by keeping or omitting certain terms. In the next section, various expansion and contraction losses are given for different geometries.

$$\frac{\Delta P}{P_1} = \frac{G^2/2g_c}{P_1\ \rho_1}\left[(K_c+1-\sigma^2) + 2\left(\frac{\rho_1}{\rho_2}-1\right) + f\frac{A}{A_c}\frac{\rho_1}{\rho_m} - (1-\sigma^2-K_e)\frac{\rho_1}{\rho_2}\right] \tag{4.1}$$

where,

A	=	Total heat transfer area
A_c	=	Free-flow area
f	=	Fanning friction factor
G	=	$\rho_a V_a = \rho_b V_b$ = mass velocity
g_c	=	Gravitational constant
K_c	=	Loss coefficient for contraction
K_e	=	Loss coefficient for expansion
P_1	=	Inlet pressure
ΔP	=	Differential pressure drop across the heat exchanger
V	=	Fluid velocity based on the free flow area of one channel
ρ_1	=	Density of fluid (inlet)
ρ_2	=	Density of fluid (outlet)
ρ_m	=	Density of fluid (mean)
σ	=	Free flow to frontal area ratio

A schematic of a typical heat exchanger, appropriate for use with Equation 4.1, is shown in Figure 4.1.

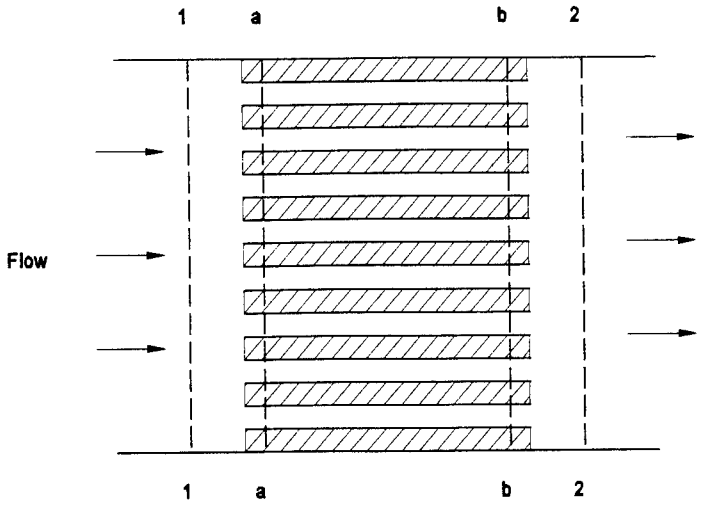

Figure 4.1: Heat Exchanger Pressure Drop

where,

A	=	Total heat transfer area
A_c	=	Free-flow area
f	=	Fanning friction factor
G	=	$\rho_a V_a = \rho_b V_b$ = mass velocity
g_c	=	Gravitational constant
K_c	=	Loss coefficient for contraction
K_e	=	Loss coefficient for expansion
P_1	=	Inlet pressure
ΔP	=	Differential pressure drop across the heat exchanger
V	=	Fluid velocity based on the free flow area of one channel
ρ_1	=	Density of fluid (inlet)
ρ_2	=	Density of fluid (outlet)
ρ_m	=	Density of fluid (mean)
σ	=	Free flow to frontal area ratio

A schematic of a typical heat exchanger, appropriate for use with Equation 4.1, is shown in Figure 4.1.

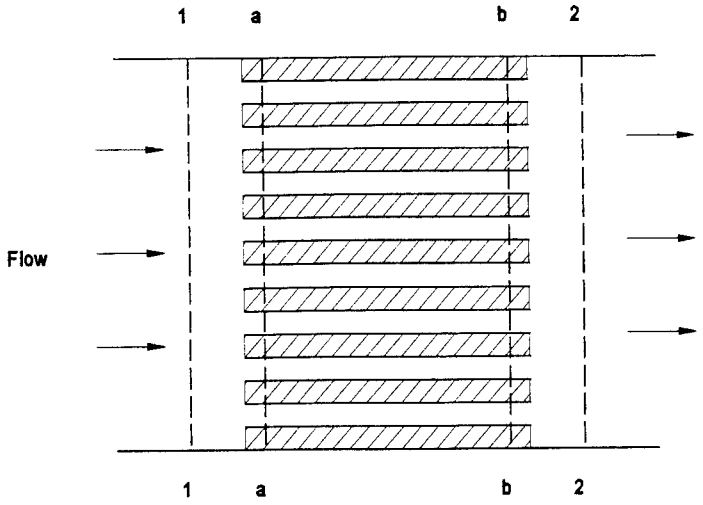

Figure 4.1: Heat Exchanger Pressure Drop

Kays (1985) defines the third term in the brackets (Equation 4.1) slightly differently. The third term represents the core friction and is shown as

$$4f\frac{L}{D}\frac{\rho_1}{\bar{\rho}} \tag{4.2}$$

By substituting for A and A_c in Equation 4.1, where $A = \pi DL$ and $A_c = \pi D^2/4$, one can easily see how this relation is obtained. It must be noted that the friction factor shown here is the Fanning friction factor which is 0.25 of the value of the Darcy friction factor.

Equation 4.1 can be modified to include extra loss terms such as 90° bends into the heat exchanger. Phillips (1987) used a modified form of Equation 4.1, as given by:

$$\frac{\Delta P}{P_1} = \frac{K_b V_1^2/2g_c}{P_1/\rho_1} + \frac{G^2/2g_c}{P_1\,\rho_1}\left[(K_c+1-\sigma^2)+2\left(\frac{\rho_1}{\rho_2}-1\right)+f\frac{L}{D_h}\frac{\rho_1}{\rho_m}-(1-\sigma^2-K_e)\frac{\rho_1}{\rho_2}\right]+\frac{K_b V_2^2/2g_c}{P_1/\rho_2} \tag{4.3}$$

This is the form of the heat exchanger pressure drop model that will be used in this study. To be consistent, the Darcy friction factor will be used as shown in Equation 4.3.

4.2 Contraction and Expansion Losses

For incompressible flow, contraction and expansion (K_c and K_e) losses may be evaluated by the following equation:

$$K = \frac{2g\,\Delta P}{\rho\,V^2} \tag{4.4}$$

By assuming that the flow has a uniform velocity distribution before entering the tubes, Kays (1950) shows that the expansion loss and the contraction loss are best represented by Equations 4.5 and 4.6, respectively.

$$K_e \simeq 1 - 2\sigma K_d + \sigma^2 \tag{4.5}$$

$$K_c \simeq \frac{1 - 2C_c + C_c^2 (2K_d - 1)}{C_c} \tag{4.6}$$

Kays (1950) presents these loss coefficients for several geometries as shown in Figures 4.2 - 4.4 which were generated from Equations 4.5 and 4.6. These data represent entrance and exit pressure loss coefficients for tubes and channels with abrupt contraction and abrupt expansion exits. However, these figures do not easily lend themselves to computer modeling. Therefore, Equations 4.5 and 4.6 have to be used directly. The next two sections describe how to calculate the contraction ratio (C_c) and the velocity distribution coefficient (K_d).

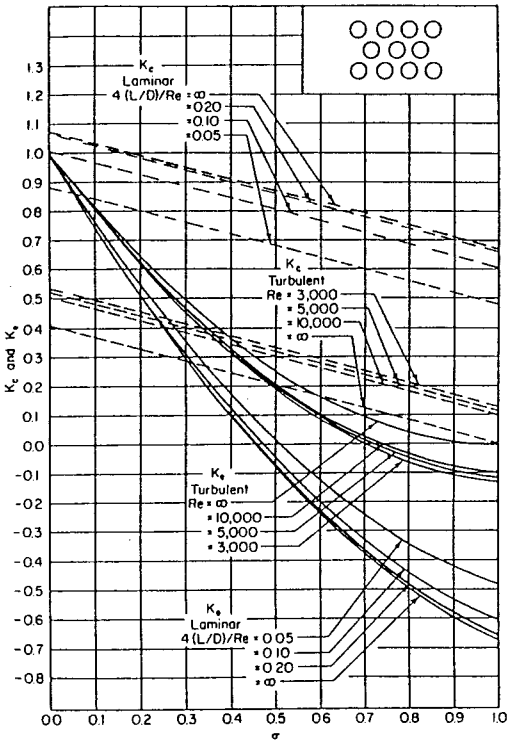

Figure 4.2: Circular Tube Loss Coefficients

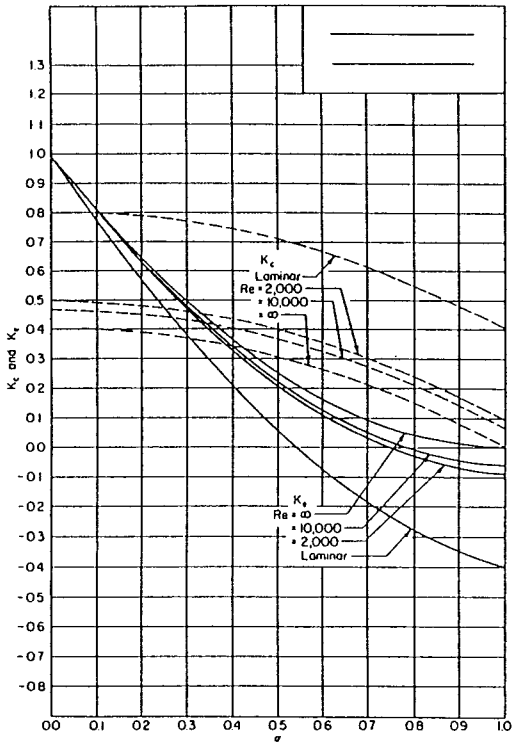

Figure 4.3: Flat Duct Loss Coefficients

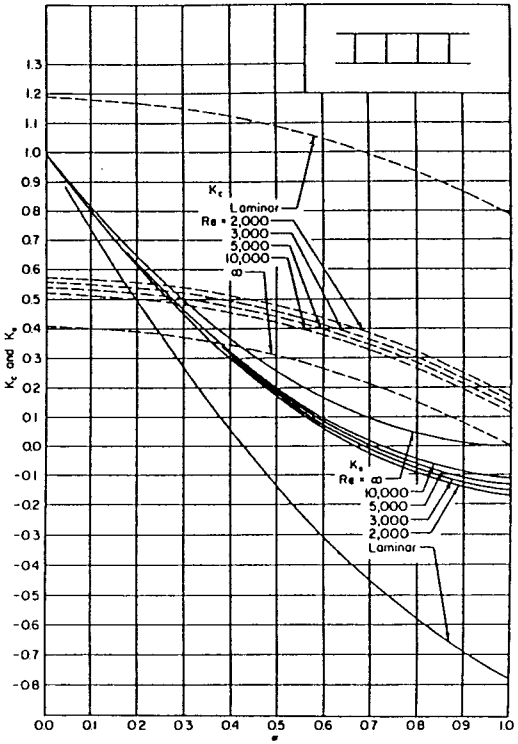

Figure 4.4: Square Duct Loss Coefficients

4.2.1 Contraction Ratio

The contraction ratio (C_c) is defined as the cross-sectional area of the vena contracta divided by the cross-sectional area of the duct. The vena contracta is shown in Figure 4.2 as the part of the flow that "necks down" to an area smaller than the duct entrance. It is not known whether data are available for rectangular-shaped ducts. However, Kays (1950) presents data for circular cross-sections and two infinite plates (gap). These data are plotted as a function of the free flow to frontal area ratio (σ) and is included in Table 4.1.

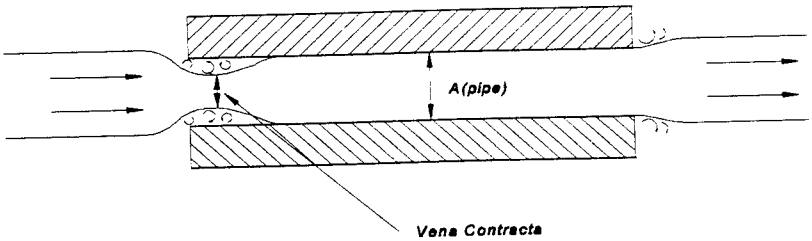

Figure 4.5: Vena Contracta

Table 4.1: Contraction Ratio

σ	C_c (circle)	C_c (gap)
0	0.6	0.6
0.1	0.615	0.61
0.2	0.633	0.62
0.3	0.65	0.625
0.4	0.67	0.63
0.5	0.689	0.64
0.6	0.715	0.67

Table 4.1: (Continued)

σ	C_c (circle)	C_c (gap)
0.7	0.74	0.685
0.8	0.78	0.725
0.9	0.83	0.78
1	1	1

To determine C_c for various aspect ratio channels, the circle will be used to represent channels that have $\alpha^* = 1$, and the gap will represent channels that have $\alpha^* \leq 0.1$. To obtain the other values, $0.1 < \alpha^* < 1$, a cubic interpolation between the two values of C_c will be used.

4.2.2 Velocity Distribution Coefficient

The velocity distribution coefficient (K_d) relates the actual momentum rate to the momentum rate obtained by using the average velocity in the channel. K_d is defined by

$$K_d = \frac{1}{A\ V_{avg}^2} \int_0^A V^2 dA \tag{4.7}$$

To calculate K_d, one must know the velocity distribution in the channel. The velocity distribution in circular tubes is well known and can be expressed as

$$u = u_{avg} \left(1 - \frac{r^2}{r_o^2}\right) = \frac{-dP}{dx} \frac{1}{4\mu} (r_o^2 - r^2) \tag{4.8}$$

where,

$$u_{avg} = \frac{1}{2}u_{\max} = \frac{-dP}{dx}\frac{r_o^2}{8\mu} \tag{4.9}$$

Integration of the velocity profile yields a value of $K_d = 4/3 = 1.333$. The velocity distribution for fully developed flow between two infinite plates, shown in Figure 4.6, is represented by Equations 4.10 and 4.11.

$$u = \frac{3}{2}u_{avg}(1-\frac{y^2}{h^2}) = \frac{-dP}{dx}\frac{h^2}{2\mu}u_{\max} = (1-\frac{y^2}{h^2})u_{\max} \tag{4.10}$$

where,

$$u_{avg} = \frac{2}{3}u_{\max} \tag{4.11}$$

Integration of this velocity profile yields a value of $K_d = 6/5 = 1.200$.

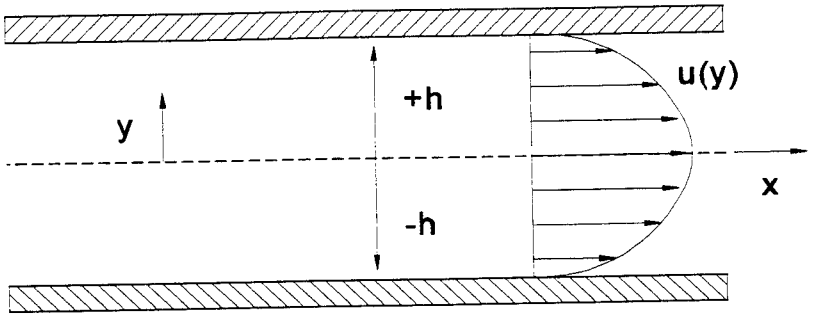

Figure 4.6: Infinite Plates

K_d may also be found for a rectangular section by substituting the velocity distribution into Equation 4.7. An exact solution is given by White (1991) for an arbitrary rectangular section.

Rectangular Section: $-a \le y \le a$, $-b \le z \le b$:

$$u(y, z) = \frac{16a^2}{\mu\pi^3}\sum_{i=1,3,5...}^{\infty} (-1)^{(i-1)/2} \left[1 - \frac{\cosh(\pi iz/2a)}{\cosh(\pi ib/2a)}\right] * \frac{\cos(\pi iy/2a}{i^3} \qquad (4.12)$$

This equation, however, would require a numerical integration to obtain K_d. In addition, it would apply only to the particular aspect ratio channel that was specified. To obtain a more general solution for K_d, Hartnett and Kostic (1989) present a simplified laminar velocity profile for arbitrary aspect ratio channels (Equations 4.13 and 4.14). This approximate profile matches the exact solution to within 2% over most of the cross-section, but can have up to 35% error near the corners.

Rectangular Section: $-b \le y \le b$, $-a \le z \le a$:

$$\frac{u}{u_{max}} = \left[1 - \left(\frac{y}{b}\right)^r\right] \left[1 - \left(\frac{z}{a}\right)^s\right] \qquad (4.13)$$

$$\frac{u_{max}}{u_{avg}} = \left(\frac{r+1}{r}\right)\left(\frac{s+1}{s}\right) \qquad (4.14)$$

where the exponents r and s are defined as

$r = 2$ *for* $\alpha^* \le 1/3$
$r = 2 + 0.3(\alpha^* - 1/3)$ *for* $\alpha^* > 1/3$
$r = 1.7 + 0.5\alpha^{*1/4}$ *for* $0 \le \alpha^* \le 1$
and $\alpha^* =$ *short side / long side*

Even with this simplified laminar velocity profile for rectangular channels, a closed form solution for the integral is not easily obtained. Therefore, a different solution procedure will be used and will be discussed later in this section.

To calculate the velocity distribution coefficient for turbulent flow, Kays (1950) presents semi-empirical velocity data for the turbulent regime for both circular tubes and flow between two infinite plates.

For tubes,

$$u = u_{avg}[\sqrt{f}\,(2.15\,\log_{10}\frac{y}{r_o} + 1.43)+1] \tag{4.15}$$

where, $y = 1 - r$

For plates,

$$u = u_{avg}[\sqrt{f}\,(2.0\,\log_{10}\frac{y}{y_o} + 0.88)+1] \tag{4.16}$$

Integration, to obtain K_d, yields the following results:

For tubes,

$$K_d = 1.09068f + 0.05884f^{1/2} + 1 \tag{4.17}$$

For plates,

$$K_d = 0.075f + 0.024f^{1/2} + 1 \tag{4.18}$$

Kays (1950) used the friction factor relation $f = 0.196Re^{-0.2}$ along with Equations 4.17 and 4.18 to generate curves for the turbulent K_d. To account for roughness effects inside heat

exchanger tubes, Kays (1950) changed the leading coefficient from the usual 0.184 to 0.196. It may be appropriate to use a correlation specifically for rough tubes at a later date since microchannels tend to have a larger relative roughness (ϵ/D).

Kays (1950) observed that

$$\frac{K_{d\ (gap)}{}^{-1}}{K_{d\ (circular)}{}^{-1}} \cong 0.6 \tag{4.19}$$

for both laminar and turbulent flow. It was concluded that similar ratios were also valid for other cross-sectional shapes.

$$\frac{K_{d\ (square)}{}^{-1}}{K_{d\ (circular)}{}^{-1}} \cong 1.17 \tag{4.20}$$

By determining the turbulent solution to the circular duct problem, K_d may now be determined for other shaped channels in the turbulent regime.

Equations 4.19 and 4.20 may be used to determine K_d for both laminar and turbulent flow in rectangular channels. By defining the channel aspect ratio such that $0 \leq \alpha^* \leq 1$, where $\alpha^* = 0$ is the gap (Equation 4.20) and $\alpha^* = 1$ is the square duct (Equation 4.19), the values for K_d may be linearly interpolated for the other aspect ratios.

4.3 Pressure Drop Model Comparison

It was shown by Tuckerman (1984) that the loss coefficients were on the order of 3 to 5. Tuckerman's experimental loss coefficient (K) was defined as

$$K = \frac{\Delta P \ 2g_c}{\rho V^2} \tag{4.21}$$

According to Kays' loss coefficient model (see Figures 4.2 - 4.4), the greatest loss coefficient for expansion and contraction combined is on the order of 2, which is a much smaller number than that presented by Tuckerman (1984).

Tuckerman used two manifold arrangements to direct the fluid into the microchannels. One was an "end-fed" arrangement, and the other was a "side-fed" arrangement. Since it is not known exactly where Tuckerman measured the pressure drop, we might assume that the loss coefficient included at least two ninety-degree bends. Ninety-degree bends can have a loss coefficient ranging from $K = .23$ to $K = 2$. If these losses are included in the value for K, then Kays' expansion and loss coefficients seem to be of the correct magnitude.

To verify further that Kays' model can accurately predict the pressure drop in the microchannel heat exchangers, a computer model, using the equations discussed in Chapters 3 and 4, was used to duplicate some of the pressure drop data reported by Phillips (1987). The exact operating conditions of the experiment were not known, so assumptions had to be made with regard to the inlet temperature of the fluid. The water was assumed to have an inlet temperature of approximately 33°C. The channel dimensions are shown in Table 4.2.

Table 4.2: Phillips Microchannel Dimensions

Chip	channel width (μm)	wall width (μm)	channel height (μm)	substrate thickness (μm)	channel length (mm)	chip width (mm)	roughness (μm)
Hex 1	90±2	160±2	100±5	310±5	2.67±.025	8.25±.025	10±3
Hex 2	60±2	65±2	80±5	360±5	2.67±.025	6.25±.025	8±3
Hex 3	160±2	90±2	160±5	260±5	9.525±.025	6±.025	5±3
Hex 4	220±2	155±2	165±5	255±5	9.703±.025	5.842±.025	10±3

Figure 4.7 shows the experimental data generated by Phillips (1987) with the pressure drop predictions by the Kays pressure drop model. The pressure drop model assumes that $K_{90} = 1.2$. This figure clearly shows that the Kays pressure drop model accurately models the *Re* dependent pressure drop in microchannel heat exchangers.

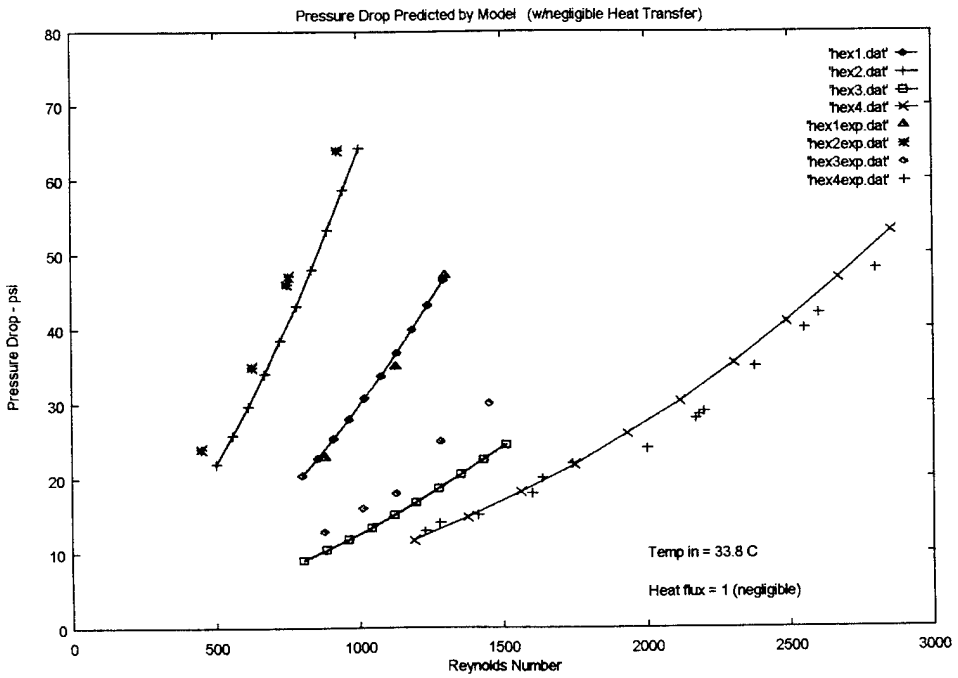

Figure 4.7: Kays' Pressure Drop Predictions for Phillips (1987) Data

CHAPTER 5

HEAT TRANSFER THEORY

The purpose of this chapter is to discuss the conventional correlations used to predict heat transfer in tubes and channels. Particular emphasis is placed on rectangular-shaped channels because this is the shape of the microchannel heat exchangers used for this thesis. The scope of discussion includes laminar, transition, and turbulent heat transfer.

Most conventional correlations are dependent on *Re*, *Pr* and channel dimensions, which results from the fact that the velocity field is tied to the temperature field by way of the energy equation. A natural extension of the math model would be to include the effects of heat transfer since the hydrodynamic flow characteristics are already known. Therefore, the following chapter shows the development of the equations used in the math model for predicting heat transfer in rectangular microchannels.

5.1 Laminar Nusselt Number

The laminar Nusselt number (Nu_D) for a constant heat flux boundary condition for fully developed flow in circular pipes is defined by

$$Nu_D = \frac{hD}{k} = 4.364 \tag{5.1}$$

In rectangular ducts, Nusselt number is a function of the aspect ratio (α = channel height / channel width). Hartnett and Kostic (1989) have included a plot for several constant heat flux boundary conditions, where $0 \leq \alpha^* \leq 1$ ($\alpha^* = 1/\alpha$).

We must determine which boundary conditions are appropriate to model the heat transfer characteristics in microchannels. By considering the cover plate on the top surface of the channels as an insulating top, the heat transfer through the top wall can be neglected. Phillips (1987) chose to differentiate according the aspect ratio α. The three heat transfer situations are described by Phillips as follows:

1. Small Aspect Ratio — Heat transfer is considered only from the base of the channel. ($\alpha \leq 0.1$)

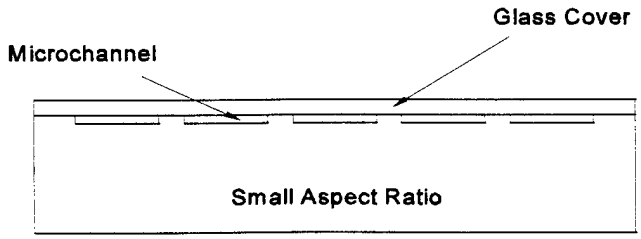

Figure 5.1: Small Aspect Ratio Channels

2. Moderate Aspect Ratio — Heat transfer is considered from the base and from the sides or "fins." ($0.1 < \alpha < 10$)

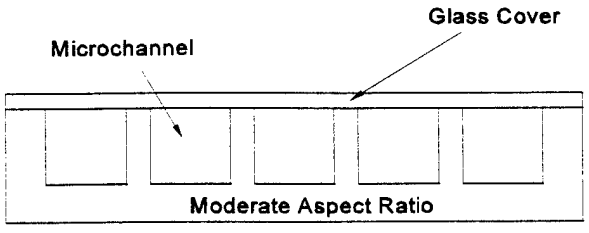

Figure 5.2: Moderate Aspect Ratio Channels

3. Large Aspect Ratio Heat transfer is considered from only the "fins." ($\alpha \geq 10$)

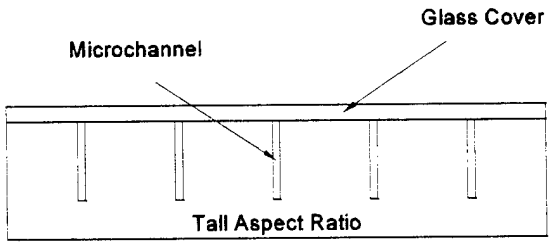

Figure 5.3: Tall Aspect Ratio Channels

The data in Table 5.1 have been obtained from a plot presented by Hartnett and Kostic and by data presented by Phillips (1987) which match the plot. Figure 5.4 shows the different boundary conditions which correspond to the table.

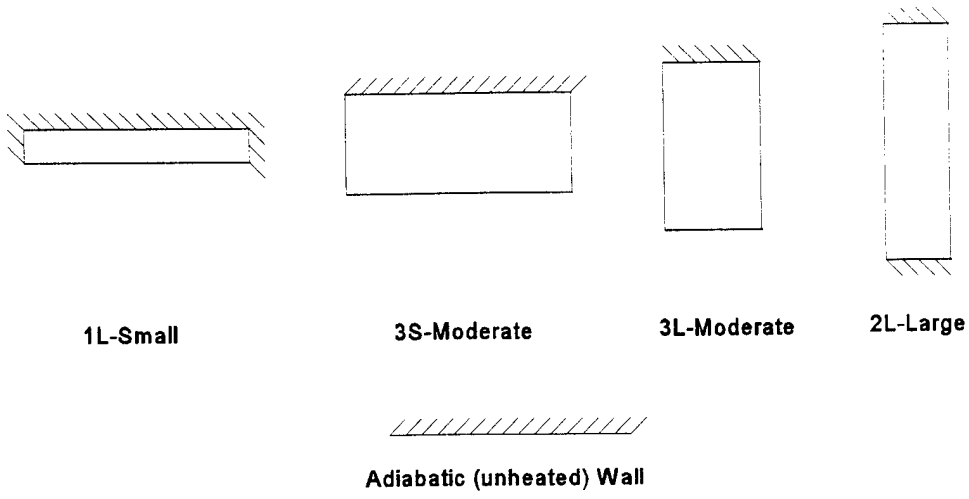

Figure 5.4: Different Boundary Conditions for Laminar Nusselt Number

Table 5.1: Laminar Nusselt Number

α^*	$\alpha \leq 0.1$	$0.1 < \alpha \leq 1.0$	$1.0 < \alpha < 10$	$\alpha \geq 10$
	Nu (Case 1L)	**Nu (Case 3S)**	**Nu (Case 3L)**	**Nu (Case 2L)**
0	*5.385*	5.385	8.235	*8.235*
0.05	*5.1*	4.75	7.5	*7.7*
0.1	*4.851*	4.252	6.939	*7.248*
0.2	4.411	*3.636*	*6.072*	6.561
0.3	4.060	*3.306*	*5.393*	5.997
0.4	3.777	*3.169*	*4.885*	5.555
0.5	3.539	*3.146*	*4.505*	5.203
0.6	3.35	*3.18*	*4.25*	4.9
0.7	3.149	*3.195*	*3.991*	4.662
0.8	3.0	*3.3*	*3.8*	4.45
0.9	2.8	*3.4*	*3.7*	4.3
1	2.712	*3.556*	3.556	4.094

These data will be used by calculating the aspect ratio, $\alpha = H_c / W_c$, and then making the necessary corrections when looking up the data. For example, $\alpha^* = \alpha$ for cases 1L and 1S and $\alpha^* = 1 / \alpha$ for cases 3L and 2L. These corrections are taken care of automatically in the computer heat transfer model. In addition, the values of *Nu* that fall between values of tabulated α^* are linearly interpolated. Finally, it must be noted that not all of the values of *Nu* will be used in the model. Only those values which fall within the specified aspect ratio ranges and match the heating situation described will be used. These values are shown in italics in Table 5.1.

5.2 Developing Laminar Nusselt Number

There is a limited amount of data on laminar, thermally developing flow. Shah and Bhatti (1987) present data for flow between two infinite flat plates (gap) for various boundary conditions. Ideally, we would like to have data for rectangular ducts of various aspect ratio channels with heat flux or temperature boundary conditions on one, two, or three walls. Unfortunately, the data presented for duct flow only has boundary conditions that are the same for all four walls and for a limited number of aspect ratios.

Phillips (1987) models thermally developing flow by considering the small, moderate, and large aspect ratio channels.

1. Small Aspect Ratio — Small aspect ratio channels have heating from only the base. Phillips considers this heating situation to be most like parallel plate flow with a uniform heat flux on one side.

2. Large Aspect Ratio — Large aspect ratio channels have heating from only the sides. Phillips considers this heating situation to be most like parallel plate flow with a uniform heat flux on both sides.

3. Moderate Aspect Ratio — Moderate aspect ratio channels have heating from both the sides and the base. This is a special case which will be discussed in Section 5.2.2.

5.2.1 Small and Large Aspect Ratio Channels

Phillips includes data of local Nu_x for flow between two infinite plates, as shown in Table 5.2.

Table 5.2: Local Nusselt Number for Gap Flow

$x^* = \frac{x}{(D_h Re\ Pr)}$	Nu_x ($\alpha \approx \infty$) (both sides heated) $\alpha \geq 10$	Nu_x ($\alpha \approx 0$) (one side heated) $\alpha \leq 0.1$
0.00025	23.8	23.5
0.0025	11.9	11.2
0.01	8.8	7.49
0.05	8.25	5.55
0.125	8.24	5.39
$\approx \infty$ (fully-developed)	8.23	5.38

A program was written to interpolate cubically between the values of Nu_x from Table 5.2. Next, a list of values from $x^* = 0.00025$ to $x^* = 0.125$ in 0.0005 increments was generated (where $x^* = x/(D_h Re_{Dh} Pr)$). Average Nu lists were then calculated from these values (shown in Table 5.3). Table 5.3 was used to determine Nu_{avg} in the math model. The Nu_x and Nu_{avg} values for two heated sides are shown in Figure 5.5.

Table 5.3: Average Laminar Nusselt Number in Gap Flow

$1/x^* = \frac{D_h Re\ Pr}{x}$	Nu ($\alpha \approx \infty$) (both sides heated) $\alpha \geq 10$	Nu ($\alpha \approx 0$) (one side heated) $\alpha \leq 0.1$
0 (fully-developed)	8.23	5.38
10	8.56	6.19
20	8.88	6.99
30	9.19	7.61
40	8.23	8.09
60	10.02	8.85
80	10.49	9.45
100	10.93	9.97

Table 5.3: (Continued)

$1/x^* = \frac{D_h Re\, Pr}{x}$	Nu ($\alpha \approx \infty$) (both sides heated) $\alpha \geq 10$	Nu ($\alpha \approx 0$) (one side heated) $\alpha \leq 0.1$
120	11.34	10.44
140	11.73	10.88
160	12.1	11.3
180	12.46	11.7
200	12.81	12.07

Figure 5.6 (Shah and Bhatti, 1987) was compared to Figure 5.5 to check the validity of the interpolation procedure for obtaining Nu_{avg}. Constant heat flux and constant temperature boundary conditions applied to both sides are shown for gap flow. We are concerned only with the constant heat flux boundary condition, which is denoted by the subscript "H" on Figure 5.6. Nu_{avg} and Nu_x shown here have the same trends and are comparable in value to those shown in Figure 5.5. In particular, notice that Nu_{avg} has higher values than Nu_x for a given x^*.

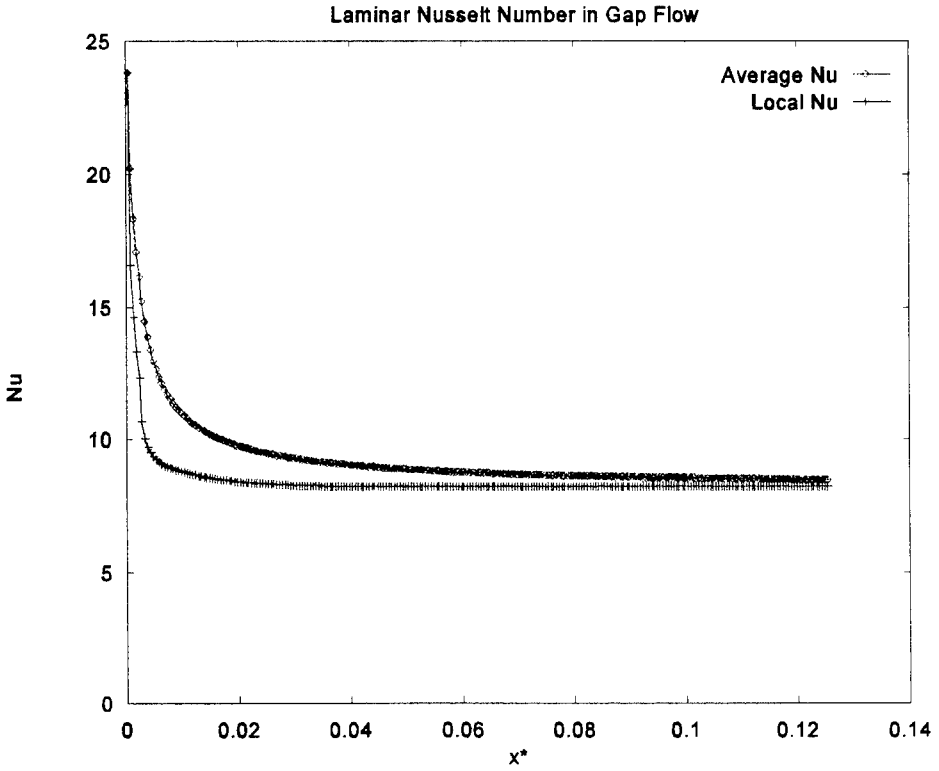

Figure 5.5: Laminar Nu (Gap Flow)

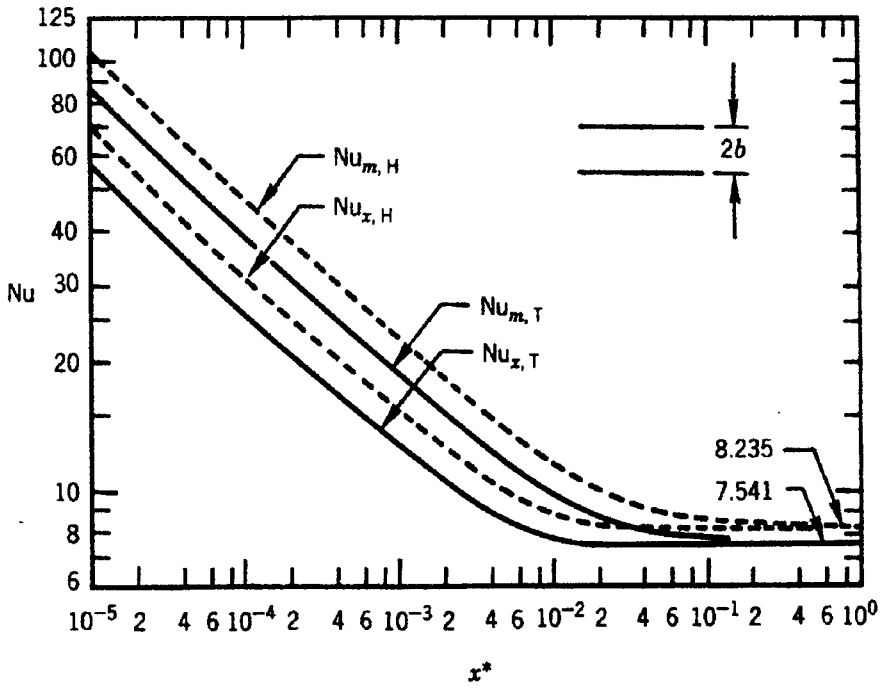

Figure 5.6: Laminar Nu (Gap Flow), (Shah and Bhatti, 1987)

5.2.2 Moderate Aspect Ratio Channels

There are no known data for thermally developing flow in moderate aspect ratio channels. However, Phillips (1987) noted that a good approximation would be to assume that the ratio of the developing flow case to the fully developed case would be approximately the same for the different heating situations. Therefore, the following equation could be used to approximate the thermally developing flow for heat flux on three sides:

$$\mathrm{Nu}_{developing}(3sides) = \mathrm{Nu}_{developing}(4sides)\ \frac{\mathrm{Nu}_{developed}\ (3sides)}{\mathrm{Nu}_{developed}\ (4sides)} \qquad (5.2)$$

The Nusselt numbers should all be calculated at the same aspect ratio. The fully developed Nusselt number for three heated sides will be either case 3L or case 3S, depending on the aspect ratio(α). The fully-developed *Nu* for four heated sides can be approximated by Equation 5.3, Hartnett and Kostic (1989), which is accurate to within ± 3%.

$$Nu_{H1} = 8.235(1 - 2.0421\alpha^* + 3.0853\alpha^{*2} - 2.4765\alpha^{*3} + 1.0578\alpha^{*4} - 0.1861\alpha^{*5}) \qquad (5.3)$$

Shah and Bhatti (1987) have included a chart of Nu_{avg} for a uniform heat flux boundary condition with developing flow on all four walls. They include data for four different aspect ratios: 1.0, 1/2, 1/3, and 1/4. Since the heat flux is the same on all four walls, data for the aspect ratios 2, 3, and 4 are also known. The Nu_{avg} values have been combined with the plate flow Nu_{avg} values to give the full range of moderate aspect ratio channels. Although the plate flow values will not actually be used in the calculations, they

are used to determine the values for $\alpha = 1$ and $\alpha = 10$ by linear interpolation. In addition, there may be situations where a double, linear interpolation is required to obtain Nu_{avg}.

Table 5.4: Average Laminar *Nu* for Moderate Aspect Ratio Rectangular Channels

1/x*	α≈0	α=1/4	α=1/3	α=1/2	α=1	α=2	α=3	α=4	α≈∞
0 (fully-developed)	5.38	5.35	4.77	4.11	3.6	4.11	4.77	5.35	8.23
10	6.19	6.03	5.45	4.94	4.48	4.94	5.45	6.03	8.56
20	6.99	6.57	6.06	5.6	5.19	5.6	6.06	6.57	8.88
30	7.61	7.07	6.6	6.16	5.76	6.16	6.6	7.07	9.19
40	8.09	7.51	7.09	6.64	6.24	6.64	7.09	7.51	9.49
60	8.85	8.25	7.85	7.45	7.02	7.45	7.85	8.25	10.02
80	9.45	8.87	8.48	8.1	7.66	8.1	8.48	8.87	10.49
100	9.97	9.39	9.02	8.66	8.22	8.66	9.02	9.39	10.93
120	10.44	9.83	9.52	9.13	8.69	9.13	9.52	9.83	11.34
140	10.88	10.24	9.93	9.57	9.09	9.57	9.93	10.24	11.73
160	11.3	10.61	10.31	9.96	9.5	9.96	10.31	10.61	12.1
180	11.7	10.92	10.67	10.31	9.85	10.31	10.67	10.92	12.46
200	12.07	11.23	10.97	10.64	10.18	10.64	10.97	11.23	12.81

5.3 Simultaneously Developing Laminar Nusselt Number

Simultaneous developing flow occurs when the flow regime is neither hydrodynamically nor thermally developed. Overall, the Nusselt numbers are predicted to be higher than fully developed flow, especially for low Prandtl number fluids. Phillips (1987) points out that the "theoretical models do not account for wakes or secondary effects at the entrance, which are usually present in 'abrupt' channel entrances." He also

points out experimental evidence that the thermal entry problem better models the flow situation here. It is for this reason that simultaneously developing flow will be neglected.

5.4 Transition Nusselt Number

It was noted in Chapter 3 that there are no reliable correlations to determine friction losses in arbitrary aspect ratio channels for transition flow. The same is true for heat transfer. This practice can cause problems in mathematically modeling the flow situation. The discontinuity, from the laminar to turbulent regime, can lead to convergence problems for the mathematical model. To alleviate the problem, a smooth cubic spline was used in this flow regime. The cubic equation was generated using *Nu* data at the maximum *Re* for laminar flow and the minimum *Re* for turbulent conditions.

5.5 Turbulent Nusselt Number

A classical Nusselt number correlation is the Dittus-Boelter equation which is given by

$$Nu_D = 0.023\, Re^{0.8}\, Pr^n \tag{5.4}$$

where,

$n = 0.4$ *for heating fluid*
$n = 0.3$ *for cooling fluid*
$Re > 10{,}000$
$0.6 \leq Pr \leq 160$
$L/D > 60$

For rectangular ducts, Hartnett and Kostic (1989) have shown that accurate predictions of *Nu* can be made by using 90% of the value indicated by the Dittus-Boelter equation at the same *Re* and *Pr*.

A better correlation for circular ducts, according to Shah and Bhatti (1987), is the Gnielinski correlation (Equation 5.5). They indicate that this correlation gives the best overall fit to the experimental data. They even use this correlation as a basis of comparison for all of the other correlations.

$$Nu = \frac{(f/2)\ (Re-1000)Pr}{1 + 12.7(f/2)^{1/2}(Pr^{2/3}-1)} \tag{5.5}$$

where,

$2{,}300 \leq Re \leq 50{,}000$
$0.5 \leq Pr \leq 2{,}000$

Phillips (1987) used a modified version (Equation 5.6) of this equation for his model which did not include the friction factor. This modified version is accurate to within - 10% and + 0% of the Gnielinski correlation.

$$Nu = 0.012(Re^{0.87}-280)Pr^{0.4} \tag{5.6}$$

where,

$1.5 \leq Pr \leq 500$

The Gnielinski correlation, with $D = D_h$ and $Re = Re_{Dh}$, will be used to predict turbulent heat transfer in rectangular microchannels in the math model used for this thesis.

CHAPTER 6

THERMAL RESISTANCE MODELS

There are two main reasons to use the resistance method for analyzing micro heat exchangers. First, resistance modeling can help determine optimal channel configurations before actual testing occurs. Second, resistance models described in this chapter can be used to determine the convective heat transfer coefficient. It must be noted that the resistance methods to be discussed in the following sections are used to determine the local convective heat transfer coefficient (h_x). To determine an average heat transfer coefficient (h), several temperatures along the channels would have to be measured.

Determination of h requires knowledge of the inlet and outlet fluid temperatures, the heat flux, and a wall temperature. The inlet and outlet temperatures along with the heat flux are easily measured. However, direct measurement of the wall temperature is not easily obtained since the measurement location would have to be located within the channels themselves. Any disturbance in micro-sized channels will affect the heat transfer and friction measurements, not to mention the difficulty of installing a thermocouple (assuming a thermocouple is used). As an alternative, a thermocouple may be installed close to the channel, and the resistance method can be used to determine indirectly the microchannel wall temperature. Hence, the resistance method provides a means of

determining h. Therefore, the final math model will consist of the equations found in Chapters 3 - 6.

Two resistance models will be discussed. Tuckerman's (1984) resistance model will be discussed in Section 6.1. Tuckerman (1984) was the first person to analyze microchannels using this method. Phillips' (1987) resistance model will be discussed in Section 6.2. Phillips (1987) extended Tuckerman's work (1984) by including developing flow considerations and considerations for the various mechanisms of heat transfer for different aspect ratio channels.

6.1 Tuckerman's Model

Tuckerman (1984) defines thermal resistance as $\theta = \Delta T / q$. The ΔT is the temperature rise of the heat source above the ambient temperature, and q is the power dissipation or heat used. A microchannel heat exchanger that has a low thermal resistance will remove heat more efficiently than one with a high thermal resistance. Thus, thermal resistance modeling is used to quantify the effectiveness of the different configurations of microchannel heat exchangers. Five components of thermal resistance were identified for microchannel heat exchangers used to cool integrated circuits. The components are defined below.

1. θ_{spread} Resistance of several individual heating elements in the substrate. This contribution is considered negligible for a very large number of devices and becomes less important when the dimensions are scaled down.

2. θ_{bulk} Resistance caused by bulk conduction through the circuit. This resistance can be reduced by thinning the substrate.

3. $\theta_{interface}$ Resistance caused by the heat sink / integrated circuit interface. This can be eliminated by manufacturing the heat source onto the back of the heat sink.

4. $\theta_{convection}$ Resistance caused by convection heat transfer. This resistance can be reduced by increasing the convection heat transfer coefficient (h) or the surface area of the channels. A higher value of h is usually associated with turbulent flow which requires high flow rates leading to very high pressure drop.

5. $\theta_{caloric}$ Resistance caused by heating the fluid as it passes through the microchannels ($q = (\rho AV)C_p \Delta T$). This resistance can be reduced by choosing a fluid with a high specific heat and by increasing the flow rate. However, increasing the flow rate also increases the pressure drop.

Figure 6.1 shows the thermal resistance terms.

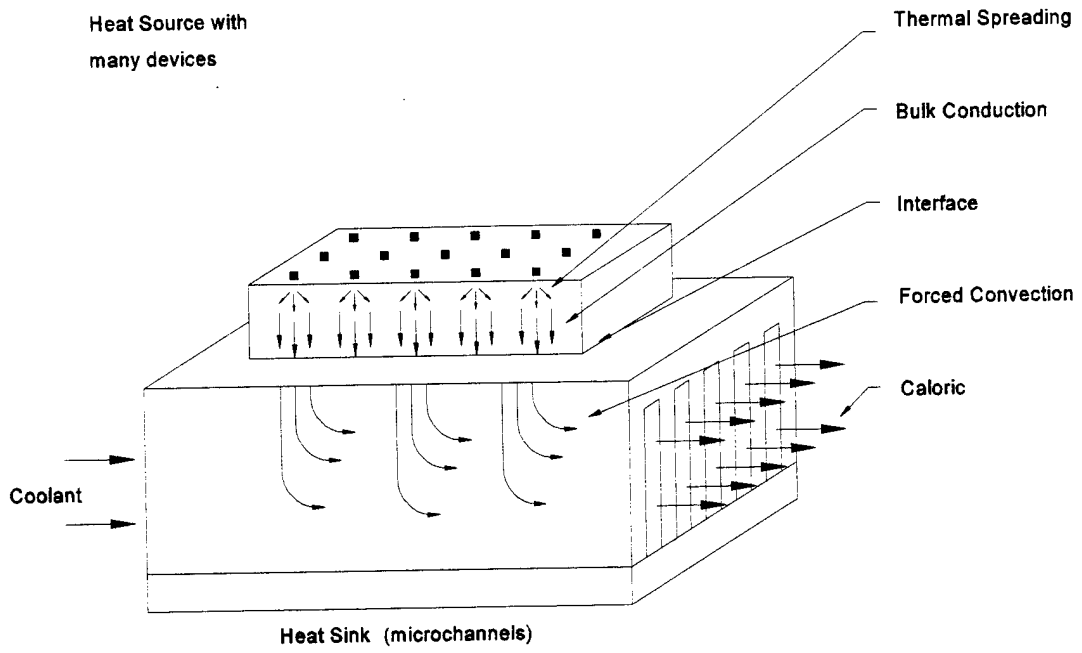

Figure 6.1: Tuckerman's Thermal Resistance Model

The overall thermal resistance (θ) that includes all of the effects discussed above is given by

$$\theta \equiv \frac{T_w(x) - T_{inlet}}{q} = \theta_{spread} + \frac{t_{Si}}{k_{Si}\, A} + \theta_{interface} + \frac{1}{h\, A} + \frac{1}{\dot{m}\, C_p} \qquad (6.1)$$

Tuckerman (1984) considers only two components of the resistances shown in his model. He assumes that the spreading resistance is negligible because of the small scales involved. By thinning the substrate, the conduction resistance is made much smaller when compared to the others. In addition, the model is further simplified by making the heat sink and the heat source an integral unit to eliminate the interfacial resistance. A first order approximation of the two remaining resistances, convection and caloric, are discussed in the next section.

6.1.1 Tuckerman's First Order Approximation of θ

Tuckerman (1984) analyzed the conduction/convection heat transfer for microchannels. The following analysis considers only first order approximations. He describes a more detailed analysis of the flow conditions (e.g., modeling with an analytically determined wall temperature profile.) The purpose of this discussion is to describe, in general terms, his resistance model formulation.

The following are variables used to define dimensions in his microchannels.

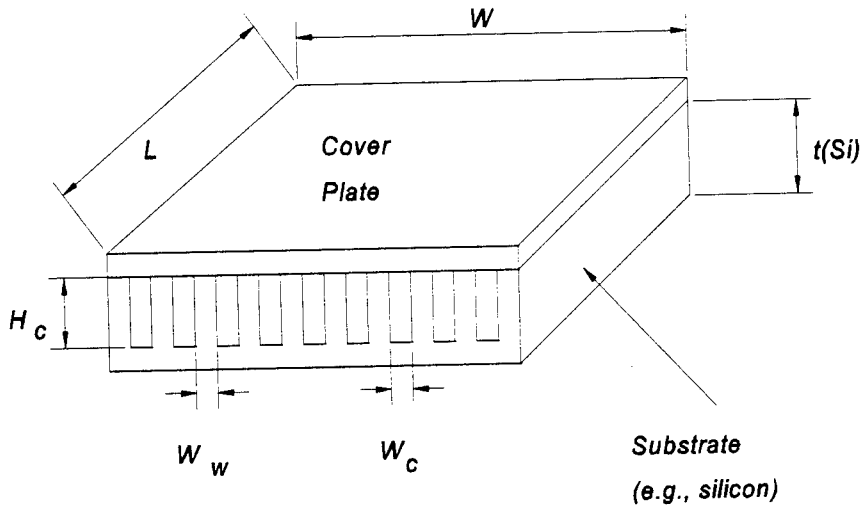

Figure 6.2: Tuckerman's Microchannel Heat Exchanger

Where,

Perimeter:	$p = (2*W_w + 2*W_c)$
Number of channels:	$n = W / (W_w + W_c)$
Aspect Ratio:	$\alpha = \frac{\text{total surface area of duct}}{\text{area of circuit}}$
	$\alpha = (n*p*L) / (W*L)$
Hydraulic Diameter:	$D_h = 4*(\text{cross-sectional area}) / p$
	$D_h = 4*(W_w * W_c) / (2*W_w + 2*W_c)$
Hydraulic Radius:	$R_h = (\text{cross-sectional area}) / p$

Note: *Tuckerman refers to the aspect ratio (α) not as the height-to-width ratio of the channels, but as the ratio of heat transfer area in the channels to the area of the circuit.*

Tuckerman's resistance model consists of the following two components:

$$\theta \equiv \frac{T_w(x) - T_{inlet}}{q} = \frac{1}{h\,A} + \frac{1}{\dot{m}\,C_p} \qquad \text{where, } \dot{m} = \rho A_{flow} V \tag{6.2}$$

Equation 6.2 is derived by considering Newton's Law of Cooling (Equation 6.3), with a constant wall temperature at a given x location, and conservation of energy (Equation 6.4).

$$q_x = h_x A[T_w(x) - T_{bulk}(x)] \qquad where\ A = npL \tag{6.3}$$

$$q_x = \rho AVC_p[T_{bulk}(x) - T_{bulk}(0)]\ \frac{L}{x} \qquad where\ A = n(W_c * H_c) \tag{6.4}$$

Tuckerman's work (1984) was concerned with cooling an integrated circuit (I.C.) chip with microchannel heat exchangers. His work also dealt with determining the peak temperature rise of an I.C. chip. This is important because I.C. circuits are required to work within a specified temperature range; outside this range they cease to function properly. Tuckerman was primarily concerned with keeping the temperature of the circuit below the maximum operating temperature. Therefore, the analysis is performed at the end of the microchannels where the peak temperature rise will occur. The temperatures are represented by $T_{bulk}(L)$ and $T_w(L)$.

$$q_{x=L} = h_L A[T_w(L) - T_{bulk}(L)] \tag{6.5}$$

$$q_{x=L} = \rho AVC_p[T_{bulk}(L) - T_{bulk}(0)] \tag{6.6}$$

By adding Equations 6.5 and 6.6, the following relation may be obtained:

$$T_w(L) - T_{bulk}(0) = \frac{q_L}{h_L A} + \frac{q_L}{\rho AVC_p} \tag{6.7}$$

$T_{bulk}(0)$ is the fluid inlet temperature, and $T_w(L)$ is the wall temperature at the exit. Equation 6.7 can be reduced to the form of Equation 6.2 by dividing both sides by q_L.

Tuckerman (1984) makes further refinements by modeling the convection heat transfer that results from flow over a fin. In addition, other resistance terms may be included should they become more important. It should be noted that the temperature difference, $T_w(L) - T_{bulk}(0)$, would change if the additional terms were added. For example, if we were to include the conduction resistance, the temperature difference would be $T(L) - T_{bulk}(0)$, where $T(L)$ would be the temperature measured on the top surface of the integrated circuit. Phillips (1987) extended the work of Tuckerman (1984) to include additional resistance terms. The formulation of his model is included in the next section.

6.2 Phillips Model

Phillips (1987) extended Tuckerman's (1984) work by including additional resistance terms. Phillips considered the differing mechanisms of heat transfer for different aspect ratio channels in an attempt to generalize the work done by Tuckerman (1984) by making it applicable to more flow situations. As alluded to in the previous discussion, Phillips also models the convection resistance including the effects of the fin. In addition, he considers the "constriction" effects as heat is transferred from the base of the microchannels up through the sides or "fins." These two effects are discussed in Sections 6.2.1 and 6.2.2. Phillips also considered developing flow (discussed in the previous two chapters). This resistance model is used in the math model.

6.2.1 Heat Source

Depending on the channel dimensions, Phillips (1987) considers the heat source in microchannels to be a long strip heat source in a finite conducting medium. This type of heat source (Figure 6.3) may be used to help determine the heat flow path from the base through the fins. In other words, this models the "constriction" effect of the heat flow in the fins (Figure 6.4). The temperature difference at the base of the fins caused by the constriction effect is given by Bar-Cohen (1985) as

$$\Delta T_c = \frac{q}{\pi p k_w} \ln\left[\frac{1}{\sin(\pi a/2b)}\right] \tag{6.8}$$

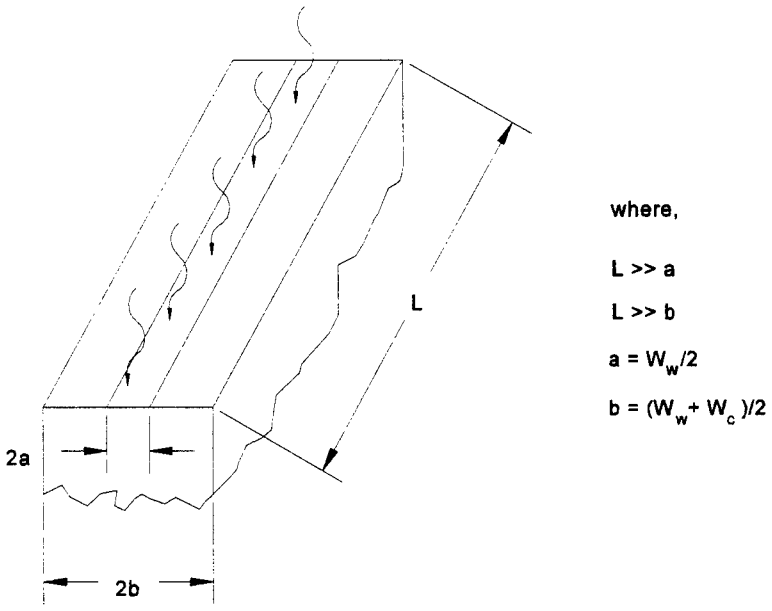

Figure 6.3: Heat Source with Constriction Effect

Thus, ΔT_c is the temperature difference that is seen in addition to the difference when there is a uniform heat sink and uniform heat source (see Figure 6.3). In other words, the steady state temperature difference between points 1 and 2 for a plane wall (no constriction) would be $\Delta T_{1\text{-}2} = \Delta T_o$. However, by adding the constriction effect, the steady state temperature difference between 1 and 2 would become $\Delta T_{1\text{-}2} = \Delta T_o + \Delta T_c$.

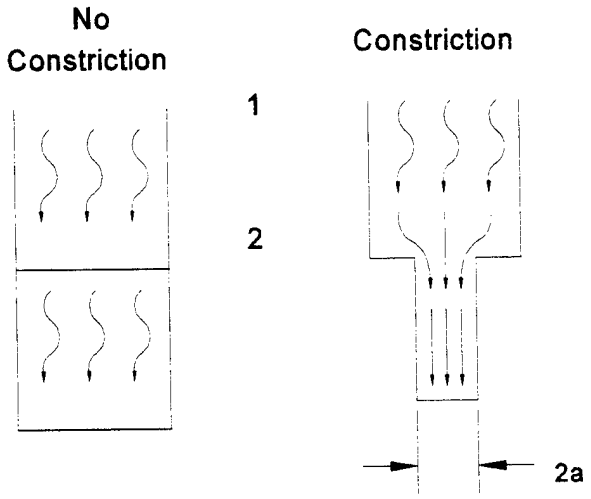

Figure 6.4: Constriction Effect

The fins in the small aspect ratio ($\alpha = H_c / W_c \leq 0.1$) channels are used only for structural purposes and are not considered to contribute a significant amount to the heat transfer. The constriction effect will be neglected in small aspect ratio microchannels. This effect is seen mostly in large aspect ratio ($\alpha \geq 10$) channels and to a lesser degree in the moderate aspect ratio channels.

6.2.2 Fin Model

Phillips (1987) makes the following assumptions so that he can model the walls of the microchannels as a fin with an insulated tip.

1. The liquid coolant flow is steady and incompressible.
2. The power dissipation is constant.
3. The thermal conductivity of the fins is constant over the length.
4. The fin thickness is constant.
5. The temperature gradient over the width of the fin is much smaller than the gradient along its length.
6. There is no internal heat generation within the fins.
7. There is negligible heat transfer caused by natural convection and radiation.
8. The fin base is at a constant temperature.
9. The temperature of the surrounding coolant at some axial distance, x, down the channel is uniform.
10. The convection heat transfer coefficient at some axial distance, x, down the channel is a constant.

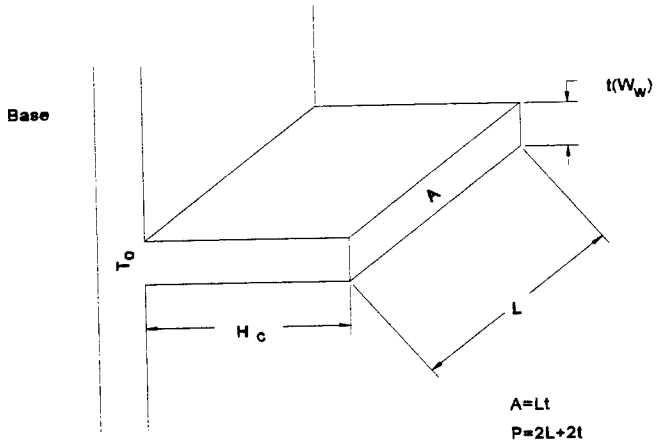

Figure 6.5: Rectangular Fin

The solution for a fin with an insulated tip is given by Holman (1990) as

$$\frac{\Theta}{\Theta_o} = \frac{T-T_\infty}{T_o-T_\infty} = \frac{\cosh[m(H_c-z)]}{\cosh(mH_c)} \qquad where \qquad m = \sqrt{\frac{hP}{k_{fin}A}} \tag{6.9}$$

The heat transfer is given as

$$q = \sqrt{hPk_{fin}A}\ \Theta_o\ \tanh(mH_c) \tag{6.10}$$

The fin efficiency is expressed as

$$\eta_{fin} = \frac{\tanh(mH_c)}{mH_c} \tag{6.11}$$

If $L >> W_w$, then the following approximation can be made:

$$m = \sqrt{\frac{2h}{k_{fin}w_w}} \tag{6.12}$$

The heat flux can now be expressed as

$$q'' = \frac{q}{A} = mk_{fin}\Theta_o\ \tanh(mH_c) \tag{6.13}$$

As alluded to in the discussion in the previous section, the contribution of the fin to heat transfer in the small aspect ratio channels is minimal and is therefore neglected.

6.2.3 Modified Thermal Resistance (θ")

Phillips (1987) considers the various mechanisms of heat transfer for the different aspect ratio channels. Thus, there are three different models for small, moderate, and large

aspect ratio channels. Phillips modified the thermal resistance by normalizing with the surface area over which the heat transfer occurs ($A_{cross} = L\,(W_w + W_c)$).

Thermal resistance is usually defined as

$$\theta = \frac{\Delta T}{q} \tag{6.14}$$

In this case, ΔT is the peak temperature rise above ambient, and q is the total heat rate. Phillips modifies the thermal resistance by multiplying it by A_{cross} to give Equation 6.15.

$$\theta'' = \theta\, A_{cross} = \frac{\Delta T}{q} A_{cross} = \frac{\Delta T}{q''} \tag{6.15}$$

6.2.3.1 Components of Resistance. Phillips considers six main components in his analysis. A description of each is included below.

1. θ_{spread} Resistance of several discreet heating elements (shape dependent).

2. θ_{bulk} Resistance caused by bulk conduction through the bottom of the channels

$$\theta''_{bulk} = \frac{t}{k_w} \tag{6.16}$$

where the thickness (t) is defined differently than by Figure 6.2. The thickness (t) is measured from the base of the channel to the heat source interface ($t = t(Si)\text{-}H_c$).

3. $\theta_{interface}$ Resistance caused by the heat sink / integrated circuit interface (if any).

4. $\theta_{convection}$ Resistance caused by convection heat transfer on the base of the channel and walls of the fins. By assuming that the fin base and channel base are at the same temperature, the fins and the channel base can be considered to be thermally connected in parallel. For large aspect ratio channels, the base contribution is negligible. For small aspect ratio channels, the fin contribution is negligible.

$$\theta_{convection} = \frac{1}{hA_{base} + k_w m A_{fin} \tanh(mH_c)} \tag{6.17}$$

$$\theta''_{convection} = \theta_{convection}(L(W_w+W_c)) \tag{6.18}$$

$$= \frac{L(W_w+W_c)}{h(LW_w m(LWw)\tanh(mH_c)} \tag{6.19}$$

where, $A_{base} = L\,W_c$
$A_{base\ of\ fin} = LW_w$

5. $\theta_{caloric}$ Resistance caused by heating the fluid as it passes through the microchannels ($q = (\rho AV)C_p\,\Delta T$).

$$\theta''_{caloric} = \frac{L(W_w+W_c)}{\rho A_{channel} V C_p} \tag{6.20}$$

6. $\theta_{constriction}$ Resistance caused by the constriction effect at the fin base. This is determined by substituting the temperature change, ΔT_c, into Fouriers conduction equation.

$$\theta''_{constriction} = \frac{\Delta T}{q} A_{cross} = \frac{qA_{cross}}{qLk_w\pi} \ln\left[1/\sin\frac{\pi W_w/2}{2(W_w+W_c)/2}\right] \tag{6.21}$$

$$= \frac{W_w+W_c}{k_w\pi} \ln\left[1/\sin\frac{\pi W_w}{2(W_w+W_c)}\right] \tag{6.22}$$

6.2.3.2 Resistances for Different Aspect Ratios. The components of resistance for different aspect ratio channels are listed below.

1. Small Aspect Ratio ($\alpha \leq 0.1$)

$$\theta'' = \frac{t}{k_w} + \frac{L(W_w+W_c)}{h(LW_c)} + \frac{L(W_w+W_c)}{\dot{m}C_p} \tag{6.23}$$

2. Moderate Aspect Ratio ($0.1 < \alpha < 10$)

$$\theta'' = \frac{t}{k_w} + \frac{(W_w+W_c)}{\pi k_w}\ln\left[1/\sin\frac{\pi W_w}{2(W_w+W_c)}\right] + \frac{L(W_w+W_c)}{h(LW_c)+k_w m(LW_w)\tanh(mH_c)} + \frac{L(W_w+W_c)}{\dot{m}C_p} \tag{6.24}$$

3. Large Aspect Ratio ($\alpha \geq 10$)

$$\theta'' = \frac{t}{k_w} + \frac{(W_w+W_c)}{\pi k_w}\ln\left[1/\sin\frac{\pi W_w}{2(W_w+W_c)}\right] + \frac{L(W_w+W_c)}{k_w m(LW_w)\tanh(mH_c)} + \frac{L(W_w+W_c)}{\dot{m}C_p} \tag{6.25}$$

6.3 Conclusion

The development of this math model was used to help predict configurations of microchannels that would maximize heat transfer and minimize pressure losses. These configurations will be tested in future work at the Institute for Micromanufacturing at Louisiana Tech University. The microchannels tested for this work are compared to this model to determine its prediction reliability. These results are shown in Chapter 8. In addition, the resistance modeling method shown in this chapter will be used to determine h_{avg}.

CHAPTER 7

EXPERIMENTAL APPARATUS

This chapter gives an overview of the apparatus used to determine friction and heat transfer in microchannels. Section 7.1 details the fabrication process used to make the microchannels and test fixture. Section 7.2 discusses the flow loop which includes equipment selection criteria and the limiting conditions of the equipment. Section 7.3 describes the data acquisition system. In addition to this chapter, Appendix E lists detailed specifications for the equipment used in the experimental apparatus.

7.1 Test Section

The test section is the part of the experimental apparatus where the microchannels are tested. The microchannel fabrication technique is discussed in some detail because of the effect it has on determining the channel dimensions. The surface finish and metrology are also discussed in some detail because of the strong effect they can have on experimental uncertainty. In addition, there is a discussion about the fixture used to direct the fluid flow into the microchannels.

7.1.1 Microchannel Fabrication

The microchannels were fabricated from 0.3175 cm (0.125 in) thick 6061-T6 aluminum bars. Aluminum was chosen for its high thermal conductivity. Conventional cutting and milling processes were used to machine the aluminum pieces, channel blanks, to the final 2.54 cm x 10.16 cm (1 in x 4 in) shape. In an attempt to standardize the channel blanks, a Computer Numeric Control (CNC) program was written to manufacture the blanks by a uniform method. The CNC program, or G-code, is listed in Appendix A. Manifolds and glue channels were cut into the aluminum using a Bridgeport milling machine. Both the manifold and the glue channels were cut to a depth one half the thickness of the aluminum (0.3175 cm (0.0625 inch)). A 0.635-cm (0.25-in) hole was drilled through the blank to allow the fluid into the manifold. The microchannel blank configuration is shown in Figure 7.1. Notice that the maximum length for the microchannels is 6.35 cm (2.5 in). The microchannel length can be easily shortened by making the manifold section larger. The 6.35-cm length was chosen for several reasons. One was that other researchers (see Table 2.1 and 2.2) had maximum channel lengths of 4.1 cm (1.61 inches) and duplication of their results was desired. The channel length was also chosen to ensure that the majority of the flow in the channels is fully developed and not developing (see Equations 3.7 and 3.21).

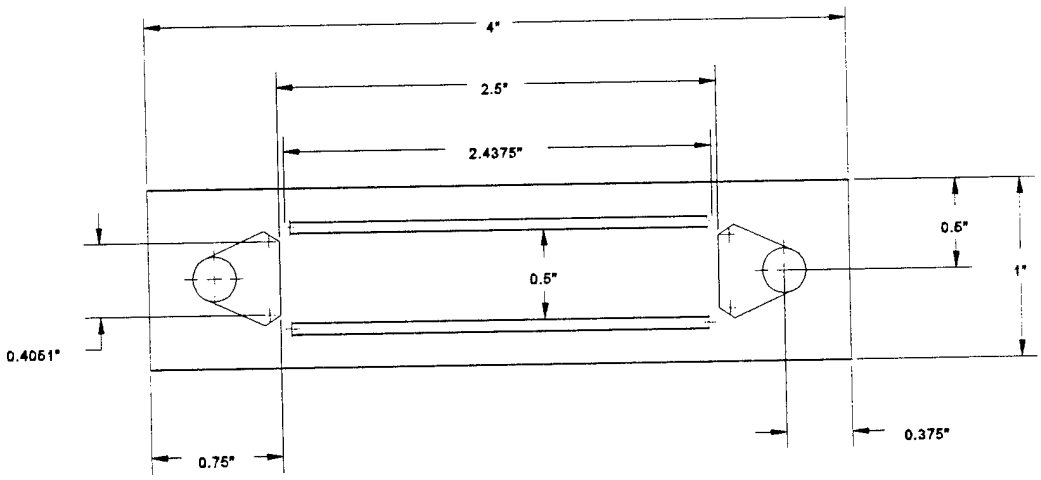

Figure 7.1: Microchannel Blank with Manifold and Glue Channels

The microchannels were cut to a depth of approximately 504 μm (0.02 in) with a 504-μm diameter milling tool. Different sizes and configurations of channels will be milled at a later time. Initially, the Bridgeport milling machine was used to cut the channels. However, even at the slowest feedrate with a spindle speed of 2000 rpm, the surface finish of the channels was extremely rough. By using a microscope to observe the cutting process, it was discovered that the cutting tool was moved through the material in steps. For each incremental movement, the tool would amass material on the forward side, continue rotating, and then move again. It was obvious that the conventional milling process could not feed the tool uniformly through the cutting material at this small scale. Therefore, a different milling machine, with a much finer resolution, was used to cut the microchannels. The milling machine, referred to as the Ultra Precision Milling Center, is a one-of-a-kind machine that was specially built by Dover Instrument Corporation for the Louisiana Tech University Institute for Micromanufacturing. The Ultra Precision Milling Center is controlled by Program Multi-Axis Controlled (PMAC) executive program

version 2.2 by Delta Tau Data Systems. The code written to control the cutting tool is similar to G-code, but is considered a higher level language. The code, written by Dr. Craig Friedrich of the Institute of Micromanufacturing, is shown in Appendix B. The microchannels are located in the center region of the channel blank, as shown in Figure 7.2. The larger channels at the top and bottom of the blank are used to keep excess glue out of the microchannel section.

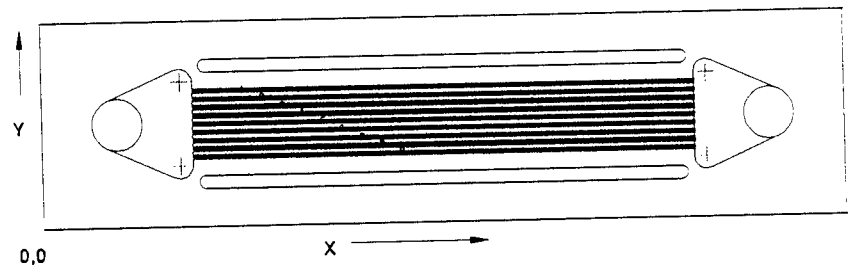

Y locations for tool path

0.34"
0.38"
0.42"
0.46"
0.50"
0.54"
0.58"
0.62"
0.66"

Array of 9 microchannels:
0.020" endmill used to cut channels
0.020" deep

Spacing:
0.020" of material between each channel
(ie., path from center of tool to next path is 0.040")

X locations (using center marks on fillet)
0.6875" to 3.3125
for a total length of 2.5"

Figure 7.2: Microchannel Locations

A Scanning Electron Microscope (SEM) photograph comparing the conventional milling process versus Ultra Precision milling process is shown in Figure 7.3. This figure clearly shows that the Ultra Precision milling process gives a cleaner channel with a better surface

finish. The figure shows a speck of loose debris in the upper part of the Ultra Precision channel. This should not be confused as a rough chip as shown in the conventional channel.

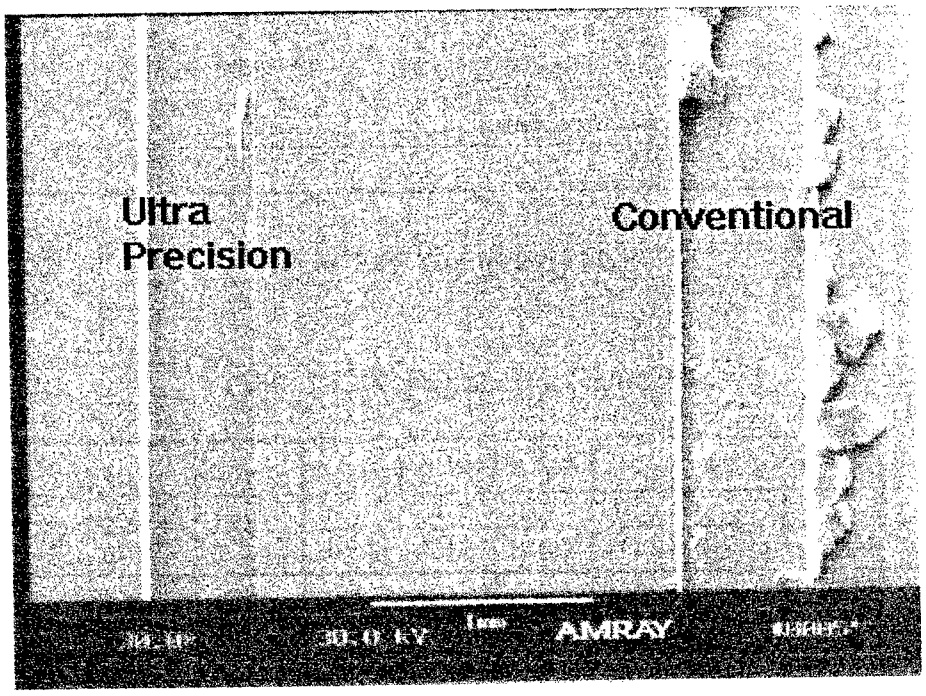

Figure 7.3: Comparison of Ultra Precision vs. Conventional Milling

7.1.2 Microchannel Surface Finish and Metrology

The aluminum, as received from the manufacturer, had scratched surfaces and was not level. Therefore, the surface had to be sanded on a lapping machine to smooth and level the surface. Though the surface visibly appeared to be very smooth, it was determined that the surface was not flat by using the z axis movement of the Ultra Precision Milling Center. By choosing some arbitrary z location as zero, the surface of the aluminum (where the channels were eventually cut) was mapped. The topography of the

surface (before milling the channels) is shown in Table 7.1 with the locations shown in Figure 7.4, indicating how irregular the surface was before milling the channels.

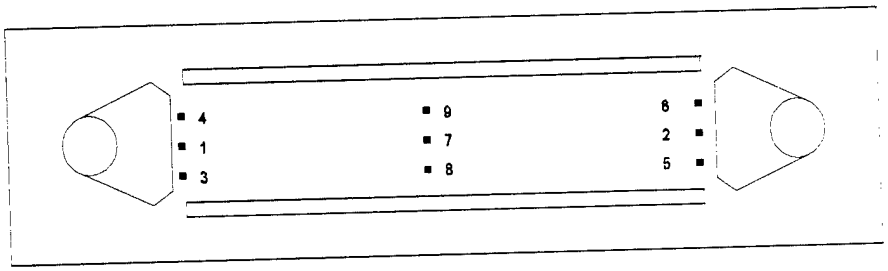

Figure 7.4: Topography Map

Table 7.1: Topography of Figure 7.4

Point	1	2	3	4	5	6	7	8	9
X Location cm (in)	2.24 (0.88)	7.92 (3.12)	2.24 (0.88)	2.24 (0.88)	7.92 (3.12)	7.92 (3.12)	5.08 (2)	5.08 (2)	5.08 (2)
Y Location cm (in)	1.27 (0.5)	1.27 (0.5)	0.89 (0.35)	1.65 (0.65)	0.89 (0.35)	1.65 (0.65)	1.27 (0.5)	0.89 (0.35)	1.65 (0.65)
Height (μm)	0	-5.2	11.5	-13.7	-1.4	-17	58.5	70.2	45.9

In addition, the height of the surface was measured in the center of the blank along the length of the middle channel (Y = 1.27 cm (0.5 in)) from point 1 to approximately point 2 on Figure 7.4. These data are presented in Table 7.2. The height calculations are shown in Appendix C along with the statistical analysis of the measurements, which are discussed later in this section. It should be noted that the channel blank height varied as much as 58 μm along the length.

Table 7.2: Topography in Center of Blank

X cm (in)	2.24 (0.88)	2.84 (1.12)	3.48 (1.37)	4.09 (1.61)	4.72 (1.86)	5.33 (2.1)	5.94 (2.34)	6.5 (2.56)	7.19 (2.83)	7.8 (3.07)
Y cm (in)	1.27 (0.5)	1.27 (0.5)	1.27 (0.5)	1.27 (0.5)	1.27 (0.5)	1.27 (0.5)	1.27 (0.5)	1.27 (0.5)	1.27 (0.5)	1.27 (0.5)
Height (μm)	0	21.1	39.6	52.7	58.2	56	47	33.6	16	0

Since the blank was uneven, a weighted average of 36 μm above the surface was used as the tool zero (true sample average = 32.4 μm). The tool was fed to a depth of 254 μm (0.01 in = ½ the tool diameter). One pass was made (to point 2), and then the tool was fed 254 μm deeper for a total depth of 508 μm from the origin. The tool was then fed back to point 1. Since the surface was not uniform along the aluminum blank, the channel depth varies along the length of the channel and also varies from channel to channel. In the future, the microchannel area of the blank will be milled flat before the channels are cut. The code for flattening the surface prior to cutting is shown in Appendix B. This code should reduce the error in the channel height considerably.

To obtain the depth measurement, photographs from an SEM were taken from a known angle. By using simple geometry and the scale bar on the photograph, a measurement of depth may be obtained. The scale bar, for this particular SEM, has a fixed error when measuring dimensions using this method. The actual dimensions are 6% larger than the value measured. However, a much better way to obtain the depth is to use a statistically determined mean from the depth of cut measurements taken by the Ultra Precision Milling Center. The average value of the channel depth in the middle channel (y = 1.27 cm (0.5 inches)) is 504.4 ± 15.8 μm (95% confidence interval). Using the

topography map, Table 7.1, the average channel depth is 491.47 ± 25.25 μm (95% confidence interval). Since the second depth measurement has a wider error band and includes most of the confidence interval shown by the middle channel calculations, the channel depth will be taken as 491.47 ± 25.25 μm. It must be noted that the confidence interval includes only the precision (statistically determined) error. The total bias error in the z measurement is very conservatively estimated to be ± 1 μm. This error is negligible when compared to the precision error and is therefore neglected. It is hoped that by flattening the microchannel surface prior to cutting, the total error on the depth will be on the order of ± 2 μm. Dr. Friedrich has demonstrated that the Ultra Precision Machining Center can mill a channel with a peak to valley variation in depth of no more than ± 1 μm.

The roughness of the channels was obtained by using a WYKO Roughness/Step Tester (RST) along each of the nine channels at the left, middle, and end locations. In addition, five more measurements were taken in the middle (fifth) channel. The raw data are shown in Appendix D. The average roughness was shown to be 800 nm with an RMS roughness of 36 nm. The manifold had an RMS roughness of 2.98 μm with an average roughness of 2.44 μm.

The WYKO RST was also used to determine the channel width. The measurement is taken by focusing the RST on the top surface of the aluminum blank. The RST scans the field of view crossing the width of a channel. After mapping the surface, the data are stored and may be analyzed at a later time. By moving the cursor to particular locations on the display screen, roughness values for that location may be obtained. Once the cursor is moved to a point above the channel, roughness values are no longer available since the

focal length was focused initially on the top surface of the aluminum (the maximum focal length is 100 μm for the RST in this case). Another cursor was then moved to the opposite side of the channel. In both cases, the cursor was moved to a point where the roughness readings just disappeared. The resolution is limited by the number of pixels on the display screen. In this case, one pixel represents 10 μm. The width was shown to be 495 ± 15 μm. The precision of the width measurement is limited using this technique. In the future, it is hoped that an optical microscope with frame-grabber software will be used to obtain the width values. However, the frame-grabber software has not been formatted to display a scale bar on the display screen. Therefore, accurate width measurements cannot yet be determined using this method.

Finally, the channel length was obtained by using a Max Cal digital dial caliper with readings accurate to 0.001 cm (0.0005 in). The channel length was found to be 6.353 ± 0.001 cm (2.501 ± 0.0005 in). Only one length measurement was taken prior to glueing the glass cover to the microchannels, so the precision error cannot be determined without destroying the sample. However, the G-code was written so that the length of the microchannels would be 6.35 cm (2.5 in); the length reported above is a reasonable value.

7.1.3 Microchannel Sealing and Headering

7.1.3.1 Sealing. A glass cover was affixed onto the surface of the blank with an optically clear, UV-cured glue (Impruv™ by Loktite®). An optically clear glue was used because, initially, the entire surface of the glass was to be covered with a thin film of glue. The intention was to glue the glass to the tops of the microchannels. It was later decided

to glue only the area outside of the microchannel section, since the glue was sure to seep into the microchannels resulting in a smaller flow area than measured before affixing the glass top. If the glue were used in the microchannel section, the dimensions would have to be remeasured after testing by slicing a cross-section of the microchannel blank (this will be done to check for fouling at a later date). It is probable that the cross-sections would not be uniform which would make it more difficult to get accurate microchannel dimensions. To ensure that the glue did not enter the microchannel area, a glue channel was milled on both sides of this section (see Figures 7.2 and 7.4).

It was subsequently found that the glue channels did not perform as well as expected. The glue seeped around the end of the glue channel near the manifolds. To prevent the glue from entering the microchannel section of the blank, the glue channels were extended around the manifold, as shown in Figure 7.5. In addition, the section of the blank outside of the glue channel, shown by the hatch marks on Figure 7.5, was milled down 254 μm (0.01 in) to allow the glass cover to seat on the top surface of the microchannels after the glue has been applied. Although it was not done for the first microchannel blank, the microchannel area of future blanks will be milled flat with the Ultra Precision Milling Center prior to cutting the microchannels. This procedure will ensure that the glass is in contact with the top surface of the microchannels. Having a slightly uneven top surface for the microchannels, leading to gaps between the glass and the top surface of the microchannels, is not expected to be too much of a problem. Since the channels are connected in parallel, the transverse pressure drop should be equal in each of the channels. Therefore, no cross flow between channels should occur.

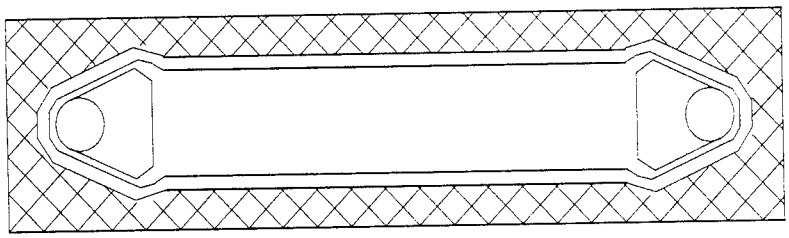

Figure 7.5: Redesigned Blank with Extended Glue Channels

7.1.3.2 Test Fixture. The test fixture is used to hold the test section in place and to provide a means for fluid ingress and egress to the microchannels. It is also used to obtain temperature and pressure measurements at the inlet and outlet of the test section. In addition, it houses the heater and insulates the area around the microchannels. Figure 7.6 shows the test fixture with a microchannel test section mounted in it. Other details shown in Figures 7.7, 7.8, and 7.10 are the cover plates used to press the microchannel onto the O-rings and the stainless steel inlet and outlet tubes (o.d. = 0.635 cm (0.25 in) and i.d. = 0.493 cm (0.194 in)), which are located in the bottom of the manifold.

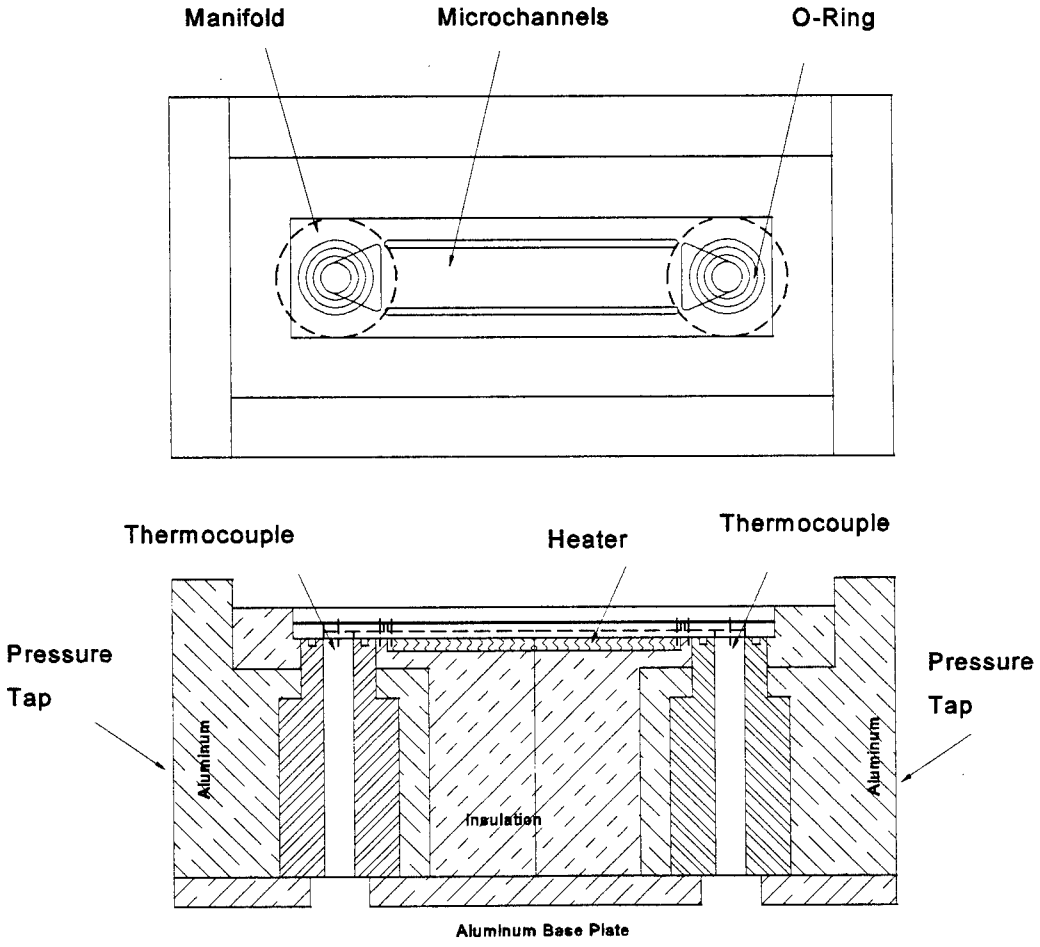

Figure 7.6: Top View and Side Cut-Away View of Test Fixture

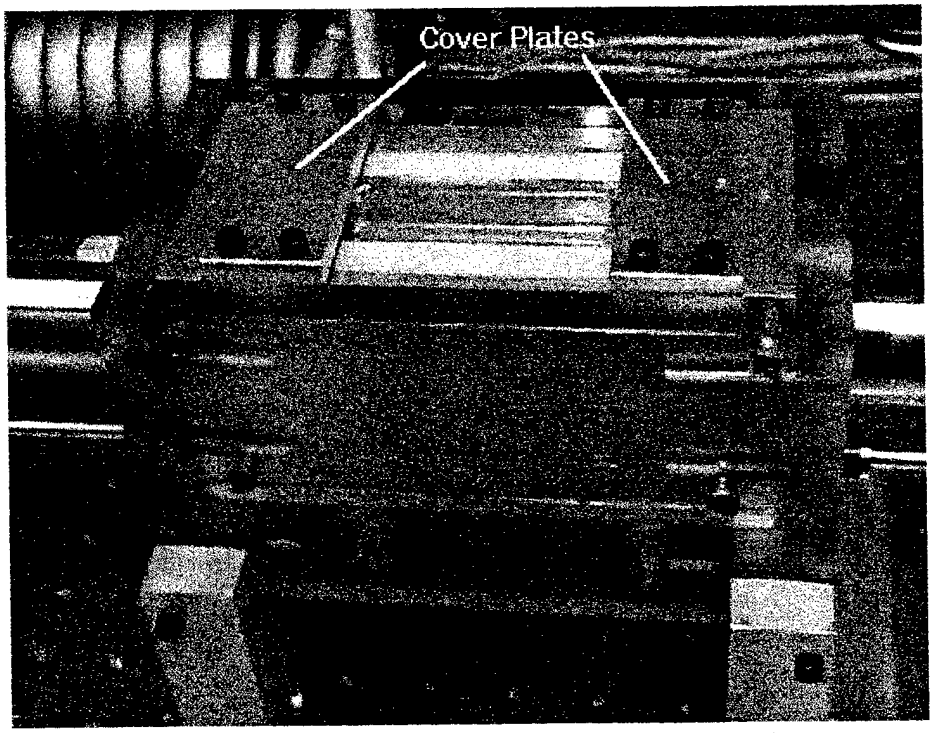

Figure 7.7: Cover Plates Securing Microchannels

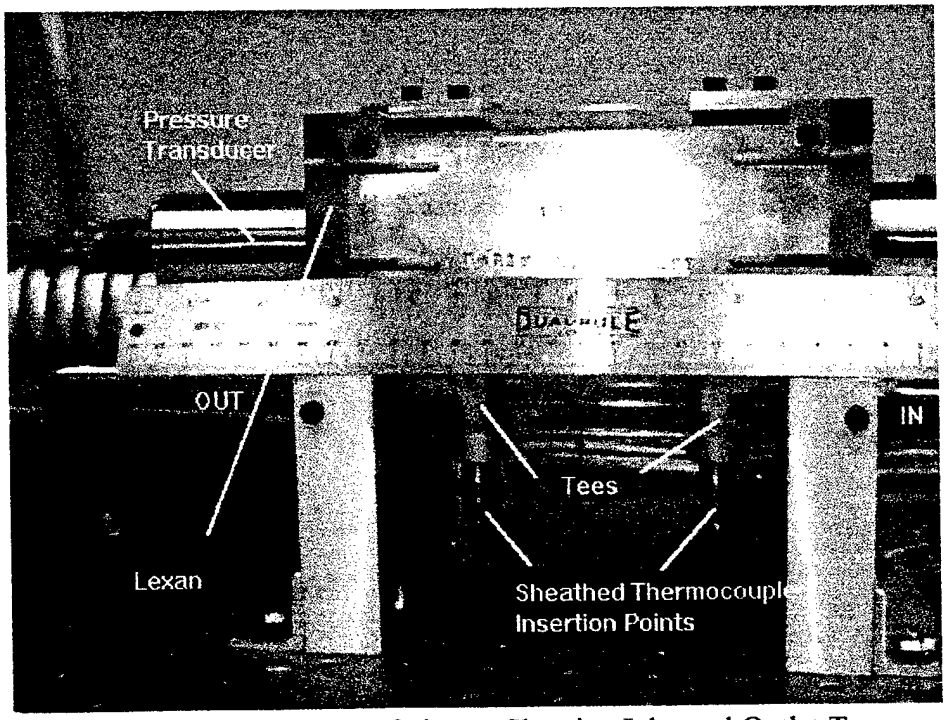

Figure 7.8: Side View of Fixture Showing Inlet and Outlet Tees

The main body of the test fixture is made of machined aluminum. Aluminum was chosen for its easy machinability and strength. Although aluminum is more conductive than most polymers and insulating materials, the microchannel blank does not come into contact with the outer aluminum body. The channel blank rests on an O-ring mounted in the manifold. In addition, insulation surrounds the other areas of the microchannel blank. Therefore, the only way a significant amount of heat can be transferred to the aluminum outer body is through the fluid and through the stainless steel manifold (as shown in Figure 7.6). The dimensions of the aluminum part of the test fixture are shown in Figure 7.9.

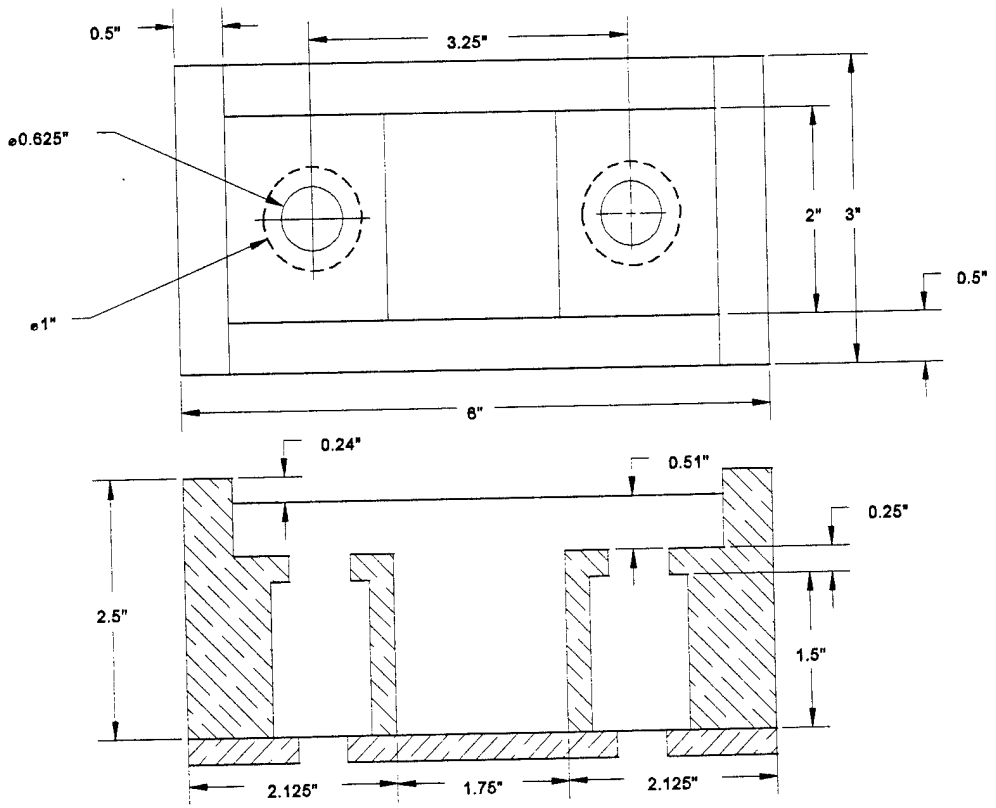

Figure 7.9: Test Fixture Dimensions

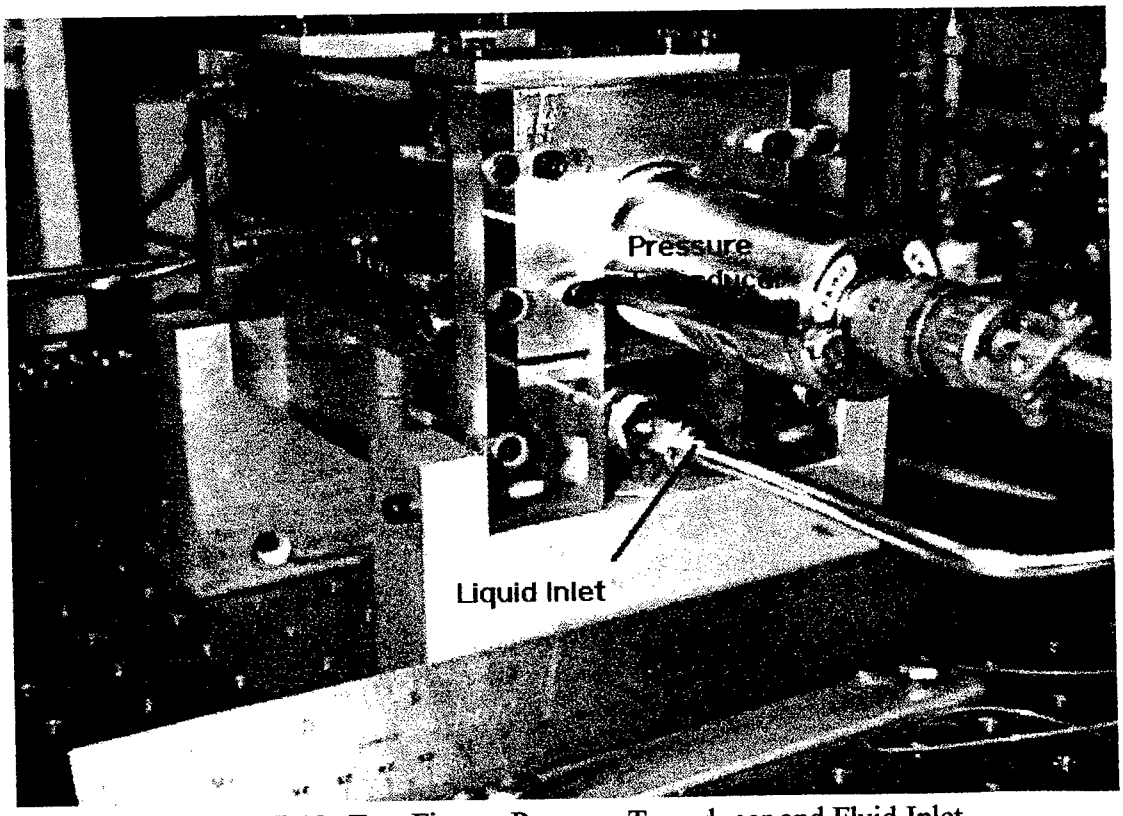

Figure 7.10: Test Fixture Pressure Transducer and Fluid Inlet

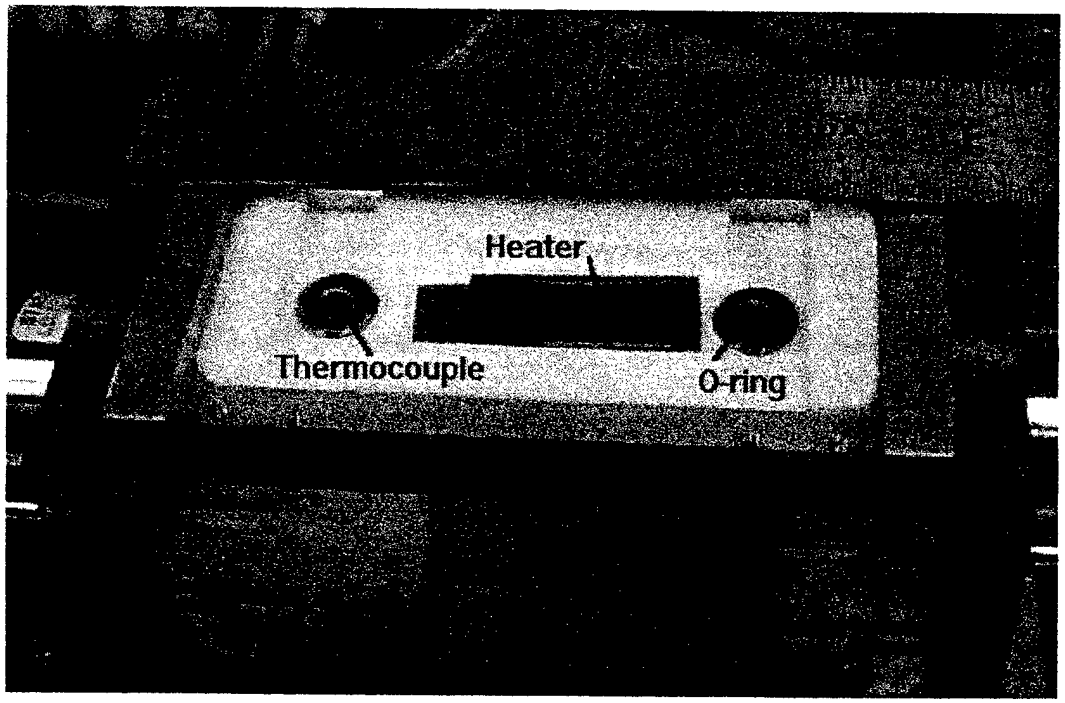

Figure 7.11: Test Fixture Heater and O-Rings

Figure 7.12: Microchannels in Test Fixture

The O-rings (see Figure 7.11) are made of ethylene propylene, EPDM, as are all of the seals in the flow loop. EPDM was chosen for its resistance to corrosion. There are other seal materials such as Buna-N and Viton. However, based on conversations with Judi Cuta (1995) of Battelle Pacific Northwest Laboratories in Richland, Washington, experience shows that these materials tend to degrade when used with certain refrigerants (e.g., R-124™ by 3-M®). It was recommended by researchers there that EPDM or neoprene be used for corrosion resistant seals.

The insulating material (see Figure 7.12) used inside the aluminum body of the test fixture is Teflon®. Lexan® sheets (1.27 cm (0.5 in) thick) insulate the outside of the aluminum test fixture. The Lexan® also isolates the aluminum from the table by serving as a mount for the fixture. The two different insulating materials were used because Teflon® has a higher melting point which makes it more suited for heater insulation. Lexan® has better insulating properties and machines much better than Teflon®. Therefore, Lexan® is used to insulate areas away from the heater. In addition to the insulation around the test section, all of the stainless steel tubing is insulated with 1.27 cm (0.5 in) thick flexible polyethylene pipe insulation. The thermal and mechanical properties of materials used in the construction of the test fixture, microchannel blanks, and the flow loop are shown in Table 7.3.

Table 7.3: Selected Thermal and Physical Properties of Experimental Apparatus Materials

Material	Thermal Conductivity (k) W/m·K	Thermal Expansion (α) 1/°C	High Temperature (melting point or distortion temp.) (°C)	Yield Tensile Strength Mpa (psi)
Teflon® (tetrafluorethylene)	0.25	$10x10^{-5}$	> 287	17 - 31 (2,500 - 4,500)
Lexan® (polycarbonate plastic)	0.19	$8x10^{-5}$	148 (crystalline melting point = 268)	55 - 62 (8,000 - 9,000)
Polyethylene (Pipe Insulation)	0.036	—	93	—
EPDM (ethylene propylene)	—	—	150 softening temp.	—
Glass	1.08	$80x10^{-6}$	820	—
Aluminum (6061-T6)	177	$23.6x10^{-6}$	527	255 (37,000)
Stainless Steel	14.7	$17.3x10^{-6}$	1,400	520 (75,000)
Omegatherm®201 Thermally Conductive Paste	2.3	—	200	—

Note: Properties are approximate values at 300 K (23°C)

7.1.4 Heaters

The heater used in the test fixture (see Figure 7.11) during the initial stages of experimentation is a commercially available flexible Kapton® heater manufactured by Watlow Electric. The heaters are manufactured in a sheet of plastic with various resistance elements. A 40-ohm, 1 cm by 4 cm heater was cut from the sheet and attached to a <100> piece of silicon wafer with J.B. Weld ™. (The silicon was used for stiffness only.) The leads were then attached to a direct current (DC) source manufactured by Harrison Laboratories (model number 6456B). The power source has a range of

0 to 100 amps and 0 to 36 volts. In addition, Omegatherm®201 Thermally Conductive Paste (T_{max} = 200°C) was used to ensure that the heater is in intimate contact with the bottom of the test section.

For future experiments, thin film resistance elements will be used to provide a higher heat flux. Inconel will be deposited onto <100> silicon wafers with a thickness of 2 - 16 nm. The largest heater will have an area of approximately 8 cm^2, and the smallest will have an area of approximately 0.8 cm^2. With 1,000 W of power supplied, it is anticipated that a heat flux range of 124 W/cm^2 to 1,240 W/cm^2 can be obtained. This range is dependent on the amount of heat that can be dissipated by the heat sinks since too high a temperature will "burn out" the heater. Eight gauge wires will be silver soldered to the resistance elements to supply the electric power to the resistor. These heaters will use the same power supply as the Kapton® heaters. Since these heating elements were not available at the time of the experiment, further details on the thin film heaters are omitted. An additional heater, Omegalux™ flexible heating tape, was used to preheat the fluid before it enters the test section. This was used to "fine tune" the inlet temperature as needed.

7.2 Flow Loop

The flow loop (Figures 7.13 - 7.16) is designed to conduct heat transfer and friction experiments for a variety of fluids and flow conditions. The fluids include gases, refrigerants (two-phase studies), and liquids. However, only one fluid, water, will be

tested for this work. In addition, the flow loop was designed to handle a variety of inlet pressures, temperatures, and flow rates. These are discussed in the following sections.

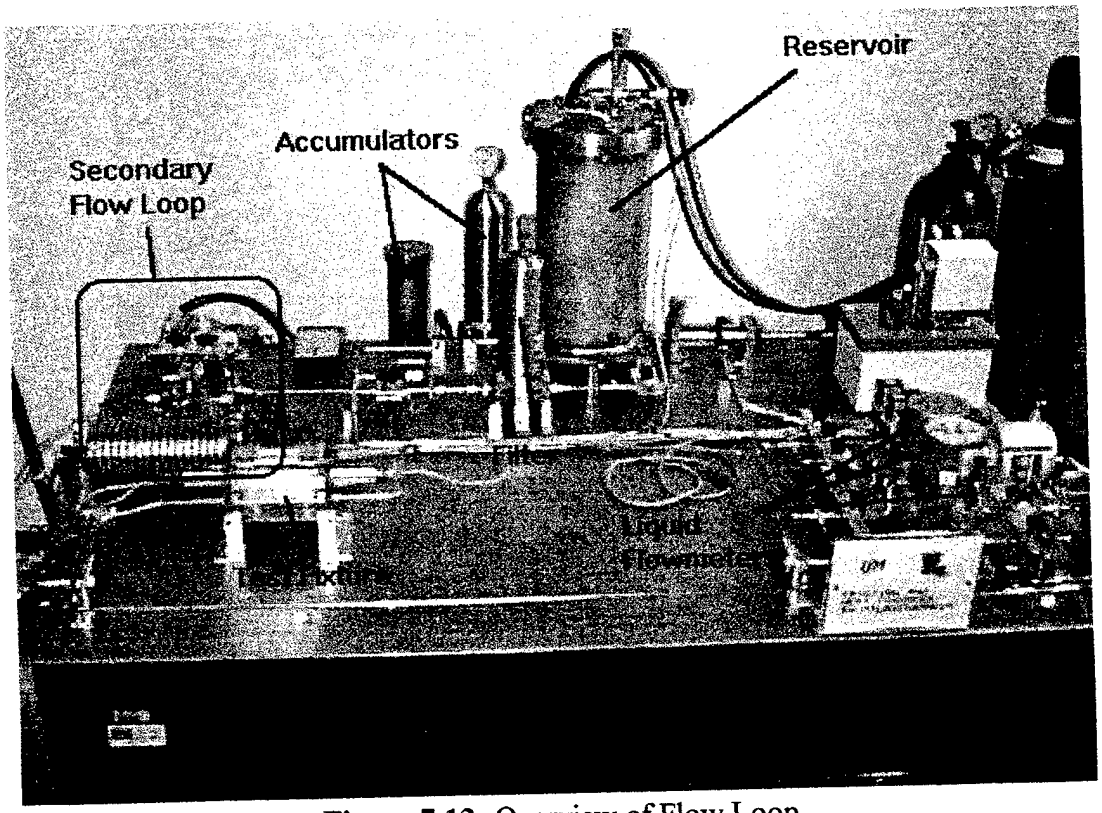

Figure 7.13: Overview of Flow Loop

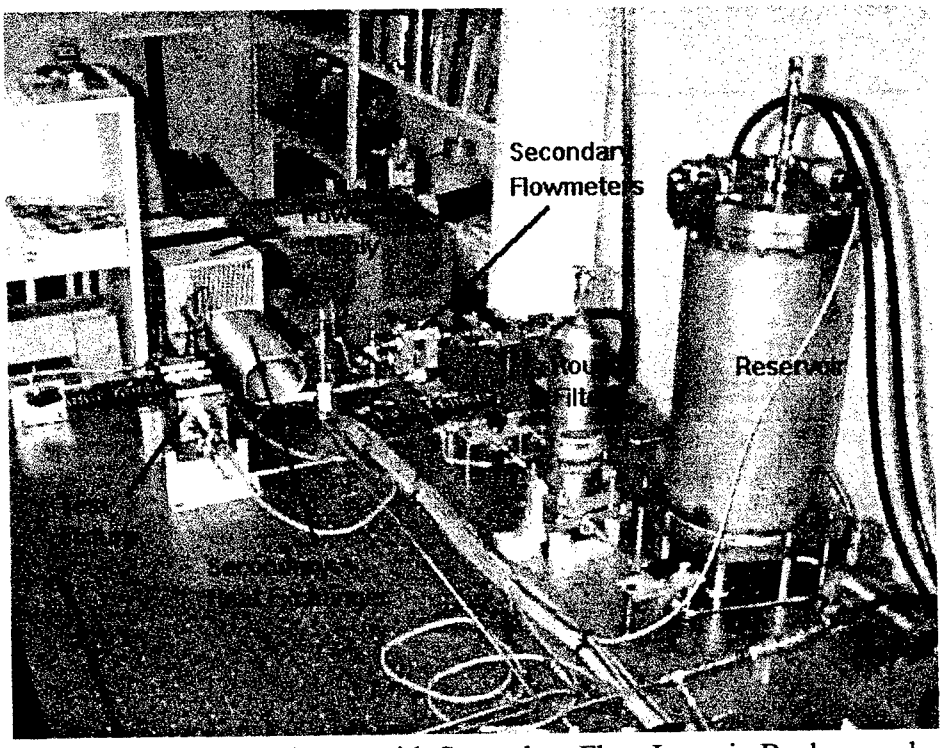

Figure 7.14: Test Fixture with Secondary Flow Loop in Background

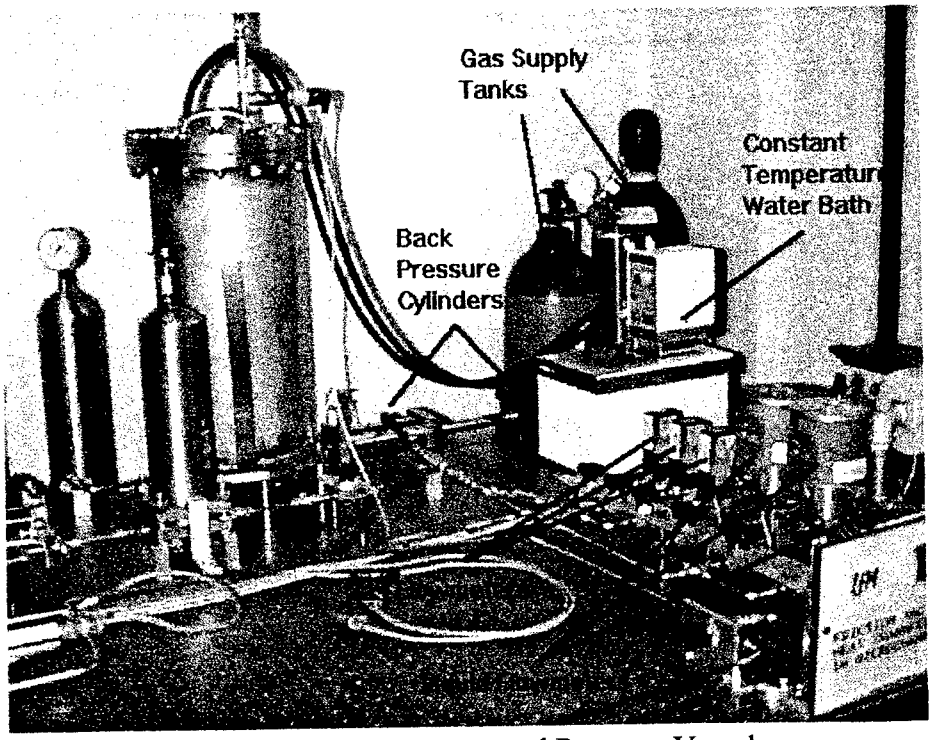

Figure 7.15: Flowmeters and Pressure Vessels

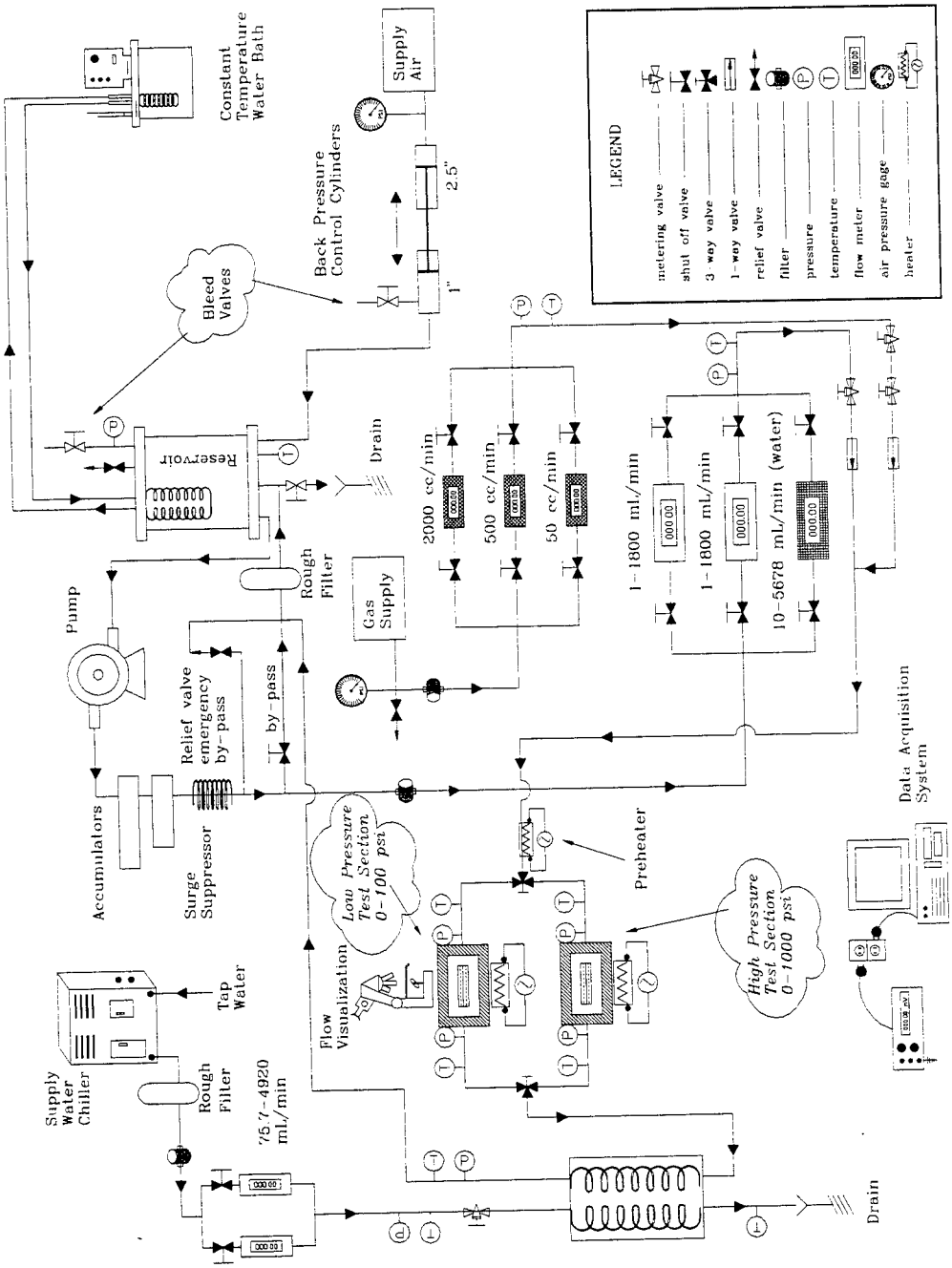

Figure 7.16: Flow Loop for Micro Heat Transfer Experiments

7.2.1 Primary Flow Loop

The limiting conditions for the primary flow loop are listed in Table 7.4. Since the test fluid for this thesis is water, only the components pertaining to testing this fluid will be discussed. Water will flow through the primary loop in the following order:

1. Reservoir (also pressure and temperature measurement)
2. Pump
3. Accumulator (pressure vessel with an air/water interface)
4. Surge suppressor (nine feet of coiled stainless steel tubing)
5. Valve (some of the flow recirculates in the bypass loop)
6. Fine filter (0.5 μm or 7.0 μm)
7. Flow rate measurement (model 234)
8. Temperature and pressure measurement
9. Fine metering valve to control flow rate
10. Temperature and pressure measurement (high accuracy transducer)
11. Microchannels (flow visualization)
12. Temperature and pressure measurement (high accuracy transducer)
13. Heat exchanger
14. Temperature and pressure measurement
15. Rough filter
16. Reservoir

Note: Initially, the fluid will be recirculated for several minutes through the bypass loop to coarse filter the fluid.

The wetted parts of the flow loop are constructed almost entirely of stainless steel with EPDM seals. This construction is mainly for corrosion resistance, but it also helps to reduce the heat transfer from the test section to other areas of the flow loop. In addition, the equipment was chosen so that experiments could be conducted with the broadest range of flow rates, temperatures, pressures, and fluid choices.

Table 7.4: Limiting Conditions of Equipment in the Primary Flow Loop

Component	**Maximum Pressure kPa (psi)**	**Temperature °C**	**Flow Rate mL/min**
Pump	8,274 (1,200)	82 (max.)	0 to 8,300
Water Flowmeter (Max model # 234)	13,788 (2,000)	-40 to 110	10 to 5,678
Flowmeter (Max model # 213)	6,894 (1,000)	-250 to 265	1 to 1,800 (x 2 flowmeters)
Test Section Pressure Transducer (PX-951) (0 to 689.4 kPa) (0 to 100 psig)	1,034 (150) (proof pressure)	-17.7 to 85 (operable range) 15.5 to 71 (compensated range)	N/A
Test Section Pressure Transducer (PX-951) (0 to 6894 kPa) (0 to 1000 psig)	10,341 (1,500) (proof pressure)	-17.7 to 85 (operable range) 15.5 to 71 (compensated range)	N/A
Loop Pressure Transducers (PX-213) (0 to 6894 kPa) (0 to 1000 psig)	10,341 (1,500) (proof pressure)	-20 to 85 (operable range) -20 to 80 (compensated range)	N/A
Type "T" Thermocouple	N/A	148 (max.)	N/A
Kapton® Heater Kit	N/A	200 (max. for Kapton®)	N/A
Preheater (Omegalux™ flexible heating tape)	N/A	482 (max.)	N/A
Omegatherm®201 Thermally Conductive Paste	N/A	-40 to 200	N/A
Exergy Heat Exchanger	31,023 (4,500) (inner tube) 13,788 (2,000) (outer tube)	≈ 400 (max.)	N/A
Reservoir	2,068 (300) design with factor of safety = 2	≈ 150 (max. for EPDM seals)	N/A

7.2.1.1 Reservoir. The reservoir was fabricated from stainless steel and is capable of withstanding pressures of approximately 2,068 kPa (300 psi) or greater. However, the flow loop pump has a limitation of 689 kPa (100 psig) on the back pressure, so the tank design pressure should not be reached. To insure that the pressure is maintained below 689 kPa (100 psig), a safety relief valve is mounted on the tank. The reservoir may be used as a pressure vessel for the refrigerant experiments or simply as an open tank for experiments where no back pressure is required.

The tank was designed so that the pressure and temperature could be maintained at some known value. The back pressure is controlled by two cylinders. A 6.35-cm (2.5-in) cylinder is pressurized with the building supply air which is connected to a 2.54-cm (1-in) cylinder by a connecting rod. This means that for a 68.9 kPa (10 psig) inlet supply air, the tank will be pressurized to 172.4 kPa (25 psig). The temperature is controlled by using a constant temperature water bath to recirculate water through coiled stainless steel tubing inside of the tank. The water bath has a temperature range of 0°C to 100°C.

7.2.1.2 Pump. It was determined that for single and multiple microchannels, using the Darcy-Weisbach equation (Equation 3.2) and the heat exchanger pressure drop model (Equation 4.1), respectively, that a high pressure, low flow rate pump was required to test microchannels with diameters less than 500 μm. As the diameter decreases, the pressure requirements increase, and the flow rate requirements decrease. Figure 7.17 shows the pressure drop and flow rates for water at 23°C in single round microchannels. Multiple channels would have a larger overall flow area and would not be as restrictive. For

example, the 25-μm channel (length = 1 cm) has a pressure drop greater than 8,274 kPa (1,200 psi) with a flow rate of 1 mL/min. However, multiple 25-μm channels would have a pressure drop of approximately 3,447 kPa (500 psi) for the same flow rate. This is assuming a 25-μm spacing between channels on a 1 cm x 1 cm test section (approximately 200 microchannels).

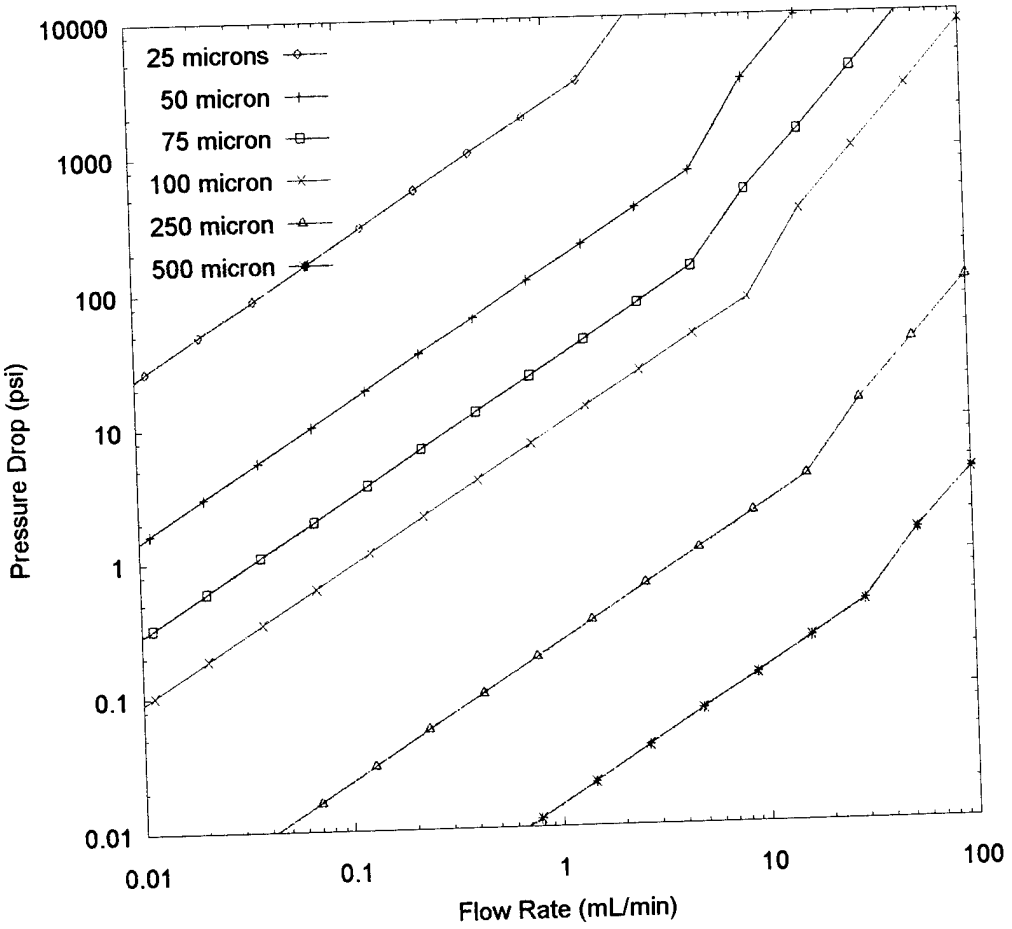

Figure 7.17: Darcy-Weisbach Pressure Drop in Single Channels with Water

There are some tradeoffs that must be made when choosing the pump for the flow loop. The ideal pump would be capable of providing a pulseless flow rate

(0 to 5,000 mL/min or better) and a high enough pressure (6,894 kPa (1,000 psig) or better) to test the full range of microchannel test sections (10 μm to 500 μm). There are many pumps available that can dispense at low to moderate flow rates; however, only a few of these types of pumps will give a high enough pressure (above 689 kPa (100 psig)). By requiring a minimum pressure output of 689 kPa (100 psig), the choices are narrowed even more to positive displacement pumps such as piston, diaphragm, and progressing cavity pumps.

The primary flow loop uses a positive displacement diaphragm pump. Unfortunately, diaphragm pumps do not have pulseless flow. This particular type of pump was chosen for its high pressure output and low flow rate range. To vary the test section flow rate, some of the fluid flow has to be recirculated in the bypass loop.

To lessen the pulse effect, a pulse dampener and two accumulators were added to the system. The pulse dampener is made of approximately nine feet of coiled stainless steel tubing. The accumulators are stainless steel pressure vessels with an air/liquid interface. The air/liquid interface may be a concern in the future because of the possibility of the two fluids mixing. However, with this experiment, this possibility is not seen as a problem.

A microscope will be used to visualize the flow within the microchannels. To reduce external vibrations, the flow loop (except for the pump and the constant temperature water bath) is mounted on an air isolation table. It is hoped that flow visualization will help to determine mechanisms that may be prevalent in microchannel that

are not seen in larger channels. Some of the effects of these mechanisms may include earlier transition to turbulence, increased heat transfer, and a lower friction factor.

7.2.1.3 Flowmeters. The flowmeters for the primary loop were chosen to meter the widest range of flow rates. This was done by first considering flowmeters that could measure the low range flow rates (< 10 mL/min). The meters chosen cover the widest range of flow rates with the most precision. The meter limitations are shown in Table 7.4. The precision of the meters is discussed in Chapter 9.

The flowmeters are piston-type volumetric flowmeters. By using pressure transducers and thermocouples at the exit of the meter, the mass flow rate can be determined. The mass flow rate through the test section will be a constant value assuming uniform flow. Therefore, the Reynolds number can always be calculated for the test section even if phase change occurs.

7.2.1.4 Pressure Transducers. The pressure transducers were chosen based on an expected maximum pump outlet pressure of 8,274 kPa (1,200 psig). In general, measurement uncertainty increases with pressure transducer range (e.g., 0 to 6,894 kPa (0 to 1,000 psig) compared to 0 to 689.4 kPa (0 to 100 psig)). It was decided to use two types of high precision pressure transducers on the test section for different pressure ranges. Lower precision transducers are used elsewhere in the loop for economic reasons. The flow loop pressure transducers are primarily used to determine fluid properties; therefore, the transducer precision is not as critical in the flow loop as it is in the test section. The pressure transducers' specifications are listed in Table 7.4. The selected test

section pressure transducers have a temperature limitation of approximately 85°C (which is the limiting component in the test fixture).

7.2.2 Secondary Flow Loop

The limiting conditions for the secondary flow loop are listed in Table 7.5. The cooling water will flow through the secondary loop in the following order:

1. Supply water source
2. Chiller
3. Rough filter (automobile filter)
4. Fine Filter (7 μm)
5. Valve
6. Flow rate measurement (meter depends on flow range)
7. Fine metering valve to control flow rate
8. Temperature and pressure measurement
9. Secondary heat exchanger
10. Temperature measurement
11. Exit drain

The main reason for using a secondary flow loop is to determine the heat transfer to a fluid that has undergone a phase change or a change in quality. By condensing the fluid back to its liquid state (at some pressure), the heat transfer to the fluid can be determined. In addition, the secondary flow loop may also be used to determine the heat

transfer to fluids which have not undergone a phase change. The method used to determine the heat transfer will be discussed in Chapter 8.

Table 7.5: Limiting Conditions of Equipment in the Secondary Flow Loop

Component	**Maximum Pressure MPa (psig)**	**Temperature (°C)**	**Flow Rate (mL/min)**
Loop Pressure Transducers (PX-213) Range: 0 to 3.447 MPa (0 to 500 psig)	5.17 (750) (proof pressure)	-20 to 85 (operable range) -20 to 80 (compensated range)	N/A
Water Turbine Flowmeter (EG&G FTO-1NIX)	41.37 (6,000)	-50 to 200	3.78 to 303
Water Turbine Flowmeter (EG&G FTO-4NIX)	41.37 (6,000)	-50 to 200	75.7 to 4,920
Exergy Heat Exchanger	31.03 (4,500) - inner tube 13.79 (2,000) - outer tube	≈ 400 (max.)	N/A

7.2.2.1 Secondary Heat Exchanger. The secondary heat exchanger was sized based on the ability to condense refrigerants assuming a maximum heat transfer from the heaters of 1,000 W. Water is used as the cooling fluid because it is readily available and because it can be disposed of after it flows through the system. By using an open loop system on the cooling side, the problem of removing the heat transferred to the cold fluid is alleviated. In addition, water has a larger specific heat than most fluids. Therefore, the cooling loop fluid can "absorb" more heat than most fluids. However, the amount of subcooling is limited to 0°C. Should lower temperatures be needed on the cooling side, another type of heat transfer fluid will be used.

The heat exchanger was sized by using the effectiveness-*NTU* (Number of Transfer Units) method (Holman, 1990). Heat exchanger effectiveness is defined as

$$\epsilon = \frac{\textit{actual heat transfer}}{\textit{maximum possible heat transfer}} = \frac{q}{q_{\max}} \tag{7.1}$$

where the actual heat transfer (q) may be determined by

$$q = (\dot{m}C_p)_{hot}\,(T_{h1} - T_{h2}) = (\dot{m}C_p)_{cold}\,(T_{c1} - T_{c2}) = \epsilon q_{\max} \tag{7.2}$$

and the maximum heat transfer (q_{max}) is determined by:

$$q_{\max} = (\dot{m}C_p)_{minimum}\,(T_{h\ inlet} - T_{c\ inlet}) = C_{\min}(T_{h\ inlet} - T_{c\ inlet}) \tag{7.3}$$

The minimum fluid is the fluid with the smallest mass flow rate times its respective specific heat (C_{min}). The minimum fluid also has the higher ΔT. Typical temperature profiles for a counterflow heat exchanger are shown in Figure 7.18. The hot fluid is shown as the top curve, and the cold fluid is shown as the bottom curve.

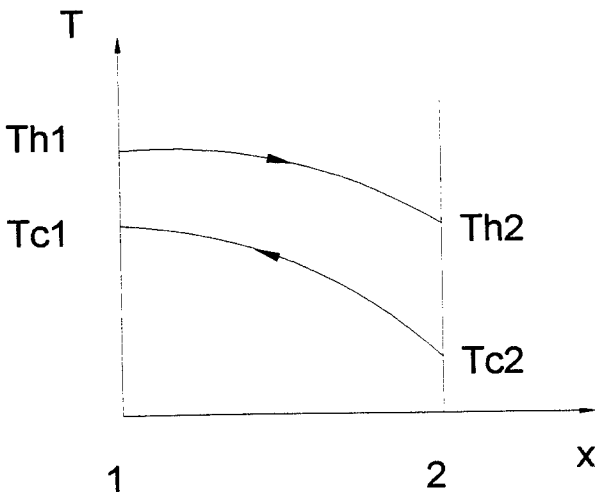

Figure 7.18: Counterflow Double-Pipe Heat Exchanger Temperature Profiles

The heat transfer area (A) required for the heat exchanger can be calculated by using the definition of NTU.

$$NTU = \frac{UA}{C_{\min}} \tag{7.4}$$

where U is the overall heat transfer coefficient. U may be calculated by using a thermal resistance method similar to that shown for the microchannel heat exchangers in Chapter 6. The overall heat transfer coefficient is defined by

$$q = UA\Delta T_{overall} \tag{7.5}$$

For the case of a well-insulated double-pipe heat exchanger, U would be defined by (based on the outside area, A_o)

$$U_o = \frac{1}{\frac{A_o}{A_i}\frac{1}{h_i} + \frac{A_o \ln(r_o/r_i)}{2\pi k_{wall} L} + \frac{1}{h_o}} \tag{7.6}$$

The subscripts "o" and "i" represent the outer and inner tube variables. Typical values of U are shown in Table 7.6 (Holman, 1990).

Table 7.6: Typical Values of Overall Heat Transfer Coefficient (U)

Situation	**U ($W/m^2 \cdot °C$)**
Freon-12 condensed with water coolant	280 to 850
Water to water heat exchanger	850 to 1,700

NTU can be calculated from one of the following relations for double-pipe heat exchangers:

Counterflow:

$$NTU = \frac{1}{C_{min}/C_{max} - 1} \ln\left[\frac{\epsilon - 1}{C_{min}/C_{max}\,\epsilon - 1}\right] \tag{7.8}$$

Counterflow ($C_{min} = C_{max}$):

$$NTU = \frac{\epsilon}{1 - \epsilon} \tag{7.9}$$

Condensing or Boiling:

$$NTU = -\ln(1 - \epsilon) \tag{7.10}$$

By calculating the *NTU* from one of the previous relations, the required heat transfer area can be determined from Equation 7.4. The heat transfer area required to condense Freon-12 with water, using the following conditions (Table 7.7), is shown in Figure 7.19. It should be noted that these conditions are used to "estimate" heat transfer characteristics to "size" the heat exchanger. They are not intended to be used in a rigorous analysis of the heat transfer characteristics.

Table 7.7: Flow Conditions for Freon-12 Condensation

U (assumed constant)	0.5 kW/m^2·°C
Back pressure	≈ 600 kPa
Th1 = Th2	23 °C (Tsat @ ≈ 600 kPa)
Tc2	0.1 °C
Cold flow rate	250 to 5,000 mL/min (in 35 equivalent intervals)

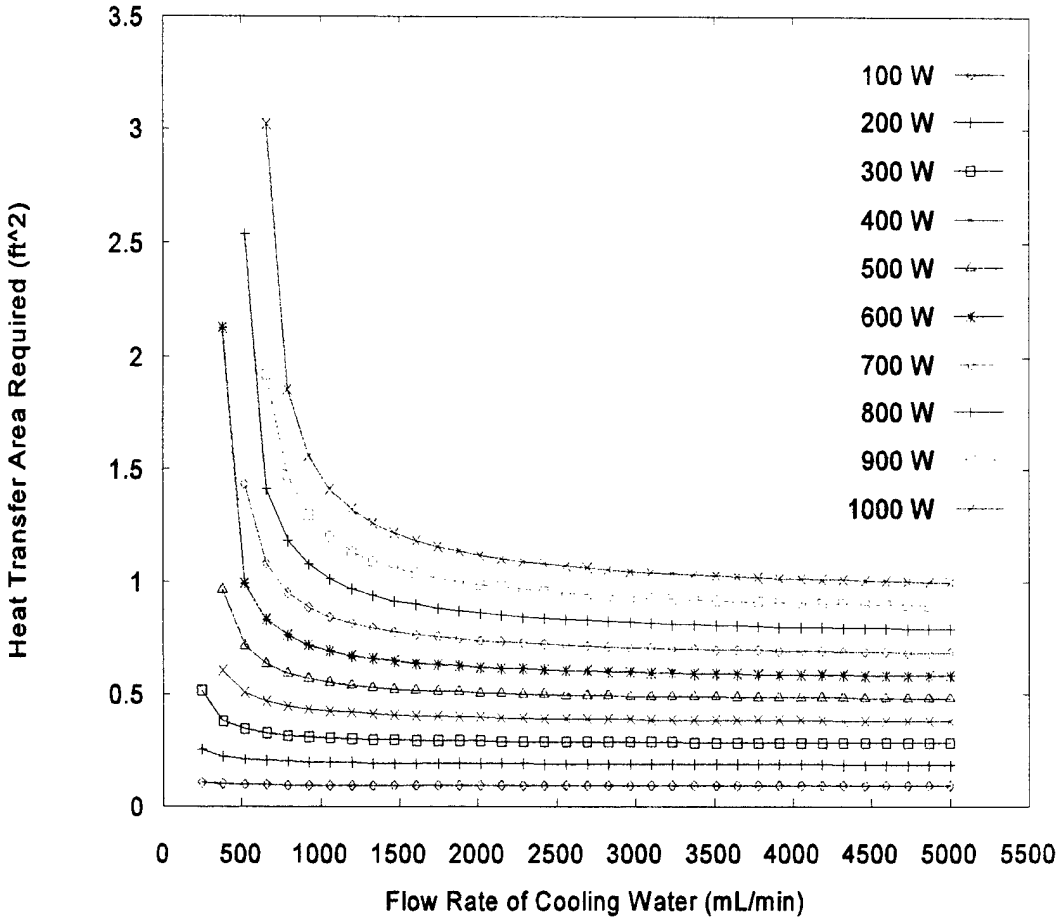

Figure 7.19: Heat Transfer Area Required to Condense Freon-12 (Tsat = 23 °C) with 0.1 °C Cooling Water

The corresponding temperature change of the cold fluid is given in Figure 7.20. It is important to get a sufficiently large temperature change on the cold side to be able to determine the heat transfer. For example, the type "T" thermocouples used in the flow loop have an error of ± 1 °C or ± 0.75% whichever is greater. If the measured temperature rise is small, it may be impossible to specify the actual temperature change, and thus the heat transfer, because of the measurement uncertainty. Therefore, the temperature changes corresponding to Figure 7.19 are shown in Figure 7.20 and Table 7.8 to

demonstrate that the heat exchanger specified for the flow loop will be adequate to determine the heat transfer to the refrigerant.

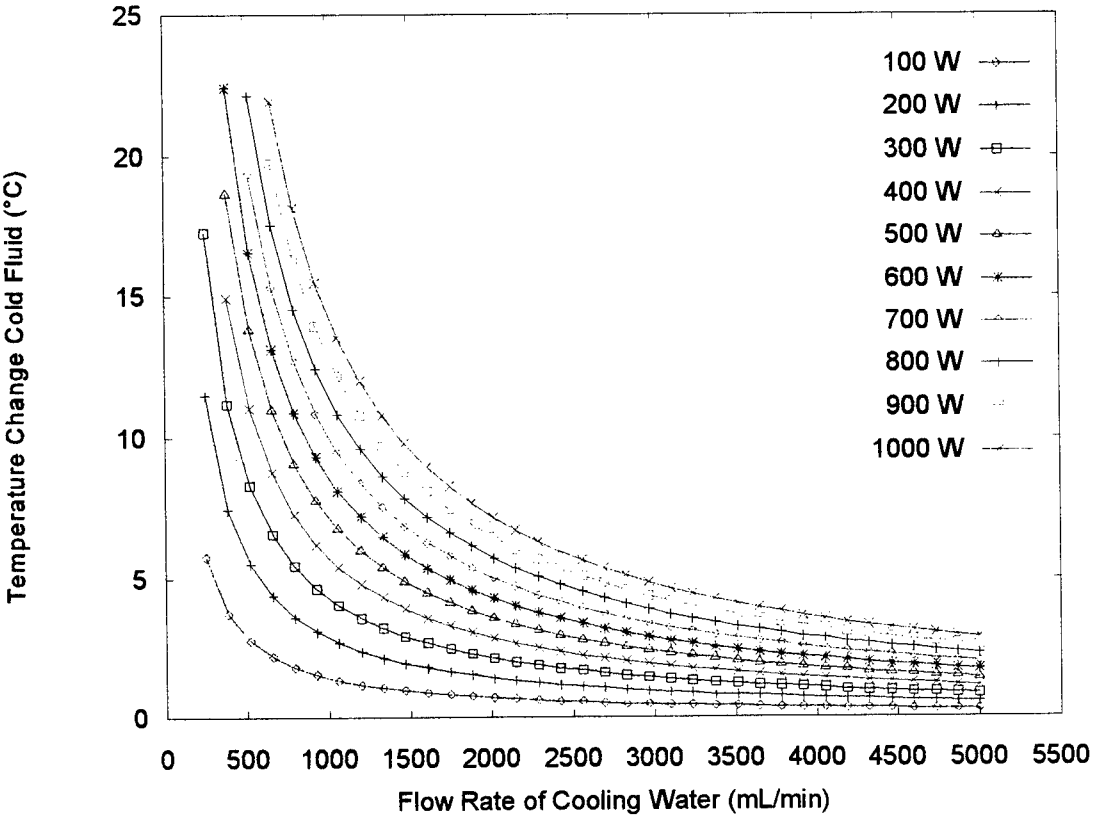

Figure 7.20: Temperature Change of Cooling Water Corresponding to Figure 7.19 and A = 1.2 ft^2

It must be noted that, when using Figure 7.20, the maximum heat transfer area of the actual heat exchanger is 0.1115 m^2 (1.2 ft^2). Notice that the flow rate at $\Delta T_{cold} \approx 22°C$ is approximately 700 mL/min for 1,000 W of heat removal; however, the required heat transfer area is greater than 0.1115 m^2 (1.2 ft^2) (as shown in Figure 7.19). Since only 0.1115 m^2 (1.2 ft^2) of heat transfer area is available, $\Delta T_{cold} \approx 22°C$ cannot be obtained assuming the conditions listed in Table 7.7 are true. Figure 7.19 shows that, for a heat

transfer area of 0.1115 m^2 (1.2 ft^2) and 1,000 W of the removal, the required cold flow rate is approximately 1,600 mL/min. Figure 7.20 shows that the corresponding ΔT_{cold} for this point is approximately 9°C. Therefore, the heat exchanger is adequate for removing the heat that will be added to the system by the heater, and the temperature change is large enough to determine the heat transfer to the cold fluid.

There is some point, however, when the heat transfer (q) is large enough so that the heat transfer area (0.1115 m^2 (1.2 ft^2)) is too small to give a theoretical effectiveness of 100%. This means is that there is no flow rate that will give the highest possible temperature change of 23°C for the conditions listed in Table 7.7. The maximum temperature changes and the corresponding cooling water flow rates, for the conditions shown in Table 7.7, are listed in Table 7.8. Increasing the flow rate will only decrease the temperature change and thus increase the experimental uncertainty. Therefore, Table 7.8 may be used to set optimal cooling water flow rates when performing two-phase studies with Freon-12.

Table 7.8: Maximum ΔT and Flow Rate for Condensing Freon-12 with Water

Heat Transfer (kW)	Approximate ΔT (°C)	Approximate Water Flow Rate (mL/min)
0.1	23	62
0.2	23	125
0.3	23	190
0.4	22	260
0.5	21	350
0.6	19	455

Table 7.8: (Continued)

Heat Transfer (kW)	Approximate ΔT (°C)	Approximate Water Flow Rate (mL/min)
0.7	17	590
0.8	15	770
0.9	12	1,080
1	9	1,600

Since the experimental apparatus was used for single-phase (water/water) experiments initially, it is advantageous to determine the required cold side flow rates for the maximum ΔT_{cold}. The conditions shown in Table 7.9 predict "ideal" flow rates.

Table 7.9: Flow Conditions for Water/Water Flow

U (assumed constant)	1.0 kW/m^2·°C
Heat transfer	0.1 to 1.0 kW
Heat transfer area (A)	0.1115 m^2 (1.2 ft^2)
Back pressure	neglected
T_{h2} (outlet)	23°C
T_{c2} (inlet)	0.1°C
Hot flow rate	250 to 5,000 mL/min (in 35 equivalent intervals)
Cold flow rate	varies
density = constant	998 kg/m^3
C_p = constant	4.178 kJ/kg·°C

The flow rates required to generate the highest possible temperature change on the cold side are shown in Figure 7.21. The maximum temperature changes are shown in Figure 7.22.

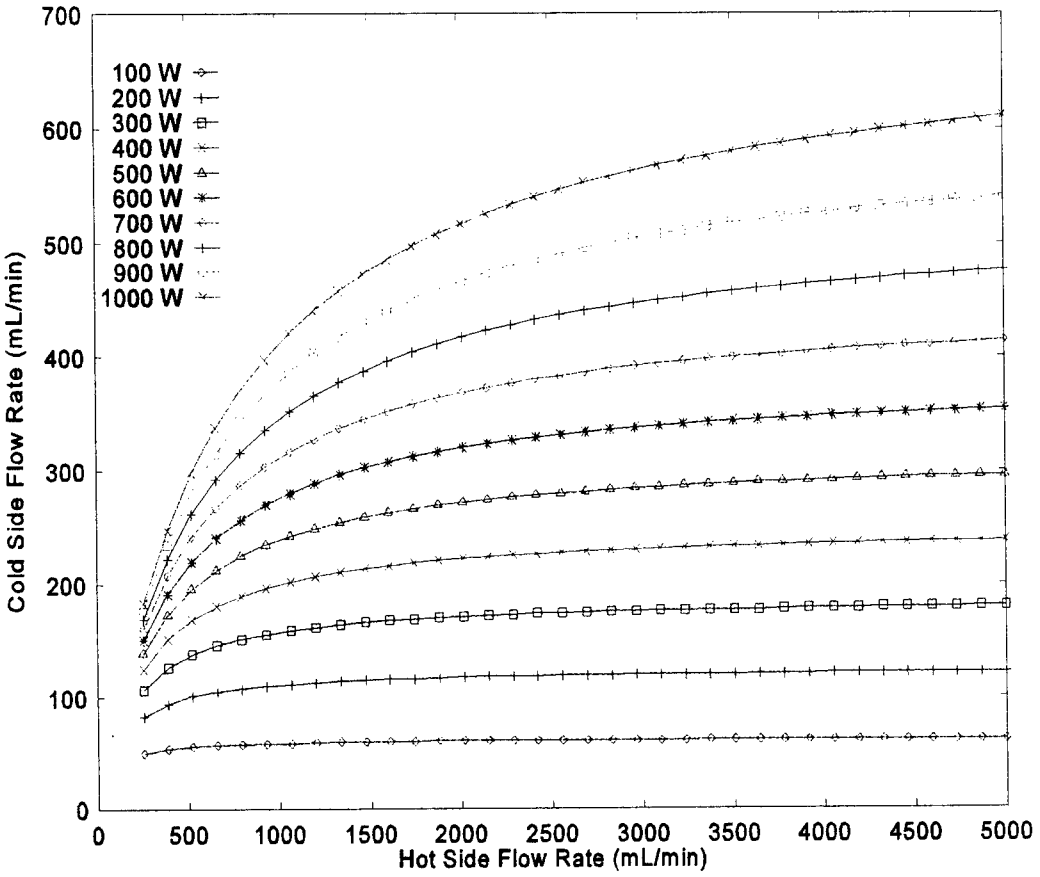

Figure 7.21: Flow Rates Required for Maximum ΔT in Water/Water Heat Exchanger

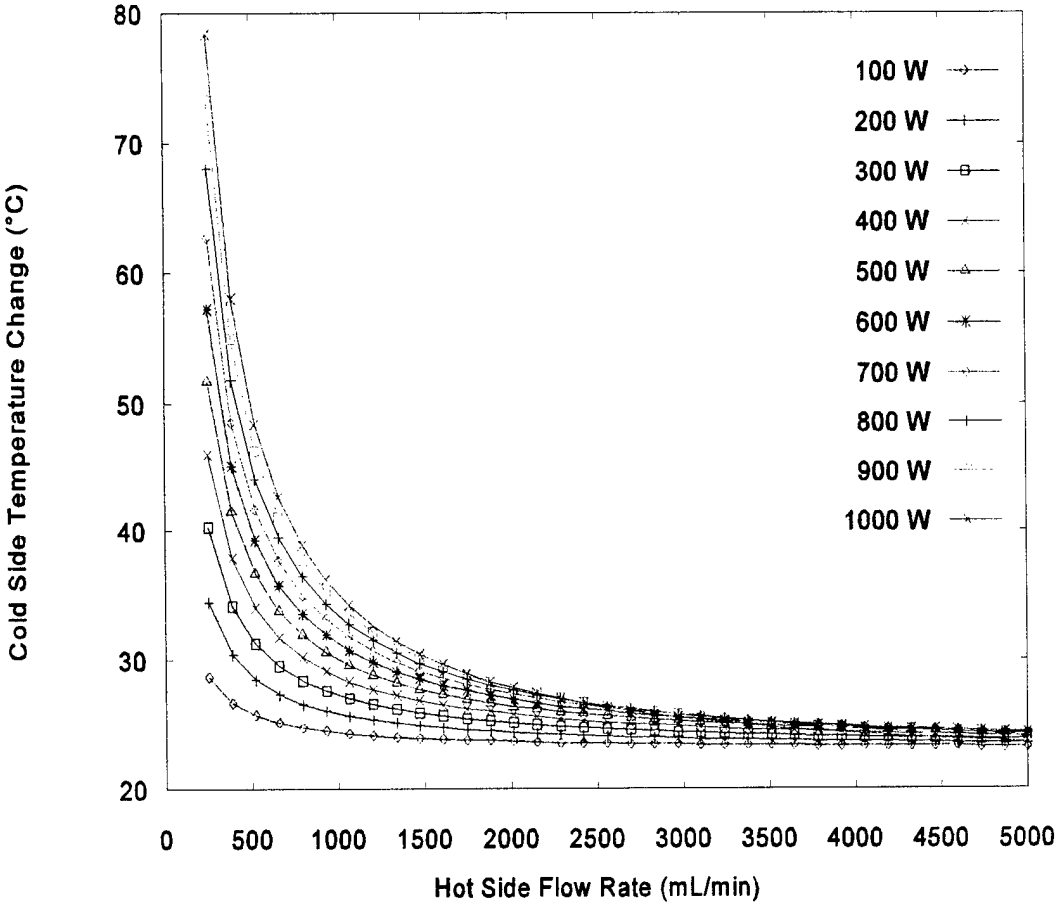

Figure 7.22: Maximum Temperature Change for Water/Water Heat Transfer

7.2.2.2 Flowmeters in the Secondary Flow Loop. The flowmeters on the secondary flow loop were required to measure the flow rate of the cooling water. The range of the flow meters was chosen with respect to the range of the primary flow loop measurement capabilities listed in Table 7.4. It was demonstrated in the previous section that it is most desirable to obtain a temperature difference as large as possible on the cold side (secondary loop). For water/water flow, this occurs when the cold fluid has a lower flow rate than the hot fluid. This lower flow rate is limited by the effectiveness of the heat

exchanger for a given heat transfer area. Therefore, precise turbine flowmeters were chosen to measure flow rates at or below the measurable flow rates of the primary flow loop. Additional specifications are included in Table 7.5 and Appendix E.

7.2.2.3 Temperature and Pressure Measurement in Secondary Flow Loop.

The thermocouples and pressure transducers used in the secondary flow loop are identical to the ones used in the primary flow loop. The only difference is the range of the pressure transducers. The pressure transducer range, on the cold side of the heat exchanger, varies from 0 to 3,447 kPa (500 psig). This pressure transducer range was chosen with the foresight that an extended pressure range may have to be measured in the event that a pump is added to the secondary flow loop to obtain higher flow rates.

7.3 Data Acquisition System

The data acquisition system consists of a Gateway 2000 personal computer equipped with a LabVIEW for Windows data acquisition system. The computer has a 75 Mhz Pentium processor and 16 Megabytes of RAM. The raw data consist of temperature readings (°C) for the thermocouples (LabVIEW automatically converts from millivolts to °C), voltage output from the pressure transducers, and frequency from the flowmeters. Converted data are displayed on the monitor to allow the user to determine when steady state has been reached. The raw data can be sent to an Excel spreadsheet when desired. Once in the spreadsheet, the voltage output can be converted into pressure, and the frequency output can be converted into volumetric flow rate by using the calibration curve

supplied with the meters. In addition, the pressure and temperature readings at the exit of the flowmeter can be used to convert the volumetric flow rate into a mass flow rate.

The power supplied to the heater is measured by using two digital multimeters. The voltage drop can be measured directly. However, these particular multimeters can measure only up to 2 amps. In case the current is higher than 2 amps, the current can be measured indirectly by placing a shunt resistor (0.01 ohms resistance) in series with the heater power leads. The voltage drop across the resistor is measured directly, and the current can be determined by using Ohm's law ($V = iR$). The power supplied to the heater can then be calculated by using Equation 7.11. As an additional check, the resistance of the heater can be used to determine power (Equation 7.11).

$$Power = Vi = i^2R = \frac{V^2}{R} \tag{7.11}$$

CHAPTER 8

EXPERIMENTS

This chapter discusses the methods used to reduce the raw data to obtain Darcy friction factor (f) and average Nusselt number ($\overline{Nu}_D$). The experimental results will then be compared to conventional correlations for friction and heat transfer.

8.1 Friction Factor

The easiest way to determine f is to use the Darcy-Weisbach equation (Equation 3.2). However, this procedure requires that pressure measurements be taken at two points along the length of the channel. Unfortunately, it is difficult to measure the pressure drop directly in small channels. Therefore, the pressure transducers should be located as close as possible to channel inlet and outlet to obtain the best results. The heat-exchanger pressure drop model (Equation 4.3) may then be used to determine f. Equation 4.3 must be modified to account for additional expansion and contraction losses caused by the manifold technique used in the test fixture. The modified form of Equation 4.3, used to determine f, is

$$\frac{\Delta P}{P_1} = \frac{V_1^2/2g_c}{P_1/\rho_1}[K_b+(K_{c2}+1-\sigma_2^2)]+\frac{V_2^2/2g_c}{P_1/\rho_2}[K_b-(1-\sigma_2^2-K_{e2})]+\frac{G^2/2g_c}{P_1\ \rho_1}[(K_c+1-\sigma^2)+2(\frac{\rho_1}{\rho_2}-1)+f\frac{L}{D_h}\frac{\rho_1}{\rho_m}-(1-\sigma^2-K_e)\frac{\rho_1}{\rho_2}] \tag{8.1}$$

Figure 8.1 shows the pressure measurement locations in the test fixture. Notice that there are expansions, contractions, and bends which contribute to the total pressure drop (in addition to that shown by the Darcy-Weisbach equation) measured by the transducers. These additional pressure losses may be determined by using the methods discussed in Chapter 4.

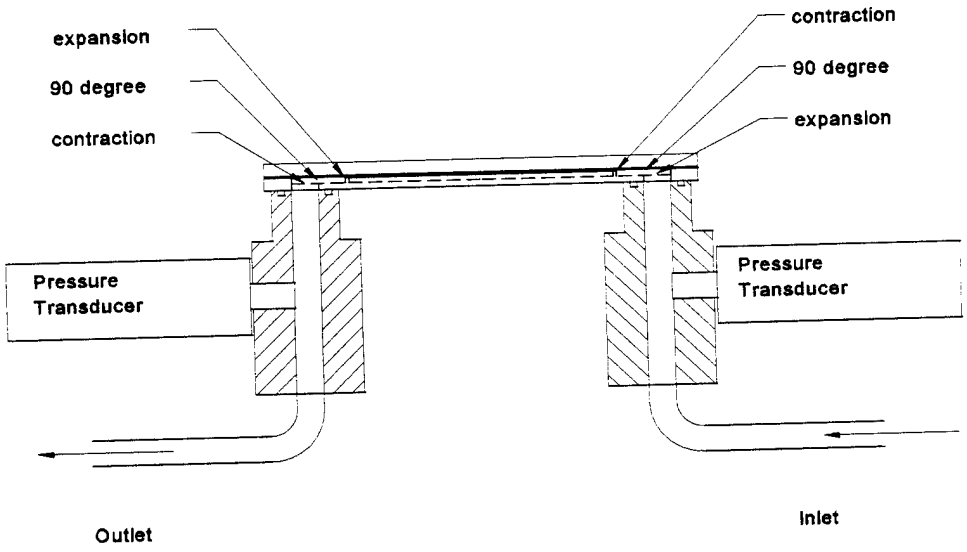

Figure 8.1: Additional Pressure Losses in Test Section

8.1.1 Manifold Expansion and Contraction Losses

The manifold expansion (K_b) and contraction (K_c) losses are functions of the free flow to frontal area ratio (σ). The free flow to frontal area ratio for the microchannels is calculated by considering the areas shown in Figure 8.2. The frontal area is a function of the height of the manifold and a width determined by the channel configuration. The height of the manifold is a constant value for each microchannel blank regardless of the

microchannel size and configuration (0.1588 cm or 0.0625 in). The width is determined by adding the channel width and the spacing between the channels. In the case of the 508-μm microchannels tested for this work, this value would be 0.0508 cm + 0.0508 cm = 0.1016 cm (0.04 in). The channel width and channel height were approximately 508 μm (0.02 inches), so the free flow area is 0.002581 cm^2 (0.0004 in^2). Thus, $\sigma = 0.16$.

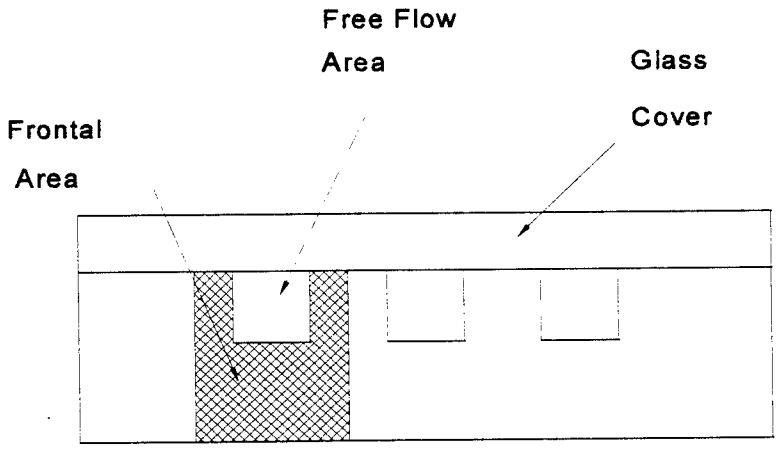

Figure 8.2: Microchannel Free Flow and Frontal Areas

The free flow to frontal area ratio for the manifold (σ_2) is calculated by considering the areas shown in Figure 8.3. The frontal area is represented by the enclosed triangle and has a value of 1.183 cm^2 (0.1833 in^2). The hole has a free flow area of 0.317 cm^2 (0.0491 in^2). This gives a constant value of $\sigma_2 = 0.267$ for every microchannel blank used in this work, since each blank has the same manifold design.

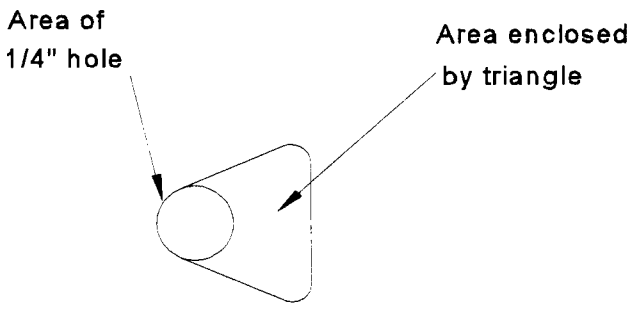

Figure 8.3: Manifold Free Flow and Frontal Areas

The expansion (K_e) and contraction losses (K_c) (Equations 4.5 and 4.6, respectively) are also functions of the contraction ratio (C_c) and the velocity distribution coefficient (K_d). The C_c is a function of σ, for which values are easily obtained by using Table 4.1 (e.g., for $\sigma_2 = 0.267$, $C_c \approx 0.644$). The K_d for laminar flow is a constant (e.g., for round tubes $K_d = 1.333$). However, for turbulent flow, K_d must be calculated by using Equation 4.17 or 4.18 which is a function of friction factor (f). This makes it slightly more difficult to determine f, since f is the result desired from the experiment. Therefore, rather than directly calculating K_e and K_c, estimates of their values may be determined using Figures 4.2 through 4.4 once σ and Re are known from the experimental results.

8.1.2 Ninety-Degree Bend Pressure Losses

The losses (K_b) for the ninety-degree bends at the entrance and exit of the microchannels may be estimated by using the data shown in Table 8.1 (White, 1986).

Table 8.1: Loss Coefficients, $K = h_f / V^2 / 2g$, for Elbows

Nominal Diameter (inches)	0.5	1	2	4
90° Screwed Regular Elbow	2.0	1.5	0.95	0.64

Since the manifold inlet is smaller than the diameters listed, a conservative estimate of $K_b = 1.2$ was used.

8.2 Convective Heat Transfer Coefficient

The average convective heat transfer coefficient (h_{avg}) is defined by the following relation:

$$q = h_{avg} A (\overline{T_w} - T_{bulk}) = h_{avg} A (\overline{T_w} - \frac{T_{in}+T_{out}}{2}) \quad (8.2)$$

The heat supplied to the test section can be determined by using q = (voltage)(current). The conservation of energy equation may also be used to determine the heat transfer. Equation 8.3 will be used to determine h_{avg} because this is the amount of heat that was transferred to the fluid.

$$q = \dot{m} C_p (T_{out} - T_{in}) \quad (8.3)$$

In addition to the heat transfer, determination of h_{avg} requires that several temperatures be known. The inlet and outlet temperatures are easily determined with thermocouples inserted into the fluid stream near the manifold. However, determining the average wall temperature is not as straightforward. Ideally, thermocouples could be used to determine the wall temperature profile along the channel. Problems may arise because temperature measurements within the small channels, such as those used in this work, could disturb the velocity profile which could affect heat transfer. In addition, there is

always the problem associated with sealing the thermocouple holes to prevent leakage. Therefore, the wall temperature measurements are done as close to the channel as possible.

In this work, it was desired to be able to test the heat transfer characteristics of many different microchannel configurations. To accomplish this goal, it was decided to attach the thermocouples and the heater to the test fixture. The microchannel heat sinks could then be easily interchanged without having to connect new thermocouples and heaters for each new test. The thermocouple locations are shown in Figure 8.4, and the heater/thermocouple configuration is shown in Figure 8.5. Three thermocouples were affixed to the top surface of the heater. To ensure that the heater was in contact with the bottom surface of the aluminum microchannels, a thermally conductive paste was applied to the heater surface.

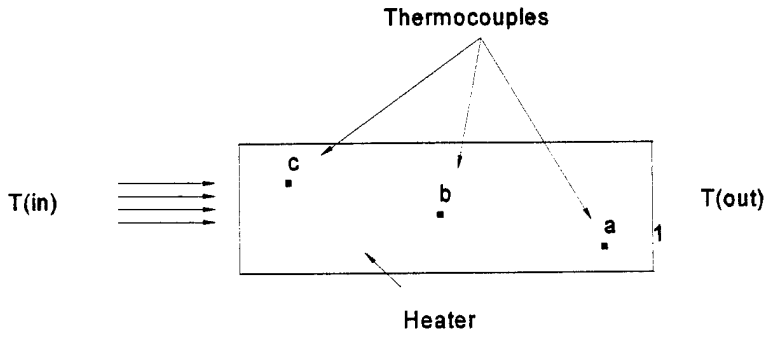

Figure 8.4: Thermocouple Locations

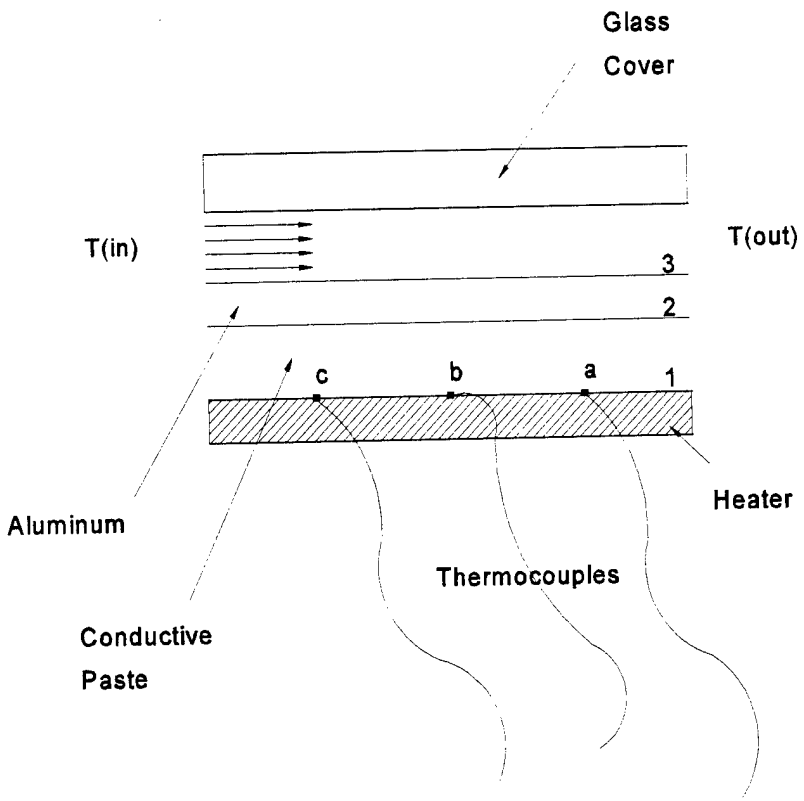

Figure 8.5: Thermocouple Configuration

The thermocouples actually measure the temperature of the heater surface (T_1). To determine the local wall temperature, Fourier's Law of Conduction was used. Several assumptions were made:

1. The thermal conductivity of the paste remains essentially constant, and its thickness, Δz = 1.5 mm, is uniform.

2. Since small (36 A.W.G.) wire was used to make the thermocouples, conduction through the wires is negligible.

3. The wall temperature of the microchannel cross-section at a given x- location has a uniform temperature (T_3) as shown in Figure 8.6.

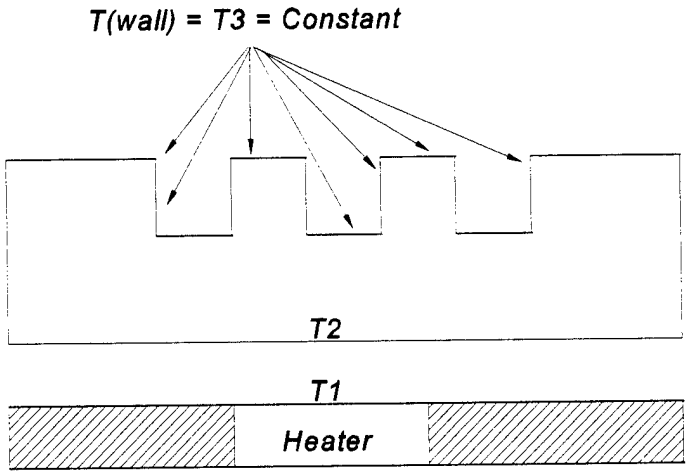

Figure 8.6: Cross-Section of Microchannel

Conservation of energy requires the heat transfer through the paste must be equal to the heat transfer through the aluminum (neglecting heat losses). Therefore, the following relation holds true:

$$q = k_{paste} A_{paste} \frac{(T_1 - T_2)}{\Delta z_{2-1}} = k_{Al} A_{Al} \frac{(T_2 - T_3)}{\Delta z_{3-2}} \tag{8.4}$$

By rearranging the terms, the following relation may be used to determine the wall temperature where $A_{paste} = A_{Al} = A_{heater}$. The areas are considered to be equivalent because 1-D conduction through the bottom of the channel blank is assumed.

$$\Delta T_{overall} = \Delta T_{1-2} + \Delta T_{2-3} = q \left(\frac{\Delta z_{2-1}}{A_{paste} k_{paste}} + \frac{\Delta z_{3-2}}{A_{Al} k_{Al}} \right) \tag{8.5}$$

Once the wall temperatures were obtained, an average wall temperature was calculated. This value was then substituted into Equation 8.2 to solve for h_{avg}, where the area (A) is taken as the heat transfer area of one of the channels. Therefore, the heat transfer area is defined as $A = (L_{heater} W_c + 2 L_{heater} H_c)$. The heat transfer area is based on one channel because the mass flow rate, and thus the heat transfer, is based on one channel.

The average Nusselt number was then calculated using

$$\overline{Nu_D} = \frac{h_{avg} D_h}{k_f} \tag{8.6}$$

8.3 Comparison of Experimental Data to Conventional Correlations

The raw data (shown in Appendix H) were sent to an Excel spreadsheet during the experiment. Once in the spreadsheet, the sample standard deviation for each data set was determined so that the data reduction program (shown in Appendix F) could be used to reduce the data and determine the experimental error. The methods used to determine the uncertainty intervals (error bars) are discussed in Chapter 9. These data are shown in Figures 8.7 - 8.10 as well as in Appendix I.

8.3.1 Friction Measurements

Figure 8.7 shows average friction factor data for nine 508-μm channels. The friction factor agrees with the Haaland equation (Equation 3.18) in the turbulent regime within 4.7% for data set 4 and 3.7% for data set 5. (Data set 5 is in closer agreement with

the Haaland Equation because more high *Re* data were taken where the agreement is closer). However, the "laminar" data, $Re < 2{,}300$, were lower than theory predicts. In addition, the experimental laminar friction factor increased as *Re* increased. This type of behavior is consistent with flow in the transition regime. However, there are not enough experimental data where laminar flow occurs. The channels would have to be lengthened to obtain low *Re* data. Therefore, neither the laminar nor transition region can be determined for this set of microchannels with this experimental set up.

The deviations from theory in the "laminar" regime are primarily due to the small differential pressure drop over the channel length. For example, the first data point of data set 4, which used the 0 to 689.4 kPa (0 to 100 psi) pressure transducer on the inlet, has error bars of 175% of the measured friction factor. The pressure drop here is approximately 1 kPa (0.15 psi), which is smaller than the measurement uncertainty of the pressure transducers. As the flow rate is increased, resulting in a larger differential pressure drop ($\Delta P > 25$ kPa (3.5 psi)), the error bars decrease to an average value of approximately 15% of the friction factor. Data set 5, which used the 0 to 6,894 kPa (0 to 1,000 psi) pressure transducer on the inlet, has larger error bars in the "laminar" regime because the transducer is less precise than the pressure transducers used for data set 4. The first data point has an error band of 228% for a differential pressure drop of 5.6 kPa (0.81 psi). The uncertainty interval decreases to less than 20% at a pressure drop of 107 kPa (15 psi) and eventually decreases to approximately 15% at higher pressures.

Figure 8.8 shows friction factor data for the single 254-μm channel. These friction data follow the trend of the theoretical values, but are lower in magnitude. This seems to

be consistent with the literature review in Chapter 2. Both sets of data appear to indicate laminar flow for $Re < 2{,}400$, in transition for the range $2{,}400 < Re < 3{,}500$ and in the turbulent regime for $Re > 3{,}500$. The theoretical laminar friction constant, $C = fRe = 56.91$, is 17% higher than the constant for data set 6 ($C = 47$) and 30% higher than the constant for data set 7 ($C = 40$). Both data sets are approximately 55% lower than the Haaland equation in the turbulent regime. It should be noted that there are only a few data points in the laminar regime because of the low flow requirements in this region. More laminar data could be taken if multiple 254-μm channels were used or if a different flow meter were used to measure the lower flow rates (flow rate < 10 mL/min). In addition, higher *Re* data could be obtained by using the 0 to 6,894 kPa (0 to 1,000 psi) pressure transducer on the inlet.

The error bars for both data sets, shown in Figure 8.8, are an average of 12.5% of the experimental friction factor. The differential pressure drop for the first data point on both sets of data was greater than 100 kPa (14 psi). This differential pressure drop is well above the uncertainty of the pressure transducers (± 1.5 kPa (0.21psi) for the root sum of the squares of uncertainty for two transducers) used in the test section (0 to 689.4 kPa (0 to 100 psi)). Therefore, the error band size remained relatively constant throughout the full *Re* range. However, the error bars shown in Figure 8.8 are smaller than those in Figure 8.7 because the channel dimensions are known with greater precision. The size of the error bars can be further decreased by using a more accurate method to determine the channel dimensions.

8.3.2 Heat Transfer Measurements

Figure 8.9 shows average *Nu* data for the nine 508-μm channels (supplied $q = Vi = 33.83$W). The "laminar" heat transfer data, $Re < 2{,}300$, are approximately 14% higher than the theoretical laminar value of $Nu = 3.556$ (constant heat flux on three sides of a rectangular duct). The turbulent data are shown to be, on average, 258% lower than the theoretical turbulent values represented by the modified Gnielinski equation (Equation 5.6). However, the error bars on the data are so large that the actual value of *Nu* could be very close to the theoretical values. The error bars increase in size, from 26% to 312% of the measured value, as *Re* is increased because the resulting ΔT approaches the uncertainty of the thermocouples (± 0.28°C). The temperature difference for data set 4 ranges from 2.08°C to 0.35°C.

These heat transfer data show the importance of obtaining a large temperature difference between the inlet and outlet. The error bars for data set 4 range from 26% for the low flow rates to 312% for the high flow rates. The average error bars were 200%. The temperature measurements are the largest source of uncertainty for these heat transfer measurements. However, other large sources of uncertainty are the length and area variables associated with Equation 8.2 which are used to determine the wall temperature. The sensitivity coefficients for these variables are one to four orders of magnitude larger than the sensitivity coefficients associated with temperature measurement. Therefore, it is very important to determine A_{heater}, Δz_{paste}, and Δz_{Al} accurately. The effects that the other variables have on the final result may be seen by observing the sensitivity coefficients and errors shown in Appendix F.

Figure 8.10 shows two sets of *Nu* data for the 254-μm channel. Exp6Nu.dat had a supplied q = 20.18 W, and exp7Nu.dat had a supplied q = 39.20 W. The laminar *Nu* data are approximately 240% (data set 6) to 370% (data set 7) higher than the theoretical laminar value of $Nu = 3.556$. The turbulent heat transfer data are, on average, from 10% lower (data set 6) to 7% higher (data set 7) than the theoretical values. The error bars for these data are an average of 21% (data set 6) and 25% (data set 7) of the measured value.

The data for the 254-μm channels (Figure 8.10) show much smaller error bars than the data associated with the 508-μm channels (Figure 8.9). This is primarily due to a decrease in the mass flow rate, thus allowing the fluid to absorb more heat and have a larger outlet temperature. The ΔT ranged from 3.27°C to 8°C for data set 6 and from 7.8°C to 18.9°C for data set 7.

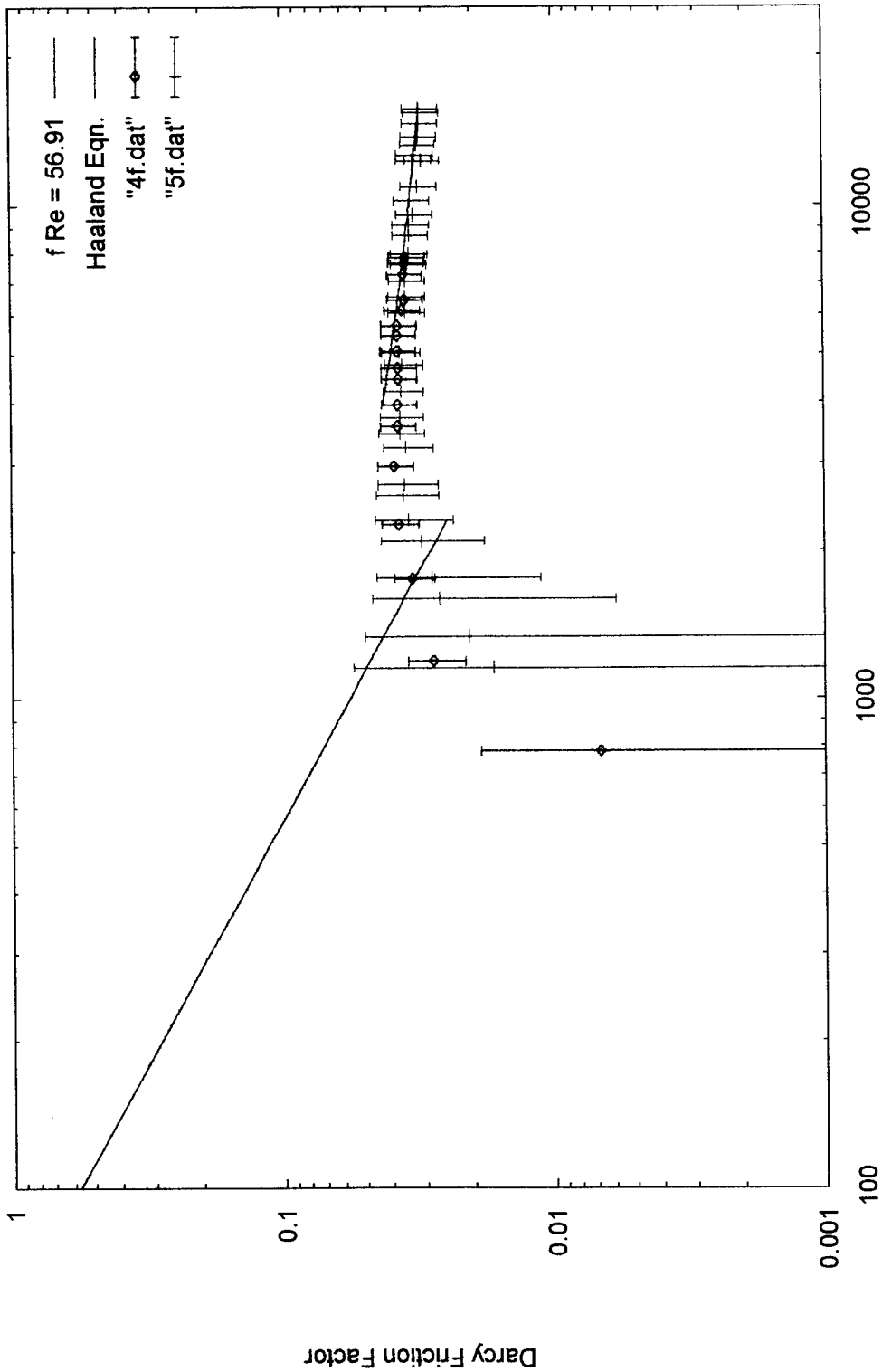

Figure 8.7: Average Friction Factor for Nine 508-μm Channels

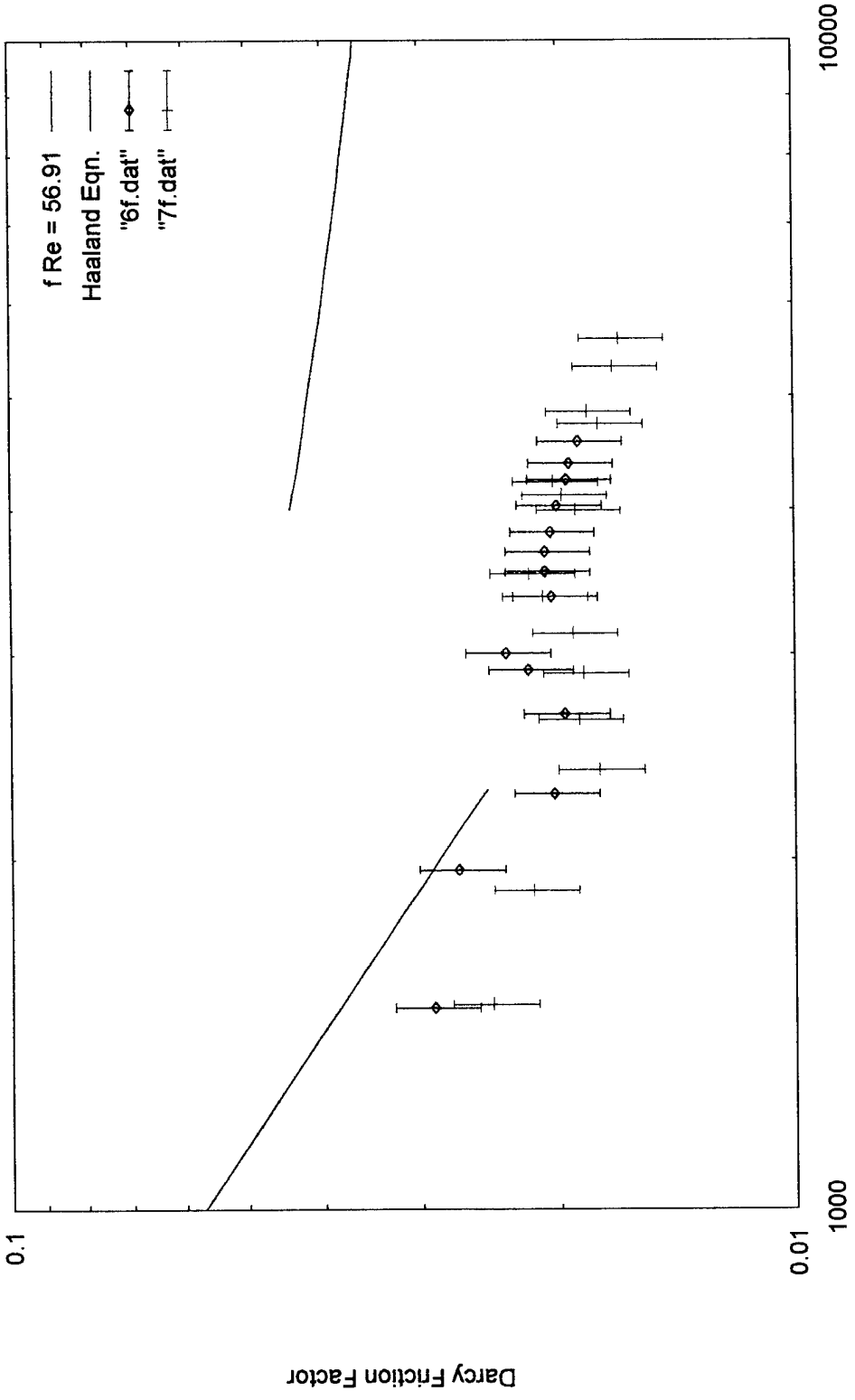

Figure 8.8: Friction Factor in Single 254-μm Channel

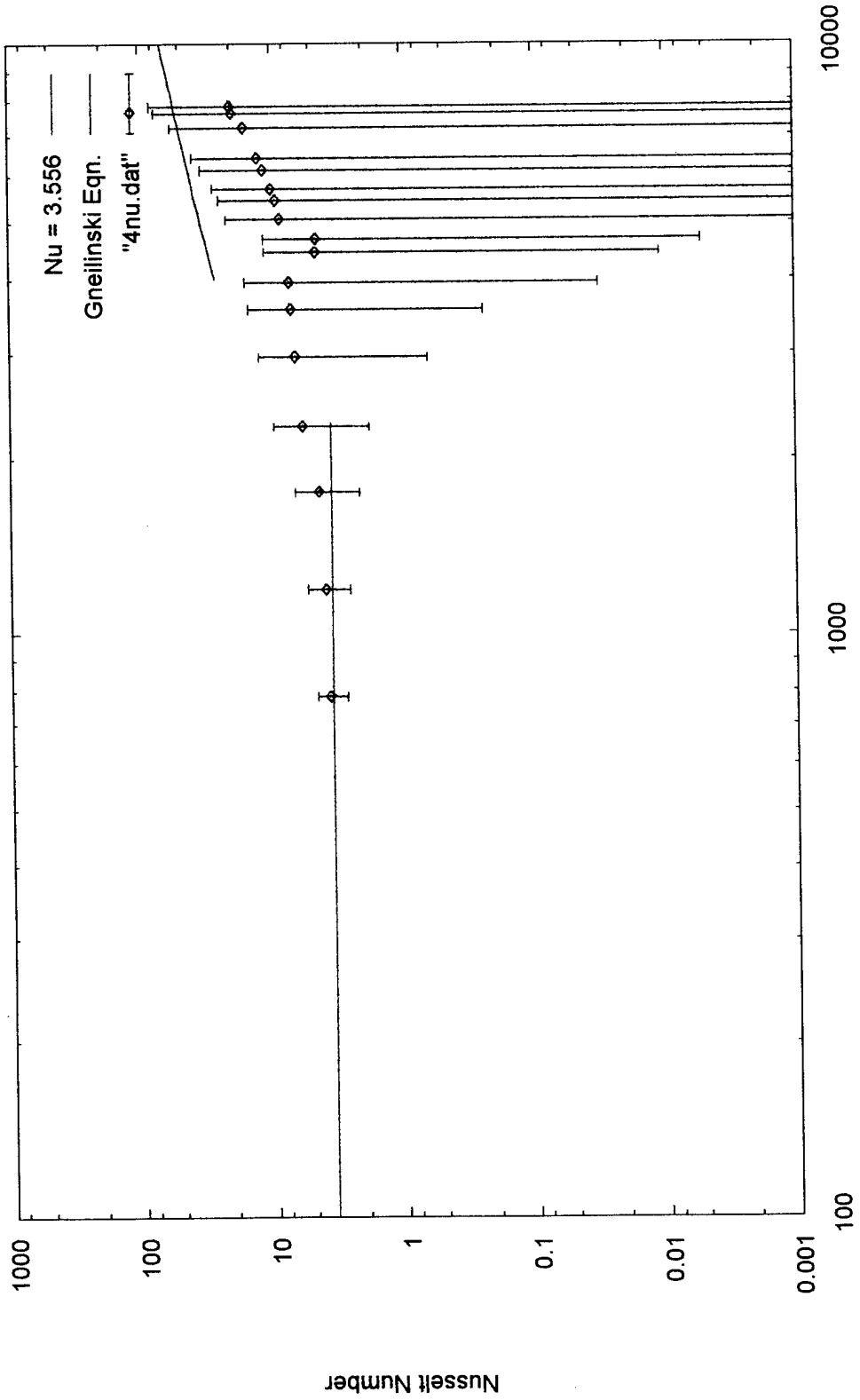

Figure 8.9: Average Nusselt Number for Nine 508-μm Channels

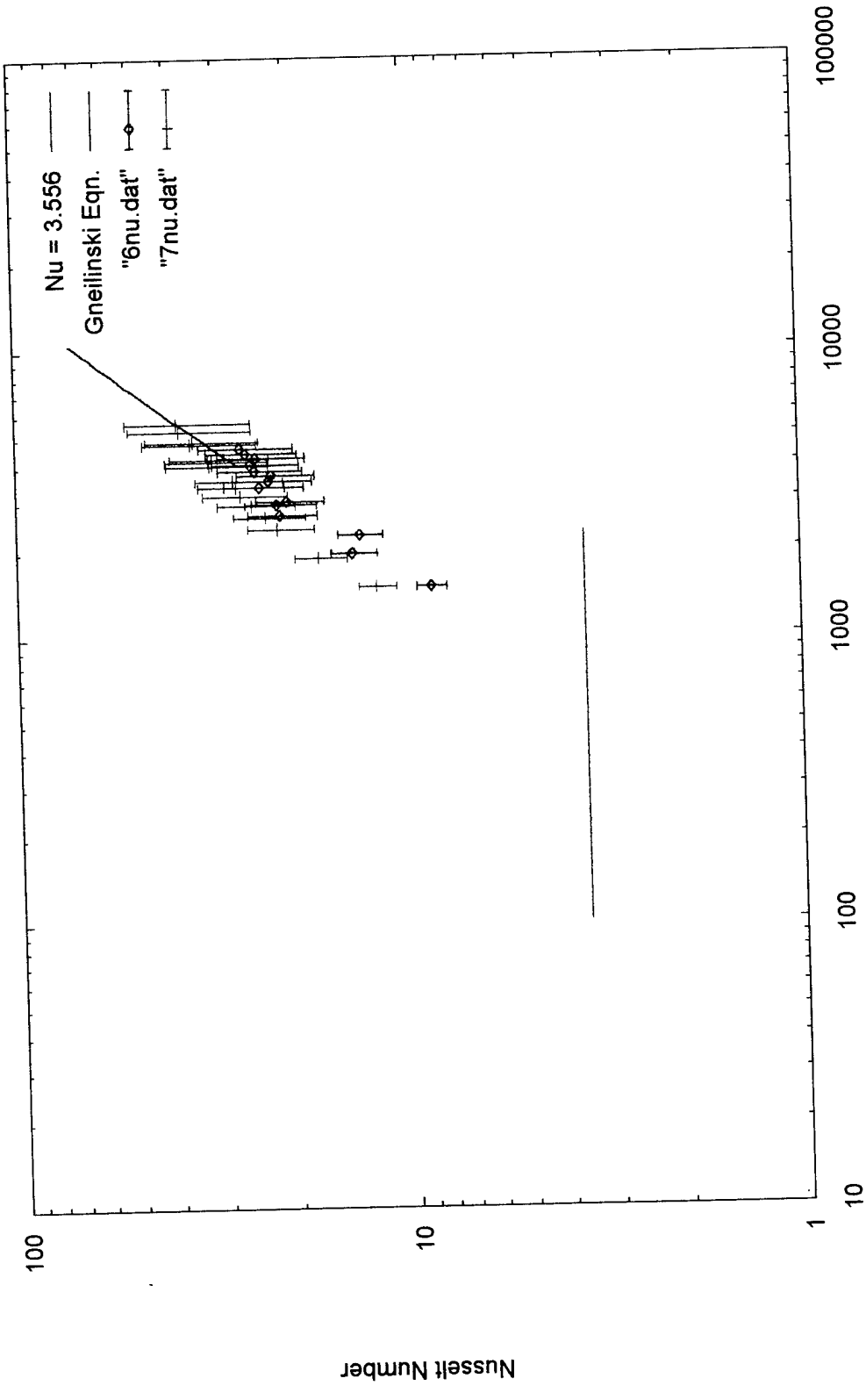

Figure 8.10: Average Nusselt Number in Single 254-μm Channel

8.4 Comparison of Experimental Data to Math Model

The math model (shown in Appendix J) was used to determine pressure drop and the bulk temperature change between the inlet and outlet of the microchannels for the 508-μm channels. Unfortunately, this type of comparison could not be made for the single 254-μm channel because the model is formulated for multiple channels. The heat transfer is modeled by treating the walls separating the channels as if they were fins. This is not the case for a single channel.

The input data for the model include the channel dimensions, the heat flux, flow rate, and the inlet temperature. Expected pressure drop was calculated using the model and is shown compared to experimental data in Figure 8.11. The model with losses included (K_e, K_c, K_b) predicts a higher pressure drop than the experimental data. However, at the highest flow rate for the experimental data, the difference between the model and the experimental data is only 14%. The model was also used to predict the pressure drop without losses. In this case, the model predicted a lower pressure drop than the experimental data. The largest difference was within 15% of the experimental values. This indicates that the model may be used to predict pressure drop in microchannels of this size. However, there is a need to be able to determine losses more accurately for accurate prediction of pressure drop. This also points out the fact that the pressure measurement locations should be located within or very near the ingress and egress of the channels.

The model was compared to the raw data obtained from data set 4 (no heat transfer data was taken for data set 5). The model predicted 121% higher at the low flow rates and 16% higher at the higher flow rates. The average difference between the model

and the data was 43%. These differences are the result of using the supplied heat ($q = Vi = 33.83$W) to the test section to determine the temperature differences in the model. The model does not account for heat lost to the surroundings; therefore, the temperature change is over predicted.

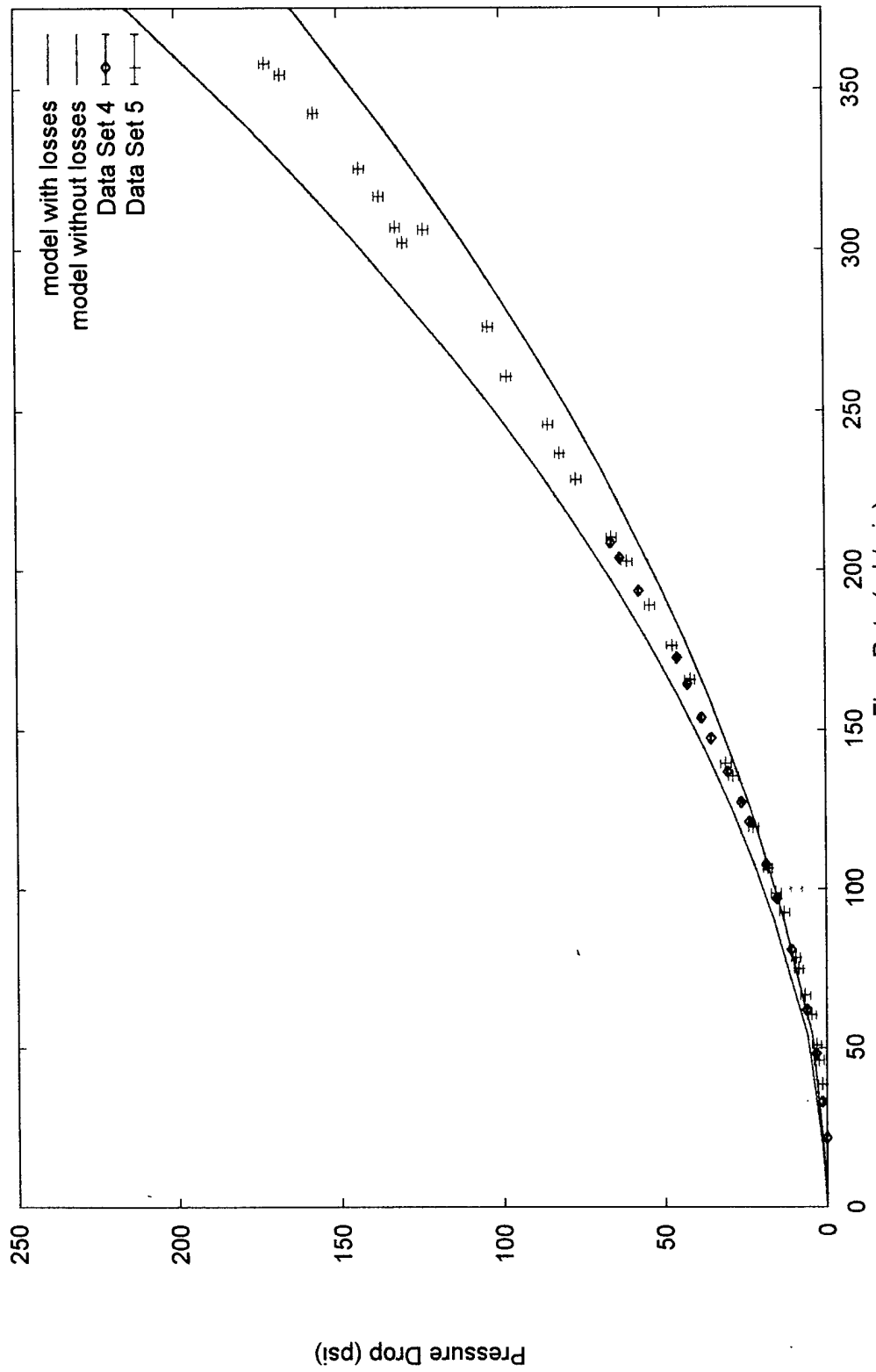

Figure 8.11: Math Model Comparison to Experimental Pressure Data

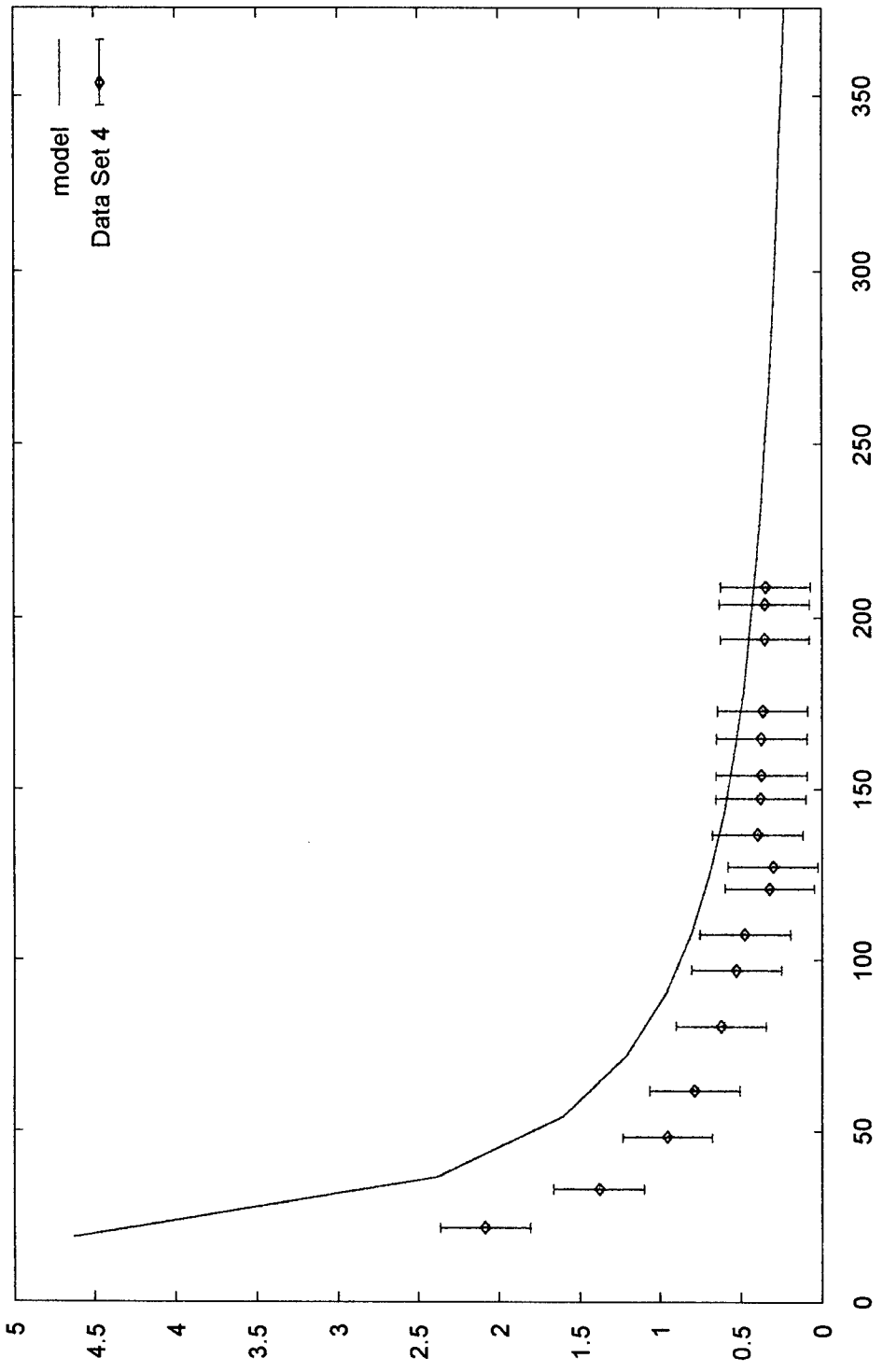

Figure 8.12: Math Model Comparison to Experimental Temperature Data

CHAPTER 9

ERROR ANALYSIS

This chapter discusses the methods used to determine the 95% uncertainty interval in the reported data. The analysis accounts for both precision errors and bias errors. In addition, a method for propagating these uncertainty errors to the final result will be discussed. The uncertainty, or bias error, of the measurement instruments and critical dimensions are also listed in this chapter. A computer program was written to determine the sensitivity coefficients and bias error for the error analysis and is included in Appendix F.

9.1 Uncertainty of a Result

The purpose of this section is to outline the procedure for determining the uncertainty of a derived result (which is a function of several measured parameters, e.g., pressure, temperature). First, the sample mean of each individual parameter may be calculated from a set of data $x_1, x_2, \ldots x_n$ using the following equation:

$$\bar{x} = \frac{\sum_{i=1}^{n} x_i}{n} \tag{9.1}$$

There is a range about this sample mean where there is a 20:1 probability that the true population mean (μ) will lie. This uncertainty interval is a combination of two types of errors: precision error and bias error. Precision error is the statistically determined variation of a set of measurements from its sample mean. Precision error results from random variations. Bias error is an estimate of the fixed error from the population mean (μ). This error is usually estimated by using the specifications of the measurement instruments. If the measurement instruments could be calibrated to the true value, then there would be no bias error - only random, or precision, error. Calibrations can, however, reduce bias error.

The uncertainty interval is determined by taking the root sum of the squares of the precision (P) and bias (B) errors.

$$U=[B^2+P^2]^{1/2} \tag{9.2}$$

The estimate for the true value of the result is

$$r = \bar{r} \pm U \tag{9.3}$$

9.1.1 Precision Error

Precision errors are statistically determined errors. The sample standard deviation (S) is used to calculate the precision error for m measured parameters ($p_1, p_2 \ldots p_m$).

$$S_p = \sqrt{\frac{\sum_{i=1}^{n} (x_i - \bar{x})^2}{n-1}} = \sqrt{\frac{\sum_{i=1}^{n} x_i^2 - \frac{(\sum_{i=1}^{n} x_i)^2}{n}}{n-1}} \tag{9.4}$$

where $x_1, x_2, \ldots x_n$ are considered to be the individual data for each of the measured parameters. The precision index of the result is given by

$$S_r = \sqrt{\sum_{i=1}^{m} (\frac{\theta_i S_{p_i}}{\sqrt{n}})^2} \tag{9.5}$$

where the sensitivity coefficient (θ_i) is defined as

$$\theta_i = \frac{\partial r}{\partial p_i} \tag{9.6}$$

Some expressions may be too complicated to obtain an analytical solution easily for the sensitivity coefficient. This is the case with the work here. The partial derivatives were determined by using a central difference representation of the partial derivative.

$$\theta_i = \frac{\partial r}{\partial p_i} \cong limit_{\Delta p_i \to 0}[\frac{r_{p_i + \Delta p_i} - r_{p_i}}{\Delta p_i}] \cong \frac{r_{+\epsilon_i} - r_{-\epsilon_i}}{2\epsilon_i} \tag{9.7}$$

The error analysis program which utilizes this method of determining partial derivatives is shown in Appendix F. The program first calculates the result (r) using the input parameters (p_i). The first input parameter is increased a small percentage, and a new value of r is determined ($r_{+\epsilon i}$). Next, the input parameter is decreased by the same small

percentage, and a new value of r is determined ($r_{-\epsilon i}$). These quantities are subtracted and divided by $2\epsilon_i$. This procedure is repeated for each input parameter.

The resulting precision error may be expressed as

$$P = t\, S_r \tag{9.7}$$

where the t is the student's two-sided t statistic.

9.1.1.1 Two-Sided Student's t Statistic. The student's two-sided t distribution is used to determine uncertainty when a small number of samples (n) are taken from a population with a true average μ. The degree of freedom, ν = n - 1, determines the value of the t statistic (Table 9.1).

Table 9.1: Two-Sided Student's t Statistic

Degrees of Freedom (ν = n - 1)	95% Confidence Interval
1	12.706
2	4.303
3	3.182
4	2.776
5	2.571
6	2.447
7	2.365
8	2.306
9	2.262
10	2.228
11	2.201
12	2.179
13	2.16

Table 9.1: (Continued)

Degrees of Freedom ($\nu = n - 1$)	95% Confidence Interval
14	2.145
15	2.131
16	2.12
17	2.11
18	2.101
19	2.093
20	2.083
21	2.08
22	2.074
23	2.069
24	2.064
25	2.06
26	2.056
27	2.052
28	2.048
29	2.045
30	2.042
40	2.021
60	2
120	1.98
∞	1.96

The t distribution is different from the normal distribution (from which the standard deviation is calculated). However, as the number of samples is increased, $n > 30$, the shape of the curve starts to approach that of the normal distribution. Notice that the student's t statistic at $\nu = 30$ is very close to the value for an infinite number of samples

(representing the normal distribution). Therefore, it is desirable to obtain 30 or more data points for a single measurement during experimentation (which was done for this work).

The degrees of freedom are dependent on the number of samples taken for each parameter. If each parameter has the same number of samples for a given data set, then the t statistic is based on n - 1. However, more often than not, the number of samples is not the same. In this situation, the Welch-Satterthwaite formula (Figliola and Beasley 1995) may be used to estimate ν_r.

$$\upsilon_r = \frac{[\sum_{i=1}^{m} (\theta_i P_i)^2]}{\sum_{i=1}^{m} [(\theta_i P_i)^4 / \upsilon_i]} \tag{9.10}$$

9.1.2 Bias Error

The bias limit of the result is given as

$$B_r = \sqrt{\sum_{i=1}^{m} (\theta_i B_{p_i})^2} \tag{9.11}$$

where the sensitivity coefficient (θ_i) is defined by Equation 9.6. The bias error estimate (B_{pi}) is usually determined by using the manufacturer's specifications or past experience. The bias errors shown in Table 9.2 were used in the uncertainty analysis (further details about the measurement equipment are shown in Appendix E).

The experimental results, presented in Chapter 8, were based on several measurements. These measurements included the flow rate, inlet and outlet pressure, flow loop pressure and temperature near the flow meter, and the test section temperatures.

These temperatures include the inlet and outlet temperatures and three temperatures on the heater.

Table 9.2: Bias used in Uncertainty Analysis

Measurement	**Bias**
Volumetric Flow Rate	± 0.64% of reading
Temperature Measurement	± 0.2°C
Test Section Pressure (0 to 689.4 kPa) (0 to 100 psig)	± 0.15 % of full scale (root sum square of errors)
Test Section Pressure (0 to 6894 kPa) (0 to 1000 psig)	± 0.15 % of full scale (root sum square of errors)
Loop Pressure (0 to 6894 kPa) (0 to 1000 psig)	± 1.52 % of full scale maximum (root sum square of errors)
Voltage	± 0.1 V
Current	± 1 mA

There were cases where the bias in Table 9.2 was different from the experimental bias. For example, the bias listed in Table 9.2 for the test section pressure transducer does not include error for temperature effects such as sensitivity and zero shift within the expected operating range. These errors may be accounted for by using the root sum of the squares to combine them. For example, the individual errors in the test section transducer are listed in Table 9.3 (also listed in Appendix E).

Table 9.3: Precision of Test Section Pressure Transducers

Performance	**Precision**
Hysteresis	± 0.10% full scale
Repeatability	± 0.05% full scale
Zero Balance	± 1.0% full scale
Thermal Zero Effect	± 0.009% full scale / °C
Thermal Sensitivity Effect	± 0.009% full scale / °C

The thermal effects are measured from a reference temperature of 24°C (75°F). The zero balance uncertainty is not used in the calculation because the transducers are zeroed before each test run at ambient temperature. However, the other effects are combined, as shown in the following equation.

$$Uncertainty\ (\%) = \sqrt{(0.001)^2 + (0.001)^2 + 2(0.00009(°C-24))^2} \tag{9.12}$$

Another example where the bias may differ is in the flow rate measurement uncertainty. The raw data is given as frequency. This value may be multiplied by the best fit K factor given on the manufacturer's calibration sheet. The bias error for the best fit K factor is less than 0.64% of the reading for flow rates > 20 cc/min. However, a more accurate flow rate measurement would be given by using the individual K factors (pulses/cc) from the factory calibration sheet (listed in Appendix E). These values are accurate to ± 0.05% of the reading based on the calibration standard.

CHAPTER 10

CONCLUSIONS AND RECOMMENDATIONS

10.1 Conclusions

The experimental data showed that the test apparatus could be used to obtain good friction data given the right conditions. For example, when the pressure drop across the microchannels was above 25 kPa (3.5 psi) for the 0 to 689.4 kPa (0 to 100 psig) transducer and 107 kPa (15 psi) for the 0 to 6,894 kPa (0 to 1,000 psig) transducer, good results were obtained. This was demonstrated in the high *Re* flow for the 508-μm channels. However, at low *Re*, when the pressure drop was less than the values indicated above, the uncertainty in the pressure measurement predominated and introduced an unacceptable amount of error. This shows the importance of reducing errors in pressure measurements. By calibrating, or zeroing, the pressure transducers before experiments, errors up to 1% of the full scale reading can be eliminated. This zero offset may be added directly into the data acquisition program so that the raw pressure data are corrected without having to recalibrate the transducer physically.

The 254-μm channels also produced good friction factor data primarily because $\Delta P \geq 100$ kPa (14 psi), which is much larger than the pressure transducer measurement uncertainty. The data follow the trend of the theoretical values, though lower in

magnitude, which may be due to microscale effects. However, it should be noted that there is a limited amount of laminar data because the flow meter cannot measure flow rates less than 10 mL/min (experimental data for water showed that the lowest flow rate was actually closer to 20 mL/min). In channels smaller than 254 μm, it may not be possible to obtain any valid laminar friction factor data without using multiple channels to produce a larger total flow rate or by measuring the flow rate with a lower flow rate (< 10 mL/min) flow meter.

The uncertainty of the friction factor data is, on average, 15% for the 508-μm channel and 12.5% for the 254-μm channel. These uncertainties are higher than the values presented by Yu et al. (1994). Their average uncertainty values ranged from 4% to 11.9%. The main reason for the larger experimental uncertainty presented in this thesis is a result of the uncertainty of the channel width measurement. By improving this measurement uncertainty to ± 2.5μm, the friction factor uncertainty will be improved to 3% to 4% over the range of values. This is a significant improvement over the work presented here and the work done by Yu et al. (1994). This improvement in the uncertainty demonstrates the importance of careful determination of channel dimensions.

It should be noted that the pump supplied ample flow rates (0 to 8,300 mL/min) and pressures (up to 8,274 kPa (1,200 psi)) to test the microchannel sizes used in this and future studies (10 μm to 500 μm). By using the bypass loop, low flow rates are easily obtained. However, the pump work on the fluid while recirculating increased the fluid temperature up to an average of 0.3 °C over ten minutes. This problem was alleviated by

circulating cool water through coiled tubes in the reservoir and by using the secondary loop to cool the water exiting the test section.

The cooling loop and the cooling coil in the reservoir allowed steady state temperatures to be reached in approximately ten minutes; nonetheless, the heat transfer data for the 508-μm channels were much lower than expected. This can be attributed to experimental uncertainty resulting from a low ΔT_{bulk}, ranging from 2.08°C to 0.35°C. These errors were primarily associated with thermocouple uncertainty (± 0.28°C). However, the uncertainty associated with the heat transfer areas and the dimensions (A_{heater}, Δz_{paste}, and Δz_{Al}) used to determine the wall temperature also played a role. These dimensions had large sensitivity coefficients. This indicates that accurate determination of these dimensions is essential. The heat transfer data in the 254-μm channel closely matched the conventional correlations because $\Delta T_{bulk} \geq 3.27$°C for data set 6 and $\Delta T_{bulk} \geq 7.8$°C for data set 7. However, the precision of the measurements can be improved by reducing the uncertainty or eliminating the need to know heat transfer dimensions such as Δz_{paste}. The average uncertainty for the 254-μm channel *Nu* data is approximately 23%. The magnitude of this uncertainty is approximately the same as that indicated by the researchers that were discussed in Chapter 2. This is reasonable since the same type of measurement equipment was used.

The flow loop will provide good friction and heat transfer data for two-phase studies as long as ΔP is larger than the pressure measurement uncertainty, $\Delta T_{bulk} > 2$°C, and T_{max} remains below 80°C (temperature limitation of the transducers). This indicates that two-phase studies with water cannot be done with these pressure transducers because

the saturation temperature of water is too high; therefore, the two-phase studies will be limited to refrigerants and other low boiling point fluids. In addition, there will be flow range limitations, depending on the channel size, as discussed previously. Overall, though, the flow loop may be used to test a wide variety of fluids with varying inlet conditions in microchannel sizes ranging from 10 μm to 508 μm.

The results from the math model were shown to be very close to the experimental values obtained for the multiple (nine) 508-μm channels. This indicates that the math model can be used to predict optimal channel configurations based on friction and heat transfer characteristics prior to testing; however, further experimental validation may be required to determine how well it will predict in channels smaller than 508 μm.

10.2 Recommendations

10.2.1 Friction Measurements

The most important way to reduce the uncertainty in friction factor measurements is to ensure that the pressure drop between the inlet and outlet is as large as feasible. Next, accurate determination of the channel dimensions is essential. At the small scales involved in microchannels, it becomes increasingly important to keep records of the manufacturing process. The Ultra Precision Milling Center is more accurate than most of the metrology equipment. This may be the best method available to determine channel depth without dissecting the microchannel blank to obtain a measurement from the microchannel cross-section. Another important aspect, is starting with a "level" surface before milling the microchannels. This was the major source of channel uncertainty of the

508-μm channels. The channel width can be best measured by using an optical microscope with calibrated scale bars. The channel length can be measured using a high precision dial caliper.

Another means to reduce the friction factor uncertainty would be to measure the inlet and outlet pressures within the microchannel (or as close as possible). This would eliminate the need to know or estimate the minor losses incurred in the entrance, exit, and ninety-degree bends. Currently the losses are estimated using Kays' (1950) and other methods which may not be accurate in microchannel flow. These losses can affect the pressure drop by as much as 15% at a pressure drop of 1,187 kPa (170 psi) (demonstrated in Figure 8.11).

More data are required for the 508-μm channels at lower flow rates to determine the *Re* range for "laminar" regime. With the current instrumentation, the only way to obtain this data would be to test longer channels. This would require refixturing the test apparatus and could be a topic for future work. Since the flow appeared to agree with theory in the turbulent regime, it would not be surprising if the flow followed theory in the laminar regime.

A limited amount of laminar data was obtained for the 254-μm channel. More laminar data may be obtained for the 254-μm channel by increasing the number of channels. For example, if the measured flow rate is 20 mL/min for five channels, then the average flow rate would be 4 mL/min per channel. As an alternative, high precision, low flow rate rotameters may be used to measure flow rates outside of the range of the flow

meters currently used. These meters are available at a fraction of the cost of the flow loop flow meters; however, they are limited to certain fluids and flow ranges.

10.2.2 Heat Transfer Measurements

In order to reduce the uncertainty in Nusselt number data, it is suggested that the following improvements in instrumentation and experimental procedure be implemented.

1. Calibrate each thermocouple over the range from 0 to 100°C.
2. Accurately determine the heat transfer areas between the heater and the microchannels.
3. Eliminate the need to know the paste thickness by measuring the temperature at the base of the microchannels instead of the heater surface.
4. Install more thermocouples on the bottom section of the microchannel.
5. Replace the low-power heaters with higher heat flux heaters to produce a larger temperature difference in the fluid.
6. Install additional thermocouples in the test fixture to measure the amount of heat lost to the surroundings.
7. Accurately measure the heater dimensions to determine the wall temperature.
8. Develop a new method to obtain temperature measurements within the channels. One suggestion would be to mount thermocouples directly to the bottom of the test section to eliminate the need to know Δz_{paste}. Although the ease of changing microchannel blanks will be affected, the experimental results will be better.

10.2.3 Fabrication

Here are several general suggestions that will aid others who may want to manufacture microchannels to be used in the flow loop.

1. Conventional CNC milling machines are not capable of manufacturing microchannels with an acceptable surface finish; therefore, it is recommended that the Ultra Precision Milling Center (UPMC) be used to manufacture the microchannels.

2. Conventional CNC milling machines perform well when cutting microchannel blanks; however, there are a couple of suggestions that should be made.

    a. Never remove the microchannel blank from the vice until all cutting has been completed because it is very difficult to reposition the blank in exactly the same place.

    b. The direction of the cut is very important when milling a pocket because the surface finish will be affected. The direction of the cut should be in the same direction as the tool rotation. The opposite is true for cutting outside edges.

3. Use sharp tools to ensure a good surface finish.

4. Blank material (bar stock), as received from manufacturers, does not usually have a uniform thickness. Sanding or conventional lapping machines will give a surface finish that will appear very good; however, the surface height may vary tens to hundreds of microns over the surface of the blank. Therefore, it is recommended that the microchannel area be milled to a uniform height with the UPMC prior to cutting the microchannels.

APPENDIX A

MICROCHANNEL BLANK G-CODE

#CNC G-Code program for Bridgeport milling machine (MULTI2.CNC). Cuts glue channel around
#the microchannel section and removes 0.01" of material from the area outside glue channels.
N1G0G90X0Y0T1M6# (1/4" drill)
N5X.375Y.5Z.05
.N10G81Z.35F10
N15X.375
N20X3.625Y.5
N25G0G90X0Y0T2M6# (1/8" end mill)
N27G0X.375Y.5Z0.05
N29G0X.375Y.5Z-0.0313
N30G1X0.3503Y0.4426Z-0.0313F10
N35X0.6875Y0.2975
N40X0.6875Y0.7025
N45X0.3503Y0.5574
N50X0.4898Y0.5494
N55X0.6250Y0.6076
N60X0.6250Y0.3924
N65X0.3750Y0.5000
N70X0.5625Y0.5000
N80G0X.375Y.5Z0.05
N82G0X.375Y.5Z-.0625
N85G1X0.3503Y0.4426Z-0.0625F10
N90X0.6875Y0.2975
N95X0.6875Y0.7025
N100X0.3503Y0.5574
N105X0.4898Y0.5494
N110X0.6250Y0.6076
N115X0.6250Y0.3924
N120X0.3750Y0.5000
N125X0.5625Y0.5000
N240G0X3.625Y.5Z.05
N245G0X3.625Y.5Z-0.0313
N250G1X3.6497Y0.4426Z-0.0313F10
N252X3.3125Y0.2975
N255X3.3125Y0.7025
N260X3.6497Y0.5574
N265X3.5102Y0.5494
N270X3.3750Y0.6076
N275X3.3750Y0.3924
N280X3.6250Y0.5000
N285X3.4375Y0.5000
N290G0X3.625Y.5Z.05
N295G0X3.625Y.5X-0.0625
N300G1X3.6497Y0.4426Z-0.0625F10
N302X3.3125Y0.2975
N305X3.3125Y0.7025
N310X3.6497Y0.5574
N315X3.5102Y0.5494
N320X3.3750Y0.6076
N325X3.3750Y0.3924
N330X3.6250Y0.5000
N335X3.4375Y0.5000

N340G0G90X0Y0T3M6# (3/16" endmill)
N345G0X.7832Y1.1Z.05
N350G0X.7832Y1.1Z-.01
N355G1X.7832Y.9887Z-.01F50
N360X.1275Y.7065
N365X.1275Y.2935
N370X.7832Y.0113
N375X.8628Y.1187
N380X3.1372Y.1187
N385X3.2168Y.0113
N390X3.8725Y.2935
N395X3.8725Y.7065
N400X3.2168Y.9887
N405X3.1372Y.8812
N410X.8628Y.8812
N415X.7832Y.9887
N420X.3666Y.94
N425X.0275Y.7941
N430X.0275Y.2059
N435X.3666Y.06
N440X3.6334Y.06
N445X3.9725Y.2059
N450X3.9725Y.7941
N455X3.6334Y.94
N460X3.9725Y.94
N465X.0275Y.94
N470X.0275Y.06
N475X3.9725Y.06
N480X3.9725Y.94
N485X3.8725Y.94
N490X.1275Y.94
N495X.1275Y.06
N500X3.8725Y.06
N505X3.8725Y.94
N1350G0G90X0Y0T4M6# (1/16" end mill)
N1355G0X2.0Y0.7812Z.05
N1365G1X.8125Y.7812Z-.025F8
N1370X.75Y.8655
N1375X.1875Y.6234
N1380X.1875Y.3766
N1385X.75Y0.1345
N1390X0.8125Y.2188
N1400X3.1875Y.2188
N1405X3.25Y.1345
N1410X3.8125Y.3766
N1415X3.8125Y.6234
N1420X3.25Y.8655
N1425X3.1875Y0.7812
N1430X.8125Y0.7812
N1500M0
N1505G0G90X0Y0T1M6
N1510M2

APPENDIX B

PMAC MILLING CODE

```
OPEN PROG 999 CLEAR
        ;
        ;"BAILEY1.PMC" PROGRAM TO MILL TRENCHES FOR DARIN    ;BAILEY
        ;508UM WIDE BY 508UM DEEP WITH 508UM LAND IN ALUMINUM
        ;BY CRAIG FRIEDRICH 4 OCTOBER 1995
        ;
ABS(X,Y,Z)
FRAX(X,Y,Z)
LIN
        ;
Q600 =                      ;ABS Y OF LOWER LEFT REFERENCE CORNER
Q601 =                      ;ABS X OF LOWER LEFT REFERENCE CORNER
Q620 =                      ;ABS Z OF SURFACE
        ;
Q605 = Q600 - 0.69          ;ABS Y OF START OF TRENCH
Q606 = Q605 - 2.62          ;ABS Y OF END OF TRENCH
        ;
Q610 = Q601 + 0.34          ;ABS X OF 1ST TRENCH
Q611 = Q601 + 0.38          ;ABS X OF 2ND TRENCH
Q612 = Q601 + 0.42          ;ABS X OF 3RD TRENCH
Q613 = Q601 + 0.46          ;ABS X OF 4TH TRENCH
Q614 = Q601 + 0.50          ;ABS X OF 5TH TRENCH
Q615 = Q601 + 0.54          ;ABS X OF 6TH TRENCH
Q616 = Q601 + 0.58          ;ABS X OF 7TH TRENCH
Q617 = Q601 + 0.62          ;ABS X OF 8TH TRENCH
Q618 = Q601 + 0.66          ;ABS X OF 9TH TRENCH
        ;
Q630 = 0.007874             ;FEEDRATE OF 200 UM /SEC
Q635 = 0.01                 ;DEPTH OF FIRST PASS OF 254UM
Q636 = 0.02                 ;TOTAL DEPTH OF 508UM
        ;
        ;MACHINE TRENCHES
        ;
P4=5000
P3=0
P2=1                        ;START SPINDLE AT 5000 RPM
DWELL 1000
        ;
F0.3
Z3                          ;RETRACT Z
DWELL 100
X(Q610)Y(Q605)
DWELL 100
F0.1
Z(Q620+Q635)                ;MOVE TO FIRST TRENCH AND AT CUTTING DEPTH
DWELL 100
        ;
F(Q630)                     ;CUTTING FEED RATE
Y(Q606)                     ;CUT 1ST TRENCH
DWELL 10
Z(Q620+Q636)
DWELL 10
```

```
Y(Q605)
DWELL 10
Z(Q620)
DWELL 100               ;END FIRST TRENCH
        ;
X(Q611)Y(Q605)          ;START 2ND TRENCH
DWELL 100
Z(Q620+Q635)            ;MOVE TO 2ND TRENCH AND AT CUTTING DEPTH
DWELL 100
        ;
F(Q630)                 ;CUTTING FEED RATE
Y(Q606)                 ;CUT 2ND TRENCH
DWELL 10
Z(Q620+Q636)
DWELL 10
Y(Q605)
DWELL 10
Z(Q620)
DWELL 100               ;END 2ND TRENCH
        ;
X(Q612)Y(Q605)          ;START 3RD TRENCH
DWELL 100
Z(Q620+Q635)            ;MOVE TO 3RD TRENCH AND AT CUTTING DEPTH
DWELL 100
        ;
F(Q630)                 ;CUTTING FEED RATE
Y(Q606)                 ;CUT 3RD TRENCH
DWELL 10
Z(Q620+Q636)
DWELL 10
Y(Q605)
DWELL 10
Z(Q620)
DWELL 100               ;END 3RD TRENCH
        ;
X(Q613)Y(Q605)          ;START 4TH TRENCH
DWELL 100
Z(Q620+Q635)            ;MOVE TO 4TH TRENCH AND AT CUTTING DEPTH
DWELL 100
        ;
F(Q630)                 ;CUTTING FEED RATE
Y(Q606)                 ;CUT 4TH TRENCH
DWELL 10
Z(Q620+Q636)
DWELL 10
Y(Q605)
DWELL 10
Z(Q620)
DWELL 100               ;END 4TH TRENCH
        ;
X(Q614)Y(Q605)          ;START 5TH TRENCH
DWELL 100
```

```
Z(Q620+Q635)            ;MOVE TO 5TH TRENCH AND AT CUTTING DEPTH
DWELL 100
        ;
F(Q630)                 ;CUTTING FEED RATE
Y(Q606)                 ;CUT 5TH TRENCH
DWELL 10
Z(Q620+Q636)
DWELL 10
Y(Q605)
DWELL 10
Z(Q620)
DWELL 100               ;END 5TH TRENCH
        ;
X(Q615)Y(Q605)          ;START 6TH TRENCH
DWELL 100
Z(Q620+Q635)            ;MOVE TO 6TH TRENCH AND AT CUTTING DEPTH
DWELL 100
        ;
F(Q630)                 ;CUTTING FEED RATE
Y(Q606)                 ;CUT 6TH TRENCH
DWELL 10
Z(Q620+Q636)
DWELL 10
Y(Q605)
DWELL 10
Z(Q620)
DWELL 100               ;END 6TH TRENCH
        ;
X(Q616)Y(Q605)          ;START 7TH TRENCH
DWELL 100
Z(Q620+Q635)            ;MOVE TO 7TH TRENCH AND AT CUTTING DEPTH
DWELL 100
        ;
F(Q630)                 ;CUTTING FEED RATE
Y(Q606)                 ;CUT 7TH TRENCH
DWELL 10
Z(Q620+Q636)
DWELL 10
Y(Q605)
DWELL 10
Z(Q620)
DWELL 100               ;END 7TH TRENCH
        ;
X(Q617)Y(Q605)          ;START 8TH TRENCH
DWELL 100
Z(Q620+Q635)            ;MOVE TO 8TH TRENCH AND AT CUTTING DEPTH
DWELL 100
        ;
F(Q630)                 ;CUTTING FEED RATE
Y(Q606)                 ;CUT 8TH TRENCH
DWELL 10
Z(Q620+Q636)
```

```
DWELL 10
Y(Q605)
DWELL 10
Z(Q620)
DWELL 100                ;END 8TH TRENCH
        ;
X(Q618)Y(Q605)           ;START 9TH TRENCH
DWELL 100
Z(Q620+Q635)             ;MOVE TO 9TH TRENCH AND AT CUTTING DEPTH
DWELL 100
        ;
F(Q630)                  ;CUTTING FEED RATE
Y(Q606)                  ;CUT 9TH TRENCH
DWELL 10
Z(Q620+Q636)
DWELL 10
Y(Q605)
DWELL 10
Z(Q620)
DWELL 100                ;END 9TH TRENCH
        ;
        ;END CUTTING TRENCHES
        ;
F0.1
Z1                       ;RETRACT Z
DWELL 100
P2=0                     ;STOP AND RESET SPINDLE
P4=0
X0.2                     ;MOVE WORK OUT FOR CHANGING
        ;
RETURN
        ;
        ;END PROGRAM
        ;
CLOSE
 ZW1.04    M             é   2  LPT1:                    txt
```

b

```
OPEN PROG 999 CLEAR
        ;PROGRAM "LEVELTRY.PMC" FOR DARIN BAILEY'S BLANKS
        ;USED WITH LVDT TO FIND LOW SPOT AND CHECK PROGRAM
        ;WRITTEN BY CRAIG FRIEDRICH, 12/14/95
        ;
ABS(X,Y,Z)
FRAX(X,Y,Z)
LIN
        ;
        ;ESTABLISH ABSOLUTE COORDINATES OF REF PTS.
        ;
Q600 =                  ;X OF REF PT. 1 *******************************
Q601 =                  ;Y OF REF PT. 1 *******************************
        ;
        ;ESTABLISH CUTTING PARAMETERS BASED ON 1/16" MILL
        ;
Q620 = 0.0625           ;BASED ON LIGHT AXIAL CUT
Q625 = 0.03125          ;HALF MILL DIA RADIAL CUT FOR MAIN AREA
Q630 = 0.020            ;CLEARANCE FOR MOVES
        ;
P4=0
P3=0
P2=0
SEND"*************************************************************"
SEND"          STARTING SPINDLE AT 6,000 RPM              "
SEND"*************************************************************"
DWELL 2000
        ;
F0.1
X(Q600) Y(Q601)         ;MOVE TO PT. 1
Z(Q641-Q630)            ;MOVE TO HOVER
F(Q620)                 ;LOWER FEEDRATE
Z(Q641)                 ;MOVE Z TO CUTTING ELEVATION
DWELL 100
        ;
        ;SWITCH TO INCREMENTAL MOVES
        ;
INC(X,Y)
X(0.175)                ;TO PT 2
DWELL 10
X0.2035 Y-0.49          ;TO PT 3
DWELL 10
X-0.0685 Y-0.042        ;TO PT 4
DWELL 10
Y-2.467                 ;TO PT 5
DWELL 10
X0.0685 Y-0.042         ;TO PT 6
DWELL 10
X-0.2035 Y-0.49         ;TO PT 7
DWELL 10
X-0.175                 ;TO PT 8
DWELL 10
```

```
X-0.2035 Y0.49              ;TO PT 9
DWELL 10
X0.0685 Y0.042              ;TO PT 10
DWELL 10
Y2.467                      ;TO PT 11
DWELL 10
X-0.0685 Y0.042             ;TO PT 12
DWELL 10
X0.2035 Y0.49               ;BACK TO PT 1
DWELL 10
Z(Q641-Q630)                ;LIFT TOOL TO HOVER (0.020 OFF SURFACE)
        ;
        ;MILL MAIN AREA
        ;
INC(X,Y,Z)                  ;SET INCREMENTAL FOR ALL AXES
        ;
F0.2                        ;RAPID FEED
X0.31 Y3.009                ;TO INITIAL POINT RETRACTED
Q670 = 1                    ;INITIALIZE LOOP COUNTER
Q675 = 0.445/15             ;AMT TO INC EACH TIME IN X
        ;
WHILE(Q670!>15)             ;START LOOP
SEND"                                "
SEND"CUTTING LOOP"
CMD"Q670"
F(Q620)                     ;CUTTING SPEED
Z(Q630)                     ;DOWN TO SURFACE
Y2.487                      ;CUTTING
DWELL 10
Z(-Q630)                    ;RETRACT Z
DWELL 10
F0.2                        ;RAPID FEED
X(-Q675) Y-2.487            ;MOVE TO NEXT POINT RETRACTED
Q670 = Q670 + 1             ;UPDATE COUNTER
ENDWHILE
        ;
        ;END CUTTING
        ;
ABS(X,Y,Z)
F0.3
Z2
DWELL 10
P2=0
P4=0                        ;STOPPING SPINDLE
F0.5
X0.2 Y0.2
        ;
        ;END PROGRAM
        ;
RETURN
CLOSE
 ZW1.04   M                  2  n   LPT1:                txt                  b
```

```
OPEN PROG 999 CLEAR
        ;PROGRAM "LEVEL.PMC" FOR DARIN BAILEY'S BLANKS
        ;AFTER THIS STEP CHANNELS ARE CUT USING OTHER PROGRAMS
        ;WRITTEN BY CRAIG FRIEDRICH, 12/14/95
        ;
ABS(X,Y,Z)
FRAX(X,Y,Z)
LIN
        ;ESTABLISH ABSOLUTE COORDINATES OF REF PTS.
        ;
Q600 =                  ;X OF REF PT. 1 ******************************
Q601 =                  ;Y OF REF PT. 1 ******************************
Q641 =                  ;Z OF LOWEST POINT ON SURFACE ******************
        ;
        ;ESTABLISH CUTTING PARAMETERS BASED ON 1/16" MILL
        ;
Q620 = 0.0625           ;BASED ON LIGHT AXIAL CUT
Q625 = 0.03125          ;HALF MILL DIA RADIAL CUT FOR MAIN AREA
Q630 = 0.020            ;CLEARANCE FOR MOVES
        ;
P4=6000
P3=0
P2=1
SEND"*************************************************************************"
SEND"          STARTING SPINDLE AT 6,000 RPM              "
SEND"*************************************************************************"
DWELL 2000
        ;
F0.1
X(Q600) Y(Q601)         ;MOVE TO PT. 1
Z(Q641-Q630)            ;MOVE TO HOVER
F(Q620)                 ;LOWER FEEDRATE
Z(Q641)                 ;MOVE Z TO CUTTING ELEVATION
DWELL 100
        ;
        ;SWITCH TO INCREMENTAL MOVES
        ;
INC(X,Y)
X(0.175)                ;TO PT 2
DWELL 10
X0.2035 Y-0.49          ;TO PT 3
DWELL 10
X-0.0685 Y-0.042        ;TO PT 4
DWELL 10
Y-2.467                 ;TO PT 5
DWELL 10
X0.0685 Y-0.042         ;TO PT 6
DWELL 10
X-0.2035 Y-0.49         ;TO PT 7
DWELL 10
X-0.175                 ;TO PT 8
DWELL 10
```

```
X-0.2035 Y0.49              ;TO PT 9
DWELL 10
X0.0685 Y0.042              ;TO PT 10
DWELL 10
Y2.467                      ;TO PT 11
DWELL 10
X-0.0685 Y0.042             ;TO PT 12
DWELL 10
X0.2035 Y0.49               ;BACK TO PT 1
DWELL 10
Z(Q641-Q630)                ;LIFT TOOL TO HOVER (0.020 OFF SURFACE)
        ;
        ;MILL MAIN AREA
        ;
INC(X,Y,Z)                  ;SET INCREMENTAL FOR ALL AXES
        ;
F0.2                        ;RAPID FEED
X0.31 Y3.009                ;TO INITIAL POINT RETRACTED
Q670 = 1                    ;INITIALIZE LOOP COUNTER
Q675 = 0.445/15             ;AMT TO INC EACH TIME IN X
        ;
WHILE(Q670!>15)             ;START LOOP
SEND"                                "
SEND"CUTTING LOOP"
CMD"Q670"
F(Q620)                     ;CUTTING SPEED
Z(Q630)                     ;DOWN TO SURFACE
Y2.487                      ;CUTTING
DWELL 10
Z(-Q630)                    ;RETRACT Z
DWELL 10
F0.2                        ;RAPID FEED
X(-Q675) Y-2.487            ;MOVE TO NEXT POINT RETRACTED
Q670 = Q670 + 1             ;UPDATE COUNTER
ENDWHILE
        ;
        ;END CUTTING
        ;
ABS(X,Y,Z)
F0.3
Z2
DWELL 10
P2=0
P4=0                        ;STOPPING SPINDLE
F0.5
X0.2 Y0.2
        ;
        ;END PROGRAM
        ;
RETURN
CLOSE
ZW1.04   M                  2  O   LPT1:          txt                  b
```

APPENDIX C

MICROCHANNEL DIMENSIONS

TABLE A: TOPOGRAPHY OF SURFACE BEFORE CUTTING

conversion =

20,550,557 counts/inch

Zero location on the lower left corner of workpiece using Dr. Friedrich's milling machine

Xo= -17,849,449 counts = -0.87 inches

Yo= 10,900,689 counts = 0.53 inches

LOCATION		COUNTS	(zero correction)	INCHES	(zero correction)	HEIGHT (microns)
1	X=	-7,574,170	10,275,279	-0.3686	0.5000	0
	Y=	-7,241,350	18,142,039	-0.3524	0.8828	
2	X=	-7,574,170	10,275,279	-0.3686	0.5000	-5.2
	Y=	-53,159,500	64,060,189	-2.5868	3.1172	
3	X=	-10,574,170	7,275,279	-0.5145	0.3540	11.5
	Y=	-7,241,350	18,142,039	-0.3524	0.8828	
4	X=	-4,574,170	13,275,279	-0.2226	0.6460	-13.7
	Y=	-7,241,350	18,142,039	-0.3524	0.8828	
5	X=	-10,574,170	7,275,279	-0.5145	0.3540	-1.4
	Y=	-53,159,500	64,060,189	-2.5868	3.1172	
6	X=	-4,574,170	13,275,279	-0.2226	0.6460	-17
	Y=	-53,159,500	64,060,189	-2.5868	3.1172	
7	X=	-7,574,170	10,275,279	-0.3686	0.5000	58.5
	Y=	-30,200,425	41,101,114	-1.4696	2.0000	
8	X=	-10,574,170	7,275,279	-0.5145	0.3540	70.2
	Y=	-30,200,425	41,101,114	-1.4696	2.0000	
9	X=	-4,574,170	13,275,279	-0.2226	0.6460	45.9
	Y=	-30,200,425	41,101,114	-1.4696	2.0000	

Note: From the conversion given by Dr. Friedrich, the surface mapping took place with point #7 in the middel of the workpiece. Corrected values represent the location on the workpiece, Friedrich's values represent the movement of the table relative to the tool spindle.

(I.E., THE X AND Y AXES ARE REVERSED, height is conventional z "+" axis)

TABLE B: HEIGHT ALONG LENGTH FROM POINT #1 TO POINT #2 (middle channel)

each increment (Y) = 5,000,000 counts

LOCATION	X	Y	X (inch)	Y(inch)	Height (microns)
1	10,275,279	18,142,039	0.5	0.8828	0
2	10,275,279	23,142,039	0.5	1.1261	-21.1
3	10,275,279	28,142,039	0.5	1.3694	-39.6
4	10,275,279	33,142,039	0.5	1.6127	-52.7
5	10,275,279	38,142,039	0.5	1.8560	-58.2
6	10,275,279	43,142,039	0.5	2.0993	-56
7	10,275,279	48,142,039	0.5	2.3426	-47
8	10,275,279	53,142,039	0.5	2.5859	-33.6
9	10,275,279	58,142,039	0.5	2.8292	-15.8
10	10,275,279	63,142,039	0.5	3.0725	0
				Average height=	-32.4

Note: Location #10 here is approximately the same as point #2.
(z height is the negative of the conventional direction)

CALCULATING THE AVERAGE CHANNEL DEPTH

Average height above the surface before cutting using the height from point #1 to point #2 = 32.4 microns

Friedrich stated that the initial cut was 36 microns above point #1. Then the tool was fed down 0.01 inches deep. Another pass of 0.01 inches deep was made to complete the final cut. (Finish depth = 0.02 inches)

0.01 inches = 254 microns

Actual channel cut locations with the zero at the lower left corner of the workpiece (using Dr. Friedrich's axis).	
Channel	X(inches)
1	0.34
2	0.38
3	0.42
4	0.46
5	0.5
6	0.54
7	0.58
8	0.62
9	0.66

Average channel depth for channel #5 from point #1 to point#2
(height along surface given in Table A)

UNITS = microns

Location	Surface height	Starting height relative to surface	final depth
1	0	36	-472
2	21.1	14.9	-493.1
3	39.6	-3.6	-511.6
4	52.7	-16.7	-524.7
5	58.2	-22.2	-530.2
6	56	-20	-528
7	47	-11	-519
8	33.6	2.4	-505.6
9	15.8	20.2	-487.8
10	0	36	-472

Average Channel Depth =	504.4	microns
Sample Standard Dev.=	22.12	microns
Average Deviation=	18.54	microns

CALCULATING 95% CONFIDENCE INTERVAL

Degrees of Freedom=	9	
Two-Sided Student's t-Statisti	2.262	
Delta	15.82	
Channel Height=	504.4 +/-	15.82

Since the only initial height values were taken in the middle of the blank, channel #5, the value of channel height with the 95% confidence interval will be used for all channels. In the future, it is hoped that the surface can be level before the channels are actually cut. This will decrease the error in the depth measurement, thus giving more accuracy for the flow rate and friction values.

Average channel depth using topography map

Location #		inches	height (microns	final depth
1	X=	0.5000	0	-508
	Y=	0.8828		
2	X=	0.5000	-5.2	-513.2
	Y=	3.1172		
3	X=	0.3540	11.5	-496.5
	Y=	0.8828		
4	X=	0.6460	-13.7	-521.7
	Y=	0.8828		
5	X=	0.3540	-1.4	-509.4
	Y=	3.1172		
6	X=	0.6460	-17	-525
	Y=	3.1172		
7	X=	0.5000	58.5	-449.5
	Y=	2.0000		
8	X=	0.3540	70.2	-437.8
	Y=	2.0000		
9	X=	0.6460	45.9	-462.1
	Y=	2.0000		

Average Channel Depth =	491.47	microns
Sample Standard Dev.=	32.85	microns
Average Deviation=	27.78	microns

CALCULATING 95% CONFIDENCE INTERVAL

Degrees of Freedom=	8	
Two-Sided Student's t-Statisti	2.306	
Delta	25.25	
Channel Height=	491.47 +/-	25.25

Roughness Step Tester for the 500 micron channels (RST)

UNITS=microns

Channel	Location	RMS	Average	Peak to Valley
1	Left	1.04	0.8005	7.88
	Middle	1.07	0.84594	6.83
	Right	1.01	0.77166	8.22
2	Left	1.07	0.82194	7.71
	Middle	1.4	1.08	10.19
	Right	1.06	0.82092	7.49
3	Left	1.04	0.79556	7.56
	Middle	1.07	0.8147	8.07
	Right	1.03	0.79646	13.97
4	Left	1.07	0.81926	7.52
	Middle	1.05	0.80599	8.3
	Right	0.93343	0.71298	7.42
5	Left	1.02	0.78409	7.78
	b	0.9985	0.77299	7.49
	c	1.02	0.77333	7.38
	Middle	1.08	0.82242	9.13
	e	1.02	0.78416	7.71
	f	0.95597	0.73055	7.95
	Right	1.05	0.80181	8.17
6	Left	0.97824	0.7548	8.22
	Middle	1.03	0.79524	8.36
	Right	1.06	0.825	7.36
7	Left	0.95931	0.73844	8.23
	Middle	0.99385	0.7722	7.45
	Right	1.01	0.78072	10.03
8	Left	1.03	0.78667	7.4
	Middle	1.09	0.84976	8.1
	Right	0.99179	0.76495	8.1
9	Left	0.99853	0.77067	7.37
	Middle	0.97229	0.74955	7.55
	Right	1.12	0.86858	8.57
Average =		1.03942	0.800382	8.1777419
Standard Dev. =		0.04633	0.036894	0.738231
Average Dev. =		0.07942	0.062542	1.2979772

NOTE: from the Central Limit Theorem, if the number of samples is large enough then we can say that the average of the distribution of sample averages is the same as the mean of the sampled population. Thus we can say that we have an average roughness in the channels of 0.8 microns.

We have 31 samples here, for the 95% confidence level for 30 samples the t statistic is 2. 042 and for an infinite number (i.e., normal distribution) the t statistic is 1.960.

t(30)= 2.042

t(infinite): 1.96 4.02 % different than the normal distribution.

Manifold Roughness

RMS	Avg.	Peak to Valley
2.98	2.44	21.12

The average roughness here will be taken directly

Channel Width

L cursor	Rt. cursor	Difference	Resolution	channel width range
1010	1490	480	10	480 to 500
1000	1490	490	10	490 to 510
Avg. Width=		485		

Note: The cursor was moved one pixel at a time until a channel was indicated. This was shown by having a roughness measurement on one side of the channel and then by moving over until the measurement data was nonexistant. The same was done for the other side. The data in the channel was nonexistant because the RST depth of field is only 100 microns and the channel depth was approximately 500 microns. The measurements show the width that is definitely within the channel, add 10 microns to both sides and the measurement will be out of the channel.

(Each Pixel = 10 microns)

APPENDIX D

MICROCHANNEL ROUGHNESS

STEP TESTER

Title: channel 1, left

Note:

2D Analysis

Date: 10/11/95
Time: 13:40:00
Mag: 10.0 X
Mode: VSI
Rq: 1.04 um
Ra: 800.50 nm
Rt: 7.88 um

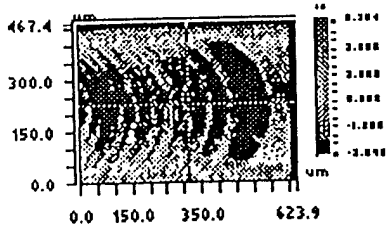

1: 183,118

X / 2 Pt / Radius Scan

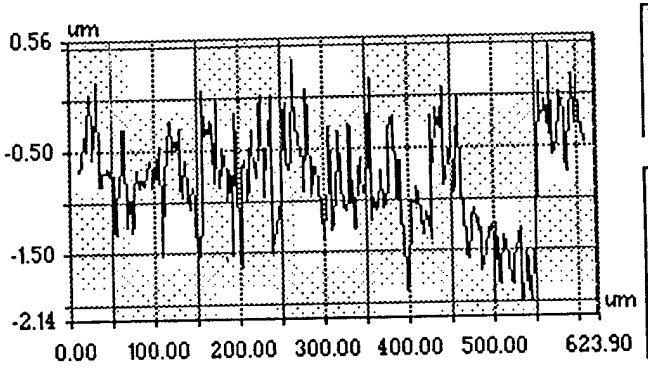

Rq: 0.49 um
Ra: 0.39 um
Rt: 2.46 um
Rp: 0.44 um
Rv: -2.02 um

L: 0.00 um ---
R: 623.90 um ---
D: 623.90 um ---
Angle: ---
Curve: 201.43 mm
Terms: None

Y / Circumference Scan

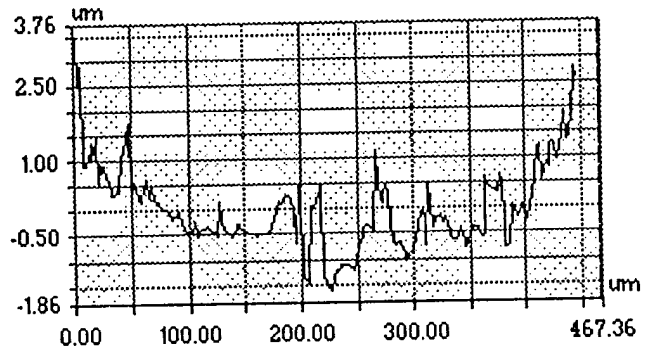

Rq: 0.84 um
Ra: 0.64 um
Rt: 5.11 um
Rp: 3.50 um
Rv: -1.61 um

L: 0.00 um 2.59 um
R: 467.36 um ---
D: 467.36 um ---
Angle: ---
Curve: 11.61 mm
Terms: None

WYKO

Title: channel 5, left

Note:

Contour

Date: 10/11/95
Time: 14:01:16
Mag: 10.0 X
Size: 368 X 238
Sampling: 1.70 um
Mode: VSI

Surface Stats:

Rq: 1.02 um
Ra: 784.09 nm
Rt: 7.76 um

Terms Removed:

Tilt

Filtering: None
Restore: No
Ref Sub: No

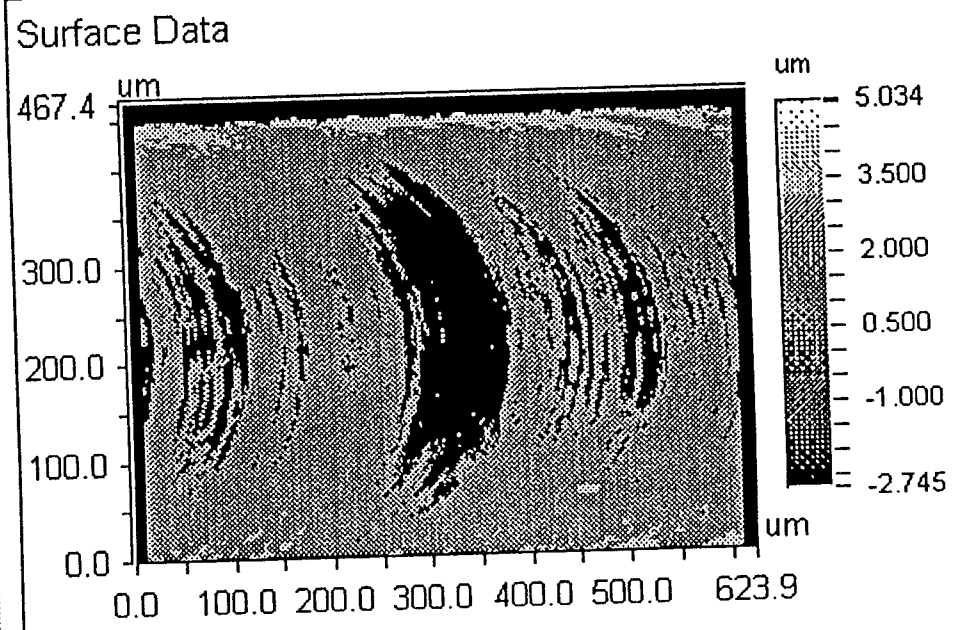

WYKO

Title: width2

Note:

Contour

Date: 10/11/95
Time: 16:05:13
Mag: 2.5 X
Size: 368 X 238
Sampling: 6.60 um
Mode: VSI

Surface Stats:

Rq: 988.65 nm
Ra: 617.76 nm
Rt: 18.23 um

Terms Removed:

None

Filtering: None
Restore: No
Ref Sub: No

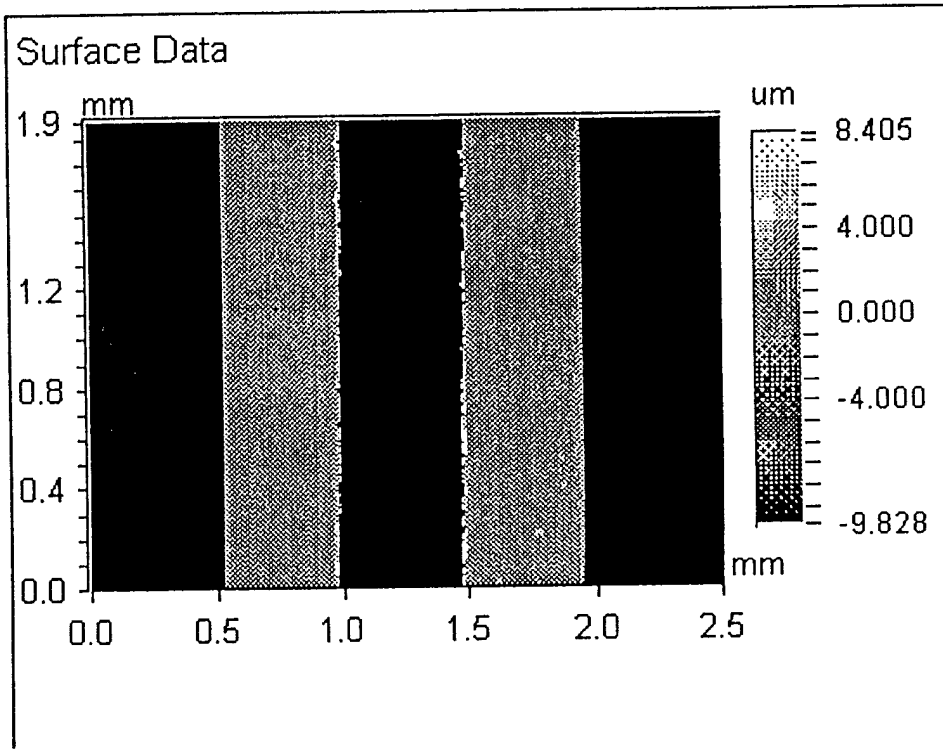

WYKO

Title: width2
Note:

2D Analysis

Date: 10/11/95
Time: 16:05:13
Mag: 2.5 X
Mode: VSI
Rq: 988.65 nm
Ra: 617.76 nm
Rt: 18.23 um

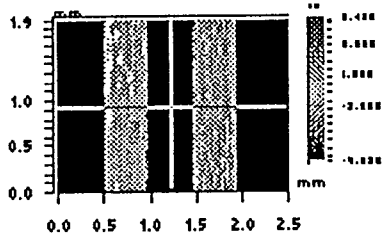

1: 183,118

WYKO

X / 2 Pt / Radius Scan

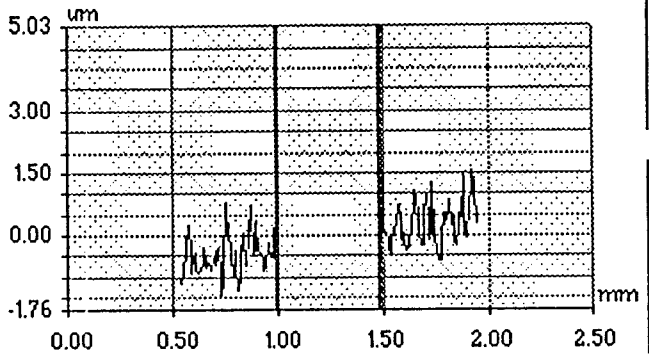

Rq: 0.76 um
Ra: 0.55 um
Rt: 6.17 um
Rp: 4.72 um
Rv: -1.45 um

L: 1.00 mm ---
R: 1.49 mm ---
D: 0.49 mm ---
Angle: ---
Curve: ---
Terms: None

Y / Circumference Scan

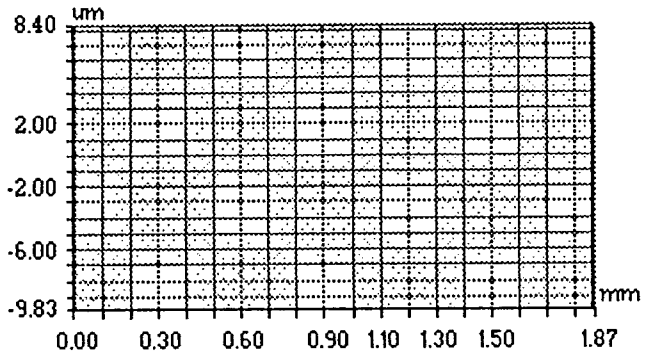

Rq: 0.00 mm
Ra: 0.00 mm
Rt: 0.00 mm
Rp: 0.00 mm
Rv: 0.00 mm

L: 0.00 mm ---
R: 1.87 mm ---
D: 1.87 mm ---
Angle: ---
Curve: ---
Terms: None

APPENDIX E

EQUIPMENT SPECIFICATIONS

Primary Liquid Flow Meters (MAX™ Machinery Piston Flowmeters)

Model 234 *(for aqueous liquids (water) that will not harm the Teflon® bearing or Neoprene seals)*

Flow Range	10 to 5678 mL/min (continuous max = 4000 mL/min)
Fluid Temp Range	-40° to 110°C
Ambient Operating Temp	-18° to 55°C
Reqd. Filtration	10 µm or better
Max. Pressure	2000 psi
Max. Viscosity	up to 30,000 centipoise (Calibrated for water)
Max. ΔP across meter	3 psi at 1 centipoise (see pressure drop chart)
Maximum error	± 0.4 mL/min or 0.75% of reading (See calibration table)
Calibration Accuracy	± 0.05% of reading (used EG&G value)
Materials	carbon pistons,Teflon® bearing, Neoprene seals, 316 SS body, ferroceramic magnets

TRANSMITTER OUTPUT	
Pulse	5V DC
Square wave	1.48 pulses/cc
Displacement of Pistons	10.8 cc/revolution (16 pulses/revolution)
K factor	≈ 1.48 pulses/cc

Model 213-310 *(for most NON-aqueous organic liquids) (like hydrocarbons and other lubricating fluids)*

Flow Range	1 to 1800 mL/min (with two meters 3600 mL/min)
Fluid Temp Range	-250° to 265°C (special startup procedure for 28°C (80°F) above ambient)
Ambient Operating Temp	-15° to 65°C
Reqd. Filtration	10 µm or better
Max. Pressure	1000 psi
Max. Viscosity	up to 30,000 centipoise (Calibrated for kerosene)
Max. ΔP across meter	3 psi at 3 centipoise (see pressure drop chart)
Maximum error	± 0.1 mL/min or 0.75% of reading (See calibration table)
Calibration Accuracy	± 0.05% of reading (used EG&G value)
Materials	303 SS body and pistons, Neoprene seals, 440C SS bearings

TRANSMITTER OUTPUT	
Pulse	5V DC
Square wave	100 pulses/revolution
Displacement of Pistons	.887 cc/revolution
K factor	≈ 110 pulses/cc

for the 284XMTR transmitter K 115 pulses/cc
*(TYPICAL) [110 pulses/cc * 0.887 cc/rev. = 97.57 pulses/rev.]*

INPUT	4.5 to 30V DC @15mA maximum
OUTPUT	0 hz (minimum) 3450 hz (maximum) (115 pulses/cc * 1800cc/min ÷ 60 = 3450 hz)

*NOTE: We can use the calibration sheet to reduce the linearity to approximately zero. The only error would be with our curvefit. However, there will be some additional error due to the meter calibration of approximately ± 1 pulse. In addition, keep the bypass lines in place so that the system may be purged of air before slowly switching over.

(Sample Calculations K factor) K*Q=f
K = 96181.963 Pulses / Liter
f = 5.377 hz = 322.62 cycles/min
Q = 3.35434 mL/min

Secondary Side Flowmeters(EG&G Flow Technology Turbine Flowmeters)
mdotCp limits delta T and since were using water this says that we already have a large Cp thus there's no need to exceed the mdot of the other fluid (second law of thermodynnamics)
FTO-1NIXWULHC-1 (FTO-6811)
extended flow range 3.78 to 303 mL/min

FTO-4NIXWULHC-1 (FTO-6812)
extended flow range 75.7 to 4920 mL/min

Temp Range	-185° to 200°C	RF Pickoffs (instead of magnetic)
Temp Range	-50° to 315°C	Jewel Bearings
Reqd. Filtration	100 µm or better	
Max. Pressure	6000 psi	
Max. Viscosity	50 centistokes (Calibrated for water though)	
Max. ΔP across meter	10 psi	
Dynamic Response	less than 100 hz (10 milliseconds) for each step change in flowrate	
Calibration Accuracy	±0.05% of reading	
Repeatability	±0.1% of reading	
Linearity	±0.1% of reading with linearizing electronics	
Materials	tungsten carbide shaft, Teflon O-ring, 316 SS body	
INPUT	22 to 32V DC @30mA maximum	
OUTPUT	0 to 10 V DC (peak-to-peak)	

*NOTE: We can use the calibration sheet to reduce the linearity to approx. zero. The only error would be with our curvefit. However, there will be some additional error should the viscosity of the fluid change. This could range from say 0.1% to 0.5% for small changes due to temperature.

*(Sample Calculations K factor) K*Q=f*
K = 96181.963 Pulses / Liter
f = 5.377 hz = 322.62 cycles/min
Q = 3.35434 mL/min

Filters
Primary side
Filterite Filter - pressure max = 500 psig on bypass loop
7 micron filter
Secondary side (low pressure, supply from water faucet)
Car Filter
7 micron filter

Stainless Steel Pressure Transducers (Omega)

PX-951, 0-100 and 0-1000 psi (On Test Sections)
(Stainless Steel body and Diaphragm)

Accuracy	±0.15% F.S.
Hysteresis	±0.10% F.S.
Repeatability	±0.05% F.S.
Frequency Response	1000 hz (catalog says 3000 hz)
Zero Balance	±1% F.S.
Thermal Zero Effect	±0.005% full scale / °F (Difference from 75°F)
Thermal Sensitivity Effect	±0.005% full scale / °F (Difference from 75°F)
Proof Pressure	1.5 x Range (150 psi and 1500 psi)
Burst Pressure	5 x Range (500 psi and 5000 psi)
Operable Temp Range	0° to 185°F (-17.7° to 85°C)
Compensated Temp Range	60° to 160°F (15.5° to 71.1°C)
Sensitivity	none listed (very accurate, 0% errror)
Output	0 to 5.0 V
Excitation	26 to 32V DC @45mA or ±15V DC (we used the ±15V DC hookup)

PX-213 models are: *Flow Loop* PX-2131000G5V (1000 psi)
Secondary Flow Loop PX-213500G5V (500 psi)

(Stainless Wetted Parts w/polysilicon strain gage)

Accuracy	±0.25% F.S. (linearity, hysteresis, repeatablity)
Frequency Response	1000 hz
Zero Balance	±1% F.S.
Combined Thermal Effects	±1.5% full scale (over -20° to 85°C)
Proof Pressure	1.5 x Range
Burst Pressure	4 x Range
Operable Temp Range	-4° to 185°F (-20° to 85°C)
Compensated Temp Range	-4° to 176°F (-20° to 80°C)
Span (Sensitivity)	5V ± 0.075V DC (±1.36% F.S.)
Output	0.5 to 5.5 V
Excitation	24V DC @ 15mA (12-36V DC is the range we can use)

DATA ACQUISITION SYSTEM

LabVIEW® for Windows by National Instruments
Gateway 2000 P5-75 Personnal Computer (Pentium processor)

PUMPS (Hydra-Cell Direct Drive Diaphragm Pump, Model MO3ERSESSEY)

Flowrate	0 to 2.2 gpm (0 - 8300 mL/min)
Outlet pressure	1,200 psig max
Inlet Pressure	7 inches Hg (vacuum) to 100 psig
Max. fluid temperature	180°F (82°C)
Materials	316SS construction with EPDM elastomers

Constant Temperature Water Bath

Haake L reservoir
Haake D1 recirculator and heater

Watts	1000 W
Temp Set	analog
Temp Readout	thermometer
Temp Range	0 - 100°C (with refrigerated chiller) 30 - 100°C (without chiller)
Temp Control	on/off
Temp Control Accuracy	±0.2°C
Bath Capacity	3L
High Temp Cutoff	120°C
Wetted Parts	304 stainless steel and HDPE
Pump	1.7 psi
Flow Rate	9 L/min

Exergy Heat Exchanger (secondary side)

Model 00413, Tube-in-Tube heat exchanger

Material	316L Stainless Steel
Heat Transfer Area	1.2 ft^2 (0.11148 m^2)
Max. Temp	approximately 400°C
Design Pressure	4,500 psi (inner tube), 2,000 psi (outer tube)

Preheater (Omegalux™ Flexible Heating Tape)

Model #	STH051-020
Volts	120
Amps	1.33
Watts	156
Phase	1
Maximum Temp.	900°F (482°C)

Test Section Heater

12 Ω (1cm x 1cm) and 40 Ω (1cm x 4cm)
(will use the 40 ohm resistor)
flexible Kapton® heater manufactured by Watlow Electric
Cole Parmer model H-36067-00 1-(800)-232-4340

Voltage Range	3 to 120V
Thickness	0.007"
Temp Range	-319° to 392°F (-195° to 200°C)

Sheathed Thermocouples

Sheath material	304 SS
Sheath diameter	0.0625"
Sheath Temp (Max.)	900°C
Wire Size	30 AWG (dia. = 0.0100")
Type	"T"
Wire Temp (Max.)	148°C
Error	1°C or 0.75% (whichever is greater) at Reference Temp. = 0°C
Voltage range	0.000 mV (0°C) to 6.602 mV (148°C)
Response Time	0.12 seconds (time reqd. To reach 63.2% of an instantanous change of temperature in water for a metal sheathed thermocouple)

**NOTE: Has an exposed junction for faster response.*

Omegatherm® 201 Thermally Conducting Silicon Paste

Temperature Range	-40° to 200°C
Thermal Conductivity (k)	16 Btu·in/(hr·ft²·F°) = 2.3 W/(m·K)

Pressure Vessel

Stainless Steel construction
Design pressure = 300 psi with a safety factor of 2
with cooling coil inside (stainless steel ~ 9 ft of tubing)

Cylinders to pressurize the Tank

2.5" on air side and 1" on fluid side. An input of 100 psi of system air will pressurize the tank to 250 psi.

Pulse Dampener

9 feet of coiled stainless steel tubing (o.d. = 0.25" i.d. = 0.194")

Relief Valves

set at 1250 psig

MAX Machinery calibration

Flowmeter
Model# 213-310
Serial# B519192

Transmitter
Model# 284-512
Serial# 406

cc/min	pulses/cc	% error	Limits
1800	110.2554	-0.45	0.75
1500	110.2886	-0.42	0.75
1000	110.3399	-0.37	0.75
300	110.4317	-0.29	0.75
100	110.2187	-0.48	0.75
30	110.7523	0.00	0.75
10	110.1581	-0.54	1
3	108.0698	-2.42	3.33
1	105.2889	-4.93	10

Kerosene (1.83 centipoise and 21 °C) K factor= 110.7536

MAX Machinery calibration

Flowmeter
Model# 213-310
Serial# B519184

Transmitter
Model# 284-512
Serial# 402

cc/min	pulses/cc	% error	Limits
1800	110.2652	-0.62	0.75
1500	110.3669	-0.53	0.75
1000	110.7113	-0.22	0.75
300	110.8861	-0.06	0.75
100	111.5433	0.53	0.75
30	111.482	0.47	0.75
10	110.6064	-0.31	1
3	108.4808	-2.23	3.33
1	104.5772	-5.75	10

Kerosene (1.83 centipoise and 21 °C) K factor= 110.9551

MAX Machinery calibration

Flowmeter Transmitter
Model# 234-250
Serial# B532014

cc/min	pulses/cc	% error	Limits
4000	1.48001	-0.32	0.75
3000	1.48119	-0.24	0.75
1000	1.48662	0.12	0.75
500	1.48716	0.16	0.75
300	1.48837	0.24	0.75
100	1.48958	0.32	0.75
20	1.4753	-0.64	2
10	1.4659	-1.27	4
7.5	1.46035	-1.65	5.3
5	1.45298	-2.14	15

Water (1 centipoise and 21 °C) K factor= 1.484795

EG&G Flow Technology calibration

Flowmeter
Model# FTO-1NIXWULHC-1
Serial# F095086811

fluid	Water
temperature	72°F
viscosity	0.98 cSt
density	8.329 lb/Gal

Meter Frequency (hz)	Meter Flow Rate (mL/min)	Meter K Factor (Pulses/Liter)	Freq / Viscosity (hz/cSt)	Meter Temp °F
1285.78	314.09597	245615.39	1307.881	70.1
723.911	187.46314	231697.2	736.728	70.2
432.653	115.24153	225258.96	440.409	70.2
251.516	70.94601	212710.78	256.047	70.2
139.424	42.37792	197400.83	141.938	70.2
84.112	27.45797	183798.02	85.642	70.2
45.372	16.58299	164164.84	46.2	70.2
25.399	10.42402	146196.92	25.857	70.2
13.536	6.41412	126623.88	13.771	70.1
5.377	3.35434	96181.963	5.468	70.1

Note: K factor = flowrate / freq.

EG&G Flow Technology calibration

Flowmeter
Model# FTO-4NIXWULHC-1
Serial# F095086812

fluid	Water
temperature	72°F
viscosity	0.98 cSt
density	8.329 lb/Gal

Meter Frequency (hz)	Meter Flow Rate (mL/min)	Meter K Factor (Pulses/Liter)	Freq / Viscosity (hz/cSt)	Meter Temp °F
1367.635	5089.20837	16123.948	1393.391	70.3
821.654	3128.18855	15759.674	837.158	70.3
503.047	1948.86931	15487.364	512.552	70.3
314.327	1228.9902	15345.617	320.296	70.3
191.077	771.19984	14865.918	194.705	70.3
117.489	488.06626	14443.386	119.721	70.3
72.166	305.84763	14157.193	73.528	70.3
43.975	190.57004	13845.276	44.804	70.3
27.279	121.54595	13465.797	27.795	70.3
16.148	74.98947	12920.263	16.453	70.3

APPENDIX F

ERROR ANALYSIS PROGRAM

AND SAMPLE OUTPUT

```
C*************************************************************
C          Program Name: UNCERT5.FOR
C
C PROGRAM TO CONDUCT UNCERTAINTY ANALYSIS BASED ON ORIGINAL
C DATA REDUCTION PROGRAM.  MUST INPUT INDICIDUAL UNCERTAINTIES
C AND ACTUAL MEASUREMENTS FOR EACH VARIABLE
C
C THIS CODE WAS ORIGINALLY WRITTEN BY DR. TIM AMEEL AND
C ADAPTED BY DARIN BAILEY FEBRUARY 1996 TO ACCEPT HIS THESIS
C DATA
C
C Used to reduce data from the 500 micron channels
C*************************************************************
C   X = RAW DATA
C   DX = UNCERTAINTY IN RAW DATA
C   S = SAMPLE STANDARD DEVIATION OF AVERAGE DATA PRESENTED
C
C
C
C
C
C
C
C
C
C
C
C    q = Watts
C*****************************************************************
     IMPLICIT DOUBLE PRECISION (A-H, O-Z)
     DIMENSION R(8), X(18), DX(18), RN(8), XN(18), S(18)
     DOUBLE PRECISION NDP,Kloss(7)
     CHARACTER*3 RN
     CHARACTER*8 XN
C*********************************
C  RENAME THE OUTPUT FILE      *
C                                    *
         OPEN (12, FILE='5A32.OUT')
C*********************************
C  SET UP ALL REQUIRED INPUT DATA FOR EACH CASE
     DATA RN/'q', 'Re','qin','Tw','h','Nu','ff','Pr'/
     DATA XN/'Tin(C)','Tout(C)','T1(C)',
    &'T2(C)','T3(C)','TL(C)','Pin(V)','Pout(V)','freq(hz)',
    &'Wc(µm)','Hc(µm)','L(in)','Volts','Amps','dZP','dZAl',
    &'Aheat','Lheat'/

C************ READ IN VALUES FROM SPREADSHEET ********
C        RENAME THE INPUT FILE TO READ RIGHT ONE    *
C                                  *
      open(unit=4,file='DARIN32.dat')
C*********************************************************
      do 1 i = 1,9
       read(4,*) X(i)
```

```
 1    continue
      do 3 J = 1,9
       READ(4,*) S(j)
 3    continue
       READ(4,*) NDP
      CLOSE(4)

C**********************************************************************
C*************MUST CHANGE WHEN GETTING NEW channels! ******************
C***** σ1 = channel, σ2=manifold=constant, and loss 3 = Kbend=1.2 *****
     Kloss(1)=0.16
     Kloss(2)=0.267
     Kloss(3)=1.2
C** the order is Ke, Kc, Ke2, Kc2** THESE CHANGE FOR EVERY DATA SET ***
     Kloss(4)=0.6
     Kloss(5)=1.18
     Kloss(6)=0.5
     Kloss(7)=0.43
ccccccccccccccccccccccccc


C  REST OF DATA X
     X(10) = 495
     X(11) = 491.7
     X(12) = 2.5001
     X(13) = 37.3
     X(14) = 0.907
     X(15) = 0.0015
     X(16) = 0.002921
     X(17) = 3.613E-4
     X(18) = 0.04
ccccccccccccccccccccccccc
C  REST OF DATA S
     DO 7 I = 1,9
      S(I+9) = 0
 7   CONTINUE
ccccccccccccccccccccccccc
     DATA DX/1.0, 1.0, 1.0, 1.0, 1.0, 1.0 ,0.05 ,0.05 ,0.00839,
    & 15, 25.25, 0.0005, 0.1, 0.001, 0.0005, 0.000254, 0.0, 0.0/
CCC INPUT THE CORRECTED VALUE FOR DX FREQUENCY
     DX(9) = 0.0064*X(9)
     EPSILN=0.00001
     N=18
     M=8
C  WRITE HEADINGS AND ALL VARIABLE VALUES AND UNCERTAINTIES
     WRITE(12,10)
 10  FORMAT(1X,'INPUT VALUE',/,'  I',3X,'VARIABLE',6X,
    &'ACTUAL VALUE', 5X,'UNCERTAINTY',5X,'SAMPLE STD. DEV.(s)',/)
     WRITE(12,15) (I,XN(I),X(I),DX(I),S(I),I=1,N)
 15  FORMAT (1X,I2,3X,A8,4X,F10.5,9X,F10.5,9X,F10.5)
     WRITE(12,17) EPSILN
 17  FORMAT (//,1X,'EPSILON',4X,E12.5)
```

```
      WRITE(12,18)
   18 FORMAT (//,1X,'X(I)',4X,'SENSIT. COEFF.',3X
     &'   BIAS**2    ',3X,'PRECISION**2',/)
C  COMPUTE UNPERTURBED VALUE OF THE OUTPUT PARAMETER
      DO 90 I = 1,M
      WRITE(6,25) I
   25 FORMAT (1X, 'IN LOOP',I2)
      CALL DATRED(X,R,Kloss)
      F=R(I)
      DG=0.0
      DG2=0.0
C  COMPUTE THE SENSITIVITY COEFFICIENTS FOR EACH VARIABLE
      DO 80 J = 1,N
      IF (X(J) .EQ. 0.00) GOTO 50
      EPS=X(J)*EPSILN
      X(J)=X(J) + EPS
      CALL DATRED(X,R,Kloss)
      FPE=R(I)
      X(J)=X(J) - 2.0*EPS
      CALL DATRED(X,R,Kloss)
      X(J)=X(J) + EPS
      FME=R(I)
      PFPX=(FPE-FME)/(2.0*EPS)
C  COMPUTE THE EFFECT OF EACH VARIABLE ON PARAMETER UNCERTAINTY
C  BIAS
      E=(PFPX*DX(J))**2
C  PRECISION
      E2=(PFPX*S(J)/SQRT(NDP))**2
      GOTO 60
   50 PFPX = 0.0
      E = 0.0
   60 WRITE(12,70) J, PFPX, E, E2
   70 FORMAT (1X,I2,5X,E12.5,8X,E12.5,7X,E12.5)
C  ACCUMULATE ALL VARIABLE UNCERTAINTIES
      DG=DG+E
      DG2=DG2+E2
   80 CONTINUE
C  COMPUTE RELATIVE AND ABSOLUTE PARAMETER UNCERTAINTY
C  COMBINING BIAS AND PRECISION UNCERTAINTIES (T = 2)
      DF=SQRT(DG+4*DG2)
      DFF=DF/F*100.0
      WRITE(12,85) RN(I), F,RN(I),DF,RN(I),RN(I),DFF
   85 FORMAT (1X,A2,T20,E12.5,/,'DELTA ',A2,T20,E12.5,/,
     &'(DELTA ',A2,')/',A2,2X,T24,F8.3,/)
   90 CONTINUE
      CLOSE(12)
      WRITE(6,95)
   95 FORMAT (' DATA ANALYSIS COMPLETE')
      PAUSE
      STOP
      END
```

```
C*****************************************************************
      SUBROUTINE DATRED(X,R,Kloss)
C*****************************************************************
C
C
C
C
C
C*****************************************************************
      IMPLICIT DOUBLE PRECISION (A-H, O-Z)
C  WILL HAVE TO CHANGE THE DIMENSION STATEMENT IF MORE VARS ADDED
      DIMENSION X(18), R(8)
      DOUBLE PRECISION mdot,mu,kp,kAl,Lheat,L,NCH,K,kf,Nu,MUmean
      DOUBLE PRECISION Kloss(7),Kb,Kc,Ke,Kc2,Ke2
C  INPUT THE NUMBER OF CHANNELS AND K FACTOR
      NCH = 9.0
      K = 1.484795
C  ASSIGN VALUES TO THE INPUT VARIABLE
      Tin  = X(1)
      Tout = X(2)
      T1   = X(3)
      T2   = X(4)
      T3   = X(5)
      TL   = X(6)
      Pin  = X(7)
      Pout = X(8)
      freq = X(9)
      Wc   = X(10)
      Hc   = X(11)
      L    = X(12)
      Volt = X(13)
      Curr = X(14)
      dZp  = X(15)
      dZAl = X(16)
      Aheat = X(17)
      Lheat = X(18)
      sigma1= Kloss(1)
      sigma2= Kloss(2)
      Kb   = Kloss(3)
      Kc   = Kloss(4)
      Ke   = Kloss(5)
      Kc2  = Kloss(6)
      Ke2  = Kloss(7)
C*****************************
C  CONVERT UNITS
C*****************************
      Wc = Wc/1.0E6
      Hc = Hc/1.0E6
      L = L*0.0254
C  CALIBRATION CURVE FOR THE MAX 234 METER (CC/MIN = OUTPUT)
c     ccMIN = 0.22509145+40.123661*freq+0.031426978*freq*freq
c    &-0.0016261406*freq**3+3.8161346E-5*freq**4-3.9007856E-7*freq**5
```

```
c   &1.439192E-9*freq**6
c IT TURNS OUT THIS EQUATION GAVE "-" VALUES FOR SOME Hz

C  THE RANGE OF Pin = 100 PSI  (Convert to Pa)
     Pin = (1000 - (5-Pin)/5*1000)/0.00014504

C  THE RANGE OF Pout = 100 PSI (Convert to Pa)
     Pout = (100 - (5-Pout)/5*100)/0.00014504

C*****************************************
C  DETERMINE THE PROPERTIES OF WATER
C*****************************************
     Tbulk = (Tin+Tout)/2.0
C  THERMAL CONDUCTIVITY (W/m/K)
     kf = 0.561+2.27E-3*Tbulk-1.9155E-5*Tbulk**2+1.3209E-7*Tbulk**3
    &-5.2448E-10*Tbulk**4
C  SPECIFIC HEAT (kJ/kg/K)
     Cp = 4.2222-4.39579E-3*Tbulk+1.84746E-4*Tbulk**2
    &-4.2517E-6*Tbulk**3+5.6624E-8*Tbulk**4-3.935897E-10*Tbulk**5
    &+1.1111111E-12*Tbulk**6
C  DENSITY (kg/m^3)
     CALL RHOS(TL,RHO)
     CALL RHOS(Tin,RHOin)
     CALL RHOS(Tbulk,RHOmean)
     CALL RHOS(Tout,RHOout)
C  KINEMATIC VISCOSITY (Pa*sec)
     CALL MUS(TL,mu)
     CALL MUS(Tbulk,MUmean)

C*****************************************
C  CARRY OUT THE NECESSARY CALCULATIONS
C*****************************************
     Dh   = (2*Wc*Hc)/(Wc+Hc)
     A    = Hc*Wc
C     FLOW = ccMIN/(6e7)/NCH
     FLOW = freq/K/NCH/1E6
     V    = FLOW/A
     V2   = FLOW/(4.0*datan(1.0)*(0.25*0.0254)**2/4.0)
     mdot = FLOW*RHO
     q    = mdot*Cp*(Tout-Tin)*1000
     Re = RHO*V*Dh/mu
     qin= Volt*Curr
C  AVERAGE HEATER TEMPERATURE
     Theater = (T1+T2+T3)/3.0
C  ADDITIONAL PROPERTIES OF ALUMINUM AND Si PASTE
     kAl = 189.0 - 14.0*(100.0-Theater)/100.0
     kp = 2.31
C  CALCULATE AVG. WALL TEMPERATURE TO GET h AND Nu
     Tw = Theater - q*(dZp/(Aheat*kp)+dZAl/(Aheat*kAl))
     h  = q/( (Wc*Lheat+2.0*Hc*Lheat)*(Tw - Tbulk))
     Nu = h*Dh/kf
C  FRICTION FACTOR
```

```
      gc = 1.0
      DeltaP=Pin-Pout
C******* INITIAL CHECK
      ff = DeltaP*Dh*2*gc/(L*V*V*RHOmean)
C******* EQUATION 8.1
C     ff =(DeltaP-V2*V2/(2*gc)*RHOin*(Kb+Kc2+1-sigma2*sigma2)
C     &+DeltaP-V2*V2/(2*gc)*RHOout*(Kb-1+sigma2*sigma2+Ke2))/
C     &((RHOmean*V)**2/(2*gc)*RHOin) - (Kc+1-sigma**2+
C     &2*(RHOin/RHOout-1)-(1-sigma**2-Ke)*RHOin/RHOout)*
C     &(Dh*RHOmean/L/RHOin)
C  PRANDTLE NUMBER CALCULATIONS TO USE WHEN COMPARING TO CONVENTIONAL
      Pr = MUmean*1000*Cp/kf
C  ASSIGN OUTPUT PARAMETERS TO POSITIONS IN THE R ARRAY
      R(1)=q
      R(2)=Re
      R(3)=qin
      R(4)=Tw
      R(5)=h
      R(6)=Nu
      R(7)=ff
      R(8)=Pr
      RETURN
      END


C*****************************************************************
      SUBROUTINE RHOS(T,RHO)
C*****************************************************************
C
      implicit double precision (A-H, O-Z)
      T = T + 273.18
      RHO= (-2403.360201-1.40758895*T+0.1068287657*T*T-0.2914492351
     &E-3*T**3+0.3734979936E-6*T**4-0.21203787E-9*T**5)/
     &(-3.424442728+0.01619785*T)
      T = T - 273.18
      return
      end

C*****************************************************************
      SUBROUTINE MUS(T,MU)
C*****************************************************************
C
      implicit double precision (A-H, O-Z)
      double precision mu
      T = T + 273.18
      mu = 0.012571873*EXP((1-0.0058064362*T)/(0.0011309108*T-
     &0.5723952E-5*T*T))
      mu = mu*1E-3
      T = T - 273.18
      return
      end
```

Run Number		6	Data Point #	1	
INPUT VALUE					
I	VARIABLE	ACTUAL VALUE	UNCERTAINTY	SAMPLE STD. DEV.(s)	
1	Tin(C)	26.60128	1	0.07829	
2	Tout(C)	34.60211	1	0.02223	
3	T1(C)	51.47361	1	0.01368	
4	T2(C)	55.55276	1	0.01243	
5	T3(C)	46.28207	1	0.01409	
6	TL(C)	25.01552	1	0.04898	
7	Pin(V)	1.39267	0.05	0	
8	Pout(V)	0.68109	0.05	0.00048	
9	freq(hz)	0.50019	0.0032	0.00073	
10	Wc(æm)	254	15	0	
11	Hc(æm)	254	5	0	
12	L(in)	2.5001	0.0005	0	
13	Volts	28.7	0.1	0	
14	Amps	0.703	0.001	0	
15	dZP	0.0002	0.0001	0	
16	dZAl	0.00305	0.00013	0	
17	Aheat	0.00036	0	0	
18	Lheat	0.04	0	0	
EPSILON	1.00E-05				
X(I)	SENSIT. COEFF.	BIAS**2	PRECISION**2		
1	-1.40E+00	1.97E+00	2.24E-04		
2	1.40E+00	1.97E+00	1.80E-05		
3	0.00E+00	0.00E+00	0.00E+00		
4	0.00E+00	0.00E+00	0.00E+00		
5	0.00E+00	0.00E+00	0.00E+00		
6	-2.89E-03	8.36E-06	3.72E-10		
7	0.00E+00	0.00E+00	0.00E+00		
8	0.00E+00	0.00E+00	0.00E+00		
9	2.25E+01	5.16E-03	5.03E-06		
10	0.00E+00	0.00E+00	0.00E+00		
11	0.00E+00	0.00E+00	0.00E+00		
12	0.00E+00	0.00E+00	0.00E+00		
13	0.00E+00	0.00E+00	0.00E+00		
14	0.00E+00	0.00E+00	0.00E+00		
15	0.00E+00	0.00E+00	0.00E+00		
16	0.00E+00	0.00E+00	0.00E+00		
17	0.00E+00	0.00E+00	0.00E+00		
18	0.00E+00	0.00E+00	0.00E+00		
q	1.12E+01				
DELTA q	1.99E+00				
(DELTA q)/q	17.69				
1	0.00E+00	0.00E+00	0.00E+00		

2	0.00E+00	0.00E+00	0.00E+00		
3	0.00E+00	0.00E+00	0.00E+00		
4	0.00E+00	0.00E+00	0.00E+00		
5	0.00E+00	0.00E+00	0.00E+00		
6	3.35E+01	1.12E+03	4.99E-02		
7	0.00E+00	0.00E+00	0.00E+00		
8	0.00E+00	0.00E+00	0.00E+00		
9	2.97E+03	9.06E+01	8.82E-02		
10	-2.93E+00	1.93E+03	0.00E+00		
11	-2.93E+00	2.14E+02	0.00E+00		
12	0.00E+00	0.00E+00	0.00E+00		
13	0.00E+00	0.00E+00	0.00E+00		
14	0.00E+00	0.00E+00	0.00E+00		
15	0.00E+00	0.00E+00	0.00E+00		
16	0.00E+00	0.00E+00	0.00E+00		
17	0.00E+00	0.00E+00	0.00E+00		
18	0.00E+00	0.00E+00	0.00E+00		
Re	1.49E+03				
DELTA Re	5.79E+01				
(DELTA Re)/Re	3.896				
1	0.00E+00	0.00E+00	0.00E+00		
2	0.00E+00	0.00E+00	0.00E+00		
3	0.00E+00	0.00E+00	0.00E+00		
4	0.00E+00	0.00E+00	0.00E+00		
5	0.00E+00	0.00E+00	0.00E+00		
6	0.00E+00	0.00E+00	0.00E+00		
7	0.00E+00	0.00E+00	0.00E+00		
8	0.00E+00	0.00E+00	0.00E+00		
9	0.00E+00	0.00E+00	0.00E+00		
10	0.00E+00	0.00E+00	0.00E+00		
11	0.00E+00	0.00E+00	0.00E+00		
12	0.00E+00	0.00E+00	0.00E+00		
13	7.03E-01	4.94E-03	0.00E+00		
14	2.87E+01	8.24E-04	0.00E+00		
15	0.00E+00	0.00E+00	0.00E+00		
16	0.00E+00	0.00E+00	0.00E+00		
17	0.00E+00	0.00E+00	0.00E+00		
18	0.00E+00	0.00E+00	0.00E+00		
qi	2.02E+01				
DELTA qi	7.59E-02				
(DELTA qi)/qi	0.376				
1	4.01E-01	1.61E-01	1.83E-05		
2	-4.01E-01	1.61E-01	1.47E-06		
3	3.33E-01	1.11E-01	3.85E-07		
4	3.33E-01	1.11E-01	3.18E-07		
5	3.33E-01	1.11E-01	4.09E-07		
6	8.27E-04	6.84E-07	3.04E-11		
7	0.00E+00	0.00E+00	0.00E+00		
8	0.00E+00	0.00E+00	0.00E+00		
9	-6.42E+00	4.22E-04	4.11E-07		

10	0.00E+00	0.00E+00	0.00E+00		
11	0.00E+00	0.00E+00	0.00E+00		
12	0.00E+00	0.00E+00	0.00E+00		
13	0.00E+00	0.00E+00	0.00E+00		
14	0.00E+00	0.00E+00	0.00E+00		
15	-1.35E+04	1.81E+00	0.00E+00		
16	-1.71E+02	4.70E-04	0.00E+00		
17	8.89E+03	0.00E+00	0.00E+00		
18	0.00E+00	0.00E+00	0.00E+00		
Tw	4.79E+01				
DELTA Tw	1.57E+00				
(DELTA Tw)/Tw	3.28				
1	-2.54E+03	6.46E+06	7.33E+02		
2	3.77E+03	1.42E+07	1.30E+02		
3	-4.11E+02	1.69E+05	5.85E-01		
4	-4.11E+02	1.69E+05	4.83E-01		
5	-4.11E+02	1.69E+05	6.21E-01		
6	-6.51E+00	4.23E+01	1.88E-03		
7	0.00E+00	0.00E+00	0.00E+00		
8	0.00E+00	0.00E+00	0.00E+00		
9	5.05E+04	2.61E+04	2.55E+01		
10	-2.80E+01	1.76E+05	0.00E+00		
11	-5.59E+01	7.82E+04	0.00E+00		
12	0.00E+00	0.00E+00	0.00E+00		
13	0.00E+00	0.00E+00	0.00E+00		
14	0.00E+00	0.00E+00	0.00E+00		
15	1.66E+07	2.75E+06	0.00E+00		
16	2.10E+05	7.13E+02	0.00E+00		
17	-1.10E+07	0.00E+00	0.00E+00		
18	-5.33E+05	0.00E+00	0.00E+00		
h	2.13E+04				
DELTA h	4.92E+03				
(DELTA h)/h	23.107				
1	-1.06E+00	1.12E+00	1.27E-04		
2	1.55E+00	2.39E+00	2.19E-05		
3	-1.69E-01	2.87E-02	9.96E-08		
4	-1.69E-01	2.87E-02	8.22E-08		
5	-1.69E-01	2.87E-02	1.06E-07		
6	-2.68E-03	7.20E-06	3.20E-10		
7	0.00E+00	0.00E+00	0.00E+00		
8	0.00E+00	0.00E+00	0.00E+00		
9	2.08E+01	4.45E-03	4.33E-06		
10	5.77E-03	7.48E-03	0.00E+00		
11	-5.77E-03	8.31E-04	0.00E+00		
12	0.00E+00	0.00E+00	0.00E+00		
13	0.00E+00	0.00E+00	0.00E+00		
14	0.00E+00	0.00E+00	0.00E+00		
15	6.84E+03	4.68E-01	0.00E+00		
16	8.67E+01	1.21E-04	0.00E+00		
17	-4.52E+03	0.00E+00	0.00E+00		

18	-2.20E+02	0.00E+00	0.00E+00		
Nu	8.79E+00				
DELTA Nu	2.02E+00				
(DELTA Nu)/Nu	22.981				
1	4.46E-06	1.99E-11	2.26E-15		
2	4.46E-06	1.99E-11	1.82E-16		
3	0.00E+00	0.00E+00	0.00E+00		
4	0.00E+00	0.00E+00	0.00E+00		
5	0.00E+00	0.00E+00	0.00E+00		
6	0.00E+00	0.00E+00	0.00E+00		
7	4.06E-02	4.13E-06	2.86E-20		
8	-4.06E-02	4.13E-06	6.93E-12		
9	-1.16E-01	1.37E-07	1.33E-10		
10	2.85E-04	1.82E-05	0.00E+00		
11	2.85E-04	2.03E-06	0.00E+00		
12	-1.16E-02	3.35E-11	0.00E+00		
13	0.00E+00	0.00E+00	0.00E+00		
14	0.00E+00	0.00E+00	0.00E+00		
15	0.00E+00	0.00E+00	0.00E+00		
16	0.00E+00	0.00E+00	0.00E+00		
17	0.00E+00	0.00E+00	0.00E+00		
18	0.00E+00	0.00E+00	0.00E+00		
ff	2.89E-02				
DELTA ff	5.35E-03				
(DELTA ff)/ff	18.509				

APPENDIX G

FLUID PROPERTIES

Density of Saturated Water - Hyland and Drexler (1980)

$$\rho_f = \frac{\sum_{i=1}^{5} F_i \, T^i}{\sum_{i=6}^{7} F_i \, T^{i-6}}$$

where ρ_f	=	density (kg/m^3)	
T	=	temperature (°K)	
F_0	=	-0.2403360201	x 10^4
F_1	=	-0.140758895	x 10^1
F_2	=	0.1068287657	x 10^0
F_3	=	-0.2914492351	x 10^{-3}
F_4	=	0.373497936	x 10^{-6}
F_5	=	-0.21203787	x 10^{-9}
F_6	=	-0.3424442728	x 10^1
F_7	=	0.1619785	x 10^{-1}

Dynamic Viscosity of Water at 1 atm (0 to 100°C) - Nagashima (1977)

$$\mu_f = A \, \exp[\frac{1 + BT}{CT + DT^2}]$$

where μ_f	=	dynamic viscosity (10^{-3} N/m^2)	
T	=	temperature (°K)	
A	=	0.12571873	x 10^{-1}
B	=	-0.58064362	x 10^{-2}
C	=	0.11309108	x 10^{-2}
D	=	-0.5723952	x 10^{-5}

Thermal Conductivity of Water (0 to 100°C) - ASME Steam Tables (1983)

$$k_f = \sum_{i=1}^{4} b_i \, T^i$$

where	k_f	=	thermal conductivity (W/m/K)	
	T	=	temperature (°C)	
	b_0	=	0.561	
	b_1	=	2.2795	x 10^{-3}
	b_2	=	-1.9155	x 10^{-5}
	b_3	=	1.3209	x 10^{-7}
	b_4	=	-5.5448	x 10^{-10}

Specific Heat of Saturated Water - ASME Steam Tables (1977)

$$C_p = \sum_{i=1}^{6} d_i \, T^i$$

where	C_p	=	thermal conductivity (W/m/K)	
	T	=	temperature (°C)	
	d_0	=	4.2222	
	d_1	=	-4.39579	x 10^{-3}
	d_2	=	1.84746	x 10^{-4}
	d_3	=	-4.2517	x 10^{-6}
	d_4	=	5.6624	x 10^{-8}
	d_5	=	-3.935897	x 10^{-10}
	d_4	=	1.1111111	x 10^{-12}

APPENDIX H

RAW DATA

				TEST 4					
	AVERAGES	AVERAGES	AVERAGES	AVERAGES	AVERAGES	AVERAGES	AVERAGES	AVERAGES	AVERAGES
Data Pt.	T in (°C)	T out (°C)	T heat 1 (°C)	T heat 2 (°C)	T heat 3 (°C)	Loop Temp (°C)	P in (V)	P out (V)	Flow meter hz
1	23.51	27.37	42.53	47.78	41.04	22.72	0.7104	0.7458	2.59198
2	23.46	25.55	40.37	45.72	39.56	22.86	0.7693	0.7624	4.82554
3	23.57	24.95	39.33	44.67	38.88	23.06	0.8440	0.7779	7.34466
4	23.75	24.70	38.35	43.66	38.35	23.28	0.9835	0.8160	10.71218
5	23.91	24.70	36.39	41.83	37.57	23.55	1.1594	0.8507	13.72596
6	24.01	24.63	35.80	41.29	37.11	23.72	1.4459	0.8990	17.94435
7	24.00	24.53	35.46	40.92	36.86	23.76	1.7283	0.9602	21.54730
8	24.02	24.50	35.32	40.79	36.79	23.80	1.9303	0.9919	23.89489
9	24.11	24.43	35.09	40.53	36.60	23.82	2.2447	1.0573	26.90566
10	24.11	24.42	35.06	40.51	36.61	23.84	2.3981	1.0840	28.28161
11	24.23	24.63	35.18	40.58	36.73	23.96	2.6515	1.1248	30.39658
12	24.24	24.62	35.12	40.51	36.69	24.00	2.9660	1.1947	32.77025
13	24.24	24.62	35.08	40.48	36.69	24.04	3.1529	1.2248	34.24637
14	24.48	24.85	35.30	40.63	36.87	24.21	3.4146	1.2822	36.64048
15	24.50	24.87	35.33	40.67	36.92	24.27	3.6126	1.3138	38.47237
16	24.83	25.18	35.53	40.83	37.14	24.41	4.3465	1.4585	43.06883
17	24.88	25.24	35.55	40.83	37.18	24.55	4.7280	1.5464	45.40462
18	24.94	25.29	35.60	40.87	37.23	24.64	4.8917	1.5853	46.49674

		TEST 5	
	AVERAGES	AVERAGES	AVERAGES
Data Pt.	P in (V)	P out (V)	Flow meter hz
1	0.0778	0.7375	7.43076
2	0.0810	0.7430	8.56392
3	0.0878	0.7568	10.23151
4	0.0928	0.7687	11.32530
5	0.1036	0.7941	13.41526
6	0.1145	0.8136	14.78521
7	0.1264	0.8310	16.61253
8	0.1310	0.8377	17.41683
9	0.1542	0.8911	20.57470
10	0.1702	0.9227	21.93283
11	0.1862	0.9582	23.68830
12	0.2137	1.0140	26.53608
13	0.2517	1.0872	30.10604
14	0.2662	1.1126	31.01310
15	0.3363	1.2688	36.94971
16	0.3729	1.3566	39.32430
17	0.4166	1.4566	42.09426
18	0.4618	1.5545	45.14380
19	0.4905	1.6135	46.89493
20	0.5597	1.7589	50.86780
21	0.5943	1.8530	52.66551
22	0.6175	1.9039	54.70728
23	0.6983	2.0795	57.99229
24	0.7358	2.1703	61.47671
25	0.8610	2.4368	68.20442
26	0.9048	2.5530	67.30165
27	0.9190	2.5886	68.34200
28	0.9512	2.6557	70.50958
29	0.9940	2.7726	72.39095
30	1.0843	2.9794	76.20365
31	1.1511	3.1367	78.92967
32	1.1840	3.2309	79.66239

				TEST 6					
	AVERAGES	AVERAGES	AVERAGES	AVERAGES	AVERAGES	AVERAGES	AVERAGES	AVERAGES	AVERAGES
Data Pt.	T in (°C)	T out (°C)	T heat 1 (°C)	T heat 2 (°C)	T heat 3 (°C)	Loop Temp (°C)	P in (V)	P out (V)	Flow meter hz
1	26.60	34.60	51.47	55.55	46.28	25.02	1.3927	0.6811	0.50019
2	26.39	32.72	47.83	51.84	42.82	24.78	1.8513	0.6657	0.77076
3	26.74	33.94	47.27	51.72	42.84	24.85	1.7941	0.6284	0.66331
4	26.41	32.84	44.54	49.17	40.60	24.67	2.2101	0.6164	0.90596
5	26.26	31.65	42.19	47.05	38.77	24.62	2.7198	0.6151	0.98927
6	26.30	31.07	41.15	46.07	37.96	24.70	3.0046	0.6138	1.01916
7	26.05	30.72	40.58	45.56	37.51	24.60	3.2202	0.6052	1.14065
8	26.21	30.40	40.08	45.10	37.09	24.80	3.5215	0.6057	1.19296
9	26.35	30.20	39.62	44.61	36.72	24.93	3.7480	0.5935	1.24067
10	26.17	30.10	39.42	44.45	36.59	24.84	3.9693	0.6168	1.29039
11	26.20	29.91	39.06	44.07	36.28	24.92	4.2813	0.6200	1.36003
12	26.36	29.76	38.78	43.75	36.04	25.09	4.5088	0.6178	1.42346
13	26.27	29.65	38.55	43.54	35.88	25.04	4.7673	0.6257	1.47169
14	26.40	29.66	38.45	43.43	35.82	25.21	4.9938	0.6235	1.53263

				TEST 7					
	AVERAGES	AVERAGES	AVERAGES	AVERAGES	AVERAGES	AVERAGES	AVERAGES	AVERAGES	AVERAGES
Data Pt.	T in (°C)	T out (°C)	T heat 1 (°C)	T heat 2 (°C)	T heat 3 (°C)	Loop Temp (°C)	P in (V)	P out (V)	Flow meter hz
1	29.68	48.58	75.91	84.71	65.81	25.75	1.3004	0.7092	0.49693
2	30.08	48.08	73.55	81.23	62.60	26.29	1.5131	0.7113	0.61580
3	30.14	46.04	70.51	77.99	59.77	26.71	1.7644	0.7126	0.77573
4	30.17	44.51	67.76	75.14	57.42	27.25	2.0342	0.7131	0.84462
5	30.32	43.81	66.19	73.83	56.35	27.76	2.2432	0.7107	0.91536
6	30.45	43.08	64.55	72.33	55.19	28.18	2.5230	0.7147	0.98051
7	30.57	42.05	62.69	70.51	53.71	28.62	2.9777	0.7197	1.04555
8	30.78	41.66	61.94	69.80	53.13	29.09	3.2356	0.7164	1.08406
9	31.05	41.39	61.31	69.09	52.68	29.53	3.4664	0.7195	1.21514
10	31.13	40.97	60.47	68.27	52.04	29.72	3.7380	0.7183	1.24778
11	31.37	40.75	60.06	67.84	51.75	30.00	3.9444	0.7172	1.27366
12	31.52	40.40	59.48	67.28	51.32	30.19	4.2521	0.7159	1.42364
13	31.90	40.49	59.41	67.21	51.36	30.81	4.4530	0.7196	1.43860
14	32.24	40.38	58.94	66.71	51.10	31.31	4.7525	0.7203	1.55381
15	32.75	40.55	58.93	66.71	51.24	32.02	5.0016	0.7183	1.61900

APPENDIX I

REDUCED DATA

#FRICTION FACTOR RESULTS FROM TEST 4

#Re	f	lower bound	upper bound
780.98	0.00679	-0.06225	0.07582
1194.20	0.02786	-0.00223	0.05794
1750.90	0.03317	0.01830	0.04805
2257.40	0.03724	0.02705	0.04743
2962.70	0.03860	0.03097	0.04624
3560.60	0.03760	0.03099	0.04421
3953.00	0.03736	0.03110	0.04361
4450.00	0.03730	0.03129	0.04331
4680.00	0.03730	0.03136	0.04324
5050.00	0.03760	0.03172	0.04348
5445.50	0.03749	0.03168	0.04330
5696.20	0.03737	0.03161	0.04313
6117.60	0.03611	0.03057	0.04164
6432.90	0.03531	0.02991	0.04070
7224.40	0.03540	0.03002	0.04077
7640.90	0.03509	0.02978	0.04039
7840.20	0.03477	0.02951	0.04003

 # FRICTION FACTOR RESULTS FROM TEST 5

#Re	f	lower bound	upper bound
1155.30	0.01680	-0.18993	0.22353
1332.40	0.02076	-0.13490	0.17642
1593.30	0.02636	-0.08275	0.13547
1760.00	0.02820	-0.06090	0.11730
2090.00	0.03060	-0.03300	0.09420
2300.00	0.03440	-0.01810	0.08690
2590.00	0.03570	-0.00600	0.07740
2720.00	0.03540	-0.00260	0.07340
3220.00	0.03490	0.00740	0.06240
3440.00	0.03680	0.01240	0.06120
3720.00	0.03660	0.01550	0.05770
4180.00	0.03620	0.01910	0.05330
4750.00	0.03590	0.02220	0.04960
5020.00	0.03660	0.02350	0.04970
6070.00	0.03490	0.02504	0.04476
6520.00	0.03490	0.02586	0.04394
7030.00	0.03480	0.02652	0.04308
7600.00	0.03420	0.02661	0.04179
7960.00	0.03400	0.02672	0.04128
8690.00	0.03370	0.02699	0.04041
9120.00	0.03350	0.02701	0.03999
9560.00	0.03250	0.02632	0.03868
10200.00	0.03320	0.02718	0.03922
10900.00	0.03120	0.02563	0.03677
12300.00	0.03020	0.02506	0.03534
12300.00	0.03260	0.02710	0.03810
12600.00	0.03220	0.02680	0.03760
13200.00	0.03140	0.02617	0.03663
13700.00	0.03110	0.02595	0.03625
14600.00	0.03080	0.02578	0.03582
15300.00	0.03060	0.02566	0.03554
15600.00	0.03090	0.02593	0.03587

 # FRICTION FACTOR RESULTS FROM TEST 6

#Re	f	lower bound	upper bound
1490.00	0.02890	0.02355	0.03425
2280.00	0.02030	0.01691	0.02369
1960.00	0.02690	0.02239	0.03141
2670.00	0.01970	0.01650	0.02290
2910.00	0.02190	0.01841	0.02539
3010.00	0.02340	0.01968	0.02712
3360.00	0.02040	0.01716	0.02364
3530.00	0.02080	0.01751	0.02409
3680.00	0.02080	0.01751	0.02409
3820.00	0.02050	0.01728	0.02372
4030.00	0.02010	0.01694	0.02326
4240.00	0.01950	0.01643	0.02257
4380.00	0.01940	0.01635	0.02245
4580.00	0.01890	0.01593	0.02187

 # FRICTION FACTOR RESULTS FROM TEST 7

#Re	f	lower bound	upper bound
1490.00	0.02890	0.02355	0.03425
2280.00	0.02030	0.01691	0.02369
1960.00	0.02690	0.02239	0.03141
2670.00	0.01970	0.01650	0.02290
2910.00	0.02190	0.01841	0.02539
3010.00	0.02340	0.01968	0.02712
3360.00	0.02040	0.01716	0.02364
3530.00	0.02080	0.01751	0.02409
3680.00	0.02080	0.01751	0.02409
3820.00	0.02050	0.01728	0.02372
4030.00	0.02010	0.01694	0.02326
4240.00	0.01950	0.01643	0.02257
4380.00	0.01940	0.01635	0.02245
4580.00	0.01890	0.01593	0.02187

 # NU RESULTS FROM TEST 4

#Re	Nu	lower bound	upper bound
780.98	3.72	-0.12	7.56
1194.20	4.00	-2.34	10.34
1750.90	4.41	-5.98	14.80
2257.40	5.77	-12.62	24.16
2962.70	6.59	-21.57	34.76
3560.60	7.08	-29.82	43.98
3953.00	7.23	-34.87	49.33
4450.00	4.59	-27.81	36.99
4680.00	4.52	-29.18	38.22
5050.00	8.52	-56.28	73.32
5445.50	9.11	-66.35	84.57
5696.20	9.87	-76.53	96.28
6117.60	11.44	-98.99	121.87
6432.90	12.45	-115.94	140.83
7224.40	15.87	-183.51	215.25
7640.90	19.28	-257.81	296.37
7840.20	20.09	-281.32	321.50

 # NU RESULTS FROM TEST 6

#Re	Nu	lower bound	upper bound
1490.00	8.79	6.77	10.81
2280.00	13.30	9.12	17.48
1960.00	13.90	9.88	17.92
2670.00	21.20	13.16	29.24
2910.00	21.50	12.10	30.90
3010.00	20.30	10.75	29.85
3360.00	23.80	11.60	36.00
3530.00	22.60	10.20	35.00
3680.00	22.20	9.20	35.20
3820.00	24.40	9.80	39.00
4030.00	25.10	9.20	41.00
4240.00	24.30	7.80	40.80
4380.00	25.80	7.80	43.80
4580.00	26.70	7.30	46.10

 # NU RESULTS FROM TEST 7

#Re	Nu	lower bound	upper bound
1500.00	12.10	10.30	13.90
1880.00	16.90	13.70	20.10
2390.00	21.50	16.42	26.58
2640.00	23.00	17.08	28.92
2890.00	24.90	17.91	31.89
3130.00	26.70	18.62	34.78
3360.00	27.40	18.65	36.15
3520.00	27.70	18.63	36.77
3990.00	31.90	20.00	43.80
4110.00	32.00	19.80	44.20
4220.00	31.40	19.40	43.40
4740.00	35.70	20.30	51.10
4850.00	35.00	19.90	50.10
5290.00	37.90	20.10	55.70
5590.00	38.60	19.80	57.40

APPENDIX J

MATHEMATICAL MODEL TO PREDICT FRICTION AND HEAT TRANSER CHARACTERISTICS IN MICROCHANNEL HEAT EXCHANGERS

TKSolver VARIABLE sheet

St	Input	Name	Output	Unit	Comment
					Darin Bailey - Thesis
					MATH MODEL
					February 21, 1995
					HAVE INITIAL GUESSES ON temp & Tsi
					***** MAIN RESULTS *****
L		deltaPs	32.7319	psi	Pressure Drop in channels (PSI)
L		Re	4675.9383		Reynolds number (based on ID)
L		R	0.3996	cm^2*K/W	Normalized é (Tuckermans)
		ëT	1.44	øC	(Tmax-Ta) (ALT-235)
					This temp rise is NOT for fluid,
					it is for the circuit temp rise!!!
					********* INPUTS *********
L	20	Q		cm^3/sec	Volumetric flow rate
	3.6	q``		W/cm^2	heat flux
					***** CHANNEL DIMENSIONS *****
	6.35	L		cm	Length of the exchanger
	1.27	W		cm	Width of the exchanger
	508	Wc		æm	width of channel
	508	Ww		æm	Width of the wall separating channels
	508	Hc		æm	height of channel
	2667	thickne		æm	thickness of base of channel
	9	n			number of channels
		Dh	508	æm	Hydraulic Diameter
	1	à			aspect ratio (Alt-224)
		å	0.1379		free flow to frontal area ratio (Alt-2
					***** heater dimensions *****
	.04	Lheat		m	Length of heater
	.09	Wheat		m	Width of heater
					***** PROPERTIES *****
L		temp	23.13	øC	Temperature that props. are evaluated
		Cp	4.1805	KJ/kg/K	Specific Heat
		rho	997.3007	kg/m^3	Density
		æ	.000933	(N*s)/m^2	Dynamic Viscosity (Alt-230)
		k	0.6032	W/m/K	Thermal Conductivity
					***** CHANNEL CALCULATIONS *****
		AreaTot	2322576	æm^2	total free flow area
		Frontal	1870964	æm^2	frontal area of one channel section
		Rh	127	æm	Hydraulic Radius
		Area	258064	æm^2	Area of one Duct
		Perimet	2032	æm	Wetted Perimeter
					***** FLOW PROPERTIES *****
L		V	8.6111	m/sec	Velocity in each channel
		mdot	.002216	kg/sec	Mass flow rate IN EACH channel
					***** CHECKS ON LIMITS & SPECIF. *****
		LoverD	125		L/D ratio that must be > entry
		Entry	17.9927		used in determining if fully developed

		Vmph	19.263094mph	Velocity in channel (miles/hr)
L		QmLpm	133.33333mL/min	Volumetric flow rate (mL/min)
		Mdot	.0199460 kg/sec	mass flow rate for ALL channels togeth
		D	.000508 m	Hydraulic Diameter (meters)
		length	.0635 m	Length of the exchanger (m)
		width	.0127 m	Width of the exchanger (m)
				***** HEAT TRANSFER CHARACTERISTICS
L		Nu	86.1854	Nusselt Number
		h	102341.13W/m^2/K	Convective heat transfer coefficient
		alpha	1.44	total duct surf. area / area of circui
		Pr	6.4659	Prandtle number
	'heating	Dummy		for Dittus-Boelter, n=.3 or .4
		é	3.9964E-5m^2*K/W	Thermal Resistance (RJ Phillips)
		Tmax	24.69 øC	Maximum Temp in exchanger
	23	Ta	øC	Inlet Temp to exchanger
		Tbulk	23.13 øC	Bulk Temperature
L		f	0.039	Friction Factor
	1	eps	æm	channel roughness
				***** PRESSURE DROP *****
		deltaP	225736.96N/m^2	Pressure Drop in channels
	1	gc	kg*m/N/s^	gravitational constant
		Kc	.49716055	Contraction loss coefficient
		Ke	.72566381	Expansion loss coefficient
	1.2	Kb		Loss coefficient for 90ø bend
				**** Kays Loss coefficient model ****
		Kdgap	1.034	aspect ratio=0
		Kdcircl	1.0542	used to get Kdsquare
		Kdsquar	1.0634	aspect ratio=1
		DUMMY	.0267326	L/D/Re
		xstar	.00260437	L/(DRePr) want to be >0.1 for Fully De
L		deltaT	.25068697	tbulk out - tbulk in
L		Tb	23.250687	bulk temperature out
				**** variable substrate properties ***
		Tsi	23.844694	Temp of substrate - first guess 80
		Kw	180	thermal conductivity of substrate
				NOTE: the Kw may be SET at some temp.

TKSolver RULE Sheet

```
S       Rule
        ; ****************** Properties ******************
        Cp=Cp(temp)
        rho=rho(temp)
        æ=mu(temp)
        k=k(temp)

        ; ***** Calculate channel dimensional properties *****
        Perimeter=2*Wc + 2*Hc
        Area = Wc*Hc
        Rh=Dh/4      ;Area/Perimeter
C       Dh=4*Area/Perimeter
        å=Area/Frontal
        Frontal = (Wc+Ww)*(thickness/2+Hc)
C       à=Hc/Wc          ;To be in the 0 to 1 range the corrections are made in Rule sheets
C       n=ceiling(W/(Wc+Ww))
        AreaTotal=n*Area
        ; ***** this is the part used to get the max delta P *****
        Hc=Dh*(à+1)/2
        Wc=Hc/à
C       Ww=Wc*Hc/(å*(Hc+thickness))-Wc

        ;NOTE FOR THE PROPERTY FUNCTIONS, I'LL DO UNITS WITHIN EQUATION
        mdot=rho*(Area/1e12)*V          ; based on area of ONE duct
        Mdot=rho*(AreaTotal/1e12)*V     ; based on total area of the duct
        Q=(AreaTotal/1e12)*V            ; based on total area of the duct
        Re = rho*V*D/æ

        ;***** Checking L/D ratio for fully developed entry length *****
        LoverD=L/Dh
        IF Re<2300 THEN Entry=0.06*Re ELSE Entry=4.4*Re^(1/6)
        DUMMY=LoverD/Re
        ; **** Doing some units conversions for comparisons and equip specs. ****
        Vmph=V
        QmLpm=Q*60000000/n
        D=Dh/1e6
        length=L/1e6
        width=W/1e6

        ; ****************** Heat Transfer ********************
        Nu = h*D/k
        Pr = æ*(Cp*1000)/k
        alpha = n*Perimeter*L/(W*L)
        Nu=Nu(à)
C       é=Resistance(à)
        é=é(à)
        R=é*10000  ;to convert to cm^2*K/W
        ; ***** CALCULATING TEMP DIFFERENCE ****
        é=ëT/q``
        ëT=Tmax-Tb       ;This takes temp at end of exchr and adds total temp rise
```

```
temp = Tbulk
deltaT=q``*(length*(Wc+Ww)/1e6)/(mdot*Cp*1000)
deltaT=Tb-Ta
Tbulk=deltaT/2+Ta
; ****** Properties for the substrate ********
Tsi=Tbulk+ëT/2              ;these 2 should be uncommented for variable Ksi
C    Kw=ksi(Tsi)
Kw=180          ;the k(si) at low q`` doesnt really change R so leaving as constant
; **** CALCULATING PRESSURE DROP AND FRICTION FACTOR ****
f=f(à)
deltaP=rho(Ta)*V^2*Kb/(2*gc)+((V^2/(2*gc))/(1/rho(Ta)))*((Kc+1-å^2)+2*(rho(Ta)/
&rho(Tmax)-1)+f/4*L/Rh*rho(Ta)/rho(Tbulk)-(1-å^2-Ke)*rho(Ta)/rho(Tmax))+rho(Tmax)*V^
&2*Kb/(2*gc)
C    deltaP=((V^2/(2*gc))/(1/rho(Ta)))*((Kc+1-å^2)+2*(rho(Ta)/rho(Tmax)-1)+f/4*L/Rh*rho(Ta)/
C    &rho(Tbulk)-(1-å^2-Ke)*rho(Ta)/rho(Tmax))
deltaPsi=deltaP*.0001450

; ********* Kays loss coeffient model *********
if Re>2300 then Kdgap=0.75*f + 0.024*f^.5 + 1 else Kdgap=1.2
if Re>2300 then Kdcircle=1.09068*f + 0.05884*f^.5 + 1 else Kdcircle=1.333
Kdsquare=1.17*(Kdcircle-1)+1
; **** this next statement placed Kd in a list to linearly interpolate ****
Kdgap=place('Kd,1)
Kdsquare=place('Kd,2)
; **** this statement calculates the Kays loss coefficients ****
call K(à;Kc,Ke)
 ; *** this statement calculates for thermally devel. flow (want X*>0.1)
xstar=Lheat/(D*Re*Pr)
```

TKSolver FUNCTION Sheets

Name	Type	Arg.	Comment
Cp	List	1;1	Specific heat (KJ/Kg/K)
rho	List	1;1	Density (kg/m^3)
mu	List	1;1	Dynamic Viscosity (N*s)/m^2
k	List	1;1	Thermal conductivity (W/m/K)
ksi	List	1;1	Thermal conductivity Si (W/m/K)
NUsmall	List	1;1	Laminar Nusselt number 0<à<=0.1
NUmedsm	List	1;1	Laminar Nusselt number 0.1<à<=1
NUmedlrg	List	1;1	Laminar Nusselt number 1<à<10
Nulrg	List	1;1	Laminar Nusselt number à>=10
Nulam	Proced	2;1	Laminar Nusselt number
Nutrans	List	1;1	Transition Nusselt number
Nuturb	Rule	1;1	Turbulent Nusselt number
Nu	Rule	1;1	Nusselt Number
fReSQ	List	1;1	Laminar f*Re for sqr. duct (laminar)
fReGAP	List	1;1	Laminar f*Re for gap in plates (laminar)
f	Rule	1;1	Darcy friction factor
flam	Proced	2;1	Laminar friction factor
fturb	Proced	2;1	Turbulent friction factor
ftrans	List	1;1	Transition friction factor
Cg	List	1;1	contraction coefficient
Cc	List	1;1	contraction coefficient
Kd	List	1;1	Kays model-velocity distrib. coefficient
K	Rule	1;2	Kays loss coefficient model
é	Proced	1;1	Resistance Model (R J Phillips)
Resistance	Rule	1;1	Resistance Model (R J Phillips)
gap1side	List	1;1	Developing Laminar Nu (à<=0.1)
Nu4th	List	1;1	Developing Laminar Nu (à=1/4)
Nu3rd	List	1;1	Developing Laminar Nu (à=1/3)
NuHalf	List	1;1	Developing Laminar Nu (à=1/2)
NuOne	List	1;1	Developing Laminar Nu (à=1)
gap2sides	List	1;1	Developing Laminar Nu (à>=10)

Comment: **Specific heat (KJ/Kg/K)**
Domain List: TEMP
Mapping: Cubic
Range List: Cp_H2O

Element	Domain	Range
1	0	4.22
2	20	4.183
3	40	4.178
4	60	4.191
5	80	4.199
6	100	4.216
7	120	4.233
8	140	4.258
9	150	4.271
10	160	4.283
11	180	4.396
12	200	4.501
13	220	4.605
14	240	4.731
15	250	4.857
16	260	4.982
17	280	5.234
18	500	5.694

Comment: **Density (kg/m^3)**
Domain List: TEMP
Mapping: Cubic
Range List: rho_H2O

Element	Domain	Range
1	0	1000
2	20	998
3	40	992
4	60	983
5	80	972
6	100	958
7	120	944
8	140	926
9	150	917
10	160	908
11	180	887
12	200	863
13	220	837
14	240	809
15	250	794
16	260	779
17	280	750
18	500	700

Comment: **Dynamic Viscosity (N*s)/m^2**
Domain List: TEMP2
Mapping: Cubic
Range List: mu_H2O

Element	Domain	Range
1	0	.0017887
2	5	.0015155
3	10	.0013061
4	15	.0011406
5	20	.0010046
6	25	.0008941
7	30	.0008019
8	35	.0007205
9	40	.0006533
10	45	.0005958
11	50	.0005497
12	55	.0005072
13	60	.0004701
14	65	.0004359
15	70	.0004062
16	75	.0003794
17	80	.0003556
18	85	.0003341
19	90	.0003146
20	95	.0002981
21	100	.0002821
22	150	.000182
23	200	.000136
24	250	.000107
25	500	.000086

Comment: **Thermal conductivity (W/m/K)**
Domain List: TEMP
Mapping: Cubic
Range List: k_H2O

Element	Domain	Range
1	0	.555
2	20	.598
3	40	.627
4	60	.651
5	80	.669
6	100	.682
7	120	.685
8	140	.684
9	150	.683
10	160	.68
11	180	.673
12	200	.665
13	220	.652
14	240	.634
15	250	.624

16	260	.613
17	280	.588
18	500	.564

Comment: **Thermal conductivity Si (W/m/K)** used Al in comparison
Domain List: TEMP3
Mapping: Cubic
Range List: k_si

Element	Domain	Range
1	0	170
2	27	120
3	57	105
4	127	98
5	177	82
6	227	70

Comment: **Laminar Nusselt number 0<à<=0.1**
Domain List: ratio
Mapping: Cubic
Range List: case1L

Element	Domain	Range
1	0	0
2	.05	5.1
3	.1	4.85
4	.2	4.4
5	.3	4.05
6	.4	3.75
7	.5	3.55
8	.6	3.35
9	.7	3.2
10	.8	3
11	.9	2.8
12	1	2.7

Comment: **Laminar Nusselt number 0.1<à<=1**
Domain List: ratio
Mapping: Cubic
Range List: case3S

Element	Domain	Range
1	0	5.39
2	.05	4.75
3	.1	4.25
4	.2	3.64
5	.3	3.31
6	.4	.4
7	.5	3.15

8	.6	3.18
9	.7	3.2
10	.8	3.3
11	.9	3.4
12	1	3.56

Comment: **Laminar Nusselt number 1<à<10**
Domain List: ratio
Mapping: Cubic
Range List: case3L

Element	Domain	Range
1	0	8.23
2	.05	7.5
3	.1	6.94
4	.2	6.07
5	.3	5.39
6	.4	4.89
7	.5	4.51
8	.6	4.25
9	.7	3.99
10	.8	3.8
11	.9	3.7
12	1	3.56

Comment: **Laminar Nusselt number à>=10**
Domain List: ratio
Mapping: Cubic
Range List: case2L

Element	Domain	Range
1	0	8.23
2	.05	7.7
3	.1	7.25
4	.2	6.56
5	.3	6
6	.4	5.56
7	.5	5.2
8	.6	4.9
9	.7	4.66
10	.8	4.45
11	.9	4.3
12	1	4.09

Comment: **Laminar Nusselt number**
Parameter Variables: Re
Input Variables: alpha,XSTAR
Output Variables: NUlam

```
S       Statement
        if alpha<=0.1 goto A
        if alpha<=1 goto B
        if alpha<10 goto C
        if alpha>=10 goto D

        A: à:=alpha
          if XSTAR>0.1 goto a1
          if Re>8000 goto a1 ;this statement added because Nulam always calculated
          NUlam:=gap1side(XSTAR)
          goto ST
        a1: NUlam:=NUsmall(à)
          goto ST

        B: à:=alpha
          NUlam:=NUmedsm(à)
          if Re>8000 goto ST
          if XSTAR>0.1 goto ST
          NUFD:=NUlam
          NUH1:=8.235*(1-2.0421*à+3.0853*à^2-2.4765*à^3+1.0578*à^4-0.1861*à^5)
          if and (à>0.1,à<=0.25) goto b1
          if and (à>0.25,à<=.3333) goto b2
          if and (à>.3333,à<=0.5) goto b3
          if and (à>0.5,à<=1.0) goto b4
        b1: NUdevel4s:=gap1side(XSTAR)-(.1-à)/(.1-.25)*(gap1side(XSTAR)-Nu4th(XSTAR))
          GOTO XB
        b2: NUdevel4s:=Nu4th(XSTAR)-(.25-à)/(.25-.3333)*(Nu4th(XSTAR)-Nu3rd(XSTAR))
          GOTO XB
        b3: NUdevel4s:=Nu3rd(XSTAR)-(.3333-à)/(.3333-.5)*(Nu3rd(XSTAR)-NuHalf(XSTAR))
          GOTO XB
        b4: NUdevel4s:=NuHalf(XSTAR)-(.5-à)/(.5-1)*(NuHalf(XSTAR)-NuOne(XSTAR))
          GOTO XB
        XB: NUlam:=NUdevel4s*NUFD/NUH1
          goto ST

        C: à:=1/alpha
          NUlam:=NUmedlrg(à)
          if Re>8000 goto ST
          if XSTAR>0.1 goto ST
          NUFD:=NUlam
          NUH1:=8.235*(1-2.0421*à+3.0853*à^2-2.4765*à^3+1.0578*à^4-0.1861*à^5)
          if and (à>0.1,à<=0.25) goto c1
          if and (à>0.25,à<=.3333) goto c2
          if and (à>.3333,à<=0.5) goto c3
          if and (à>0.5,à<=1.0) goto c4
        c1: NUdevel4s:=gap2sides(XSTAR)-(.1-à)/(.1-.25)*(gap2sides(XSTAR)-Nu4th(XSTAR)
          goto XC
```

```
c2: NUdevel4s:=Nu4th(XSTAR)-(.25-à)/(.25-.3333)*(Nu4th(XSTAR)-Nu3rd(XSTAR))
   goto XC
c3: NUdevel4s:=Nu3rd(XSTAR)-(.3333-à)/(.3333-.5)*(Nu3rd(XSTAR)-NuHalf(XSTAR))
   goto XC
c4: NUdevel4s:=NuHalf(XSTAR)-(.5-à)/(.5-1)*(NuHalf(XSTAR)-NuOne(XSTAR))
   goto XC
XC: NUlam:=NUdevel4s*NUFD/NUH1
   goto ST

D: à:=1/alpha
   if XSTAR>0.1 goto d1
   if Re>8000 goto d1
   NUlam:=gap2sides(XSTAR)
   goto ST
d1: NUlam:=NUlrg(à)
   goto ST

ST:
```

Comment:	**Transition Nusselt number**
Domain List:	REYNOLD
Mapping:	Cubic
Range List:	NUSSELT

Element	Domain	Range
1	2300	3.556
2	2600	9.382
3	3000	13.903
4	3500	23.213
5	4000	47.152

Comment:	**Turbulent Nusselt number**
Parameter Variables:	Pr,Re,f
Argument Variables:	N
Result Variables:	Nu

```
S     Rule
      Nu=(f/2)*(Re-1000)*Pr/(1+12.7*(f/2)^.5*(Pr^(2/3)-1))
C     if Re<=10000 then Nu=(f/2)*(Re-1000)*Pr/(1+12.7*(f/2)^.5*(Pr^(2/3)-1))
C     if Re>10000 then Nu=0.9*(0.023*Re^.8*Pr^N)
```

Comment:	**Nusselt Number**
Parameter Variables:	Re,Pr,Dummy,rho,Cp,D,k,V,f,Lheat
Argument Variables:	à
Result Variables:	Nu

```
S     Rule
      if Dummy='heating then N=0.4   ;heating fluid
      if Dummy='cooling then N=0.3   ;cooling fluid
```

```
; LAMINAR NUSSELT NUMBER
XSTAR=Lheat/(D*Re*Pr)
Nulam=NUlam(à,XSTAR)
if Re<2300 then Nu = Nulam
; GRADUAL TRANSITION FROM LAMINAR TO TURBULENT TO ALLOW
; CONVERGENCE
PR=rho*V*D*Cp*1000/k  ;need to divide by Re to get Prandtle #s
Nulam2=((0.012*(2600^.87-280)*(PR/2600)^.4 + Nulam)/4)
Nulam=place('NUSSELT,1)
Nulam2=place('NUSSELT,2)
NUTURB1=place('NUSSELT,3)
NUTURB2=place('NUSSELT,4)
NUTURB3=place('NUSSELT,5)
NUTURB1=((0.012*(3000^.87-280)*(PR/3000)^.4 + Nulam)/3)
NUTURB2=((0.012*(3500^.87-280)*(PR/3500)^.4 + Nulam)/2)
NUTURB3=(0.012*(4000^.87-280)*(PR/4000)^.4)
if and (Re>2300,Re<4000) then Nu=NUtrans(Re)
; TURBULENT NUSSELT NUMBER
if Re>=4000 then Nu=NUturb(N)
```

Comment: **Laminar f*Re for sqr. duct (laminar)**
Domain List: RATIO
Mapping: Cubic
Range List: fReSQ

Element	Domain	Range
1	0	142
2	.001	111
3	.003	66
4	.005	51.8
5	.007	44.6
6	.009	39.9
7	.01	38
8	.015	32.1
9	.02	28.6
10	.03	24.6
11	.04	22.4
12	.05	21
13	.06	20
14	.07	19.3
15	.08	18.7
16	.09	18.2
17	.1	17.8
18	.2	15.8

Comment: **Laminar f*Re for gap in plates (laminar)**
Domain List: RATIO
Mapping: Cubic
Range List: fReGAP

Element	Domain	Range
1	0	287
2	.001	112
3	.003	67.5
4	.005	53
5	.007	46.2
6	.009	42.1
7	.01	40.4
8	.015	35.6
9	.02	32.4
10	.03	29.7
11	.04	28.2
12	.05	27.4
13	.06	26.8
14	.07	26.4
15	.08	26.1
16	.09	25.8
17	.1	25.6
18	.2	24.7

Comment: **Darcy friction factor**
Parameter Variables: D,Re,rho,V,æ,eps,Dh
Argument Variables: alpha
Result Variables: f

```
S     Rule
      if alpha>1 then à=1/alpha else à=alpha
      Re*flam=96*(1-1.3553*à+1.9467*à^2-1.7012*à^3+0.9564*à^4-0.2537*à^5)
C     if Re<2300 then f=flam
      if Re<2300 then f=flam(flam,à)

      Dle=D*(2/3+11/24*à*(2-à))
      ReDle=rho*V*Dle/æ
      if Re>=2300 then f= (1/(-1.8*log(6.9/ReDle + ((eps/Dh)/3.7)^1.11)))^2
```

Comment: **Laminar friction factor**
Parameter Variables: Dh,Re,L
Input Variables: flam,à
Output Variables: f

```
S     Statement
        RATIO:=L/Dh/Re
        if RATIO>.2 goto C
      ; ***** DEVELOPING FLOW *****
        fReSQ:=fReSQ(RATIO)
```

```
  fReGAP:=fReGAP(RATIO)
  fRe:=(fReSQ-(1-à)*(fReSQ-fReGAP))*4 ;linear interpolation
  f:=fRe/Re
  goto ST
; ***** FULLY DEVELOPED FLOW *****
C: f:=flam
  goto ST

ST:
```

Comment: **Turbulent friction factor**
Parameter Variables: L,Dh,Re,eps
Input Variables: ReDle,ReDeff
Output Variables: f

```
S    Statement
     if Re<=28000 goto A
     if Re>28000 goto B

     A: a:=0.0929+1.01612/(L/Dh)
       b:=-0.268-0.31930/(L/Dh)
       f:=a*ReDle^b
       goto ST
     B: f:=(1/(-1.8*log(6.9/ReDeff + ((eps/Dh)/3.7)^1.11)))^2
       goto ST
     ST:
```

Comment: **Transition friction factor**
Domain List: REYNOLDf
Mapping: Linear
Range List: FRICTION

Element	Domain	Range
1	2200	.0303653
2	2400	.0122768

Comment: **contraction coefficient**
Domain List: sigma
Mapping: Cubic
Range List: Cg

Element	Domain	Range
1	0	.6
2	.1	.61
3	.2	.62
4	.3	.625
5	.4	.63
6	.5	.64

7	.6	.67
8	.7	.685
9	.8	.725
10	.9	.78
11	1	1

Comment: **contraction coefficient**
Domain List: sigma
Mapping: Cubic
Range List: Cc

Element	Domain	Range
1	0	.6
2	.1	.615
3	.2	.633
4	.3	.65
5	.4	.67
6	.5	.69
7	.6	.715
8	.7	.74
9	.8	.78
10	.9	.83
11	1	1

Comment: **Kays model-velocity distrib. coefficient**
Domain List: asp
Mapping: Linear
Range List: Kd

Element	Domain	Range
1	0	1.02672
2	1	1.05032

Comment: **Kays loss coefficient model**
Parameter Variables: å
Argument Variables: alpha
Result Variables: Kc,Ke

S Rule
if alpha>1 then à=1/alpha else à=alpha
Kd=Kd(à)
Ke=1-2*Kd*å+å^2
if à>.1 then Cc=Cc(å) else Cc=Cg(å)
Kc=(1-2*Cc+Cc^2*(2*Kd-1))/(Cc^2)

Comment: **Resistance Model (R J Phillips)**
Parameter Variables: mdot,Cp,L,Ww,Wc,Hc,thickness,h,Lheat,Kw
Input Variables: alpha alpha
Output Variables: R

```
S       Statement
C       Kw:=100    ; thermal conductivity of the base of the channels
        a:  Ww:=Ww/1e6
        m:=(2*h/(Kw*Ww))^.5
        t:=thickness/1e6
        L:=Lheat
C       L:=L/1e6
        Wc:=Wc/1e6
        Hc:=Hc/1e6
        Cp:=Cp*1000
          if alpha<=0.1 goto A
          if alpha>=10 goto B
          goto C

        A: R:=t/Kw + L*(Ww+Wc)/(h*L*Wc)+L*(Ww+Wc)/(mdot*Cp)
          goto ST
        B: R:=t/Kw + (Ww+Wc)/(pi()*Kw) * ln ( 1/ (sin( pi()*Ww/ (2*(Ww+Wc)))))+L*(Ww+W
          goto ST
        C: R:=t/Kw + (Ww+Wc)/(pi()*Kw) * ln ( 1/ (sin( pi()*Ww/ (2*(Ww+Wc)))))+L*(Ww+W
          goto ST
        ST:
```

Comment: **Resistance Model (R J Phillips)**
Parameter Variables: mdot,Cp,Ww,Wc,Hc,thickness,h,Lheat,Kw
Argument Variables: alpha
Result Variables: R

```
S       Rule
        m=sqrt(2*h/(Kw*Ww/1e6))
        t=thickness/1e6
        L=Lheat
        if alpha<=0.1 then R=t/Kw+L*(Ww/1e6+Wc/1e6)/(h*L*Wc/1e6)+L*(Ww/1e6+Wc/1e6)/(md
        if and (alpha>.1,alpha<10) then R=t/Kw+(Ww/1e6+Wc/1e6)/(pi()*Kw)*ln(1/(sin(pi(
        if alpha>=10 then R=t/Kw+(Ww/1e6+Wc/1e6)/(pi()*Kw)*ln(1/(sin(pi()*Ww/1e6/(2*(W

C       if alpha>=10 then R=t/Kw+(Ww+Wc)/(pi()*Kw)*ln(1/(sin(pi()*Ww/(2*(Ww+Wc)))))+L
```

Comment: **Developing Laminar Nu (à<=0.1)**
Domain List: Xstar
Mapping: Cubic
Range List: gap1side

Element	Domain	Range
1	.1	6.19
2	.05	6.99
3	.03333	7.61

4	.025	8.09
5	.01666	8.85
6	.0125	9.45
7	.01	9.97
8	.008333	10.44
9	.007142	10.88
10	.00625	11.3
11	.005555	11.7
12	.000001	12.07

Comment: **Developing Laminar Nu (à=1/4)**
Domain List: Xstar
Mapping: Cubic
Range List: Nu4th

Element	Domain	Range
1	.1	6.03
2	.05	6.57
3	.0333333	7.07
4	.025	7.51
5	.0166666	8.25
6	.0125	8.87
7	.01	9.39
8	.0083333	9.83
9	.0071428	10.24
10	.00625	10.61
11	.0055555	10.92
12	.000001	11.23

Comment: **Developing Laminar Nu (à=1/3)**
Domain List: Xstar
Mapping: Cubic
Range List: Nu3rd

Element	Domain	Range
1	.1	5.45
2	.05	6.06
3	.03333333	6.6
4	.025	7.09
5	.01666666	7.85
6	.0125	8.48
7	.01	9.02
8	.00833333	9.52
9	.00714285	9.93
10	.00625	10.31
11	.00555555	10.67
12	.000001	10.97

Comment: **Developing Laminar Nu (à=1/2)**
Domain List: Xstar
Mapping: Cubic
Range List: NuHalf

Element	Domain	Range
1	.1	4.94
2	.05	5.6
3	.033333	6.16
4	.025	6.64
5	.0166666	7.45
6	.0125	8.1
7	.01	8.66
8	.0083333	9.13
9	.0071428	9.57
10	.00625	9.96
11	.0055555	10.31
12	.000001	10.64

Comment: **Developing Laminar Nu (à=1)**
Domain List: Xstar
Mapping: Cubic
Range List: NuOne

Element	Domain	Range
1	.1	4.48
2	.05	5.19
3	.0333333	5.76
4	.025	6.24
5	.0166666	7.02
6	.0125	7.66
7	.01	8.22
8	.0083333	8.69
9	.0071428	9.09
10	.00625	9.5
11	.0055555	9.85
12	.000001	10.18

Comment: **Developing Laminar Nu (à>=10)**
Domain List: Xstar
Mapping: Cubic
Range List: gap2sides

Element	Domain	Range
1	.1	8.56
2	.05	8.88
3	.0333333	9.19
4	.025	9.49
5	.0166666	10.02
6	.0125	10.49
7	.01	10.93
8	.0083333	11.34
9	.0071428	11.73
10	.00625	12.1
11	.0055555	12.46
12	.000001	12.81

#Comp1si.dat		(nine 504 micron channels)		
#TKSolver model without considering losses				
#mL/min	kPa		#psi	
1.111111	0.348063		0.050482	
18.84444	10.14832		1.47188	
36.57778	24.21555		3.512147	
54.31111	42.39237		6.148455	
72.04444	76.16927		11.04735	
89.77778	111.9584		16.23809	
107.5111	153.8888		22.31955	
125.2444	201.8344		29.27343	
142.9778	255.7107		37.08747	
160.7111	315.4371		45.75	
178.4444	380.9542		55.2524	
196.1778	452.2136		65.58763	
213.9111	529.1747		76.74982	
231.6444	611.8033		88.73401	
249.3778	700.0704		101.536	
267.1111	793.9507		115.1521	
284.8444	893.422		129.5791	
302.5778	998.4663		144.8144	
320.3111	1109.067		160.8555	
338.0444	1225.207		177.7001	
355.7778	1346.875		195.3465	
373.5111	1474.059		213.7928	
391.2444	1606.748		233.0376	
408.9778	1744.933		253.0795	
426.7111	1888.604		273.9171	
444.4444	2037.755		295.5495	

#Comp1asi.dat		(nine 504 micron channels)		
#TKSolver model with losses				
#mL/min	kPa		Delta Psi	
1.111111	0.234101		0.033953	
18.84444	8.619072		1.250083	
36.57778	18.98247		2.753157	
54.31111	31.18478		4.522942	
72.04444	62.63138		9.083857	
89.77778	91.11791		13.21545	
107.5111	124.1853		18.01144	
125.2444	161.7073		23.45352	
142.9778	203.6074		29.53058	
160.7111	249.8018		36.23046	
178.4444	300.2322		43.54472	
196.1778	354.8509		51.46645	
213.9111	413.6181		59.98987	
231.6444	476.5004		69.11012	
249.3778	543.4692		78.82306	
267.1111	614.4998		89.1251	
284.8444	689.5707		100.0132	
302.5778	768.6634		111.4845	
320.3111	851.7613		123.5368	
338.0444	938.8499		136.1678	
355.7778	1029.916		149.3758	
373.5111	1124.948		163.159	
391.2444	1223.936		177.5159	
408.9778	1326.871		192.4451	
426.7111	1433.743		207.9456	
444.4444	1544.545		224.016	

# Compar3s.dat							
#Raw Data Set 4			(nine 504 micron channels)				
#mL/min	kPa	Lower	Upper		#Psi	Lower	Upper
21.66646	0.958908	-0.489	2.406816		0.139077	-0.07092	0.349077
32.9772	9.117601	7.669693	10.56551		1.322388	1.112388	1.532388
48.09724	23.09549	21.64758	24.5434		3.349697	3.139697	3.559697
61.62897	42.55937	41.11146	44.00727		6.172676	5.962676	6.382676
80.56939	75.41215	73.96424	76.86006		10.93754	10.72754	11.14754
96.74647	105.9172	104.4693	107.3651		15.36189	15.15189	15.57189
107.2871	129.3973	127.9494	130.8452		18.76737	18.55737	18.97737
120.8053	163.747	162.2991	165.1949		23.74935	23.53935	23.95935
126.9832	181.2024	179.7545	182.6503		26.28102	26.07102	26.49102
136.4794	210.5342	209.0863	211.9821		30.53522	30.32522	30.74522
147.137	244.2502	242.8023	245.6981		35.42528	35.21528	35.63528
153.7648	265.8758	264.4279	267.3237		38.56179	38.35179	38.77179
164.5142	294.0408	292.5929	295.4887		42.64675	42.43675	42.85675
172.7393	317.0044	315.5564	318.4523		45.97731	45.76731	46.18731
193.3772	398.2423	396.7944	399.6902		57.7598	57.5498	57.9698
203.8648	438.738	437.2901	440.1859		63.63317	63.42317	63.84317
208.7684	455.9433	454.4954	457.3912		66.12857	65.91857	66.33857

#Compar5s.dat							
#Raw Data Set 5							
#mL/min	kPa	Lower	Upper		#Psi	Lower	Upper
38.45165	9.244438	-1.09776	19.58664		1.340784	-0.15922	2.840784
45.93904	16.75074	6.408537	27.09294		2.429474	0.929474	3.929474
50.85012	21.96268	11.62048	32.30488		3.185397	1.685397	4.685397
60.23394	33.42198	23.07978	43.76418		4.847419	3.347419	6.347419
66.38498	45.70461	35.36241	56.04681		6.628852	5.128852	8.128852
74.58957	59.76964	49.42744	70.11184		8.6688	7.1688	10.1688
78.20083	65.14243	54.80023	75.48463		9.448052	7.948052	10.94805
92.37955	89.80477	79.46257	100.147		13.025	11.525	14.525
98.47749	107.3918	97.04955	117.734		15.57576	14.07576	17.07576
106.3595	124.5615	114.2193	134.9037		18.066	16.566	19.566
119.1459	154.7972	144.455	165.1394		22.4513	20.9513	23.9513
135.1748	197.2267	186.8845	207.5689		28.60514	27.10514	30.10514
139.2475	213.594	203.2518	223.9362		30.979	29.479	32.479
165.9026	288.7759	278.4337	299.1181		41.88315	40.38315	43.38315
176.5644	327.0893	316.7471	337.4315		47.44	45.94	48.94
189.0015	373.6788	363.3366	384.021		54.19719	52.69719	55.69719
202.6938	422.4225	412.0803	432.7647		61.26683	59.76683	62.76683
210.5562	453.9342	443.592	464.2764		65.83718	64.33718	67.33718
228.3943	529.2942	518.952	539.6364		76.76716	75.26716	78.26716
236.4659	564.0102	553.668	574.3524		81.80225	80.30225	83.30225
245.6334	588.9883	578.6461	599.3305		85.425	83.925	86.925
260.3829	676.1248	665.7826	686.467		98.06301	96.56301	99.56301
276.0278	715.2976	704.9554	725.6398		103.7445	102.2445	105.2445
306.235	851.2093	840.8671	861.5515		123.4567	121.9567	124.9567
302.1816	895.6676	885.3254	906.0098		129.9048	128.4048	131.4048
306.8527	910.3053	899.9631	920.6475		132.0278	130.5278	133.5278
316.585	945.4977	935.1555	955.8399		137.132	135.632	138.632
325.0323	988.331	977.9888	998.6732		143.3444	141.8444	144.8444
342.1511	1084.367	1074.025	1094.709		157.2732	155.7732	158.7732
354.3909	1154.717	1144.375	1165.059		167.4765	165.9765	168.9765
357.6807	1187.174	1176.831	1197.516		172.1839	170.6839	173.6839
357.6807	1187.174	1176.831	1197.516		172.1839	170.6839	173.6839

#Compar4a.dat					#Compar6.dat	
#Raw Data Set 4					#TKSolver model	
#mL/min	#Delta T (°C)	Lower	Upper		#mL/min	#Delta T (°C)
21.66646	2.084123	1.804123	2.364123		18.84444	4.625558
32.9772	1.379627	1.099627	1.659627		36.57778	2.381985
48.09724	0.958182	0.678182	1.238182		54.31111	1.603985
61.62897	0.789394	0.509394	1.069394		72.04444	1.209078
80.56939	0.625354	0.345354	0.905354		89.77778	0.970208
96.74647	0.529811	0.249811	0.809811		107.5111	0.810152
107.2871	0.479175	0.199175	0.759175		125.2444	0.695427
120.8053	0.323242	0.043242	0.603242		142.9778	0.609163
126.9832	0.304441	0.024441	0.584441		160.7111	0.541939
136.4794	0.398612	0.118612	0.678612		178.4444	0.488077
147.137	0.379917	0.099917	0.659917		196.1778	0.443954
153.7648	0.375955	0.095955	0.655955		213.9111	0.407147
164.5142	0.371723	0.091723	0.651723		231.6444	0.375976
172.7393	0.366385	0.086385	0.646385		249.3778	0.349238
193.3772	0.352816	0.072816	0.632816		267.1111	0.326051
203.8648	0.353659	0.073659	0.633659		284.8444	0.305751
208.7684	0.349169	0.069169	0.629169		302.5778	0.287831
					320.3111	0.271895
					338.0444	0.257631
					355.7778	0.244789
					373.5111	0.233166
					391.2444	0.222597
					408.9778	0.212945
					426.7111	0.204095
					444.4444	0.195951

BIBLIOGRAPHY

Abernathy, R. B., Benedict, 1985, "Measurement Uncertainty: A Standard Methodology," *ISA Transactions*, Volume 24, Number 1, New York.

ANSI/ASME PTC 19.1-1985, 1985, *Measurement Uncertainty*, The American Society of Mechanical Engineers, New York.

Ariman, T., Turk, M. A., and Sylvester, N. D., 1973, "Microcontinuum Fluid Mechanics-A Review," *International Journal of Engineering Science*, Vol. 11, pp. 905-930.

Arkilic, E. B., Breuer, K. S., and Schmidt, M. A., 1994, "Gaseous Flow in Microchannels," *FED-Vol. 197, Application of Microfabrication to Fluid Mechanics, ASME 1994*, pp. 57-66.

ASME *Steam Tables, 3rd ed.*, 1977, The American Society of Mechanical Engineers, New York.

ASME *Steam Tables, 5th ed.*, 1983, The American Society of Mechanical Engineers, New York.

Bar-Cohen, A., 1985, "Thermal Management of Air and Liquid-Cooled Multi-Chip Modules," 23rd ASME/AICHE national heat Transfer Conference, Denver, Colorado, August 4 - 7, 1985, pp. 1-36.

Beskok, A., and Karniadakis, G. E., 1992, "Simulation of Slip-Flows in Complex Micro-Geometries," *ASME Proceedings* DSC-Vol. 40, pp. 355-370.

Cheremisinoff, Nicholas P., 1987, *Practical Statistics for Engineers and Scientists*, Technomic Publishing Co., Lancaster, PA.

Choi, S. B., 1991a, "Friction Factors and Heat Transfer in Microtubes," D. E. Dissertation, College of Mechanical and Industrial Engineering, Louisiana Tech University.

Choi, S. B., Barron, R. F., and Warrington, R. O., 1991b, "Fluid Flow and Heat Transfer in Microtubes," *Micromechanical Sensors, Actuators, and Systems,* ASME, New York, NY, DSC-Vol. 32, pp. 123-134.

Curr, R. M., Sharma, D., and Tatchell, D.G., 1972, "Numerical Predictions of Some Three-dimensional Boundary Layers in Ducts," *Comput. Methods Appl. Mech. Eng. 1*, p. 143.

Cuta, Judi, 1995, personal conversation, Battelle Pacific National Laboratory, Richland, WA.

Dennis, S. C. R., and Smith, N., 1966, "Forced Convection From a Heated Flat Plate," *Journal of Fluid Mechanics,* Vol. 24, part 3, pp. 509-519.

Eringen, A. C., 1964, "Simple Microfluids," *International Journal of Engineering Science,* Vol. 2, pp. 205-217.

Eringen, A. C., 1972, "Theory of Thermomicrofluids," *Journal of Mathematical Analysis and Applications,* Vol. 38, pp. 480-496.

Figliola, R. S. and Beasley, D. E., 1995, *Theory and Design for Mechanical Measurements 2nd edition*, John Wiley & Sons, Inc., New York.

Flik, M. I., Choi, B. I., and Goodson, K. E., 1992, "Heat Transfer Regimes in Microstructures," *Journal of Heat Transfer,* Vol. 114, pp. 666-674.

Goodling, J., 1993, "Microchannel Heat Exchangers," *SPIE Vol. 1997 High Heat Flux Engineering II* , pp. 66-82.

Gravesen, P., Branebjerg, J., and Jensen, O. S., 1993, "Microfluidics-A Review," *Journal of Micromechanics and Microengineering,* Vol. 3, pp. 168-182.

Harley, J., Pfahler, J., and Bau, H., 1989, "Transport Processes in Micron and Submicron Channels," *Winter Annual Meeting of the ASME*, December 10-15, San Fransisco, Ca, ASME, New York, N.Y., Vol. 116, 1-5.

Hartnett, J. P. and Kostic, M, 1989, "Heat Transfer to Newtonian and Non-Newtonian Fluids in Rectangular Ducts," *Advances in Heat Transfer,* Vol. 19, 1989, pp. 247-356.

Hodge, B. K., 1990, *Analysis and Design of Energy Systems*, Prentice Hall Inc., Englewood Cliffs, N.J..

Holman, J. P., 1990, *Heat Transfer*, 7th edition, McGraw-Hill Inc. New York, New York.

Hyland, R. W. and Wexler, A., 1980, "Formulations for the Thermodynamic Properties of the Saturated Phases of Water from 173.15K to 473.15K," Final Report, ASHRAE Project RP216, Part 1.

Jacobi, A. M., 1989, "Flow and Heat Transfer in Microchannels Using a Microcontinuum Approach," *Journal of Heat Transfer,* Vol. 111, pp. 1083-1085.

John, J. A., 1984, *Gas Dynamics*, Allyn and Bacon, Inc., Boston , pp. 338-349.

Kays, W. M., 1950, "Loss Coefficients for Abrupt Changes in Flow Cross Section With Low Reynolds Number Flow in Single and Multiple-Tube Systems," *Transactions of the ASME,* pp. 1067 - 1074.

Kays, W. M., and London, A. L., 1964, *Compact Heat Exchangers*, 2nd ed., New York: McGraw Hill, 1964.

Kays, W. M., 1985, "Internal Flow in Ducts" *Handbook of Heat Transfer,* (Rohsenow, W. M., Hartnett, J. P., and Ganic, E. N., eds.), pp. 7.1 - 7.16, McGraw Hill, Inc., New York.

Kays, W. M. and Crawford, B., 1985, *Convective Heat and Mass Transfer*, McGraw-Hill Book Company, New York.

Liu, J. and Tai, Y., 1995, "MEMS for Pressure Distribution Studies of Gaseous Flows in Microchannels," *0-7803-2503-6©1995 IEEE*, pp. 209-215.

Ma, S. W., and Gerner, F. M., 1993, "Forced Convection Heat Transfer From Microstructures," *Journal of Heat Transfer,* Vol. 115, pp. 872-880.

Nagashima, A., 1977, "Viscosity of Water Substance - New International Formulation and its Background," *J. Phys. Chem. Ref. Data*, Vol. 6, No. 4.

Pfahler, J., Harley, J., Bau, H., and Zemel, J., 1990, "Liquid and Gas Transport in Small Channels," *Winter Annual Meeting of the ASME, Microstructures, Sensors, and Actuators,* ASME, New York, NY, Vol. 19, pp. 149-157.

Pfahler, J., Harley, J., Bau, H., and Zemel, J., 1991, "Gas and Liquid Flow in Small Channels," *Micromechanical Sensors, Actuators, and Systems,* ASME, DSC-Vol. 32, pp. 49-60.

Phillips, R. J., 1987, "Forced-Convection, Liquid-Cooled, Microchannel Heat Sinks," Master of Science Thesis, Department of Mechanical Engineering, Massachusetts Institute of Technology.

Pong, K., Ho, C., Liu, J., and Tai, Y., 1994, "Non-Linear Pressure Distribution in Uniform Microchannels," *FED-Vol. 197, Application of Microfabrication to Fluid Mechanics, ASME 1994*, pp. 51-56.

Rohsenow, W. M., Hartnett, J. P., and Ganic, E. N., 1985, *Handbook of Heat Transfer*, McGraw Hill, New York.

Shah, R. K. and Bhatti, M. S., 1987, "Laminar Convective Heat Transfer in Ducts," *Handbook of Single-Phase Convective Heat Transfer*, (S. Kakac, R.K. Shah, and W. Aung, eds.) pp. 3.1 - 3.137, Wiley (Interscience), New York.

Tuckerman, D. B., 1984, "Heat-Transfer Microstructures for Integrated Circuits," PhD Dissertation, Department of Electrical Engineering, Stanford University.

Tuckerman, D. B., and Pease, R. F. W., 1981, "High-Performance Heat Sinking for VLSI," *IEEE Electronic Device Letters,* Vol. EDL-2, No. 5, pp. 126-129.

Urbanek, W., Zemel, J., and Bau, H. H., 1993, "An Investigation of the Temperature Dependence of Poiseuille Numbers in Microchannel Flow," *Journal of Micromechanics and Microengineering,* Vol. 3, pp. 206-208.

van Oudheusen, B. W., 1992, "Silicon Thermal Flow Sensors," *Sensors and Actuators, Part A,* Vol. 30, pp. 5-26.

Vincinti, W. G. and Kruger, C. H., 1965, *Introduction to Gas Dynamics,* John Wiley and Sons, Inc., New York, NY, p. 16.

Wang, B. X. and Peng, X. F., 1994, "Experimental Investigation on Liquid Forced Convection Heat Transfer Through Microchannels," *International Journal of Heat and Mass Transfer,* Vol. 37, Supplement 1, pp. 73-82.

White, F. M., 1986, *Fluid Mechanics*, 2nd ed., McGraw-Hill Inc., New York, NY.

White, F. M., 1991, *Viscous Fluid Flow*, 2nd ed., McGraw-Hill Inc., New York, NY.

Wu, P., and Little, W. A., 1983, "Measurement of Friction Factors for the Flow of Gasses in Very Fine Channels Used for Microminiature Joule-Thompson Refrigerators," *Cryogenics,* May, pp. 273-277.

Wu, P., and Little, W. A., 1984, "Measurement of the Heat Transfer Characteristics of Gas Flow in Fine Channel Heat Exchangers Used for Microminiature Refrigerators," *Cryogenics,* August, pp. 415-420.

Yu, D., Warrington, R., Barron, R., and Ameel, T., 1994, "An Experimental and Theoretical Investigation of Fluid Flow and Heat Transfer in Microtubes," *ASME/JSME International Thermal Engineering Conference*, Maui, Hawaii.